KINEMATICS OF THE PAPAROA METAMORPHIC CORE COMPLEX, WEST COAST, SOUTH ISLAND, NEW ZEALAND

A THESIS SUBMITTED IN

FULFILLMENT OF THE REQUIREMENTS FOR

THE DEGREE OF

MASTER OF SCIENCE IN GEOLOGY

AT THE UNIVERSITY OF CANTERBURY

BY DANIEL OTTO SCHULTE

UNIVERSITY OF CANTERBURY

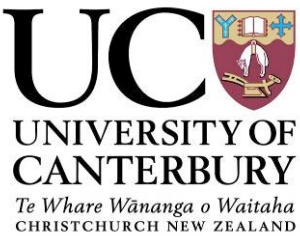

2011

Frontispiece

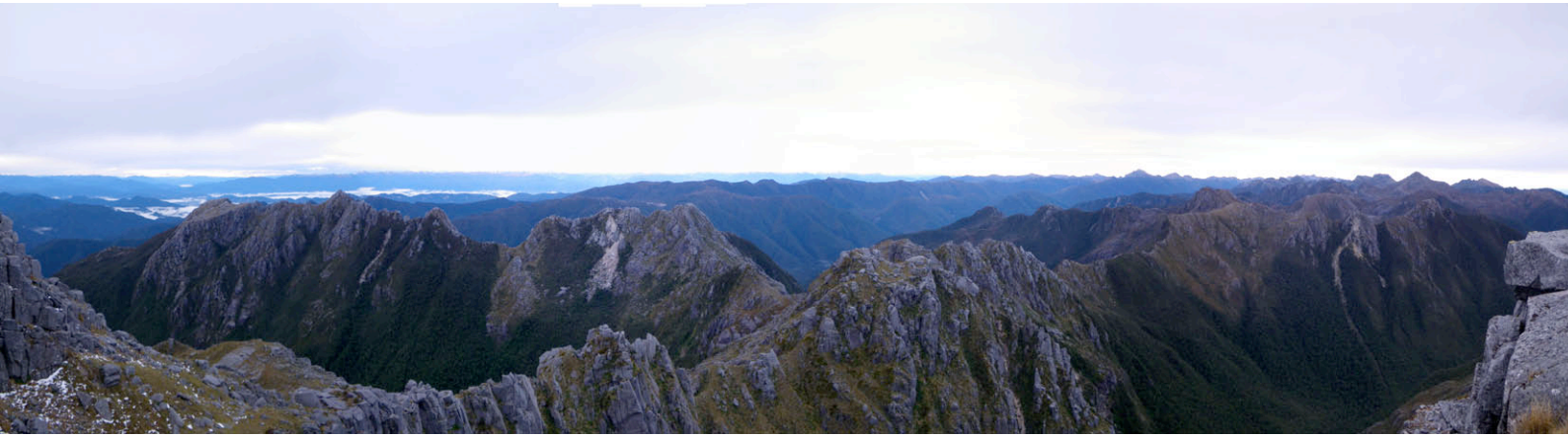

– The rugged Paparoa Range: unroofed mid-crustal rocks as a result of continental extension –

Main ridge at Buckland Peaks, southeast of Westport.

TABLE OF CONTENTS

LIST OF FIGURES

LIST OF TABLES

Acknowledgements

Firstly and most importantly I would like to thank my supervisors Uwe Ring and Mark Quigley for their support, stimulating discussions and encouragement. Their valuable comments, feedback and ideas often gave me new perspective and motivation for my research.

Many thanks go to Rob Spiers who helped me process a large amount of thin sections and to David Shelley who helped me to improve my skills with the microscope. The discussions with David Shelley were most appreciated and gave me many new insights into the matter.

Thanks also to Stuart Thomson for processing and analyzing the fission track samples collected by Uwe Ring. The opportunity to use their data for my thesis allowed a different approach to the topic. Thanks go to Stéphanie Brichau for her remote assistance and explanation of the statistical methods of the fission track analysis.

I am thankful for the exchange of ideas with all those mentioned above, as well as Malcolm Laird, my officemates and everyone else in the Department of Geology. These inspiring dialogues widened my scientific horizons during my time at the University of Canterbury.

Special thanks go to my friends Fanny Leyrat, Hamish Carrad, Jacob Ervin, Mira Schwill, Christoph Völz, Caroline Forslund and Natasha Sydorenko for accompanying me in the field, especially to the Paparoa Range, to meet safety regulations and to carry many heavy rock samples. Owing to their company and adventurous spirit I will keep my fieldwork on the West Coast in good memory.

Thanks to Alan Rosanowski and Airwest Helicopters for dropping off and picking up my fellows and me in the rugged Paparoa Range and fulfilling extra wishes like stopovers on various peaks.

Gratitude to the German Acamdemic Exchange Service (DAAD) for the financial support to come to New Zealand and to the Mason Trust Fund for the financial support of my research.

I also want to mention Pat Roberts, Janet Warburton, Sacha Baldwin-Cunningham, Kerry Swanson, John Southward and Anekant Wandres representatively for the staff. Their administrative and technical support made my work at the University of Canterbury as easy and uncomplicated as possible and their friendly nature contributed to a very comfortable atmosphere in the department, which I greatly appreciated.

Many thanks go to Tiffany DeJager-Kennedy who proofread numerous drafts of this thesis. Owing to her patience and diligence this thesis is written in acceptable English.

Finally I want to thank my family and my friends, especially those I made in New Zealand, for their support and love, which made my time in New Zealand unforgettably amazing.

Abstract

The Paparoa Metamorphic Core Complex developed in the Mid-Cretaceous due to continental extension conditioning the crust for the eventual breakup of the Gondwana Pacific Margin, which separated Australia and New Zealand. It has two detachment systems: the top-NE-displacing Ohika Detachment at the northern end of the complex and the top-SW-displacing Pike Detachment at the southern end of the complex. The structure is rather unusual for core complexes worldwide, which are commonly characterised by a single detachment system. Few suggestions for the kinematics of the core complex development have been made so far. In this study structural-, micrographic- and fission track analyses were applied to investigate the bivergent character and to constrain the kinematics of the core complex. The new results combined with reinterpretations of previous workers' observations reveal a detailed sequence of the core complex exhumation and the subsequent development.

Knowledge about the influence and the timing of the two respective detachments is critical for understanding the structural evolution of the core complex. The syntectonic Buckland Granite plays a key role in the determination of the importance of the two detachment systems. Structural evidence shows that the Pike Detachment is responsible for most of the exhumation, while the Ohika Detachment is a mere complexity. In contrast to earlier opinions the southwestern normal fault system predates the northeastern one. The Buckland Pluton records the ceasing pervasive influence of the Pike Detachment, while activity on the Ohika Detachment had effect on the surface about ~8 Ma later.

Most fission track ages are not related to the core complex stage, but reflect the younger late Cretaceous history. They show post core complex burial and renewed exhumation in two phases, which are regionally linked to the development of the adjacent Paparoa Basin and the Paparoa Coal Measures to the southwest and to the inception of seafloor spreading in the Tasman Sea in a larger context.

Background

In controlling continental breakup, extensional tectonics is one of the most fundamental processes that shape the face of our planet. Extension and breakup are major keys to understanding the evolution of continents and the origin of sedimentary basins and their hydrocarbon potential, as well as the thermohaline circulation in the oceans and thus global climate. Yet, the mechanisms by which continents split apart are poorly known. The thermal state of continental crust and its rheological structure control the variation between flow in the ductile lower crust and localised deformation in the brittle upper crust and explains the location and the layout of core complexes (e.g. Buck 1991; Bertotti et al. 2000; Rosenbaum et al. 2005; Wijns et al. 2005). The latter are the precursors of continental breakup and result from extreme extension where the lower crust is dragged to the surface (where it can be studied) below large-scale extensional faults (detachments) (e.g. Lister & Davis 1989; Spell et al. 2000; Tulloch et al. 2009). It is these initial stages of extension which precondition the lithosphere for breakup and which are thus critically important.

The thermal structure of exposed core complexes provides key answers to understanding the partitioning of deformation processes and their interaction with magmatic and metamorphic processes in the lower crust. The footwalls of the Snake Range core complex in the Basin and Range province (USA), the Naxos core complex in the Aegean (Greece), and the Fiordland and Paparoa core complexes in Westland (New Zealand) have been intruded or partially melted during extensional deformation, suggesting a hot, weak footwall region (Coney 1974; Lister et al. 1984a; Gibson et al. 1988).

The Paparoa Core Complex has two detachment systems: the top-N-displacing Ohika Detachment at the northern end of the complex and the top-S-displacing Pike Detachment at the southern end of the complex (Tulloch & Kimbrough 1989). This is rather unusual for core complexes worldwide, which are commonly characterised by a single detachment system (cf. Coney 1980). Existing data from the Paparoa Core Complex could suggest that the top-S Pike Detachment is actually the major detachment system and that the top-N Ohika Detachment is only a minor late complexity that was not important for core complex development. Critical in this regard is which detachment controlled the emplacement of the huge Buckland Granite that makes up almost half of the footwall of the Paparoa Core Complex and is exposed in the footwall of the Ohika Detachment (Nathan 1978; Tulloch & Kimbrough 1989).

CHAPTER 1: INTRODUCTION

1.1. Metamorphic Core Complexes

Tectonic models of metamorphic core complexes were developed over the course of the last 60 years. Early research on mountain belts recognized the tectonic juxtaposition of deformed and metamorphosed rocks below relatively undeformed material. These structures were classified as “mantled gneiss domes” (Eskola 1949). Eskola noticed that the gneiss was subject to shearing and ductile flow, that granites intruded into some of the gneiss dome cores and that the lowest horizon of the undeformed adjacent cover often consists of conglomerates with boulders of the gneiss core itself. Thus some of the key features of a core complex were already described.

Many metamorphic terranes showing these features were identified in the North American Cordillera from southern Canada to northwestern Mexico (cf. Coney 1980). The metamorphic areas were found to be separated from the unmetamorphosed and mildly deformed cover rocks by low-angle faults. These tectonic contacts are zones of relatively steep metamorphic gradients and were recognized as the most distinctive structural element in the entire region (Misch 1960). They became known as “décollements” while the high-grade and non-metamorphic rocks were named “infrastructure” and “suprastructure” respectively (Misch 1960; Armstrong & Hansen 1966). These first investigations in the North American Cordillera could yet not explain the origin of these structures. However, they eventually initiated a process of research that led to the development of the idea of metamorphic core complexes.

In the 1970s the tectonic and kinematic aspects gained center stage. Price & Mountjoy (1970) proposed a buoyantly rising infrastructure linked to a gravitational lateral movement away from the uprising block. This movement was seen as “denudation faulting” on the décollements with significant displacement on regional scale, and extension was considered to be a possible reason (Armstrong 1972). Finally Davis & Coney (1979) established regional high-temperature extensional deformation as a trigger for normal faulting and unroofing. For several reasons they realized that the metamorphic terranes in the North American Cordillera are something different than gneiss domes and coined the term “metamorphic core complexes”. Davis (1980) suggested a graphic concept that core complexes are in fact megaboudins which accommodate continental extension.

The nomenclature was assigned to gneiss domes and consequently the terms “infrastructure”, “suprastructure” and “décollement” were replaced by the more appropriate terms “lower plate”,

“upper plate” and “detachment” respectively (Davis & Lister 1988). These terms have been used in the scientific community since.

A summary of the metamorphic core complex model proposed by Coney (1980), Crittenden (1980), Davis (1980), Reynolds and Rehrig (1980) reads as follows:

A metamorphic core complex is a dome-like structure that consists of three main elements: a metamorphic-plutonic basement in the footwall (the lower plate), which is separated from an unmetamorphosed cover in the hanging wall (the upper plate) by a low-angle normal fault (the detachment).

The detachment is the most distinctive aspect of a core complex. It juxtaposes the unmetamorphosed cover rocks and the metamorphic basement and represents a discontinuity of extreme ductility contrast: the deformation is brittle above and ductile below. Usually, it is best developed on one side of a given complex. Thus an asymmetry in the amount of deformation can be observed in many core complexes.

Typically, the upper part of the lower plate consists of mylonitic gneiss. The bearing of the lineation, which can be found on characteristically low-dipping foliation planes, is often remarkably constant and parallels the maximum extension direction within a particular core complex. With increasing distance from the detachment the mylonitic fabric diminishes and reveals either an older metamorphic fabric or a more plutonic one. Hence, the mylonitic foliation and lineation overprint older fabrics and record the deformation induced by the detachment. In proximity to the detachment brittle deformation is superimposed on the ductile features. High angle normal faults crosscut the foliation. Right below the detachment the rocks are brecciated and show extensive alteration like retrograde chlorite or hematite.

Granitic plutons within the lower plate are very common. Some of them show the mylonitic fabric, others do not. As the detachment is approached the characteristic foliation and lineation is acquired progressively as well.

The upper plate consists of original cover material of the core complex and sometimes of metamorphic basement and granitic plutons that have been eroded as well. Adjacent basins develop in the process of uplift of the core with subsequent gravitational gliding and transport of the upper plate relative to the basement. These basins accommodate the proximal deposits of eroded original cover and basement rocks and typically contain coarse material like conglomerates. Usually the upper plate rocks are not metamorphosed. Continuous development of the core complex leads to listric faults in the upper plate, brittle deformation and tilting of entire blocks.

This model described all major features of metamorphic core complexes. But the explanation of the origin of the shallow-dipping detachment faults posed a problem and is debated to the current day.

At first a model for continental extension facilitated by shallow-dipping crustal shear zones was suggested (cf. Reynolds & Rehrig 1980; Davis et al. 1983; Lister et al. 1984a; Lister et al. 1984b; Davis et al. 1986). But low-angle normal faults could not be observed in present regions of continental extension, nor could they be easily explained (Jackson 1987; Lister & Davis 1989). However, field data indicate that shallow-dipping faults of large areal extent are forming in extending continental crust (Davis & Lister 1988). Recent continental extension is expressed in steeply-dipping and deeply-biting normal faults. It was proposed that sub-horizontal ductile shear zones could develop at the base of these faults to relax seismogenic stress rises (Jackson 1987; Jackson & White 1989). Domino-like rotation of crustal blocks confined by the faults and shear zones could expose the ductile mylonites (Proffett 1977; Davis et al. 1983; Davis 1987; Jackson & White 1989; Lister & Davis 1989). Others suggested that the detachments are listric normal faults with domino-like arrays of normal faults in the upper plate (cf. Wernicke & Burchfiel 1982). Only later recent low-angle faults were discovered, which indicate that detachments can be active at low angles (Hayman et al. 2003) and are coupled to steeper normal faults in the hanging wall similarly to the model of Jackson and White (1989).

Lister and Davis (1989) merged these ideas into the model of evolving crustal shear zones (Figure 1.01), as summarized below:

Lower to middle crust is dragged out from beneath the extending upper crust. Detachments are merely the upper brittle equivalents of the deeper-seated ductile movement zones. They do not remain active throughout the entire geological history of core complex development. Present day detachments are only the last of a sequence of faults that splayed off a so-called primary master fault that represents the basal shear zone of the high-angle normal faults.

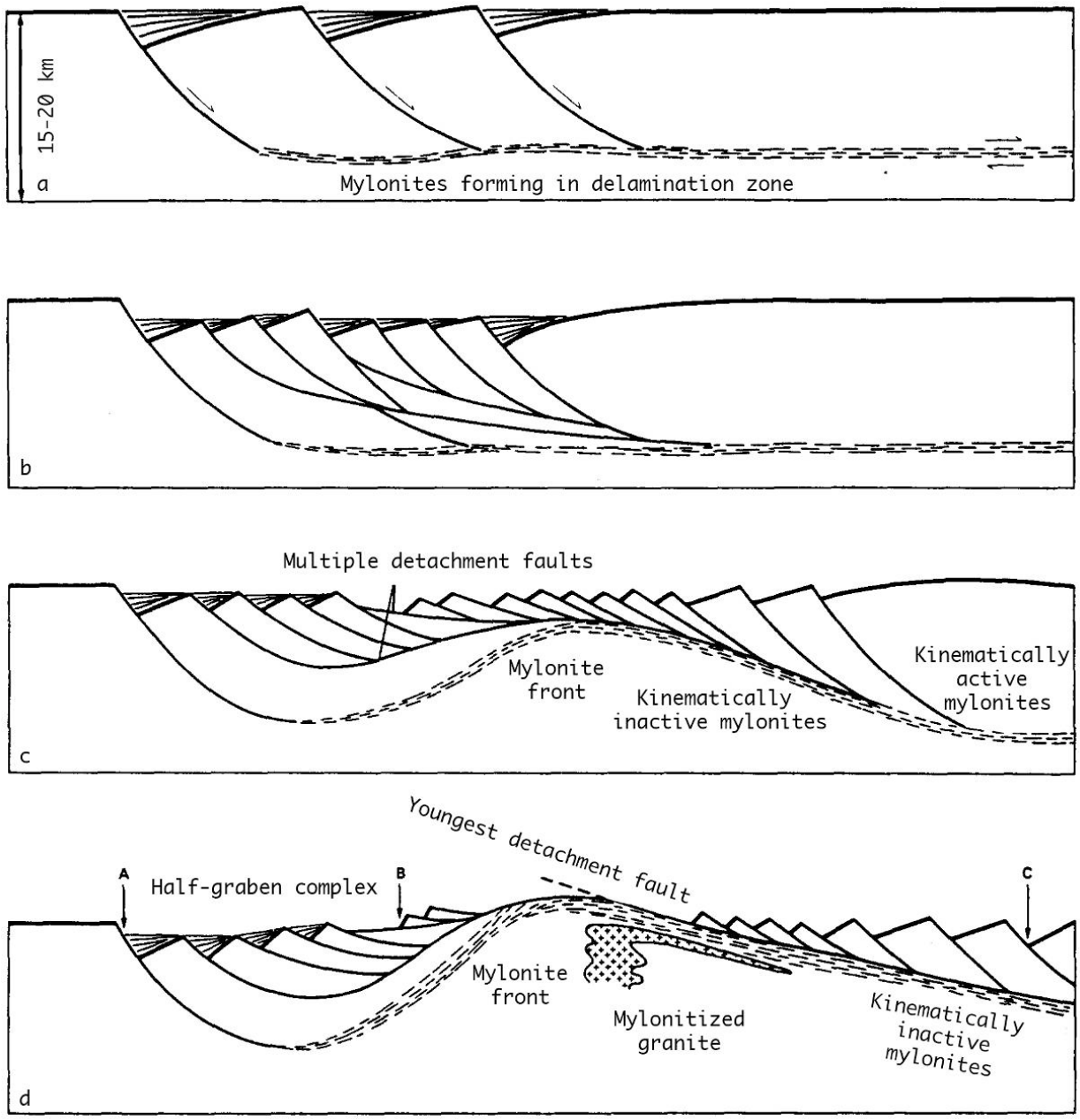

Figure 1.01 (after Lister & Davis 1989): Model of the development of a metamorphic core complex assuming (a) an initially sub-horizontal ductile shear zone at depth, decoupling the middle to lower crust beneath a steeply-dipping array of deeply-biting normal faults in the upper plate. (b) Low-angle normal faults are created from this zone, and the geometry of upper plate extension becomes increasingly complex. The detachment faults splaying from the basal shear zone act as master faults, controlling the generation of successive faults. (c) As the result of unloading and the isostatic effects of granite intrusion at depth, the lower plate bows upward, with multiple detachment faults splaying from the developing culmination. The older faults are more bowed. (d) The metamorphic core complex is exposed underneath relatively young detachment faults, with faults A and B related to earlier stages of this evolutionary process. The mylonitic front is related to an upwarped, once sub-horizontal, ductile shear zone.

1.2. Thesis Objectives

Since Tulloch and Kimbrough (1989) proposed a tectonic model of the Paparoa Metamorphic Core Complex new data has been acquired and more detailed conclusions about the development of the core complex have been inferred (White 1994; Muir et al. 1997; Spell et al. 2000; Klepeis et al. 2007). This thesis was undertaken to investigate the control of the two detachments over the emplacement of the syntectonic pluton, to assess the role of the two detachments, to narrow down the structural hinge of the core complex and to determine if the exhumation history was dominated by both or only by one detachment fault like most of the core complexes in the North American Cordillera and the Agean Sea.

These objectives were achieved by the following research:

1) Structural mapping of the exposed lower plate at Cape Foulwind, Charleston and the Paparoa Range, in particular lineations and shear sense indicators
2) Petrographic studies in order to put thermal constraints on the deformation and to determine a sense of shear on the microscopic scale
3) Fission track analyses to reconstruct aspects of the thermal history of the footwall

1.3. Location of Study

The Paparoa Metamorphic Core Complex is located in the Buller District on the West Coast of the South Island, New Zealand (Figures 1.06, 1.07). Tertiary and Quaternary sediments cover large parts of the footwall. Additionally, the dense rainforest, steep slopes and rugged terrain, which are typical for this region, limit the accessible exposure. Therefore the study area was restricted to Cape Foulwind and Siberia Bay 11 km west of Westport, the coastline at Charleston between Parson Hill and Doctors Bay, the coastline at White Horse Creek (between Morrissey Creek and Belfast Creek) and the Buckland Peaks and Mount Kelvin, both in the Paparoa Range.

1.4. Methods

1.4.1. Fieldwork

Seven weeks were spent for fieldwork on the West Coast from March to August 2010. Outcrops were suggested by the thesis supervisor (pers. comm. Ring 2010), located using NZ Geological Map Sheets S23 & S30 "Foulwind and Charleston" and S31 & S32 "Buller-Lyell" (Nathan 1975, 1978) as well as using information of previous workers (cf. Shelley 1970b; Lewthwaite 1995; Herd 2007; Klepeis et al. 2007). Structural data were measured with a Brunton compass. All compass bearings mentioned in this thesis have the format dip direction/dip (i.e. the first value is the dip azimuth) and not the format strike/dip/quadrant as commonly used in New Zealand.

Fieldwork in the remote Paparoa Range relied on assistance of friends due to safety regulations and logistic requirements. Because of the poor access to the southern part of the Buckland Granite and the central Paparoa Range helicopter transportation became necessary. On this occasion several samples for further fission track analyses were taken at some places along the ridge, which are not discussed in this thesis.

A couple of days were lost to rain and dense fog, especially in the Paparoa Range.

1.4.2. Petrographic Techniques

Ninety-nine orientated rock samples relevant to this thesis were collected from the study area. These specimens were cut perpendicular to the foliation and parallel to the dominant lineation where the latter was discernable. The resulting planes contain the axes of maximum (X-axis) and minimum (Z-axis) finite strain. Shear sense indicators were examined in these XZ thin sections. Particular attention was paid to minerals and their structures, which are indicative for constraining aspects of the temperature of deformation. Stereographic data were plotted on equal area lower hemisphere stereonet projections using the Stereonet software of Rick Allmendinger (2002).

The processed samples have been deposited in the University of Canterbury Rock Collection. They have been archived as UoC# 19264 to UoC# 19492.

1.4.3. Fission Track Analysis

Fission tracks (FT) in apatite and zircon can provide important information on the low temperature (< 300 ºC) cooling history of rocks (e.g. Jacobs & Breitkreuz 2003) as they anneal at different temperatures.

At temperatures above 60 ºC, apatite of a typical Durango composition (0.4 wt % Cl) begins to anneal over geological time. Between 100 ºC and 120 ºC the tracks are completely annealed and the FT age is entirely reset (Green et al. 1989; Ketcham et al. 1999). This temperature range (60-120 ºC) is called the apatite FT partial annealing zone. The closure temperature for the retention of FT depends on the cooling rate (Seward 1989): pressure has no significant effect on the annealing (Naeser & Faul 1969). For moderate cooling of 10-40 ºC Ma^{-1} a closure temperature of 110 ± 10 ºC can be assumed (Ketcham et al. 1999; Reiners & Brandon 2006). Zircon retains FT to higher temperatures. For pristine grains, annealing over geological time starts at about 250 ± 20 ºC and total resetting is reached above 310 ± 10 ºC (Tagami et al. 1998). As these temperatures are lower in zircons that are strongly affected by radiation damage (Brandon et al. 1998; Rahn et al. 2004), this translates to a closure temperature for the retention of fission tracks of about 280 ± 20 ºC in zircon of average radiation damage at moderate cooling rates (Bernet 2009). As the West Coast has been tectonically active, the use of values for moderate to high cooling rates seems appropriate (Seward 1989). However, if the observed FT are dominantly influenced by resetting rather than primary cooling, the FT ages are more likely to reflect the lower temperature range of the partial annealing zone – even more so if the grains suffered substantial radiation damage.

Track lengths and their distribution reveal more details of the cooling history. The amount of resetting and the subsequent cooling influence the track length and their distribution and may indicate a past event (Gleadow et al. 1986b; Gleadow et al. 1986a; Moore et al. 1986). For example, a bimodal distribution occurs if rapid cooling follows significant resetting, i.e. partial annealing. If the cooling is slow and follows only minor resetting the distribution is broad (Seward 1989).

Samples for FT analysis were taken in 2006, 2008 and 2009 and the methodology for processing as described by Thomson & Ring (2006) was applied. They were irradiated at the Oregon State University Triga Reactor, Corvallis, USA. IRMM540R and IRMM541 dosimeter glasses were used to monitor neutron fluence. Age calculations are based on zeta calibration factors (Hurford & Green 1983) 368.1 ± 14.9 (IRMM540R apatite) and 121.1 ± 3.5 (IRMM541 zircon). Obtained central ages (Galbraith & Laslett 1993) are quoted with 2σ errors and were calculated following

the IUGS recommended Zeta-calibration approach of Hurford & Green (1983). This takes into account non-Poissonian variations within a population of single grain ages belonging to an individual sample (Thomson et al. 2009). Ages for binomial parameters are presented with a 95% confidence interval (Brandon et al. 1998).

The FT ages and their geographical distribution were used to determine age-distance relationships and possible slip rates using the Isoplot plug-in for Excel 2003 (Ludwig 2008). As the exposure of basement rocks is limited to the mostly N-S trending coastline, the coordinates of the samples were projected onto a line to measure their distance to an arbitrary reference point in slip direction (Figure 1.02). The reciprocal slope of a linear regression of the age-distance relationship gives the respective slip rate. 2 σ errors for the ages and the distances (± 1 km) were taken into account for Monte Carlo calculations for the resulting errors on the slip rate where applicable.

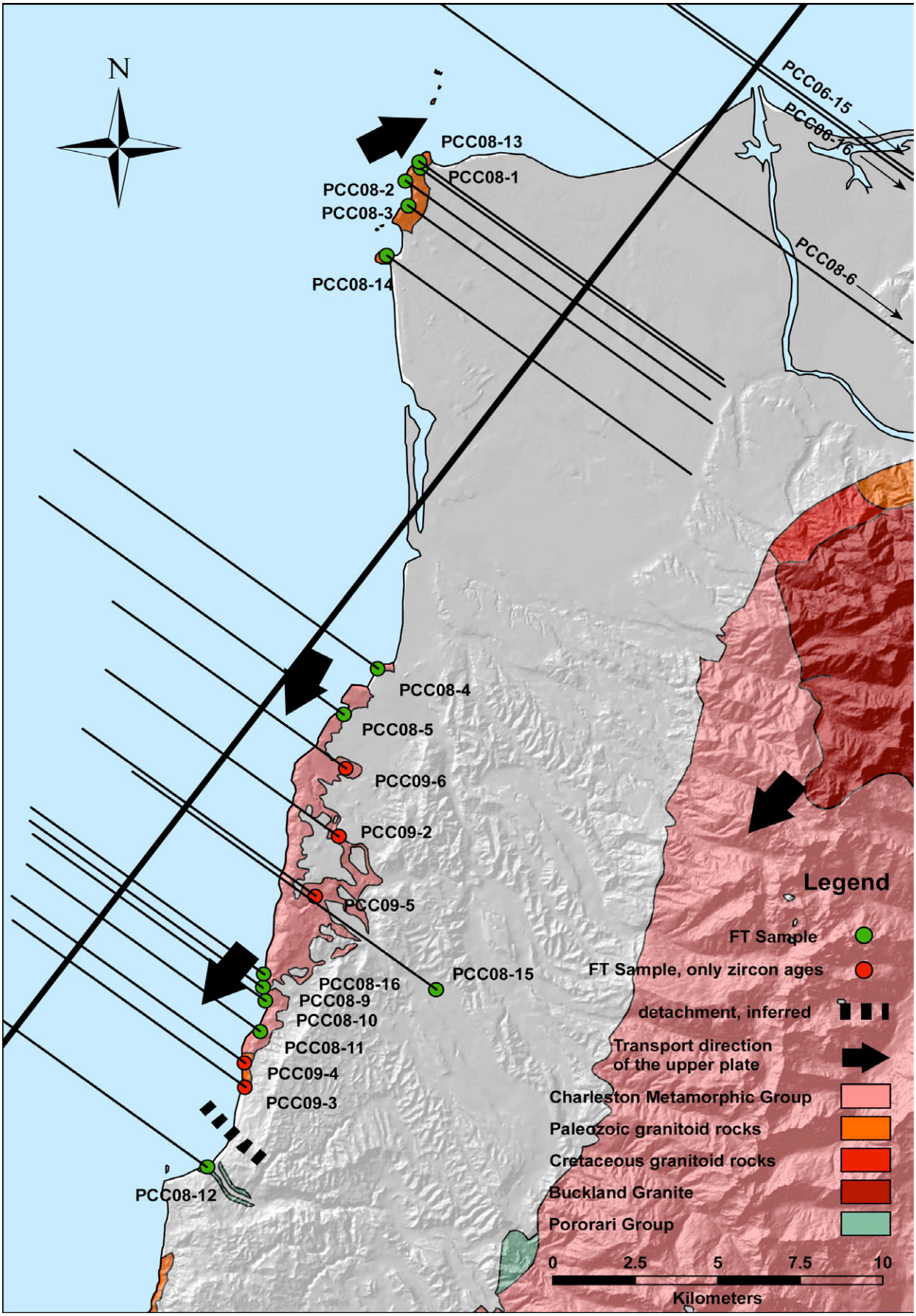

Figure 1.02: Locations of the fission track samples and the projection onto a line in slip direction, the reference point is just off the map to the SW; generalized geology after Tulloch & Kimbrough (1989) and Rattenbury et al. (1998).

1.5. Shear Sense Indicators

To determine movement on fault planes knowledge of shear sense indicators is vital. In fault zones of core complexes both brittle and ductile deformation are realized (e.g. Davis 1980). Ductile deformation ranging from regional to thin section scale is the dominating process. Depending on pressure and temperature it is mainly quartz that recrystallizes dynamically and accommodates the main share of the strain while more rigid grains like feldspar are subject to brittle deformation and often develop porphyroclasts. Resulting distinct patterns and structures can be observed in hand specimens as well as in thin sections.

Displaced marker horizons on macroscopic scale are the most reliable structures for the determination of the sense of shear. Where these are absent, features like C/S-planes, oblique orientations of recrystallized grains and porphyroclasts can be used as shear sense indicators.

1.5.1. Shear Band Cleavage

Berthé et al. (1979) examined planar fabrics within granitic rocks in a ductile shear zone called shear band cleavage. They observed two sets of surfaces whose angular relationship can be used to determine the sense of shear.

Surfaces parallel to the foliation or the main shear zone are referred to as C-planes. Along these surfaces relatively high shear was accommodated (Lister & Snoke 1984). Therefore they are also known as C-type shear bands (Passchier & Trouw 1996). In thin sections they appear as spaced thin layers of recrystallized mineral aggregates of reduced size (Simpson & Schmid 1983).

In the areas between the C-planes, which are not as strongly affected by the shearing, a shape-preferred orientation of minerals defines the second set of surfaces called S-planes. S-planes reflect the orientation of the finite strain axis and are oblique to the C-planes. The initial angle between the planes is 45º. Progressive deformation reduces this angle and rotates the S-planes towards the C-planes while the latter maintain their orientation and reduce their spacing. In the advanced case of ultramylonites C- and S-planes can no longer be distinguished (Berthé et al. 1979; Simpson & Schmid 1983).

The S-planes have a wavy shape and curve into C-surfaces analogous to the curvature of foliation in undeformed wall rock adjacent to a shear zone (Passchier & Trouw 1996). The acute angle between C- and S- planes indicates the sense of shear (Figure 1.03).

Strong planar anisotropy in strength and ductility due to the foliation of mylonites is supposed to cause asymmetric boudinage called extensional crenulation cleavage (Platt & Vissers 1980) or

C'-type shear bands (Passchier & Trouw 1996). The C'-type shear bands are oblique to the foliation and are usually short, i.e. not continuous, and anastomosing. Wavy S-surfaces curve into the C'-planes as well. C'-type shear band cleavage can be used as a shear sense indicator in the same way as the C-type but it also implies flattening normal to the foliation (Figure 1.03; Platt & Vissers 1980).

1.5.2. Oblique Elongate Recrystallized Grains

During ductile deformation quartz can develop elongated grain shapes, which have an oblique orientation (Simpson & Schmid 1983). Passive deformation and rotation are responsible for the elongate shape and the oblique orientation of the quartz grains. Recrystallization processes limit the amount of crystal plastic deformation by resetting the "finite-strain-clock" and therefore prohibit the grains to rotate towards the C-planes too much (Lister & Snoke 1984; Passchier & Trouw 1996). Thus the attitude of the resulting oblique foliation is approximately parallel to the finite strain ellipsoid at the time the grain last recrystallized. The acute angle is usually 20-40º and indicates the sense of shear like the C/S-fabric (Figure 1.03; Passchier & Trouw 1996).

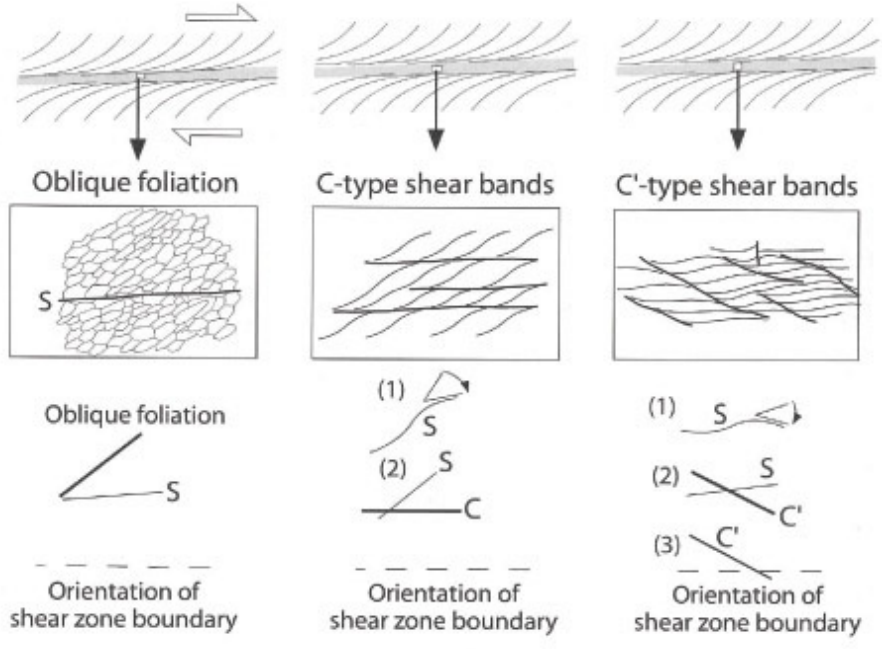

Figure 1.03: Oblique Foliation, C-type- and C'-type shear bands (Passchier & Trouw 1996)

1.5.3. Porphyroclasts and Sigmoids

Porphyroclasts are phenocrysts in a fine-grained matrix of mylonitic rocks. They consist of minerals like feldspar, pyroxene or garnet, which are rigid with respect to the ductile matrix (Passchier & Simpson 1986). If porphyroclasts have a polycrystalline rim of a different composition than the matrix, this assemblage is called a porphyroclast system. Their symmetry can be used to determine the vorticity, i.e. the sense of shear (Passchier & Trouw 1996).

The rims mantling the porphyroclasts are the result of dynamic recrystallization or of precipitation from solution in strain shadows adjacent to the clast. Due to non-coaxial flow these mantles develop wings or tails on opposite sides of the porphyroclasts parallel to the stretching direction in the mylonite (Passchier & Simpson 1986). The shape of these wings can be used as a shear sense indicator. Passchier & Simpson distinguished two main porphyroclast systems: the σ- and δ-type. The σ-type is subdivided into σ_a- and σ_b-type depending on whether they developed isolated in the mylonitic matrix or as part of a C/S-fabric. Both subtypes have wide tails close to the porphyroclast core. δ-type mantled clasts have narrow wings with characteristic bends and mainly occur in high strain mylonites whereas the σ-type is also common in low strain regimes (Passchier & Trouw 1996).

The tapering wings on both sides of the porphyroclasts often lie on different levels with respect to a reference plane. Lister & Snoke (1984) referred to this difference in elevation in association with mica fish as *stair-stepping*. The asymmetry of porphyroclast systems and the stair-stepping fabric are useful shear sense indicators (Figure 1.04; Passchier & Trouw 1996).

Aggregates of grains of a mineral that have a similar shape to σ-type clasts but lack a proper porphyroclast core are called sigmoids and can be used as shear sense indicators in the same way as σ-type clasts.

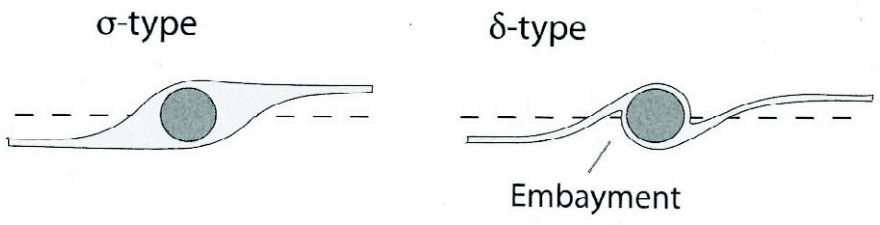

Figure 1.04: Classification of mantled porhyroclasts. Dextral sense of shear (after Passchier & Trouw 1996).

1.5.4. Mineral Fish

Mineral fish are lenticular or lozenge-shaped single crystals ending in sharp tips that often extend into trails of fragments of the same mineral. They are common in mylonites and ductile shear zones and typically lie with their longest dimension at an acute angle to the mylonitic foliation. This angle can be used to infer the sense of shear (Figure 1.05; Passchier & Trouw 1996; ten Grotenhuis et al. 2003). White mica are the most common and first described mineral fish (Eisbacher 1970). Mica fish can form as a result from boudinage of pre-existing large mica grains (Lister & Snoke 1984). In addition to white mica, several other minerals like biotite, K-feldspar, quartz and others can develop mineral fish in a similar way (ten Grotenhuis et al. 2003).

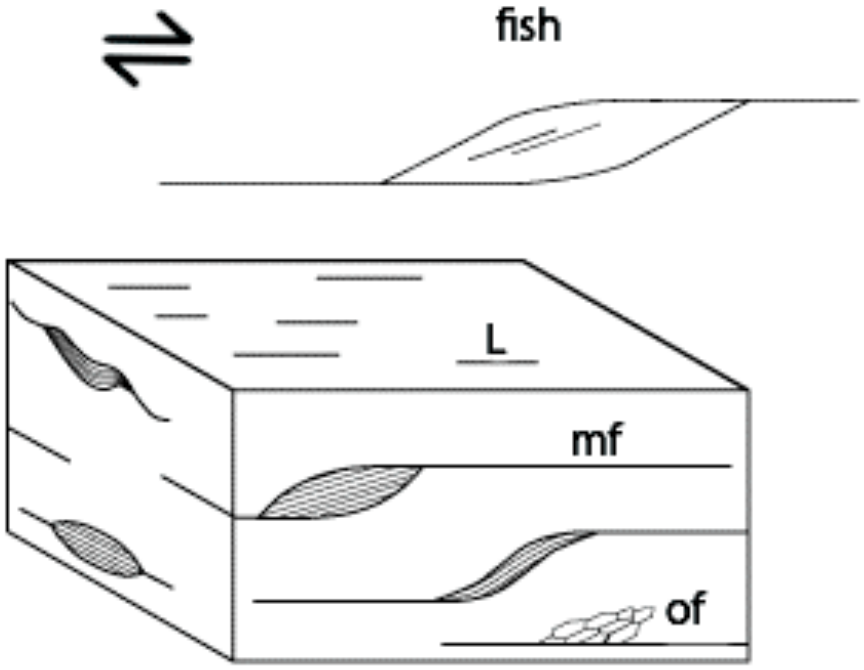

Figure 1.05: Schematic drawing of mica fish and the trails of mica fragments, in relationship with mylonitic foliation (mf), oblique foliation (of) and stretching lineation (L) (after ten Grotenhuis et al. 2003).

1.5.5. Fragmented Porphyroclasts

As porphyroclasts remain rigid due to their strength, in contrast to the mylonitic matrix they can be broken and displaced and therefore used to determine the over-all shear sense (Figure 1.06; Simpson & Schmid 1983). The fragment geometry depends not only on the bulk shear but also on the original grain shape and orientation as well as the initial orientation of microfaults and

flow type (Passchier & Trouw 1996). In particular, precursor fractures at high angles to the flow plane can provide ambiguous kinematic information (Hippertt 1993). Thus fragmented porphyroclasts are not always reliable shear sense indicators.

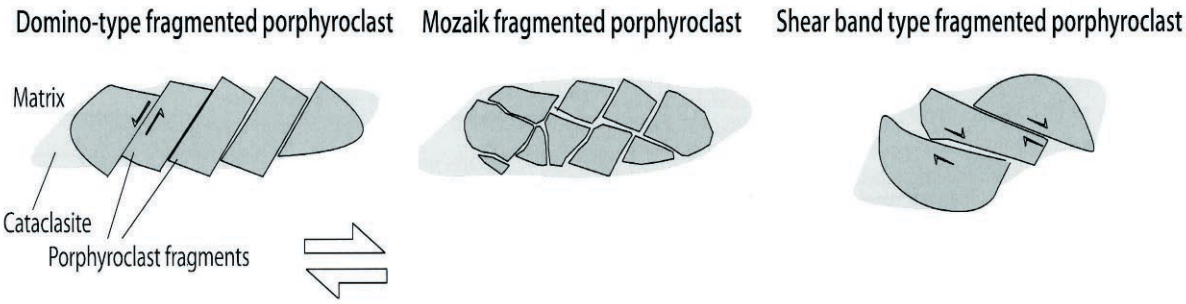

Figure 1.06: Three types of fragmented porphyroclasts and their interpretation in terms of shear sense (after Passchier & Trouw 1996)

1.6. Regional Geology

The basement rocks of the South Island of New Zealand consist of several smaller Paleozoic and Mesozoic terranes, which are divided into the Eastern Province and the Western Province along a tectonic boundary called the Median Tectonic Zone (Bradshaw 1989, 1993). The rocks were offset by 480 km along the Miocene to Recent Alpine Fault (Figure 1.07). Previous tectonic structures were overprinted by this Cenozoic movement (Landis & Coombs 1967).

The Eastern Province consists of volcanogenic material and accretionary complexes that accumulated on the convergent Pacific-Gondwana plate boundary (Bradshaw 1989). In contrast the Western Province represents a fragment of eastern continental Gondwana with obvious relationships to Antarctica and Australia (Muir et al. 1994). It consists of low grade metasedimentary rocks grouped into the Buller- and Takaka Terranes which are separated by the Anatoki Thrust.

The Takaka Terrane is structurally complex and dismembered. It is composed of several N-S trending tectonic slices of an originally diverse depositional region. Because of an apparent overall coherence of the geologic history the terrane is regarded as an entity nonetheless. Abundant Cambrian to Silurian carbonate-rich rocks as well as volcanics and volcanoclastics suggest proximity to an island arc along the active plate margin of Gondwana (Münker & Cooper 1995).

The Buller Terrane clastic sedimentary rocks are continent-derived and comprise Ordovician shales, siltstones and quartz-rich sandstones. The Greenland Group turbidites are the oldest rocks and make up the bulk of the terrane. An inferred environment of submarine fans and slope basins suggests a marginal region of the Gondwana continent. Intrusion of mid-Paleozoic granitoids implies a continental crust beneath (Cooper 1989).

The different environments of the two terranes suggest that they were originally a considerable distance apart (Cooper 1989). Middle- to Early Devonian amalgamation of the terranes was inferred on the basis of the distribution and the age of plutonic intrusions and coherent sedimentary sequences (Cooper 1989; Muir et al. 1997; Rattenbury et al. 1998).

As mentioned above the low grade metasedimentary rocks of the Western Province were intruded by several NNE-SSW trending batholiths and plutons (Fig 1.07; Muir et al. 1994). Based on their age and chemistry Tulloch (1988) defined three suites. S-type granitoids of Devonian to Carboniferous age are confined to the Buller Terrane and belong to the Karamea Suite. The Separation Point Suite comprises Cretaceous I-type granitoids like the eponymous Separation Point Granite and occurs in both terranes. Cretaceous granitoids of transitional I/S-

type signature characterize the Rahu Suite. The Rahu Suite is restricted to the Buller Terrane. It also contains alkali-lamprophyre dikes, some of the orthogneissic parts of the Charleston Metamorphic Group (CMG) as defined by Nathan and the Buckland Granite (Nathan 1975; Adams & Nathan 1978; Tulloch & Kimbrough 1989; Muir et al. 1994; White 1994). The latter is of particular importance for the development of the Paparoa Metamorphic Core Complex.

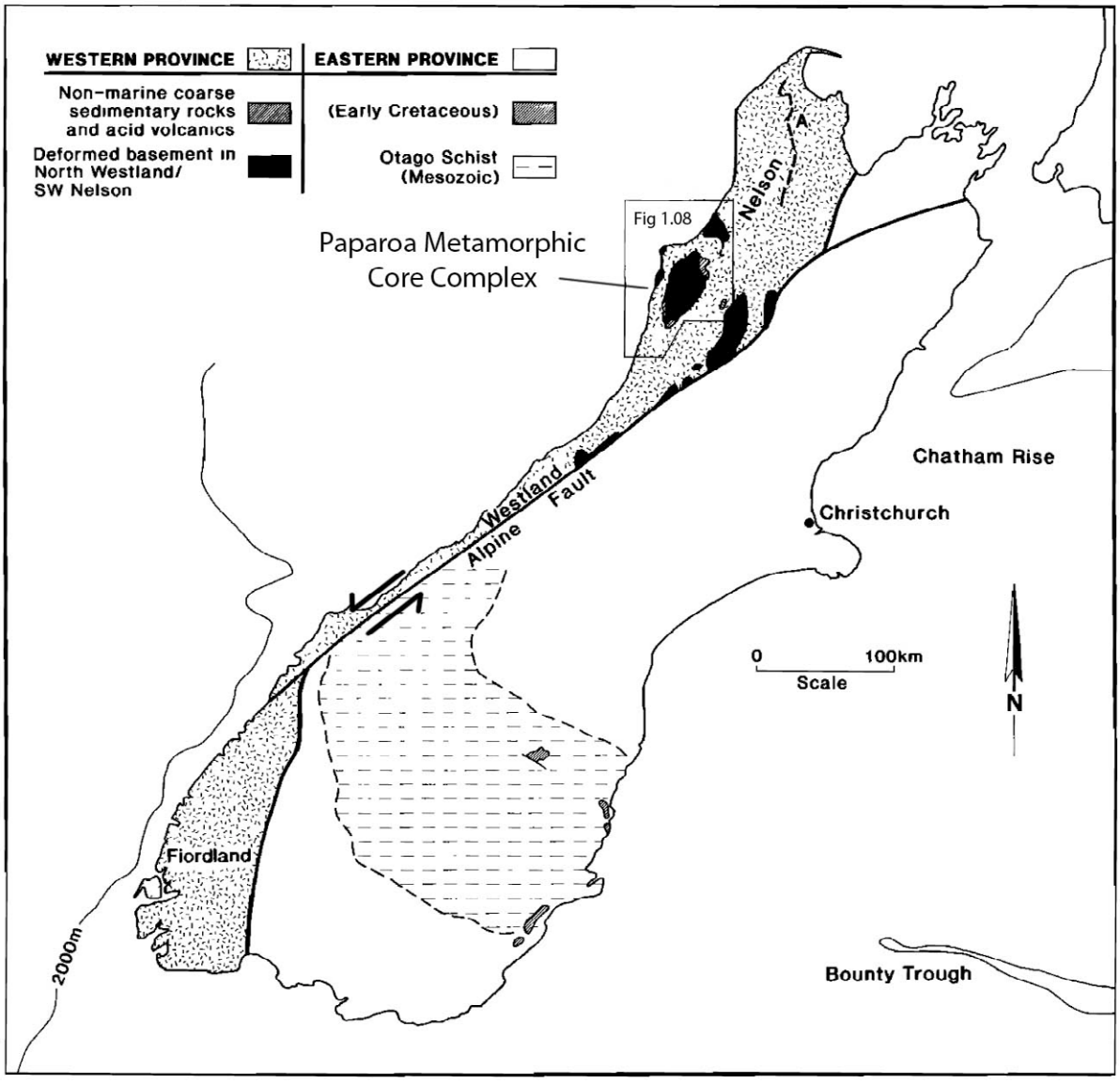

Figure 1.07: Overview and regional context: Structure of the basement of the South Island, New Zealand, after Tulloch & Kimbrough (1989); A: Anatoki Thrust.

1.7. The Paparoa Metamorphic Core Complex

In the Paparoa Range, West Coast, New Zealand, low-grade metasedimentary rocks are juxtaposed against high-grade metamorphic rocks separated by low angle faults. Tulloch & Kimbrough (1989) were the first to explain this by suggesting a metamorphic core complex. According to their idea metasediments of the Greenland Group and terrestrial Conglomerates of the Pororari Group comprise the upper plate of a core complex while the CMG rocks constitute the lower plate (Figure 1.08). The faults separating these units are low angle normal faults. Two detachment faults have been recognized: the Pike Detachment in the South and the Ohika Detachment in the North. Mid-cretaceous extension preceding the breakup of Gondwana is supposed to be the reason for development of these detachments (Laird & Bradshaw 2004).

The CMG is exposed along the coast west and south of Charleston, at Cape Foulwind and in the Paparoa Range. At Charleston it is composed of paragneiss and orthogneiss. Zircon U-Pb age analyses and whole rock geochemistry suggest igneous crystallization of at least some of the orthogneiss at 114 ± 18 Ma while the paragneiss is supposed to be ~360 million years old (Kimbrough & Tulloch 1989; Ireland & Gibson 1998). Although the Windy Point Granite in the Paparoa Range and the Cape Foulwind Granite at the coast 11 km west of Westport display a gneissic foliation they are referred to as granitoids. They have a crystallization age of 328.6 ±4.1 Ma and 327.3 ±6.2 Ma respectively (Muir et al. 1994). Granitoid plutons intruded the metamorphic basement south of the Ohika Detachment. The Buckland Granite is the youngest and dominant intrusion and yields a crystallization age of 109.6 ±1.7 Ma (Muir et al. 1994).

All exposed basement rocks show evidence of ductile deformation. Strain was accommodated variably due to compositional differences. Thus the ductile fabric is heterogeneously distributed within the basement rocks. In general, strain increases towards the upper surface of the basement culminating in ultramylonites, which can be found in relatively close proximity to the Pike Detachment. The deformation age of ultramylonites at White Horse Creek has been determined to be 116.2 ± 5.9 Ma (Ring et al. 2006). This sets a minimum age for the onset of deformation. Shear sense indicators in these mylonites show a top-to-the SSW movement, whereas the rocks associated with the Ohika Detachment show a top-to-the NE sense of shear. This is consistent with similarly trending stretching lineations in the basement rocks of the entire region. Hence, Tulloch & Kimbrough (1989) suggested that the extensional direction during the development of the core complex was NNE-SSW. WNW trending sedimentary basins of the upper plate adjacent to the detachment faults (Laird 1994) and lamprophyres (Tulloch & Kimbrough 1989) are orientated perpendicular to this inferred extensional direction and therefore support this idea.

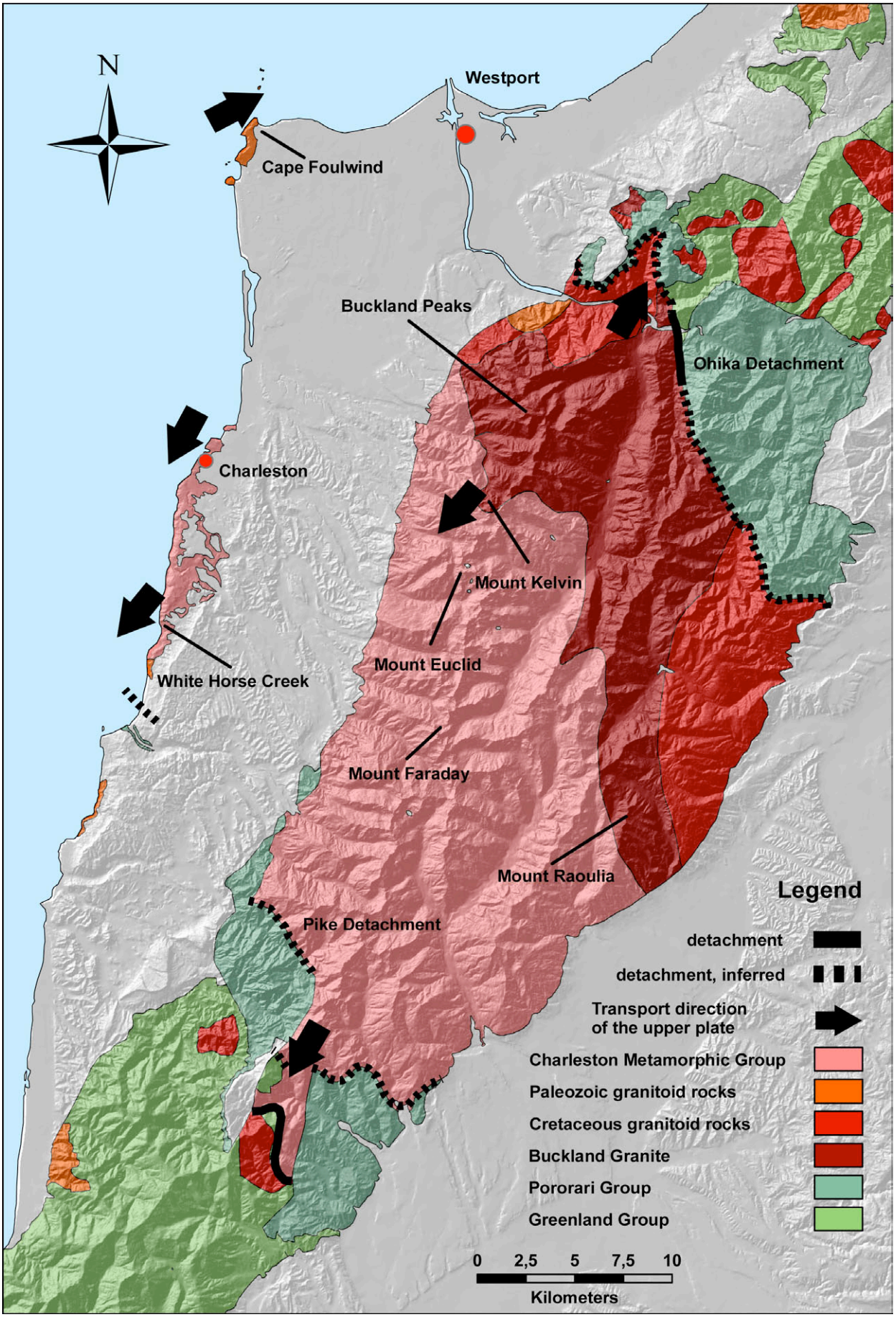

Figure 1.08: Generalized geological map the Paparoa Metamorphic Core Complex, geology after Tulloch & Kimbrough (1989) and Rattenbury et al. (1998).

The former have been filled with the Pororari Group, overlying the Greenland Group rocks of the upper plate. The Stitts Tuff at the base of the basin adjacent to the Ohika Detachment limits the maximum age of the breccia to 101 ±2 Ma and 102 ±3 Ma (Muir et al. 1997). This is in agreement with a Late Albian palynological age of the upper sequence (Raine 1984). Deposits in the southern Paparoa Range do not contain the Stitts Tuff. Thus there is no upper limit for their age. Yet, they yield a Late Albian palynological age as well (Raine 1984). Internal normal faulting and domino-style rotation towards the detachment fault within the Pororari Group indicate that extensional deformation was still active at this time, at least in the upper brittle crust (Tulloch & Kimbrough 1989).

Consequently the emplacement of the Buckland Granite and the development of the core complex overlap chronologically. Together with the occurrence of migmatites in the CMG (Shelley 1970b; White 1994) this suggests a hot and weak footwall that facilitated the migmatization and the emplacement of the pluton during the deformation.

The Paparoa Metamorphic Core Complex displays the main features of well-investigated core complexes in the Northern American Cordillera and the Aegean Sea (cf. Armstrong 1982; Brichau et al. 2007). However, two detachment faults with opposite sense of shear are unusual. Therefore the focus of this thesis lies on this oddity.

CHAPTER 2: STRUCTURAL GEOLOGY

2.1. Previous Work

The first detailed structural analyses of the metamorphic core rocks were undertaken by Shelley (1970b) along the coast southwest of Charleston. By that time the Paparoa Range had not yet been identified as a metamorphic core complex. Rocks of the CMG as defined by Nathan (1975) (formerly known as Constant Gneiss) were interpreted as metamorphosed Greenland Group (Laird 1967). The sharp contact, large differences in chemistry, petrology, texture and structure and the lack of a thermal aureole made this interpretation unlikely. Late Precambrian and lower Ordovician age of the CMG and the Greenland Group respectively (Adams 1975; Cooper 1975) finally invalidated this relationship. Thus Hume suggested that the Greenland Group was unconformably deposited on the CMG (1977), although he noted deformation near the low-angle contact and could not rule out a tectonic relationship. Tulloch & Kimbrough (1989) finally recognized a metamorphic core complex with two detachment faults in the Paparoa Range.

Shelley (1970b) distinguished three phases of deformation in the rocks southwest of Charleston. Dominant stretching lineations, folds and mylonites trending NE-SW overprinted earlier structures and represent the youngest deformation phase. Studies of Tulloch & Kimbrough (1989) confirmed the trend of these features and related them to the top-to-SSW movement of the hanging wall of the Pike Detachment. The detailed earlier observations of Laird (1967) and Hume (1977) contain much evidence consistent with such an interpretation. Furthermore Tulloch & Kimbrough (1989) described mylonitic rocks to the north at Cape Foulwind and in the northern Paparoa Range that share the ductile fabric but with an opposite sense of shear.

2.2. Fieldwork

Fieldwork was carried out at several locations to confirm previous workers' results (cf. Shelley 1970b, 1972; Tulloch & Kimbrough 1989) and to add new structural data to areas that have not yet been investigated in detail. Attention focused on lineations and shear sense indicators related to the transport direction of the upper plate and the core complex development, but other microstructures that are related to the deformational processes were also studied. Structural

features were examined in the field as well as in thin sections of orientated hand specimens that were collected during the fieldwork.

2.2.1. Cape Foulwind

The Carboniferous granite at Cape Foulwind is a clearly deformed rock and belongs to the Karamea Suite (Muir et al. 1994). It is best described as a mylonite and probably owes its classification as granite to its mineral content. Samples have been taken at three different spots along the coast at Siberia Bay within 200 m where the observed strain was the highest (Figure 2.01). It is a coarse grained rock with the striking feature of elongated feldspar phenocrysts. A distinct strain partitioning is visible with the bare eye. The fine-grained matrix consisting of quartz and mica has undergone ductile deformation and constitutes a mylonitic foliation while the feldspar crystals aligned to it experienced brittle deformation (Figure 2.02). This becomes evident in thin sections where quartz grains recrystallized dynamically in contrast to the feldspar. The foliation is bent gently to open folds on a meter scale (Figure 2.03). Several pegmatites of only a few centimeters width are associated with the granite. They are not affected by the foliation, and thus they postdate the deformation.

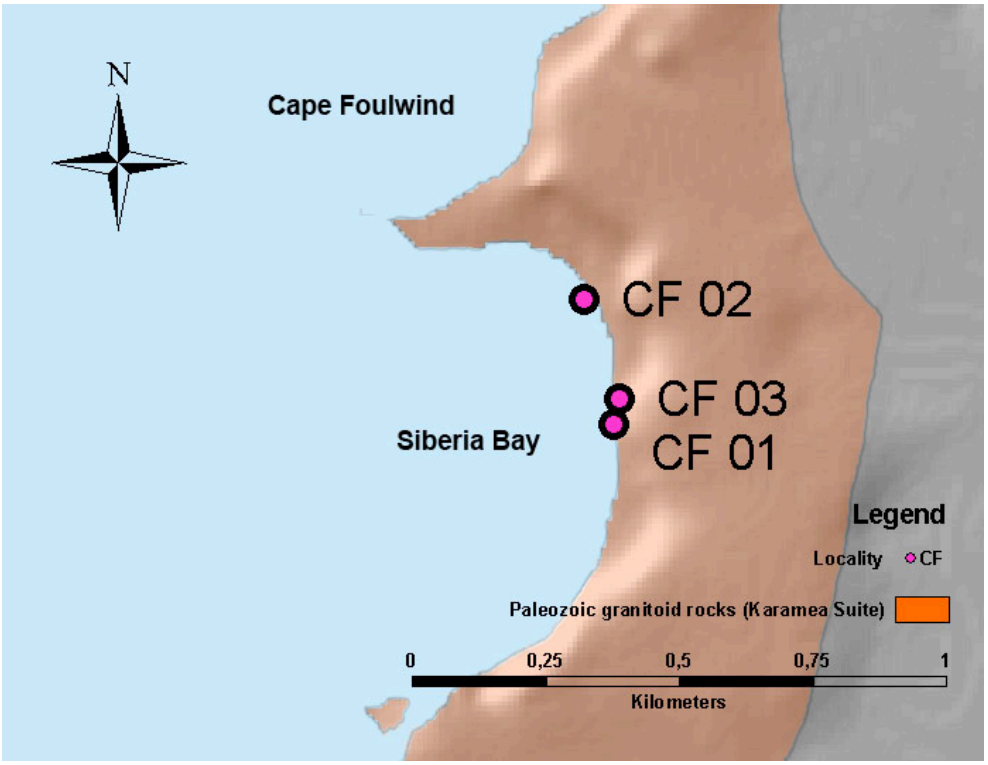

Figure 2.01: Sample area at Cape Foulwind; Geology after Rattenbury et al. (1998).

Fine-grained hornfelsic patches occur locally. They have an elongated shape and are aligned parallel to the foliation (Figure 2.04). Shelley (1972) interpreted these patches as metasedimentary fragments, which represent remains of partially molten greywacke-type sediments, probably of the Greenland Group.

As explained in the first chapter porphyroclast fragmentation patterns cannot be relied on as sole shear sense indicators. However, the porphyritic feldspar crystals show a very consistent domino-like fracture pattern, which suggests a top-to-NE sense of shear (Figure 2.05). This is compliant with NE-trending lineations measured in the field (Figures 2.06, 2.07). C/S-fabrics consist of muscovite and biotite, which embed ribbons of recrystallized quartz (Figures 2.08, 2.09). Together with mica fish (Figure 2.10) they also support a top-to-the-NE sense of shear.

Additionally, examination of thin sections reveals that the fractures within the brittle feldspar porphyroclasts are filled with dynamically recrystallized quartz and shows the strain partitioning between the two minerals (Figure 2.11). Furthermore, myrmekite (Figure 2.12) and muscovite, which is replacing feldspars (Figure 2.12), can be observed. These structures can be interpreted as deformational features (Phillips et al. 1972; Ashworth 1986; Simpson & Wintsch 1989; Cesare et al. 2002) and have already been noticed in mylonites (LaTour & Barnett 1987; Menegon et al. 2006).

According to Voll (1976) quartz begins to recrystallize dynamically at 290 ºC. Mica recrystallizing in very small grains forming the C/S-structures (Figures 2.08, 2.09) and mineral fish of primary muscovite, which are replaced by biotite in places (Figure 2.14), suggest that biotite was stable during deformation. Thus the temperature was at least as low as 400 ºC (Bucher & Frey 2002). As the feldspars remained brittle during deformation an upper temperature boundary can be estimated as well. Feldspar begins to recrystallize at temperatures exceeding 450-500 ºC (Voll 1976; Tullis 1983; Altenberger et al. 1987). Consequently the deformation temperature lies within the range from 400 ºC to 500 ºC. This is in agreement with the development of syndeformational myrmekite (Figure 2.12), which is indicative of upper greenschist facies to, more commonly, lower amphibolite facies (Simpson 1985; LaTour & Barnett 1987; Simpson & Wintsch 1989; Cesare et al. 2002; Menegon et al. 2006).

Some structural levels of the foliation have a distinctly smaller grain size. Composition and shear sense indicators remain the same, but feldspar porphyroclasts are smaller and less abundant. This heterogeneous distribution of deformation occurs not only on outcrop scale, but also adjacent to the sampled area along the coastline (Figure 2.15).

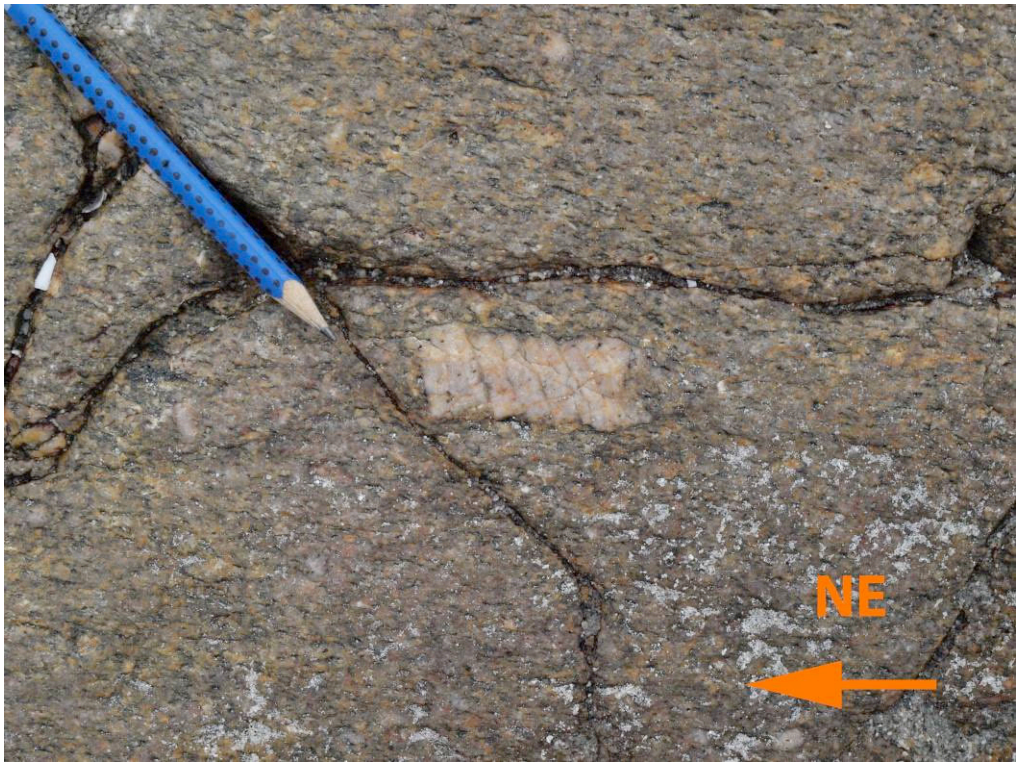

Figure 2.02: Brittle feldspar phenocryst in ductile matrix.

Figure 2.03: Open folds of foliation on a meter scale, scale: camera bag in front.

Figure 2.04: Hornfelsic patch; probably remains of Greenland Group.

Figure 2.05: Consistent domino-like fracture pattern of feldspar porphyroclasts indicating top-to-NE sense of shear.

Figure 2.06: NE-trending lineation.

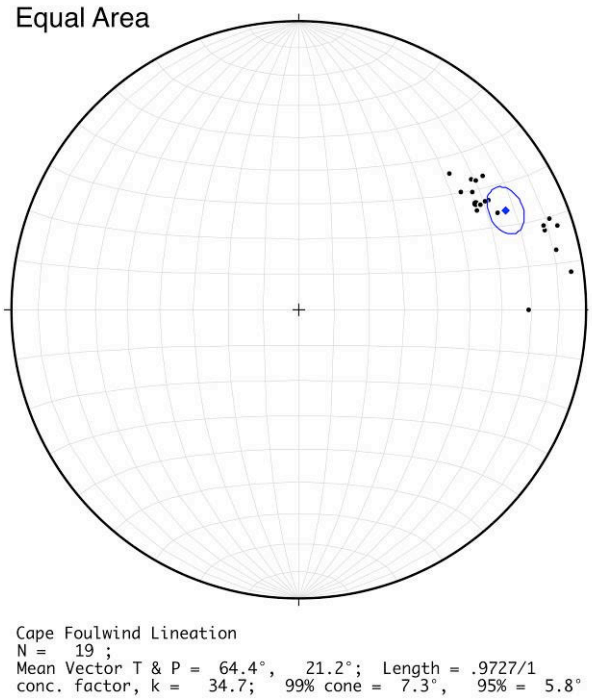

Figure 2.07: Stereographic projection of the lineations at Cape Foulwind showing a clear NE trend; blue dot representing the mean vector.

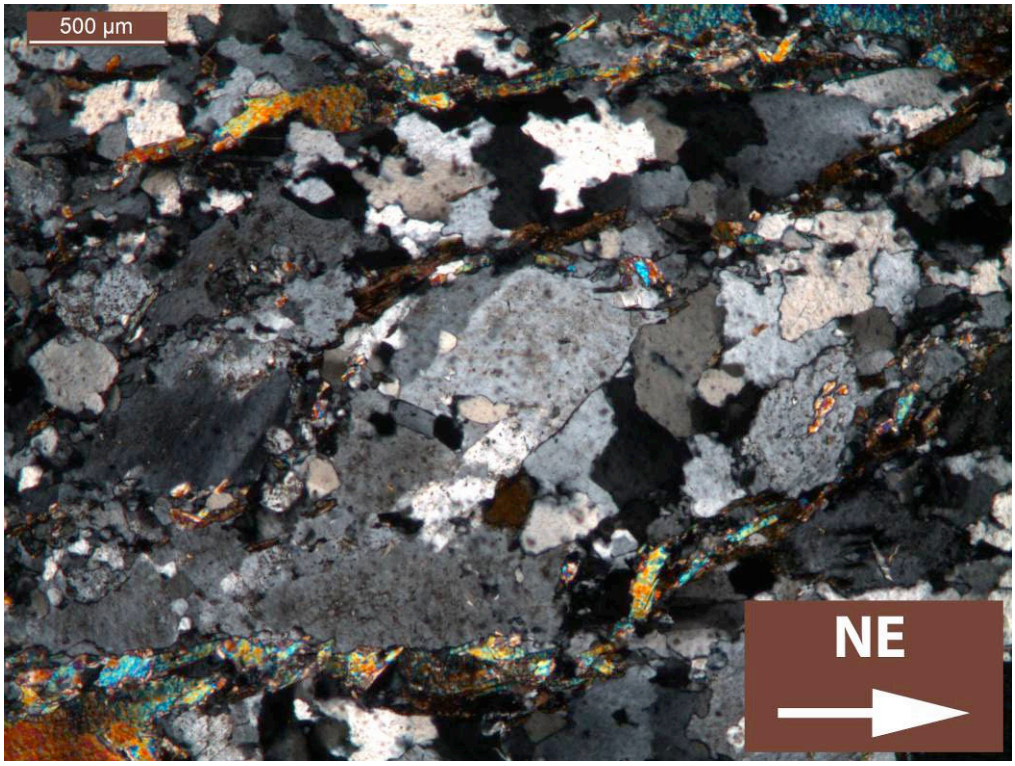

Figure 2.08: C/S-structures of mica and dynamically recrystallized quartz ribbons indicating top-to-NE sense of shear; CF010201-1, CPL.

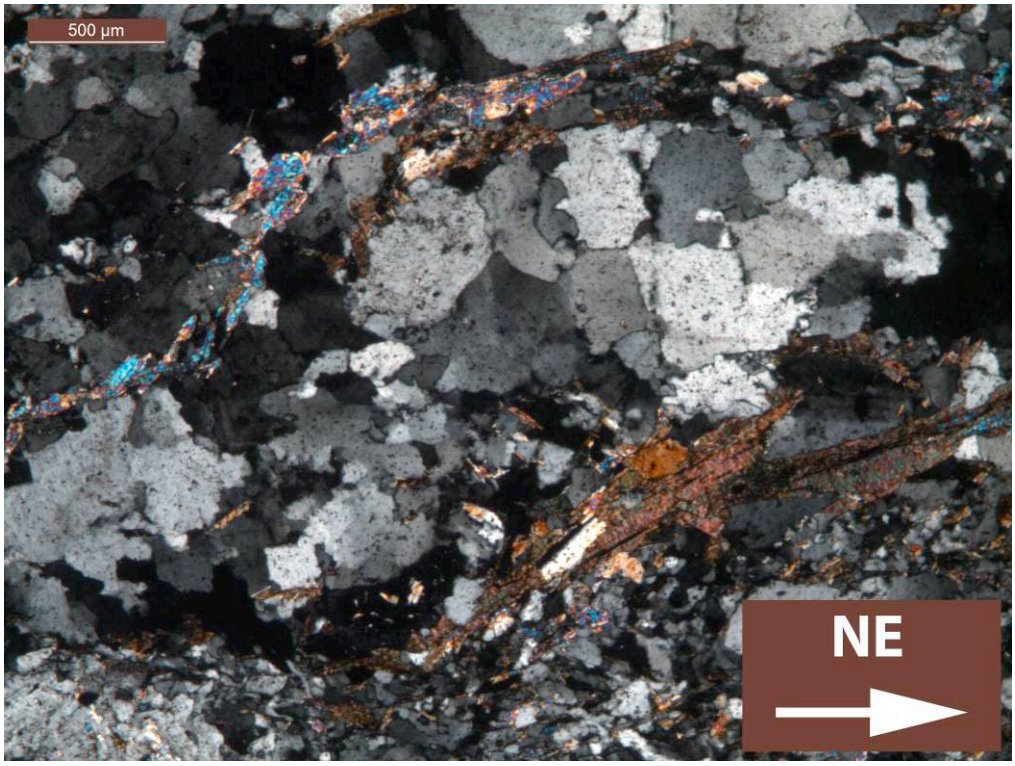

Figure 2.09: C/S-structures indicating top-to-NE sense of shear; CF030402-2, CPL.

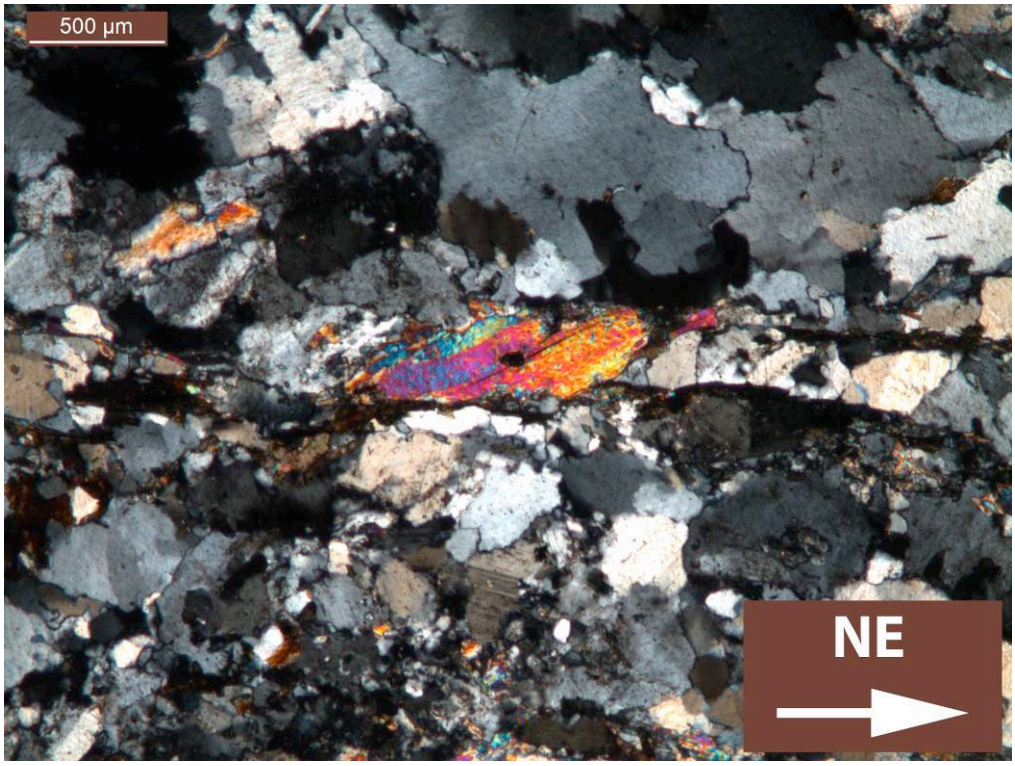

Figure 2.10: mica fish indicating top-to-NE sense of shear; CF010202-1, CPL.

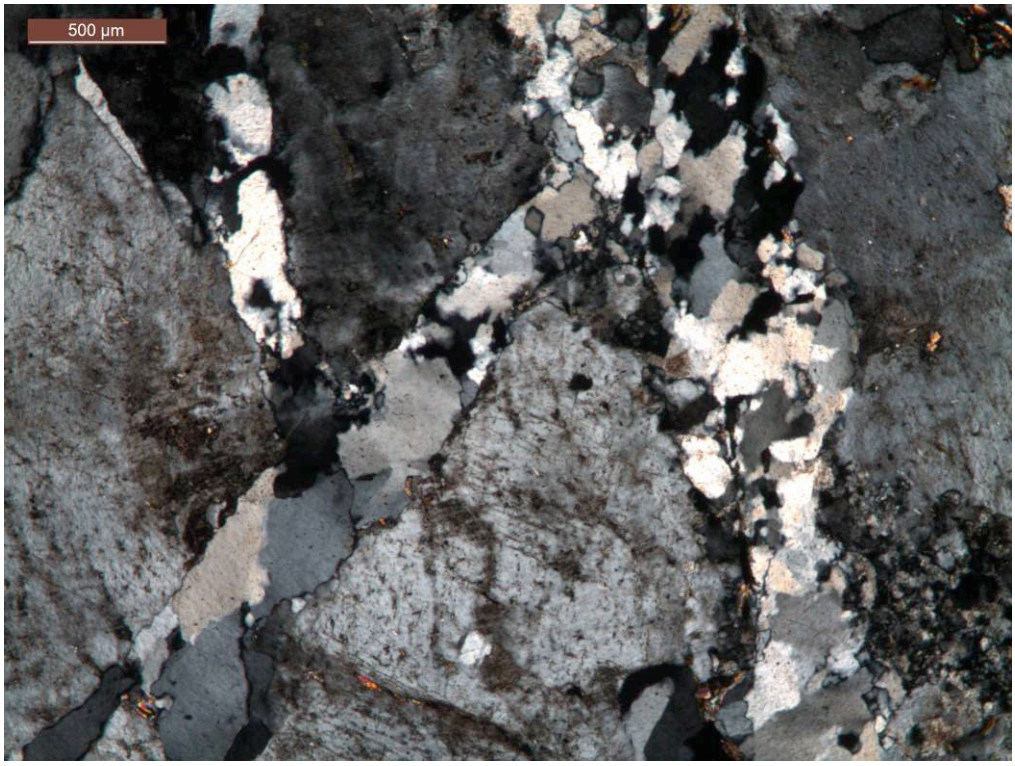

Figure 2.11: Dynamically recrystallized quartz in cracks of brittle feldspar; CF030301-1, CPL.

Figure 2.12: Myrmekite; CF030103-1, CPL.

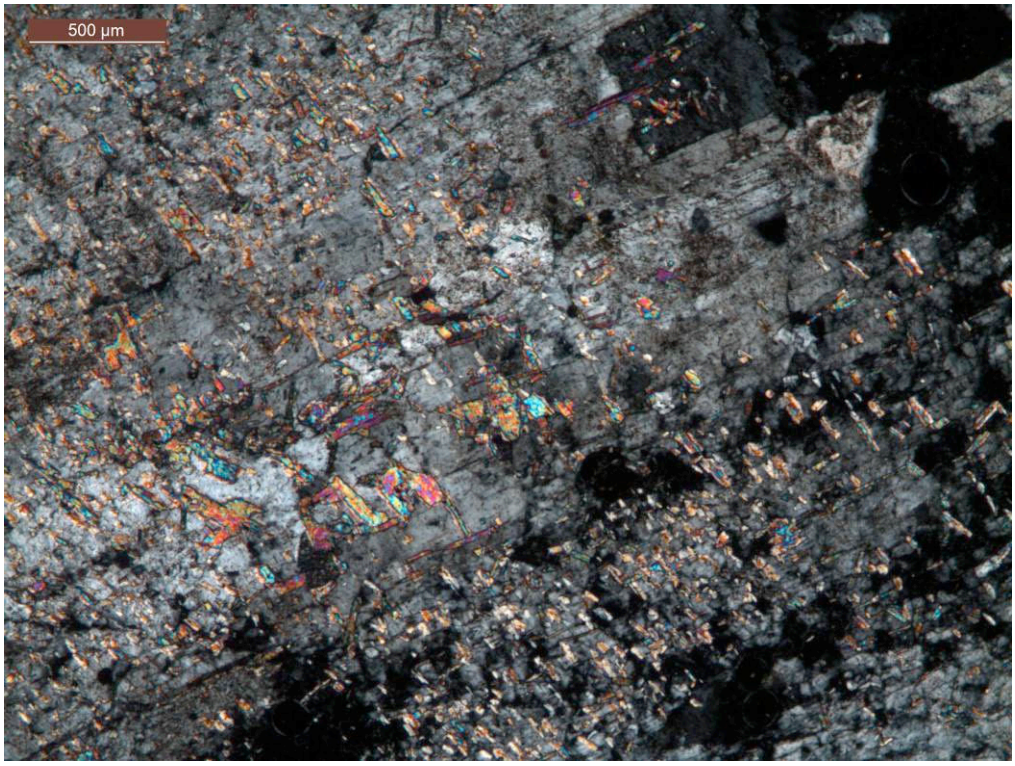

Figure 2.13: Muscovite replacing K-feldspar; CF030202-1, CPL.

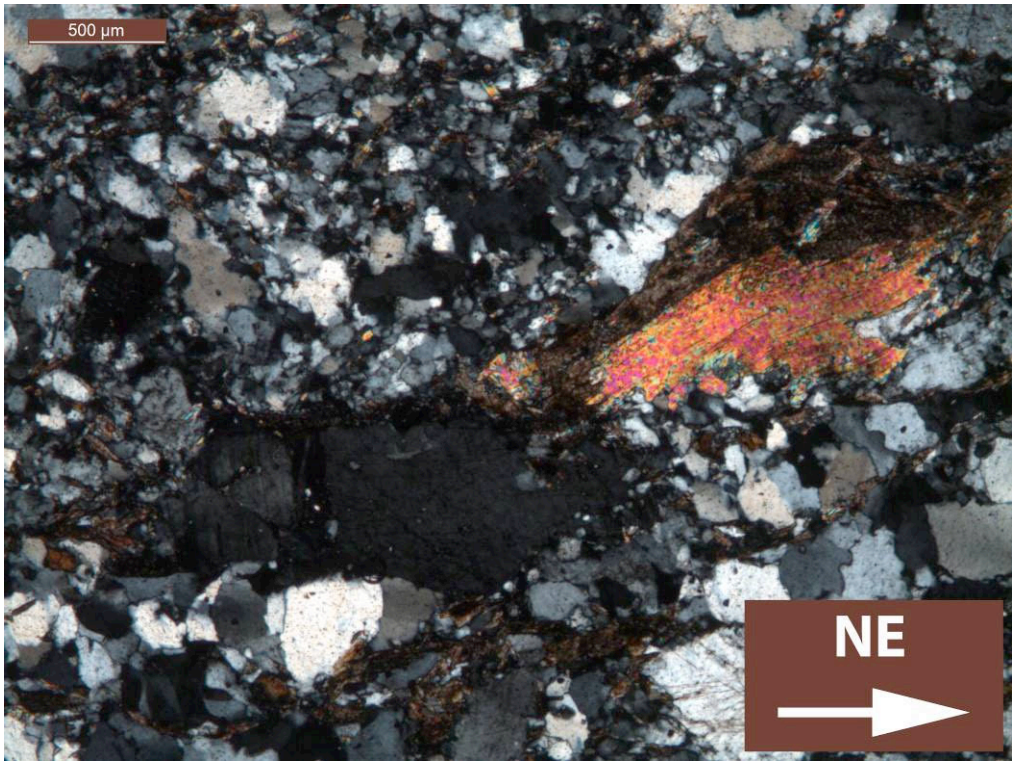

Figure 2.14: Biotite replacing a muscovite fish; CF030501-1, CPL.

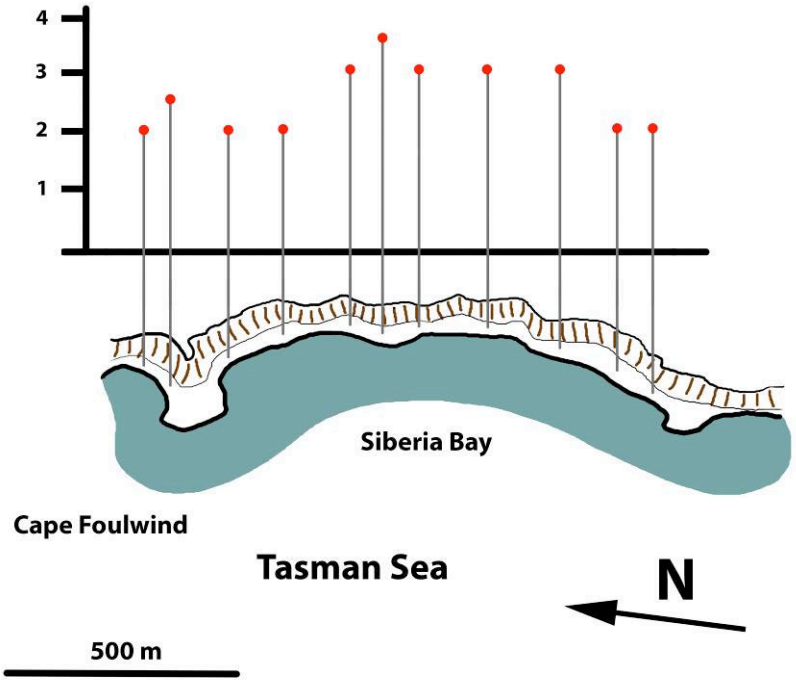

Figure 2.15: Deformation profile: 1 = undeformed. 2 = aligned feldspar phenocrysts. 3 = aligned feldspar phenocrysts, schistosity. 4 = domino-like fracture patterns in aligned feldspar, well-developed schistosity.

2.2.2. Charleston

Para- and orthogneisses comprise the Constant Gneiss at Charleston (Shelley 1970b; Tulloch & Kimbrough 1989), which have been examined and sampled at Joyce Bay and Parson Hill. Samples have been taken at three locations (Figure 2.17). The unit is very variable in composition and texture and shows a complex deformation history. As Shelley (1970b) could not map distinct boundaries due to gradual transitions between gneisses, the unit is treated as an entity in this thesis.

Three deformation phases have been identified in earlier studies (Shelley 1970b). The last phase, which overprints the earlier two, caused NE-SW trending lineations (Figures 2.18, 2.19) associated to the southward movement direction of the upper plate of the Pike Detachment (Tulloch & Kimbrough 1989). In agreement with Shelley (1970b) the foliation is gently folded and dips to the north at Joyce Bay and to the south at Parson Hill (Figures 2.20, 2.21, 2.22).

Quartz, feldspar and micas are the bulk constituents of the mineral assemblage. Biotite is not present in all rocks while muscovite flakes can reach sizes of 2 cm in places. The micas constitute a prominent foliation, whose intensity varies perpendicularly to the foliation planes together with the mean grain size of the minerals. These features reflect the finite strain, which was also accommodated heterogeneously.

In thin section, areas that are barely affected by deformation and have an igneous-like texture can be identified. They show large undeformed quartz crystals. Dynamically recrystallized grains only occur in small patches (Figure 2.23). These less deformed rocks occur at Joyce Bay where the lithology is more heterogeneous. As a result of the weak deformation the foliation is not as strongly developed (Figure 2.24). On the other side deformation appears to be more pronounced at Parson Hill in general, since the rocks are strongly foliated (Figure 2.25), quartz recrystallized in continuous bands (Figures 2.26, 2.27) and shear sense indicators are better developed (compare Figure 2.33 with Figures 2.34, 2.36, 2.37, 2.38). However, even the least deformed rocks contain fragmented mica (Figures 2.28, 2.29), myrmekite (2.30) and associated muscovite replacing feldspar (2.31), recording a deformational history (Phillips et al. 1972; Simpson & Wintsch 1989).

Hornfelsic patches aligned to the foliation like those at Cape Foulwind are also present. North of Parson Hill they reach a size of several meters in length. Remarkable boudinage of the supposed remnants of the Greenland Group (Shelley 1970b) show how the fragments were involved in the deformation process and suggest a top-to-the SW sense of shear (Figure 2.32). This is consistent with C/S-structures and mica fish visible in the thin sections of the Constant Gneiss (Figures

2.33, 2.34, 2.35, 2.36, 2.37, 2.38) and contrasts with the northeasterly sense of shear at Cape Foulwind.

Other macroscopic shear sense indicators are rare, as the rocks do not contain porphyroclasts like the granite at Cape Foulwind. At Parson Hill the foliation is continuous and the strong schistosity makes it hard to find plane surfaces perpendicular to the foliation to observe macroscopic shear bands. Rocks at Joyce Bay are exposed better but they are not sufficiently deformed to display these features macroscopically.

Although quartz appears to recrystallize less, this is only a manifestation of the heterogeneous distribution of strain and not of a different metamorphic regime. Recrystallization of biotite in the C/S-structures (Figures 2.34, 2.35, 2.36, 2.37) and replacement of deformed muscovite by biotite (Figure 2.28) show that the occurring biotite is in its stability field somewhere above 400 ºC (Bucher & Frey 2002). The formation of myrmekite requires deformation under lower amphibolite facies conditions as well (Simpson 1985; LaTour & Barnett 1987; Simpson & Wintsch 1989; Cesare et al. 2002; Menegon et al. 2006). Yet, there is no sign of ductile deformation of the feldspar crystals. Thus the metamorphic regime was approximately the same as at Cape Foulwind with temperatures ranging from 400-500 ºC.

Sericite and chlorite and their associated oxides indicate a retrogressive metamorphism under greenschist facies conditions. However, the sericite occurs in large feldspar crystals, which it replaces. The chemical reaction of sericitization of feldspar is the same as the replacement of feldspar by muscovite, which is coupled with the formation of myrmekite (Figure ; Phillips et al. 1972; Bucher & Frey 2002). Philips et al. also suggest that the excess K_2O goes towards development of retrogressive biotite replacing garnet or the further sericitization of associated plagioclase.

$$\left\{\begin{matrix}3KAlSi_3O_8\\NaAlSi_3O_8\end{matrix}\right\} + \left\{\begin{matrix}CaAl_2Si_2O_8\\NaAlSi_3O_8\end{matrix}\right\} + H_2O \rightarrow \left\{\begin{matrix}CaAl_2Si_2O_8\\2NaAlSi_3O_8\end{matrix}\right\} + 6SiO_2 + KAl_2(AlSi_3)O_{10}(OH)_2 + K_2O$$

alkali feldspar | calcic plagioclase | water | more sodic plagioclase | quartz | muscovite

myrmekite

Figure 2.16: proposed approximate reaction for destruction of feldspars after Philipps et al. (1972)

Figure 2.39 shows that sericite is growing parallel to crystallographic directions like the muscovite, and a transition to small muscovite grains is discernible. Furthermore, there is no

significant retrogression of mica to sericite. Thus it is likely that the sericitization is tied to the formation of the myrmekite under lower amphibolite facies conditions.

At Parson Hill the rocks are locally chloritized. The chloritization is associated with cataclastic bands (Figure 2.40). A shear sense cannot be inferred although the fault is nearly parallel to the foliation and a link to the primary deformation process seems likely. Biotite is replaced by chlorite (Figure 2.41), which is a typical retrogressive reaction of the greenschist facies (cf. McNamara 1966). In proximity to the chloritized areas feldspars have been pervasively sericitized as well (Figures 2.26, 2.27). The sericite is more finely grained and looks different than the sericite, which is supposed to be related to the myrmekites. The direct vicinity to bands of recrystallized quartz suggests that they served as zones of increased chemical exchange. All this records retrogressive metamorphism and semi-ductile deformation at relatively low temperatures. However, there are indications that the metamorphic regime did not shift from amphibolite facies to greenschist facies conditions progressively during deformation:

(1) Chlorite bands pervade the affected rocks. These bands contain strings of opaque minerals that are probably iron oxides (Figure 2.41). Retrogression of biotite to chlorite and opaques is common (e.g. Wickham 1987). As these strings are more or less continuous strings of beads it is very unlikely that they formed due to shearing of larger oxide grains, which would have resulted in brittly dismembered clasts. Rather, the opaques had already crystallized as strings.

(2) Some of the chlorite formed spatially independently from biotite. This chlorite developed a delicate vermicular structure (Figure 2.42). Vermicular chlorite is known as a product of hydrothermal alteration (Espejo & Lopez-Gamundi 1994), which is likely to be a result of brittle fracturing (e.g. Bruhn et al. 1994).

Both these fragile structures would have been destroyed if the primary shearing and deformation process had lasted continuously until the required greenschist facies conditions had been reached (pers. comm. Shelley 2010). Therefore the brittle fracturing and the associated chloritization belong to a separate younger event that probably involved hydrothermal activity. As the faulting occurred parallel to the foliation it cannot be ruled out that the older movement plan was reactivated. But the deformation causing the NE-SW trending lineations and the mylonitic fabric took place under amphibolite facies conditions only.

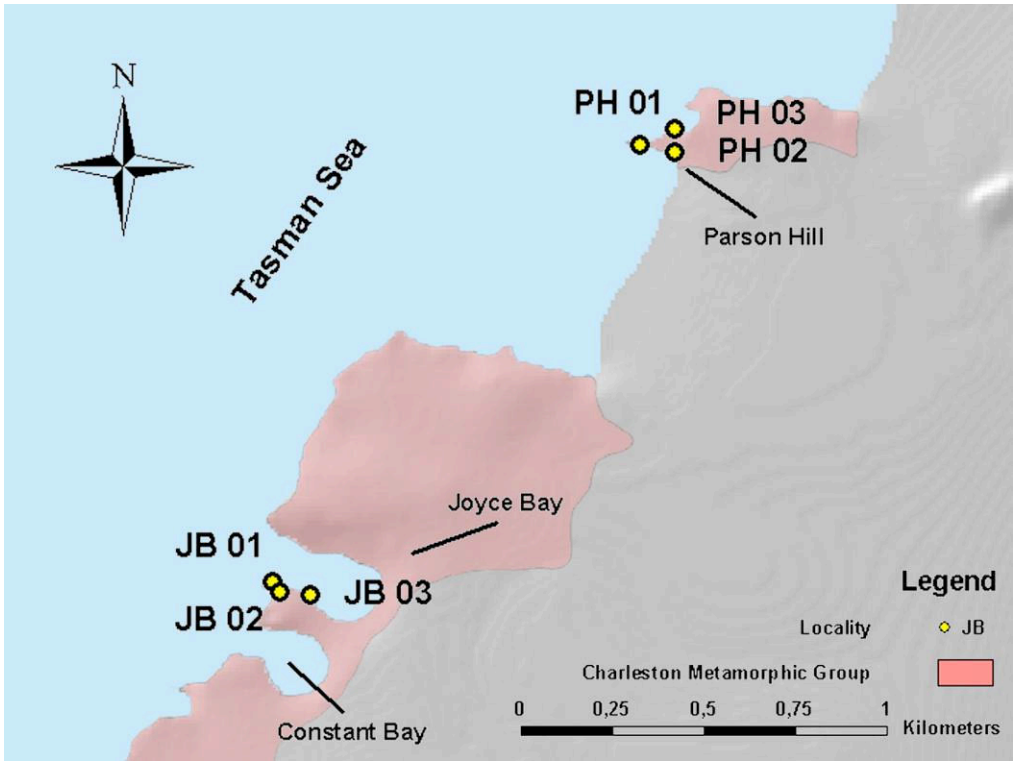

Figure 2.17: Sample area at Charleston; Geology after Rattenbury et al. (1998).

Figure 2.18: NE-trending lineations at Joyce Bay.

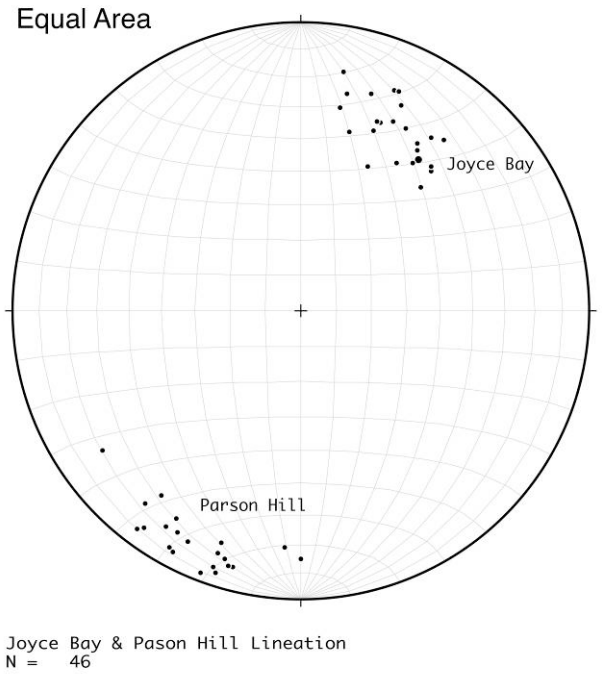

Figure 2.19: Stereographic projection of the lineations at Joyce Bay and Parson Hill showing a clear NE-SW trend.

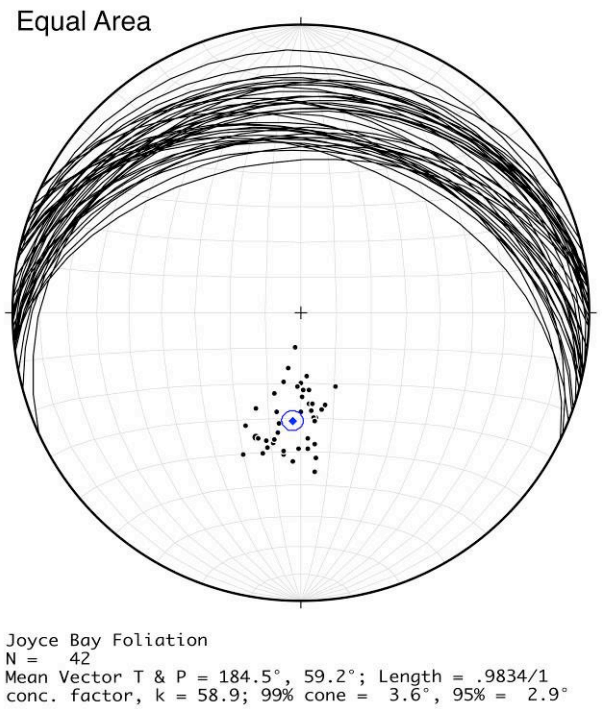

Figure 2.20: Stereographic projection of the foliation at Joyce Bay dipping gently to NNE, blue dot representing the mean plane pole.

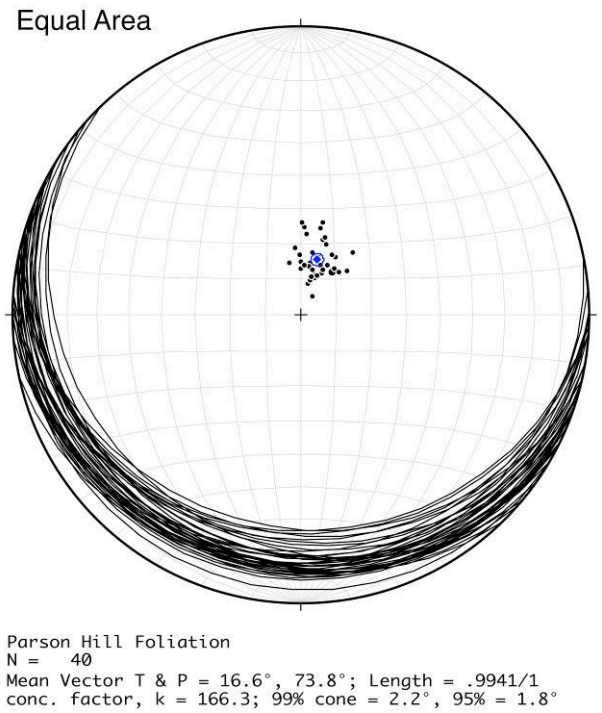

Figure 2.21: Stereographic projection of the foliation at Parson Hill dipping gently to SSW, blue dot representing the mean plane pole.

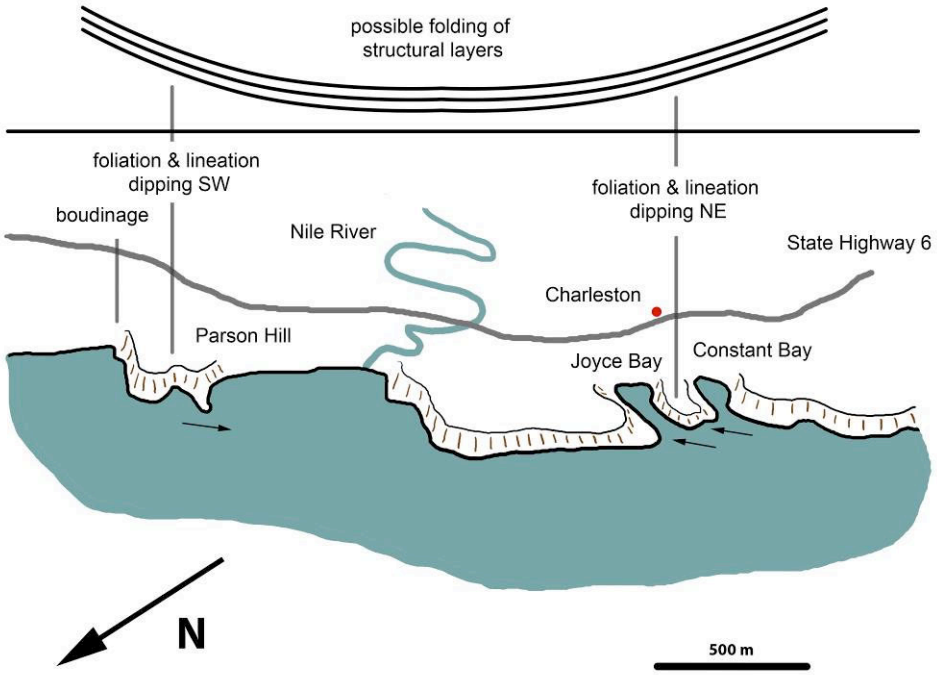

Figure 2.22: Overview over the locations at Charleston; arrows representing the trend of lineations.

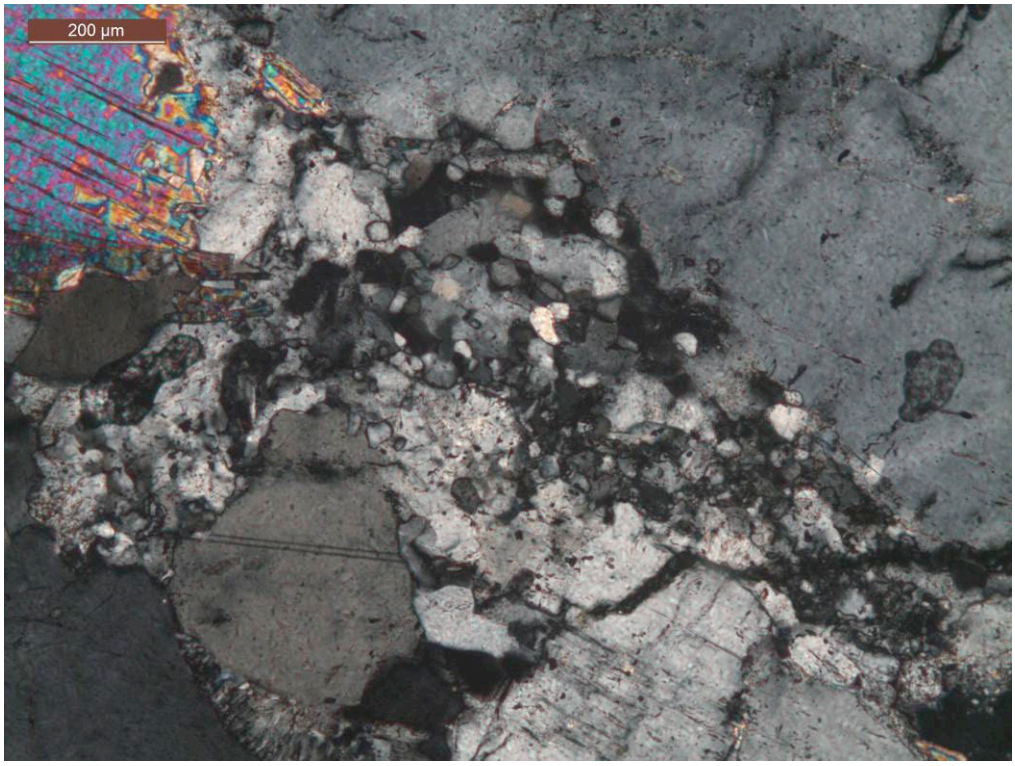

Figure 2.23: Patch of dynamically recrystallized quartz at Joyce Bay; JB010101-4, CPL.

Figure 2.24: Less deformed rocks at Joyce Bay appear to be more massive.

Figure 2.25: Rocks at Parson Hill display a well-developed schistosity.

Figure 2.26: Continuous band of recrystallized quartz at Parson Hill; seritization of feldspar; PH010106-2, CPL.

Figure 2.27: Continuous band of recrystallized quartz and C/S-structures indicating top-to-the SW sense of shear at Parson Hill; sericitization of feldspar; PH010104-2. CPL.

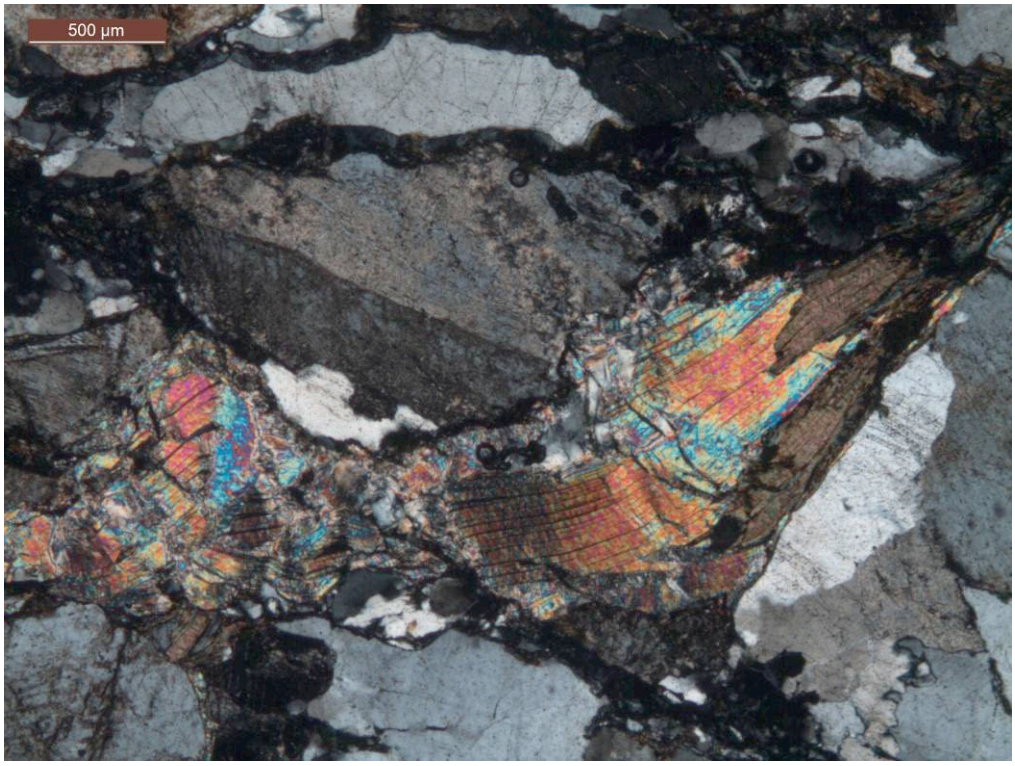

Figure 2.28: Kinked and fragmented muscovite partly replaced by biotite; PH010107-3, CPL.

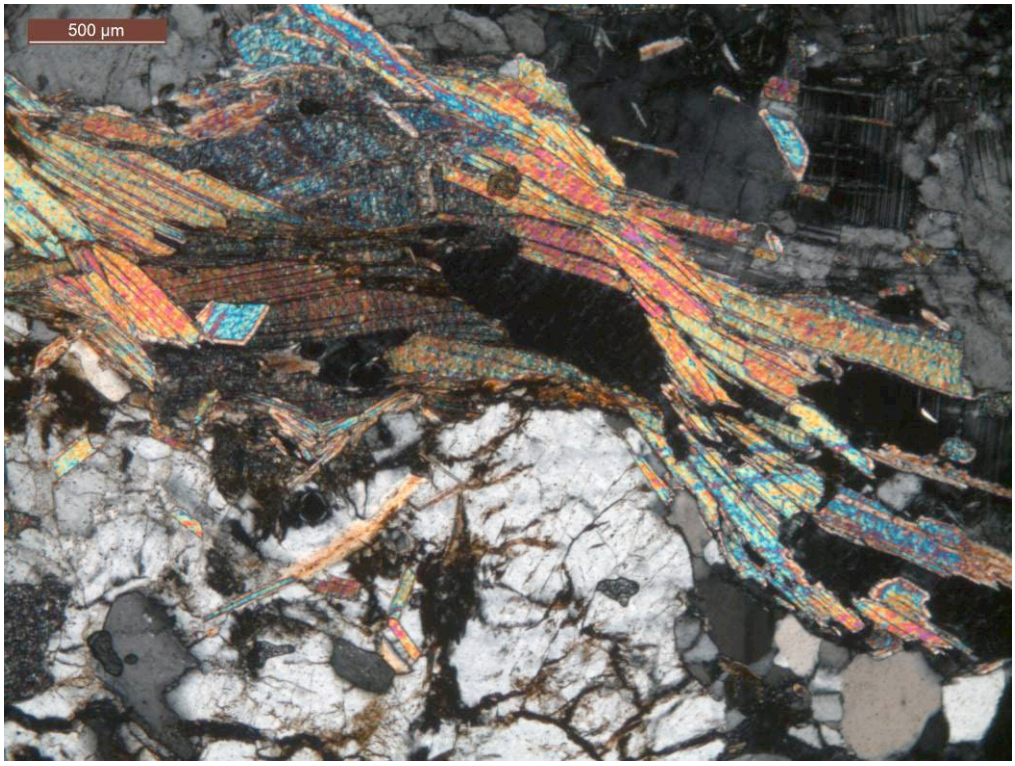

Figure 2.29: Fragmented muscovite; JB010101-3, CPL.

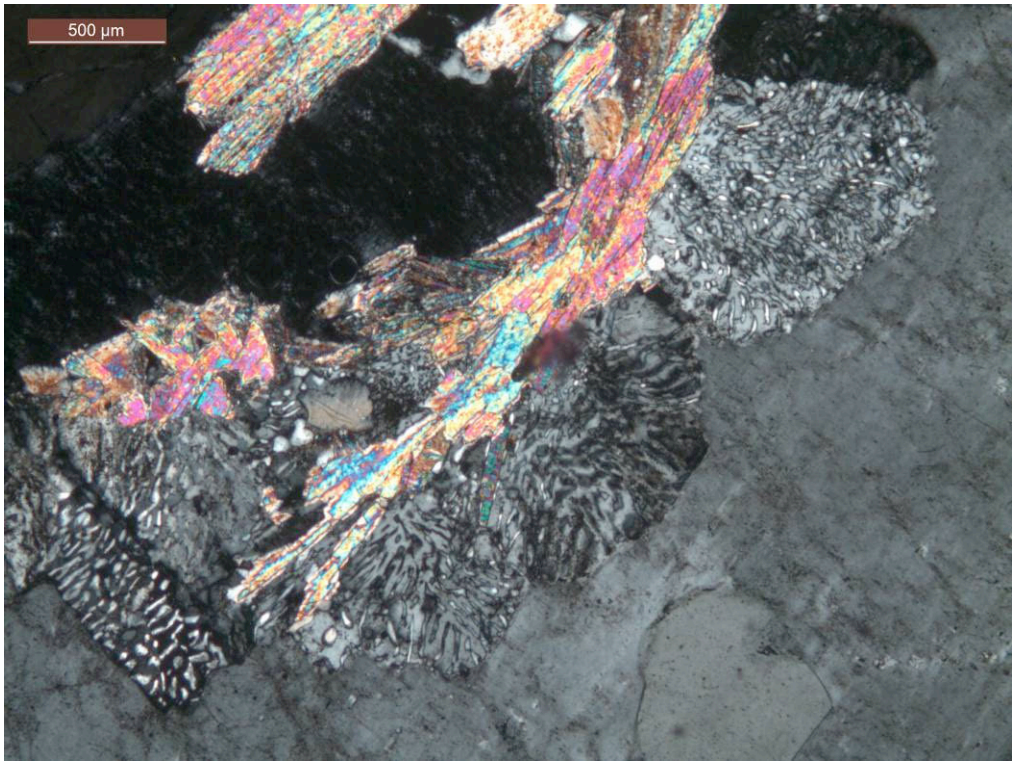

Figure 2.30: Myrmekite replacing K-feldspar; JB020201-1, CPL.

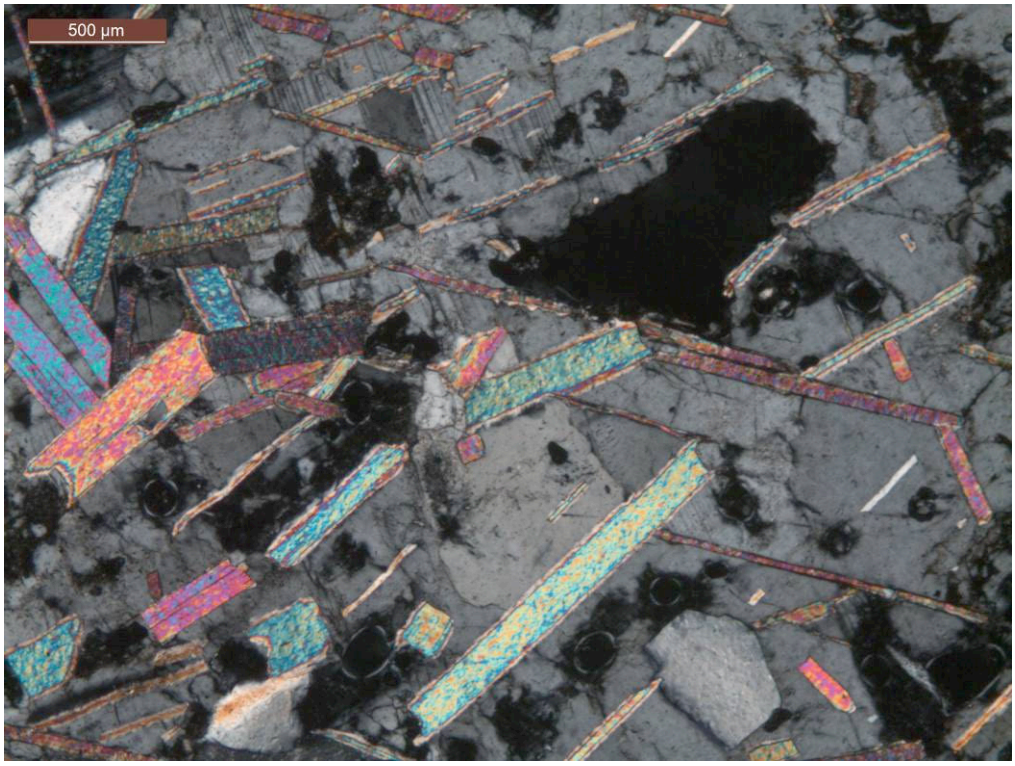

Figure 2.31: Muscovite replacing K-feldspar; JB010101-1, CPL.

Figure 2.32: Boudinage at Parson Hill suggesting a top-to-SW sense of shear.

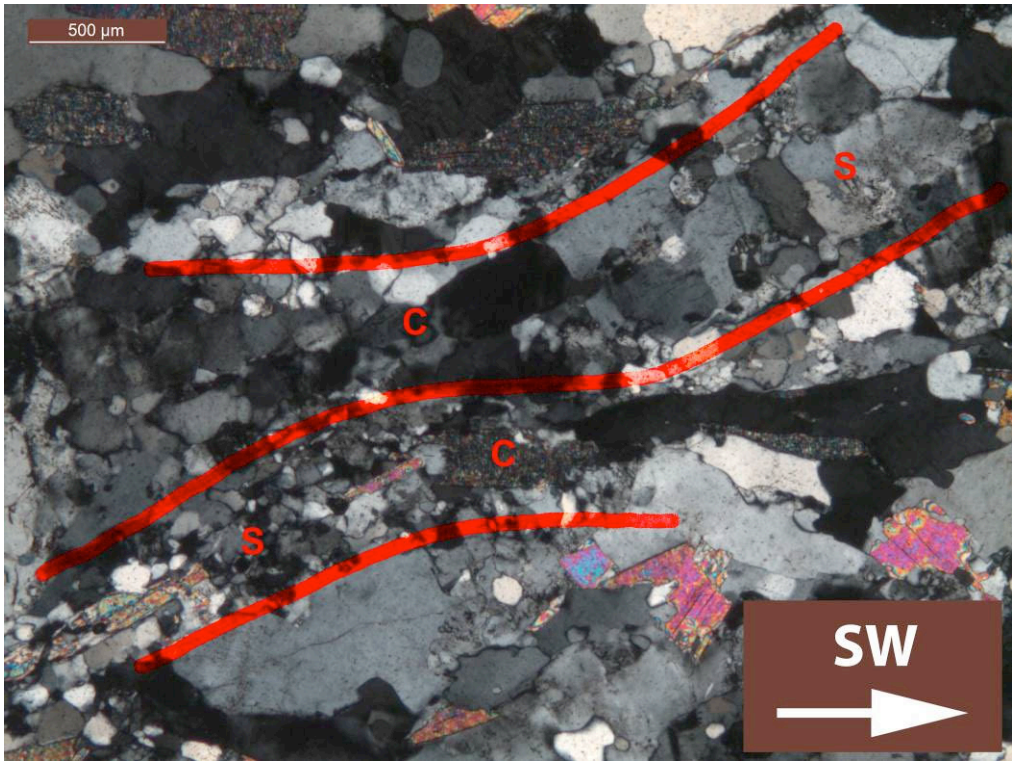

Figure 2.33: Weakly developed C/S-structures at Joyce Bay indicating top-to-SW sense of shear; JB030202-1, CPL.

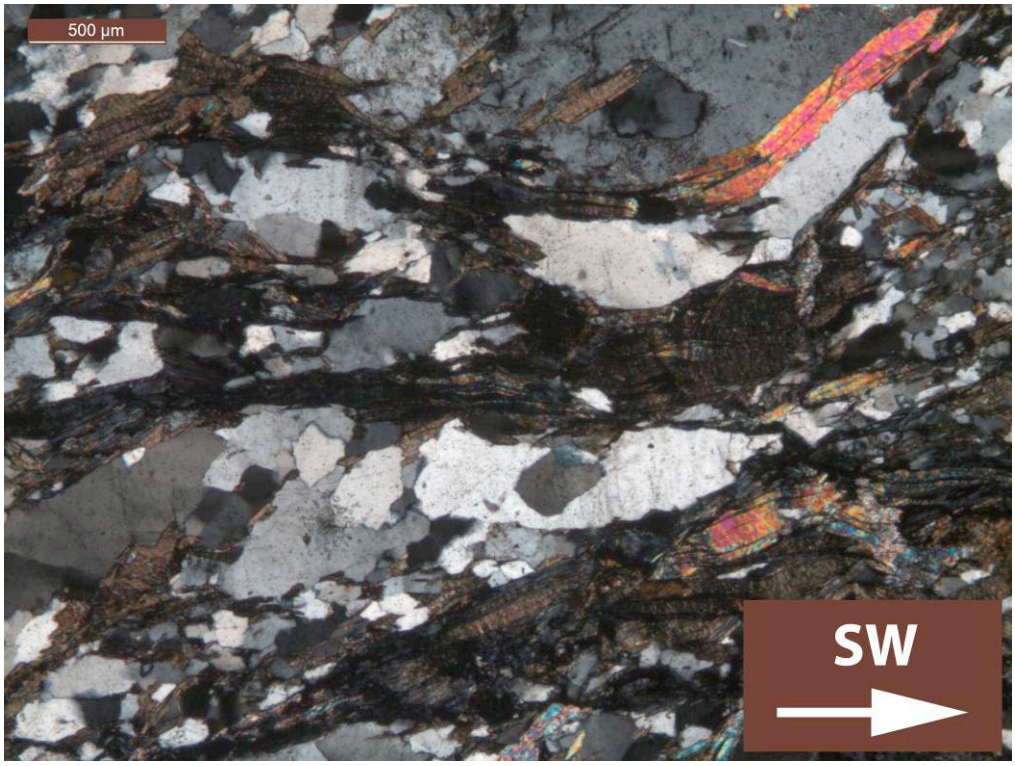

Figure 2.34: Well-developed C/S-structures at Parson Hill indicating top-to-SW sense of shear; PH010104-1, CPL.

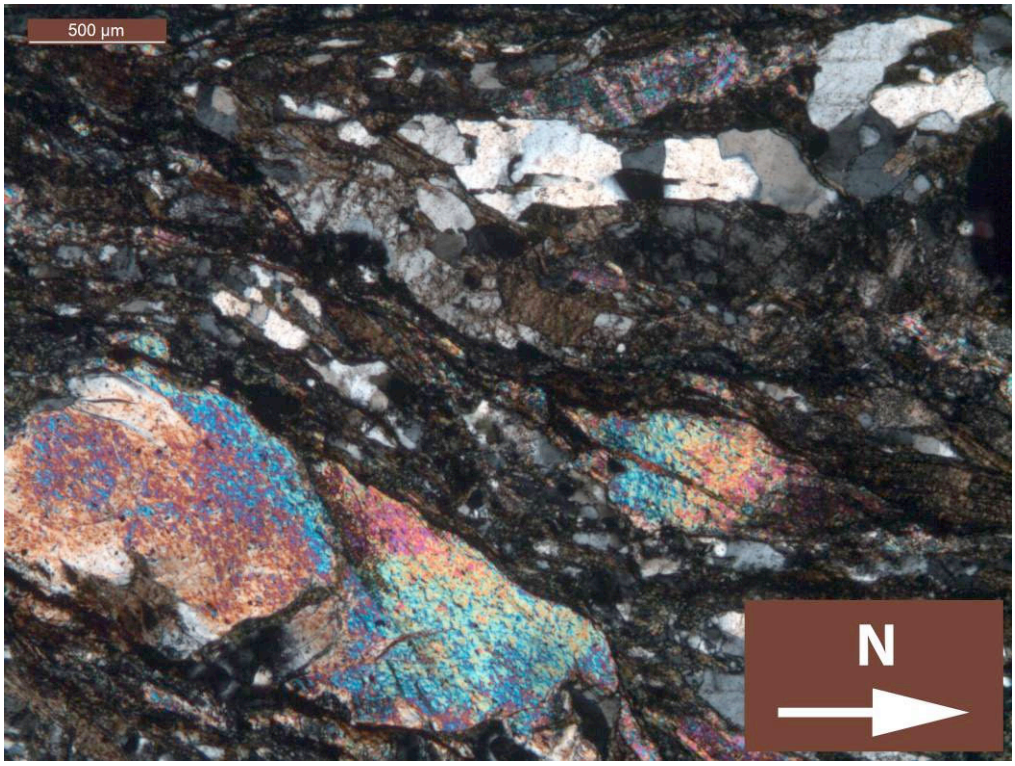

Figure 2.35: C/S-structures at Parson Hill indicating top-to-S sense of shear; PH010106-1, CPL.

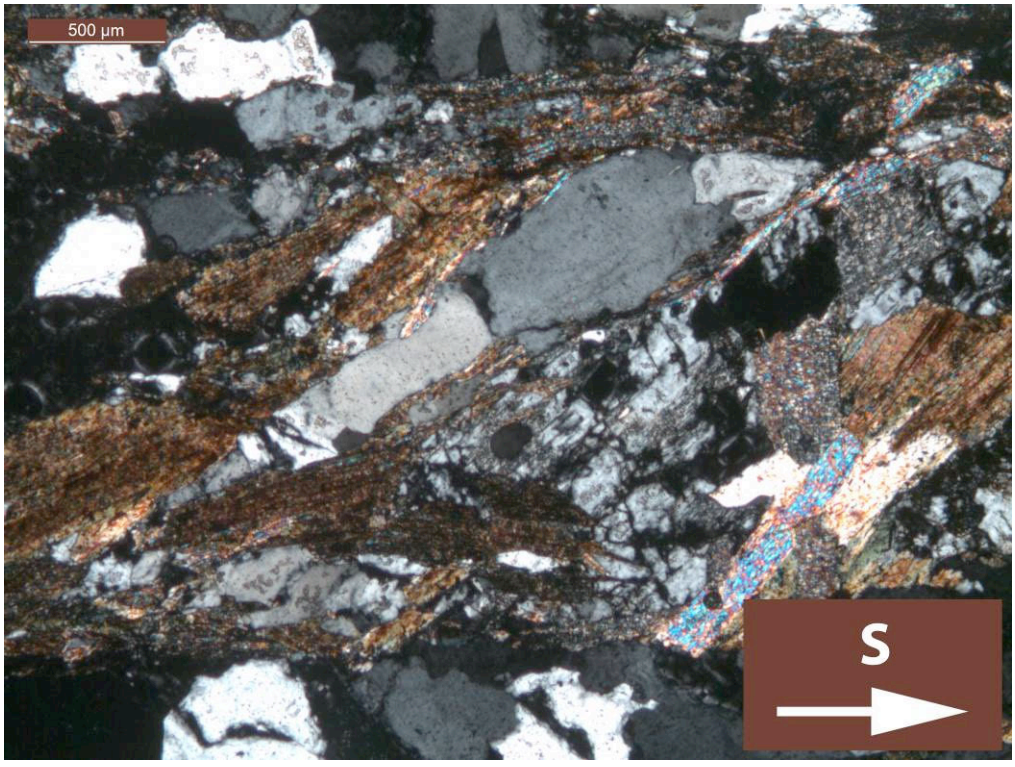

Figure 2.36: Well-developed C/S-structures at Parson Hill indicating top-to-S sense of shear; PH020102-1, CPL.

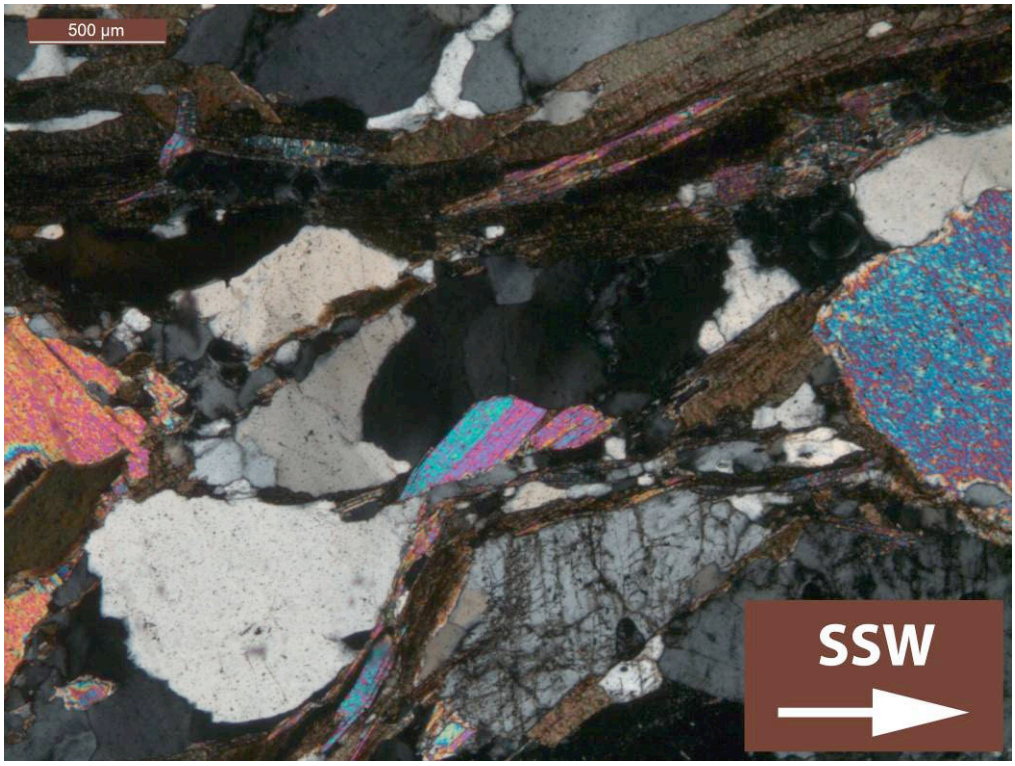

Figure 2.37: Well-developed C/S-structures at Parson Hill indicating top-to-SSW sense of shear; PH030301-3, CPL.

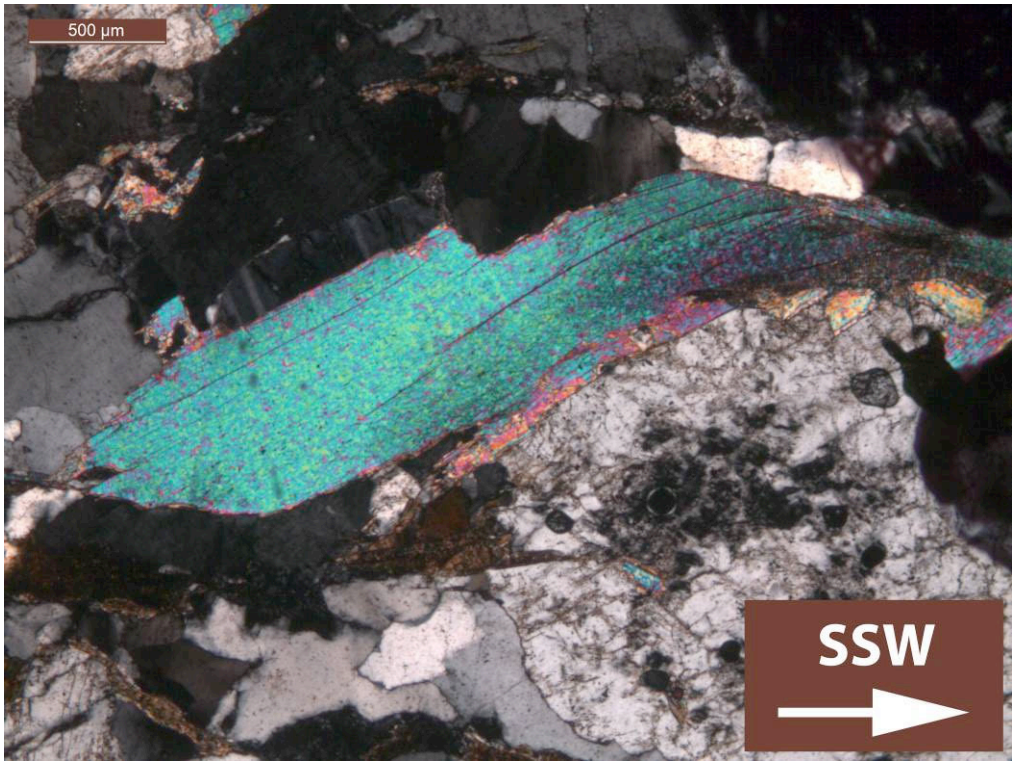

Figure 2.38: Mica fish indicating top-to-SSW sense of shear; PH030301-2, CPL.

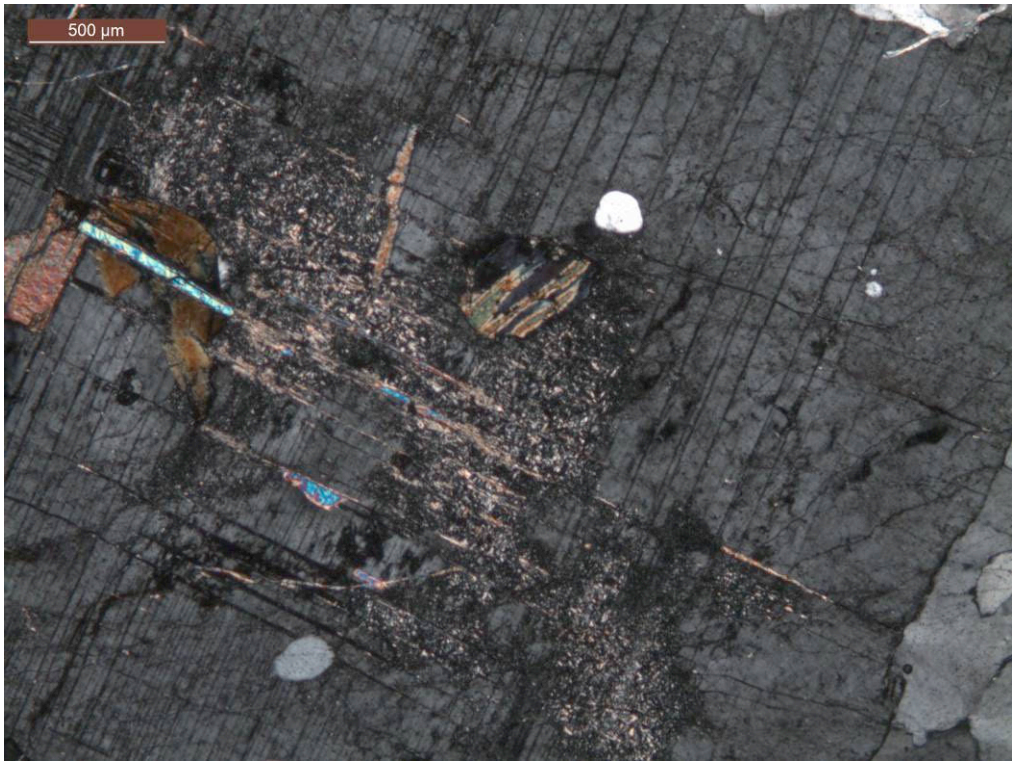

Figure 2.39: Sericite and Muscovite replacing K-feldspar; PH010107-4, CPL.

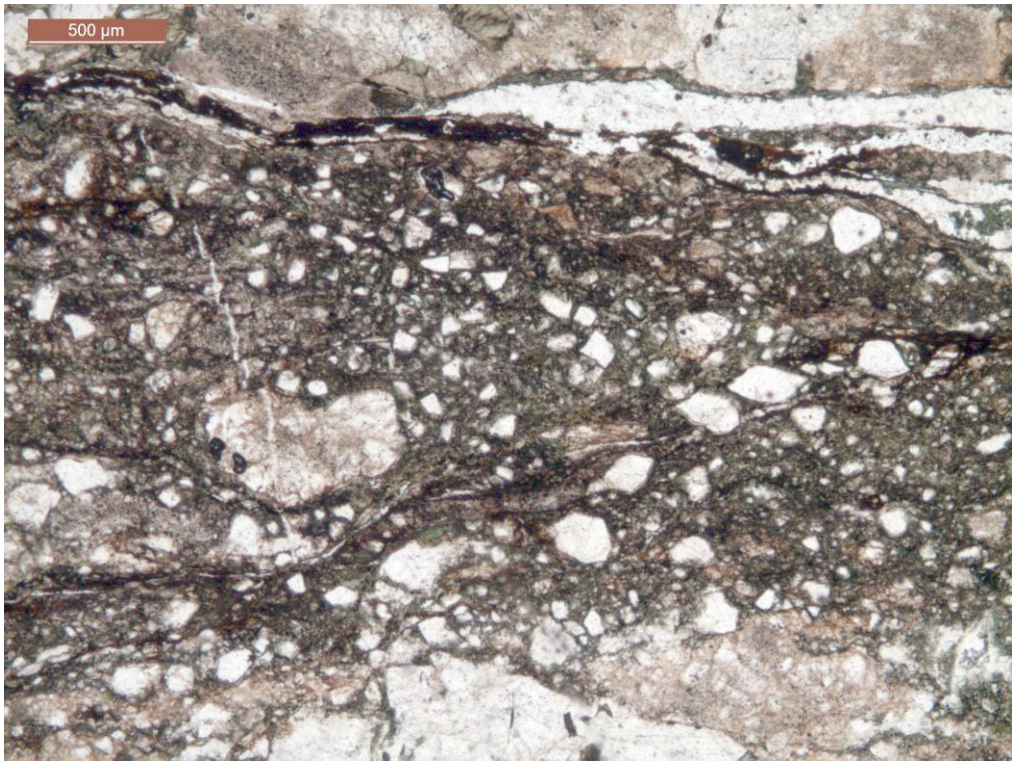

Figure 2.40: Cataclastic band with angular fragments and chlorite; PH010203-2, PPL.

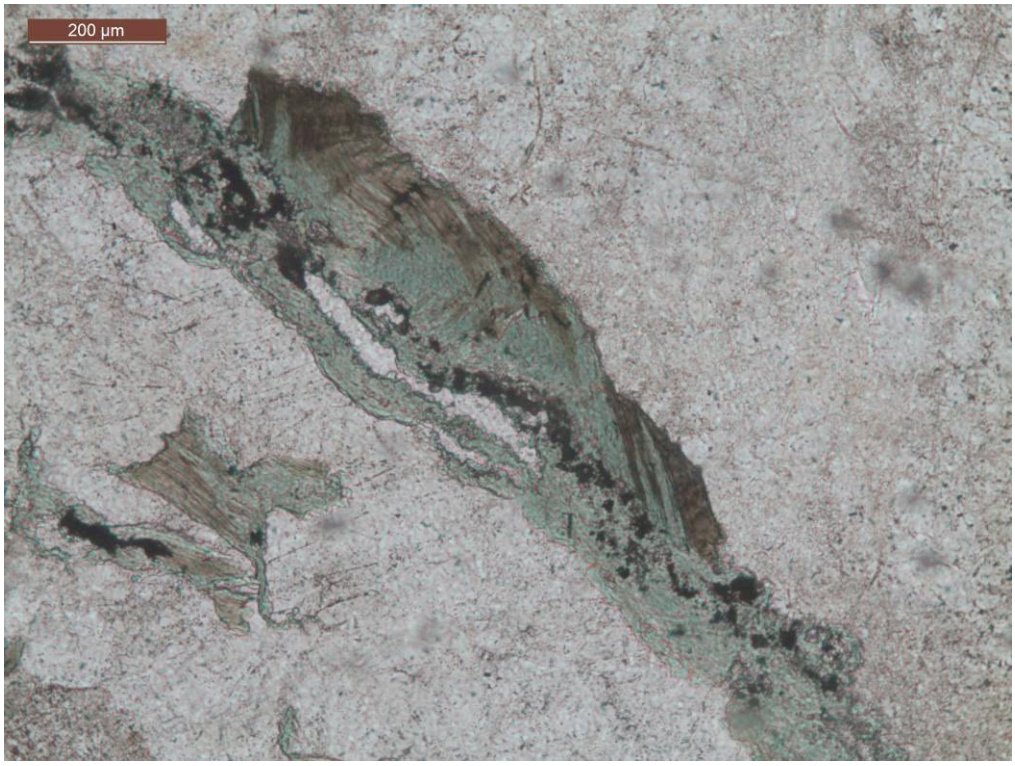

Figure 2.41: Chlorite replacing biotite, string of opaque minerals, PH010108-1, PPL.

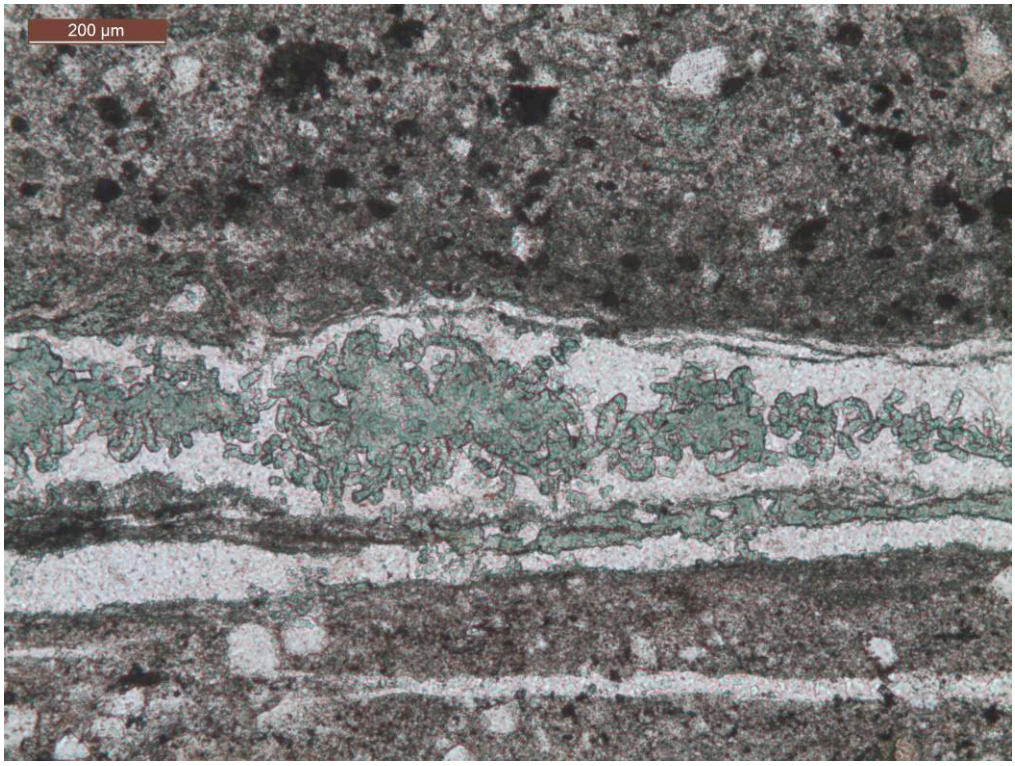

Figure 2.42: Vermicular chlorite forming parallel to the old foliation, probably hydrothermal; PH010107-2, PPL.

2.2.3. White Horse Creek Beach

South of Charleston more gneisses are exposed on the steep coastline. The mineral contents are quartz, feldspar, biotite, muscovite and in some areas garnet, oxides and magnesite. Compared to the rocks at Charleston the mica content, the deformation and the metamorphic conditions are significantly higher. A 2 km long coastal section between Morrisey Creek and Red Jacket Creek was studied and is referred to as White Horse Creek Beach in this thesis. Samples were taken at 9 different locations (Figure 2.44).

Rocks with very different fabrics are exposed along the coast. Finite strain was accommodated heterogeneously and varies in a wide range. The foliation is subhorizontal and gently folded along the entire section. The fold axis appears to trend NE-SW (Figure 2.45), which would be in agreement with Shelley's observations (1970b). But the foliation surfaces are often not plain due to crenulations and younger brittle structures. Thus the true foliation is obscured and occasionally dips shallowly in random directions. The lineation, which trends from SW-NE in the north (Figure 2.46) to SSE in the south (Figure 2.47), is also hard to determine. The rocks often lack smooth foliation planes that contain the lineation. Almost all rocks show features of ductile deformation that have been overprinted by a later brittle deformation (Figures 2.43, 2.48, 2.49).

At the northern end of the examined section just south of Morrisey Creek the coarse grained gneisses display a protomylonitic to mylonitic fabric (Locations WH01 and WH02, Figure 2.44). The ductile character increases progressively in a southward direction. Dynamically recrystallized quartz, C/S- and C'-structures are very abundant and indicate a top-to-SW sense of shear (Figures 2.50, 2.51, 2.52). The C/S- and C'-structures are defined by recrystallized biotite and muscovite, and by mica fish. Feldspar remains sturdy overall but already shows undulose extinction (Figure 2.51), a sign of initial crystal plastic deformation (Passchier & Trouw 2005).

About 400 meters south of Morrisey Creek (Location WH03, Figure 2.44) the progressively increasing deformation culminates in an ultramylonite zone of several meters thickness. Lineations trend SW to SSW (Figure 2.53, 2.54). As the location of the ultramylonites is isolated on a beach the transition to the adjacent rocks to the north and south is not visible.

A dark, very fine-grained matrix contains some feldspar porphyroclasts with long stretched tails (Figure 2.55) and folded feldspathic bands (Figure 2.56), which already indicate a top-to-SW sense of shear on macroscopic scale. In thin section it is revealed that the remaining porphyroclasts deformed ductiley and brittly. Large plagioclase crystals are bent, broken or shattered (Figures 2.57, 2.58). Thus the conditions for ductile deformation were reached but a

high strain rate still forced larger grains to brittle failure. Quartz and feldspar recrystallized dynamically in strain shadows (Figure 2.59) and in the matrix (Figures 2.57, 2.58) where they formed continuous bands (Figure 2.60). Several muscovite flakes remained as porphyroclasts and formed mica fish while the remaining muscovite and biotite recrystallized to bands of micro-sized grains in the matrix (Figure 2.61). The mica fish (Figure 2.62), porphyroclasts (Figure 2.63) and C/S-structures of mica and dynamically recrystallized quartz (Figures 2.64, 2.65) confirm the southwesterly shear sense. Some thin sections were cut at different angles to the lineation. Shear sense indicators in these thin sections show a southward sense of shear as well (Figures 2.66, 2.67).

Layers of recrystallized feldspar and quartz contain garnets. These garnets show no sign of plastic deformation. Yet some of the grains were affected by the shearing and were brittly comminuted and dispersed in the deformation process (Figure 2.68). This gives an estimate on the maximum metamorphic conditions as garnet does not deform plastically at temperatures below 700 ºC (Ji & Martignole 1994; Storey & Prior 2005). Together with the plastically deformed feldspar this results in a relatively wide temperature range of 500-700 ºC for the deformation of the ultramylonite. As the feldspars show not only plastic deformation like bending but also intense recrystallization, it is likely that temperatures were higher than ca. 550 ºC (cf. Vidal et al. 1980). Higher-grade minerals like sillimanite, which would narrow down the temperature range even more, were not observed in the thin sections but have been reported from other places by other workers (cf. White 1994).

From half way between Morrisey Creek and White Horse Creek on southwards the intensity of deformation decreases again. Yet, it is not a continuous decrease. Finite strain has been accommodated heterogeneously (Figure 2.43). However, the deformational regime is much lower than at the ultramylonite site. In some places Feldspars stop recrystallizing and become sturdy, while at others they stay ductile (Figure 2.69). The gneiss is overall more coarsely grained and less ductilely deformed. In places strain is so weak that typical features like C/S-structures or mica fish are indiscernible and thus cannot be used to determine the shear sense. Quartz is still recrystallized but the grains reach much bigger sizes in these rocks (Figure 2.70). All this suggests weaker deformation than at the previous sites on the coastline section. To the southern end of the sampled area deformation slightly increases and C/S-structures of mica become discernible again (Figures 2.71, 2.72). The sense of shear along the studied coastline is consistently top-to-SW.

In the southern part of the area the gneisses have been intruded by pegmatites of up to several meters thickness (Figure 2.73). Following the coast southwards, the brittle overprint becomes

stronger and more and more relatively steep faults cut the gneiss and the pegmatites (Figures 2.43, 2.74). The pegmatites have been boudinaged and suggest a top-to-SSW sense of shear consistent with the microstructures described previously. The strain shadows of the boudins show precipitation of Quartz (Figure 2.74). Sericitization and magnesite ($MgCO_3$) veins are associated with the brittle overprint (Figures 2.76, 2.77, 2.78 at WH06, Figure 2.44). The magnesite veins intersect C/S-structures of the gneiss and are not affected by deformation. Thus they postdate the ductile shearing. As the afflicted rocks lack biotite this is a plausible source for the Mg. Conspicuous massive alterations of biotites that were replaced by opaques, which are probably iron oxides, occur further to the north (Figure 2.79, at WH02, Figure 2.44). Iron oxides and carbonates are typical hydrothermal alterations (cf. Stringham 1952) and hydrothermal activity has been reported from many core complex detachments (cf. Kerrich & Rehrig 1987; Lister & Davis 1989; Bruhn et al. 1994; Marchev et al. 2005). With regard to the Pike detachment to the south the rocks containing the oxides represent a structurally deeper level. Iron oxides are stable at temperatures as low as 100 ºC if the hydrothermal fluid contains CO_2 (Tareen & Krishnamurthy 1981) while hydrothermal magnesite forms below this temperature (~65-80 ºC; cf. Fallick et al. 1991; Ece et al. 2005). Thus the iron oxides could be linked to the magnesites, representing a structurally deeper level of hydrothermal alteration (Figure 2.80). The low temperatures also show that these alterations formed in a brittle regime.

Ductile and brittle deformation can be distinguished quite well. The ductile deformation was accommodated heterogeneously and ranges from ultramylonites to gneisses that show almost no sign of shearing (Figure 2.43). Feldspar recrystallized or behaved at least ductilely throughout most of the coastal section while garnet remained brittle even in the ulramylonite. Therefore the deformation temperature ranges from 550 ºC to 700 ºC and indicates an overall upper amphibolite facies regime.

Brittle overprinting is expressed in relatively steeply dipping faults, fracturing of the gneiss and associated retrogressive alteration. The examined area is located 2-3 km north of the inferred Pike Detachment. Assuming a dip of 25º for the detachment fault this translates to a distance of about one kilometer between the brittly overprinted gneisses and the fault. As hydrothermal activity is common in the vicinity of detachment faults, the occurrence of retrogressive alterations makes an association of the brittle overprint with the proximal detachment likely. The increase of brittle features towards the detachment supports this idea.

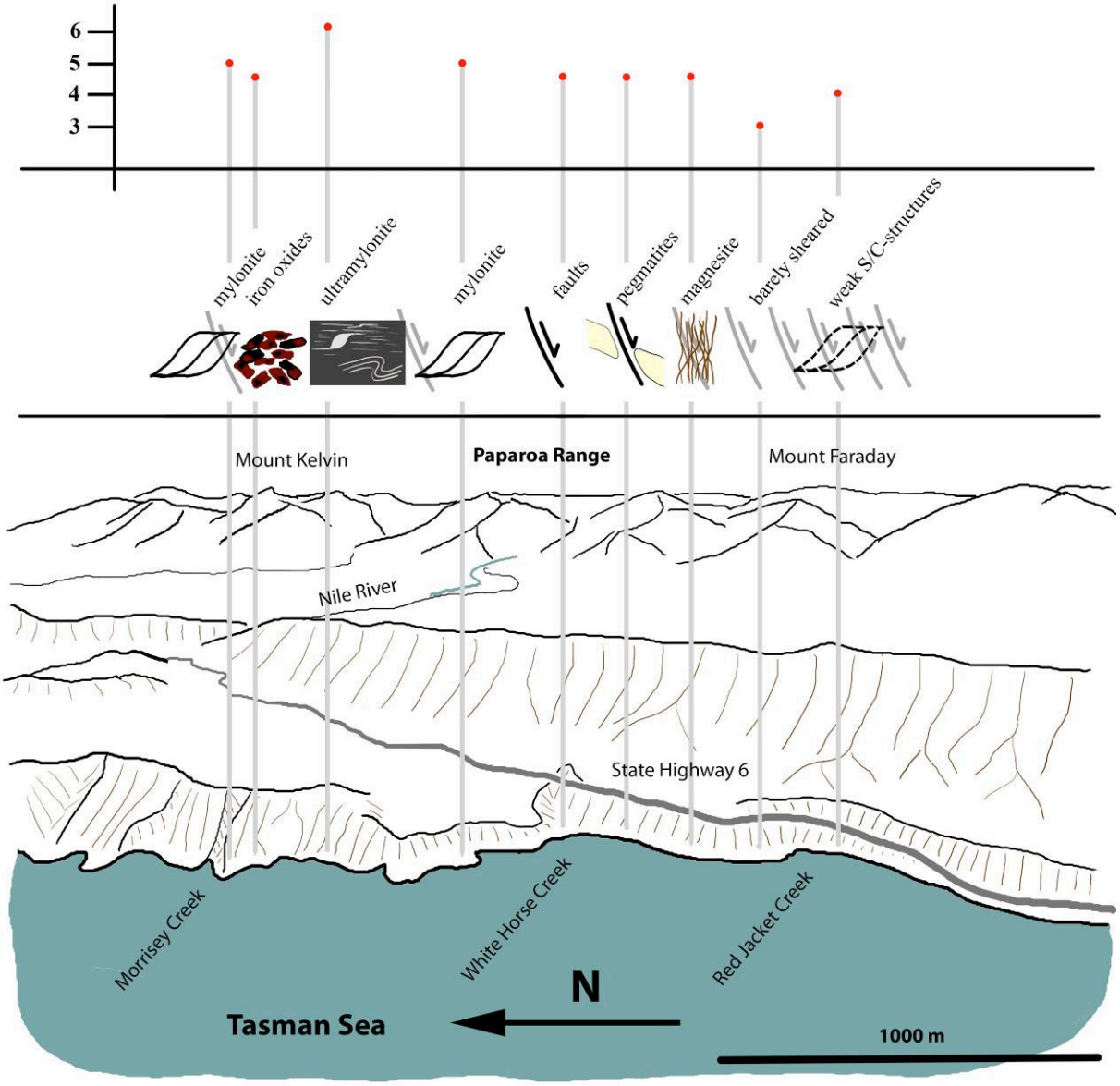

Figure 2.43: Deformation Profile: 3 = well-developed schistosity, barely sheared. 4 = weak shear sense indicators. 5 = mylonite with well-developed shear sense indicators. 6 = ultramylonite with feldspars smeared out to bands; density of faults represents intensity of brittle overprint.

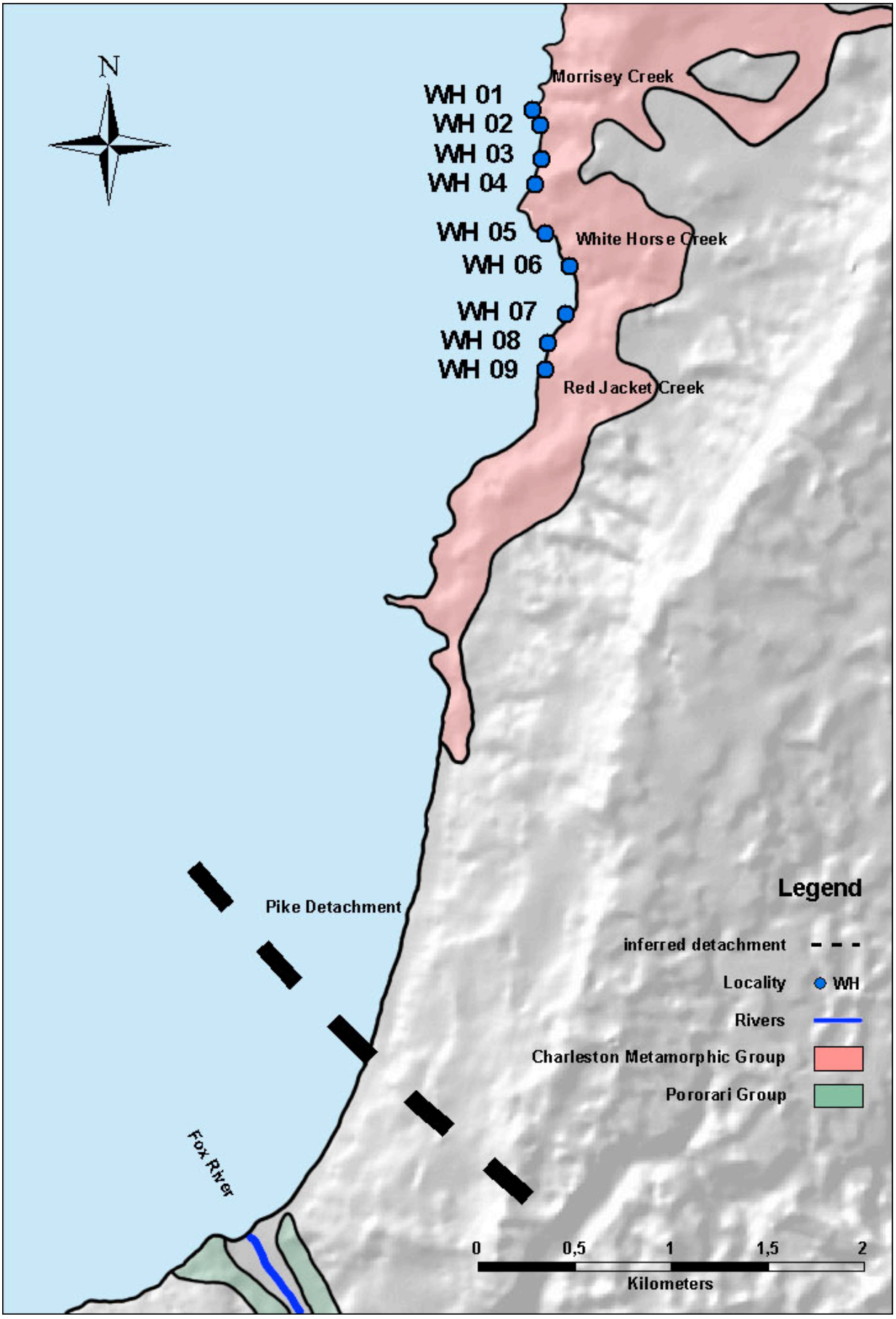

Figure 2.44: Sample area at White Horse Creek south of Charleston; Geology after Tulloch & Kimbrough (1989) and Rattenbury et al. (1998).

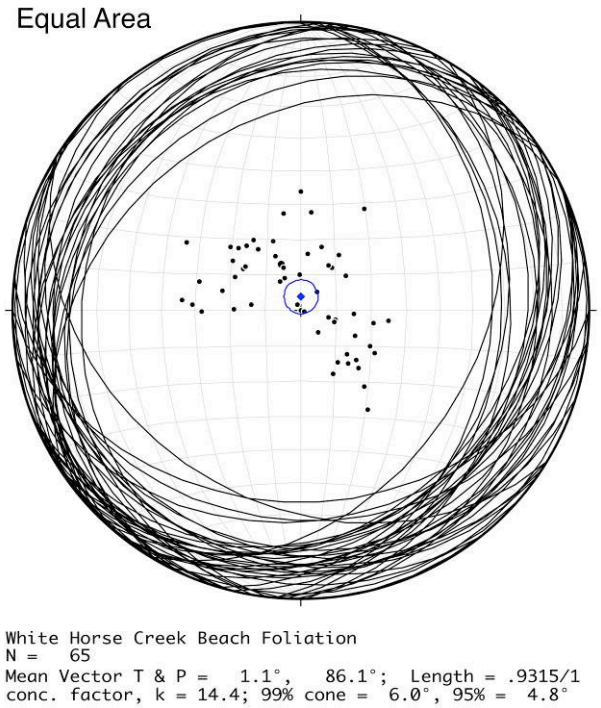

Figure 2.45: Stereographic projection of the foliation along the coastline, the alignment of the plane poles on a NW-SE axis indicates a NE-SW fold axis.

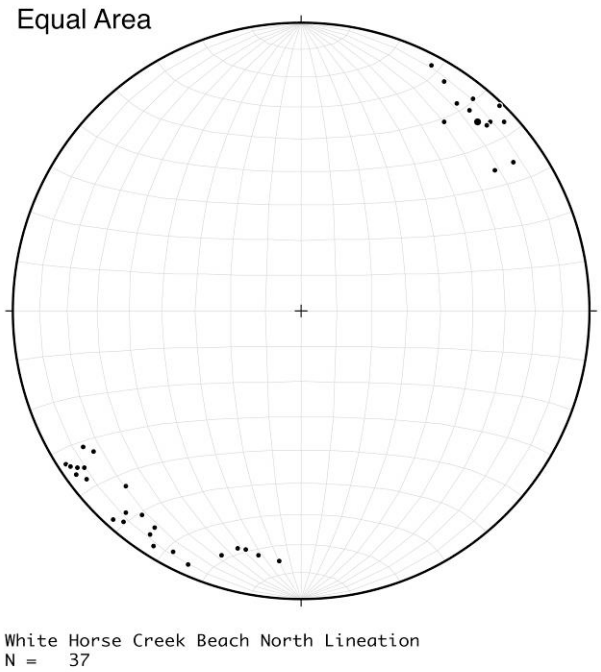

Figure 2.46: Stereographic projection of the lineations in the northern part of the sample area showing a SW to SSW trend.

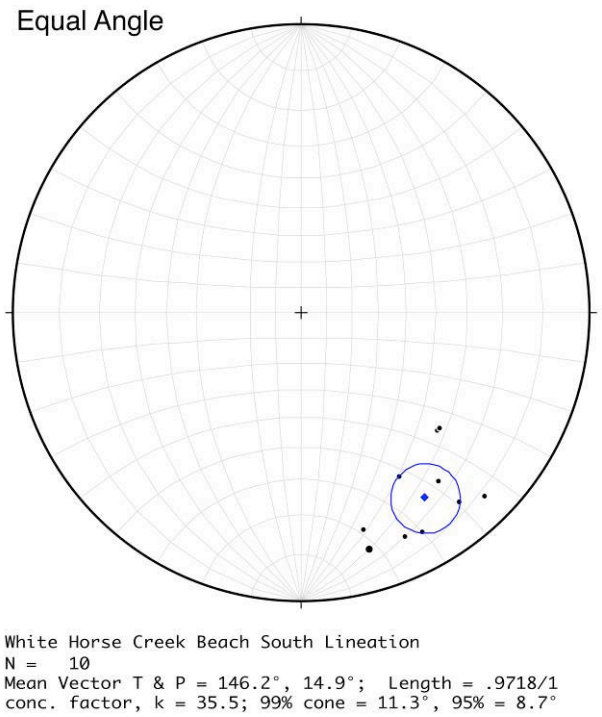

Figure 2.47: Stereographic projection of the lineations in the southern part of the sample area showing a SSE trend.

Figure 2.48: Ductilely deformed gneiss overprinted by brittle faults.

Figure 2.49: Ductilely deformed gneiss overprinted by brittle faults.

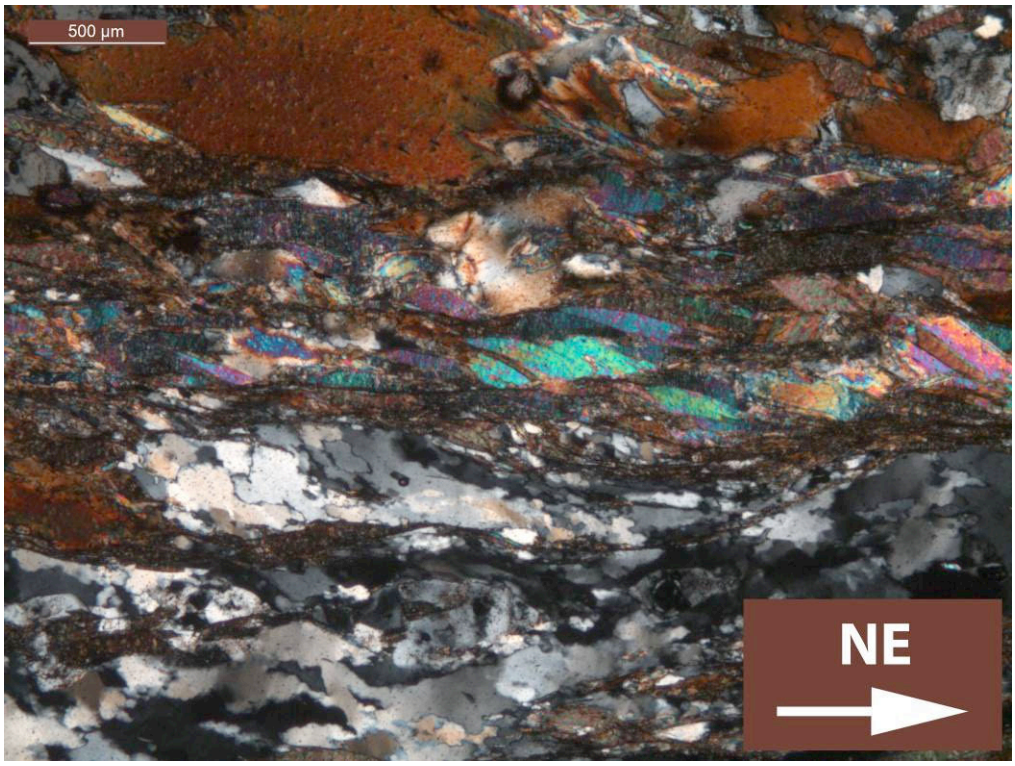

Figure 2.50: C/S-structures of mica indicating a top-to-SW sense of shear; WH010201-1, CLP.

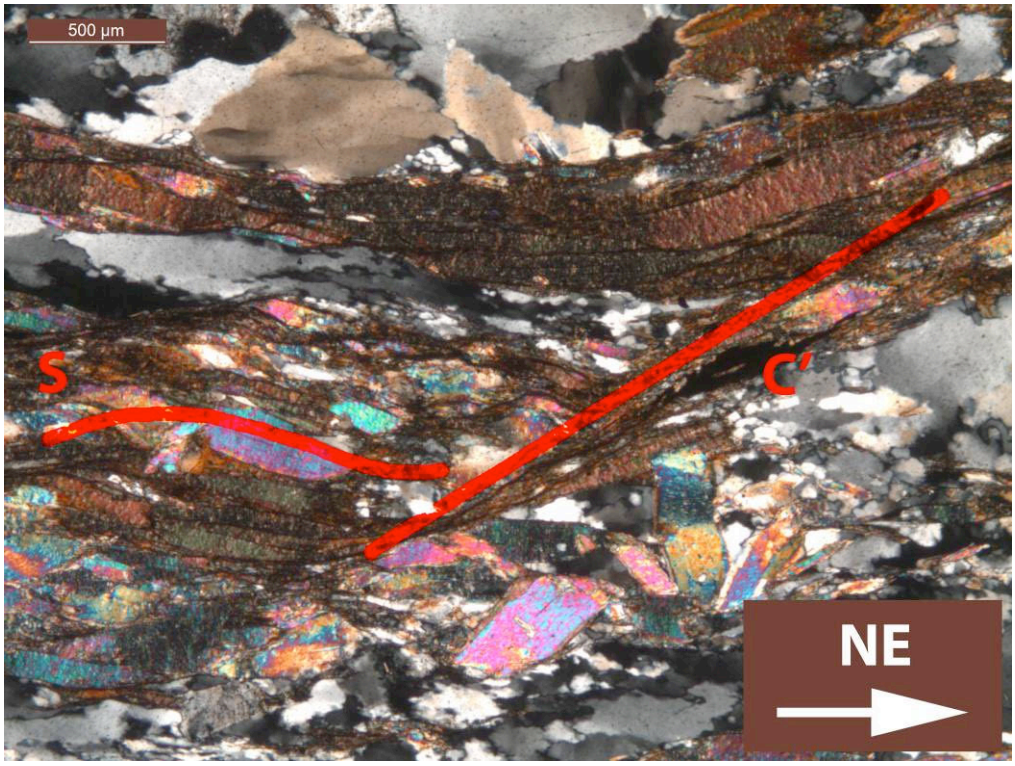

Figure 2.51: C'-structure of biotite and muscovite indicating top-to-SW sense of shear, undulose extinction in feldspar (left top), WH010201-2, CLP.

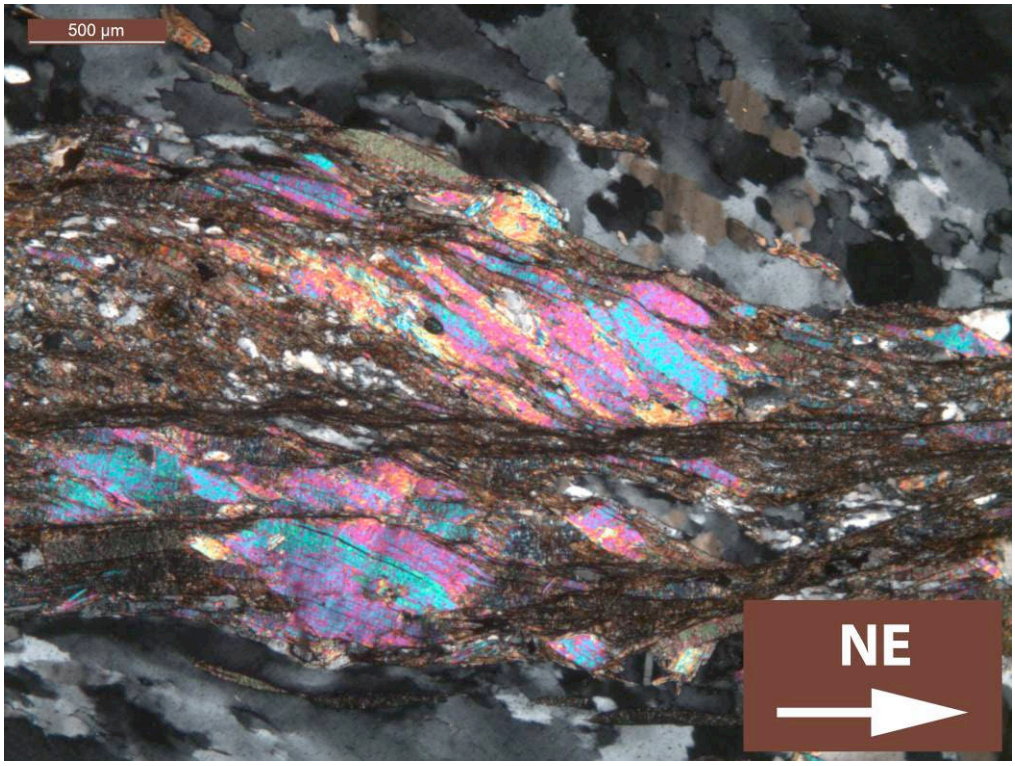

Figure 2.52: C/S-structures of mica and oblique foliation of dynamically recrystallized quartz indicating top-to-SW sense of shear; WH010201-, CLP.

Figure 2.53: Stretching lineations trending SW on ultramylonite foliation planes.

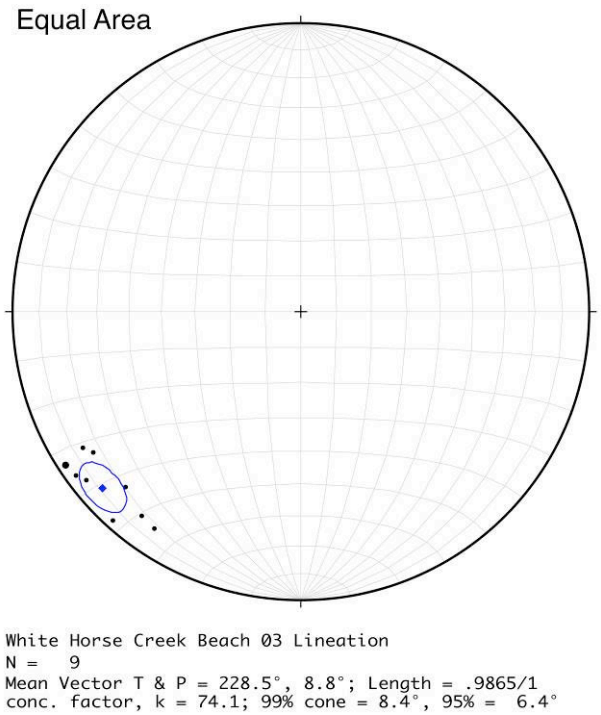

Figure 2.54: Stereographic projection of the lineations of the ultramylonite showing a SW trend.

Figure 2.55: Feldspar porphyroclasts indicating a top-to-SSW sense of shear, large feldspar porphyroslasts have a diameter of ca. 5 cm.

Figure 2.56: Folded feldspathic bands indicating a top-to-SSW sense of shear.

Figure 2.57: Bent and broken plagioclase phenocryst, recrystallizing quartz and feldspar in the matrix; WH030102-2, CLP.

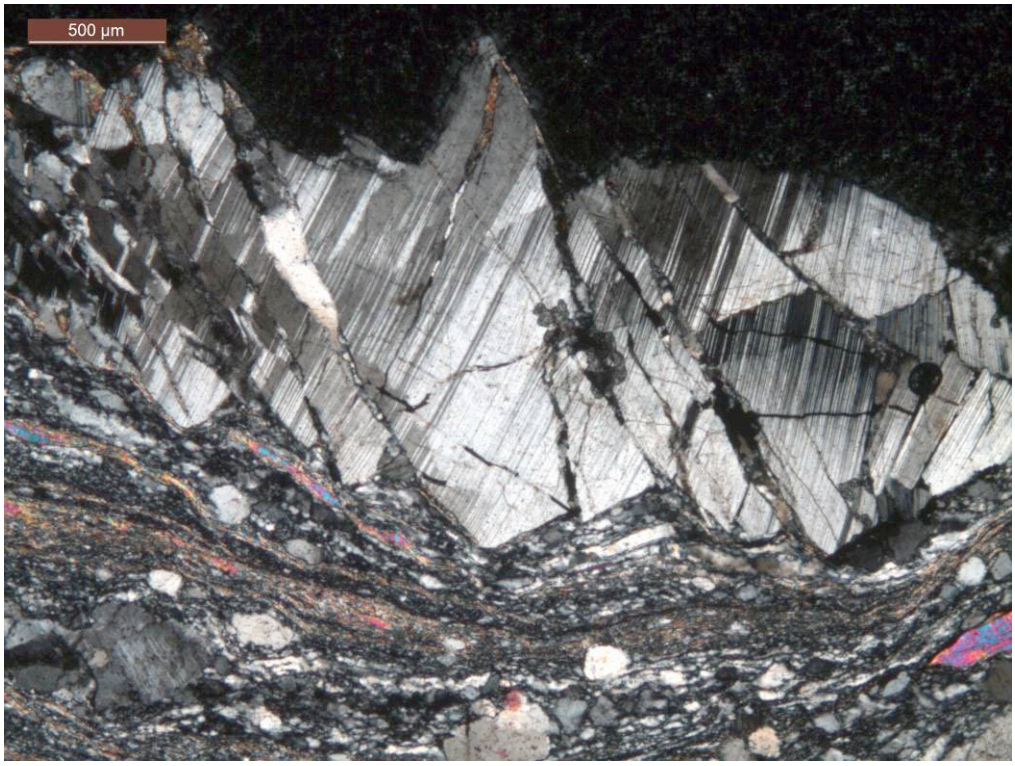

Figure 2.58: Large shattered plagioclase, dynamically recrystallized quartz and feldspar in matrix; WH030303-3, CLP.

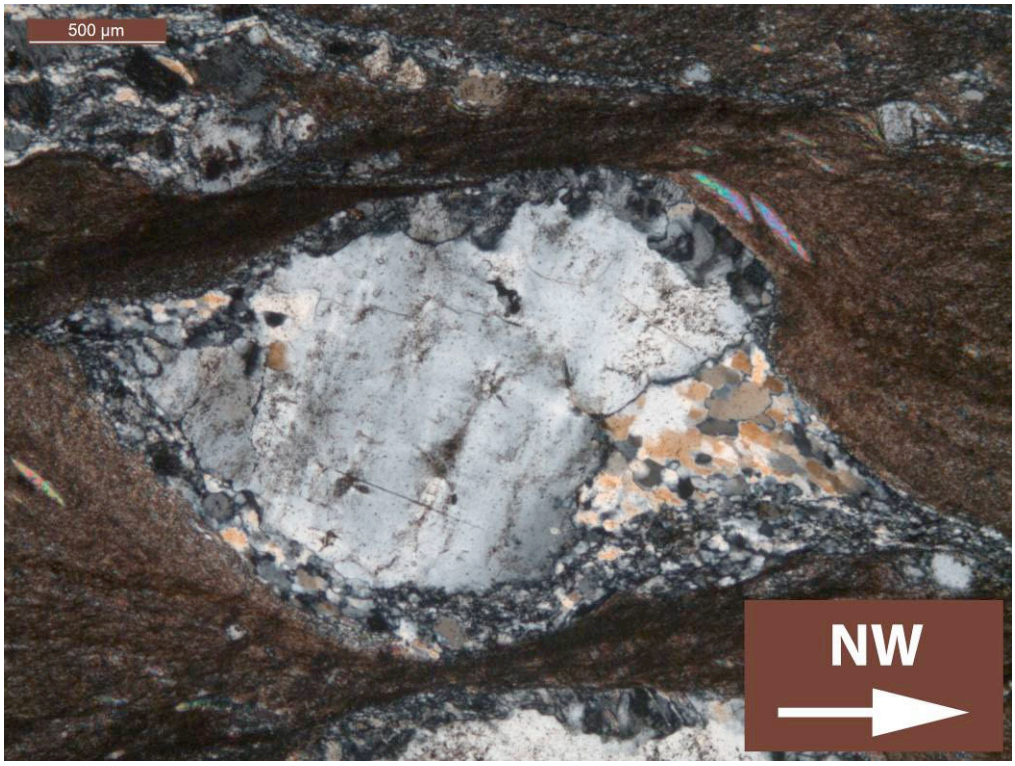

Figure 2.59: Quartz and feldspar recrystallizing dynamically in the strain shadow of a porphyroclast indicating southerly shear sense; WH030304-1, CLP.

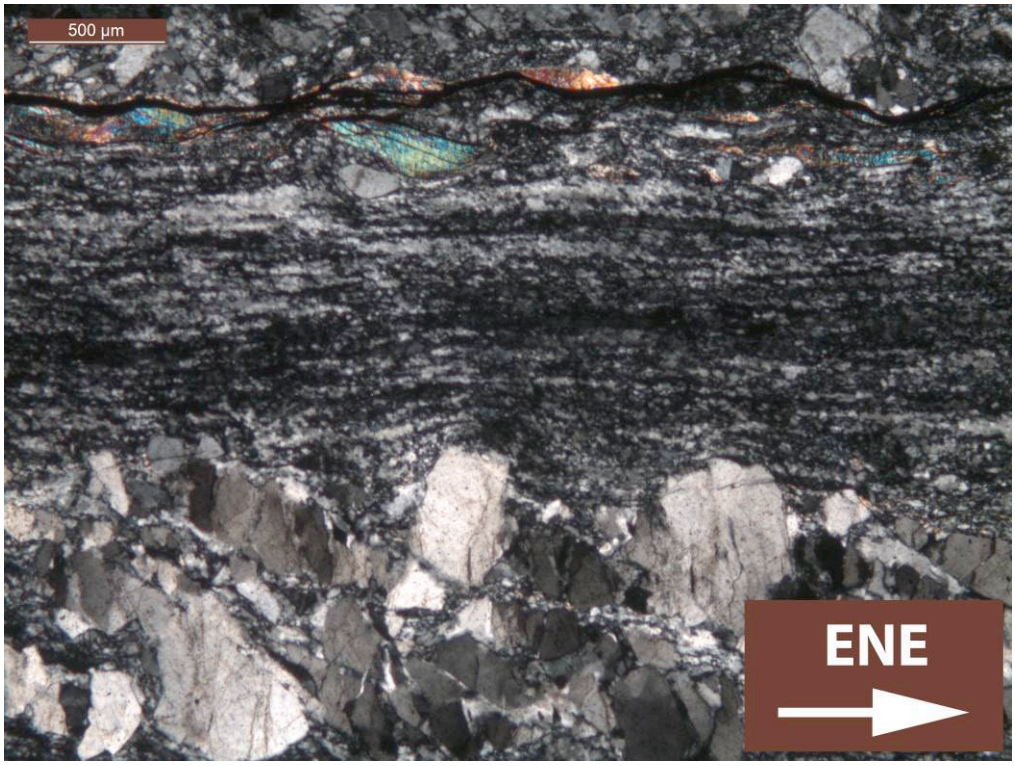

Figure 2.60: Continuous band of recrystallized quartz and feldspar, mica fish indicating top-to-WSW sense of shear; WH030202-2, CLP.

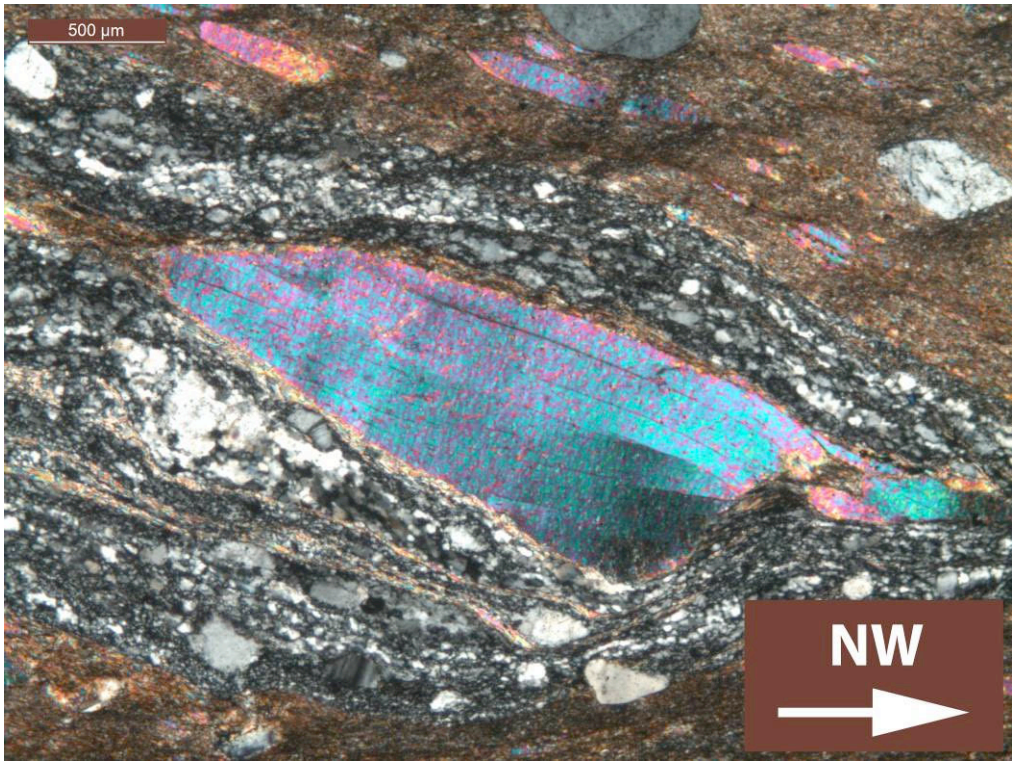

Figure 2.61: Muscovite porphyroclast indicating southerly shear sense, micro-size mica and quartzo-feldspathic bands; WH030303-2, CLP.

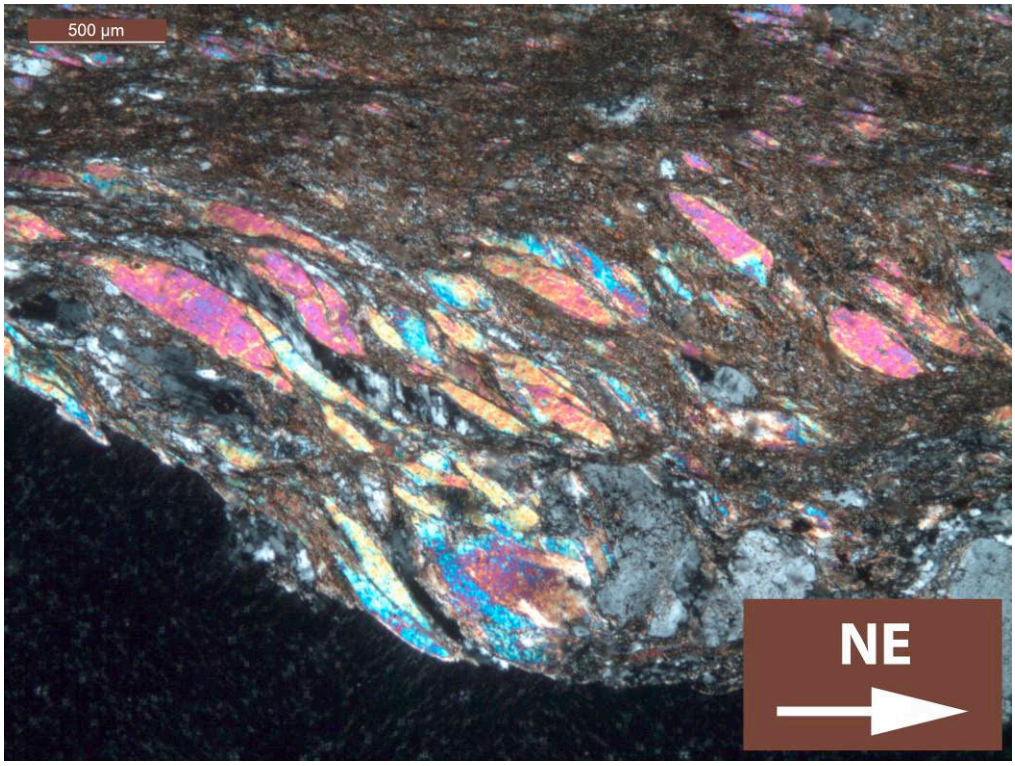

Figure 2.62: Mica fish indicating top-to-SW sense of shear; WH030102-1, CLP.

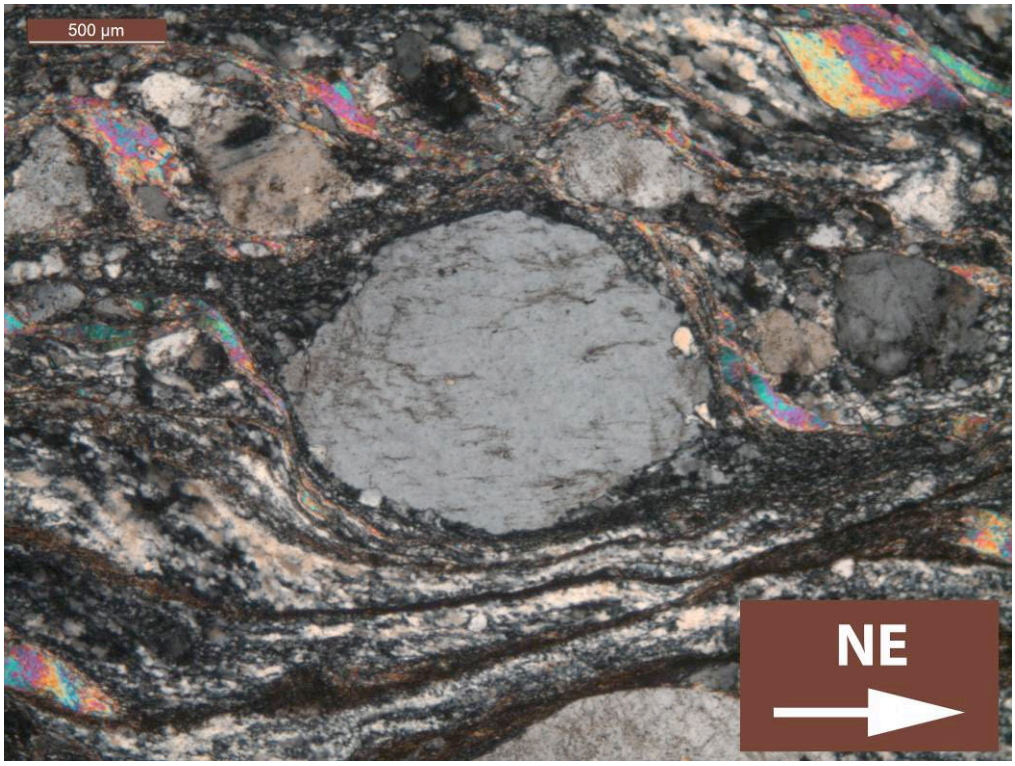

Figure 2.63: Feldspar s-type porphyroclast indicating top-to-SW sense of shear; 030102-3, CLP.

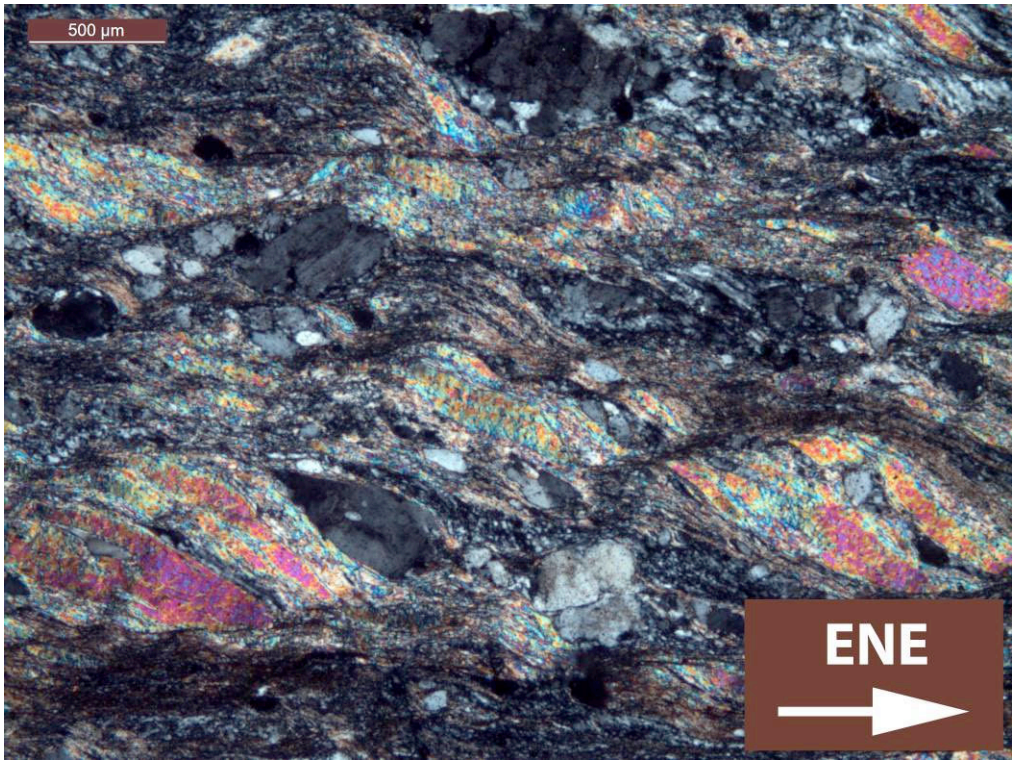

Figure 2.64: C/S-structures of mica indicating top-to-WSW sense of shear; WH030202-1, CLP.

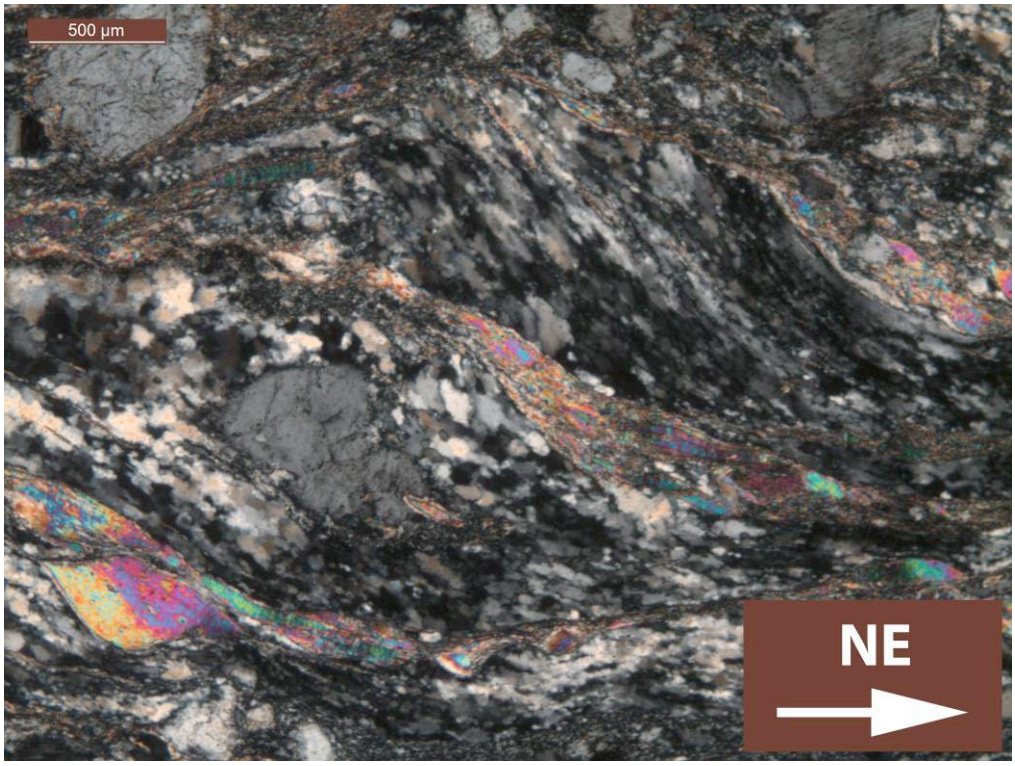

Figure 2.65: C/S-structures of mica and dynamically recrystallized quartz and feldspar indicating top-to-SW sense of shear; WH030102-4, CLP.

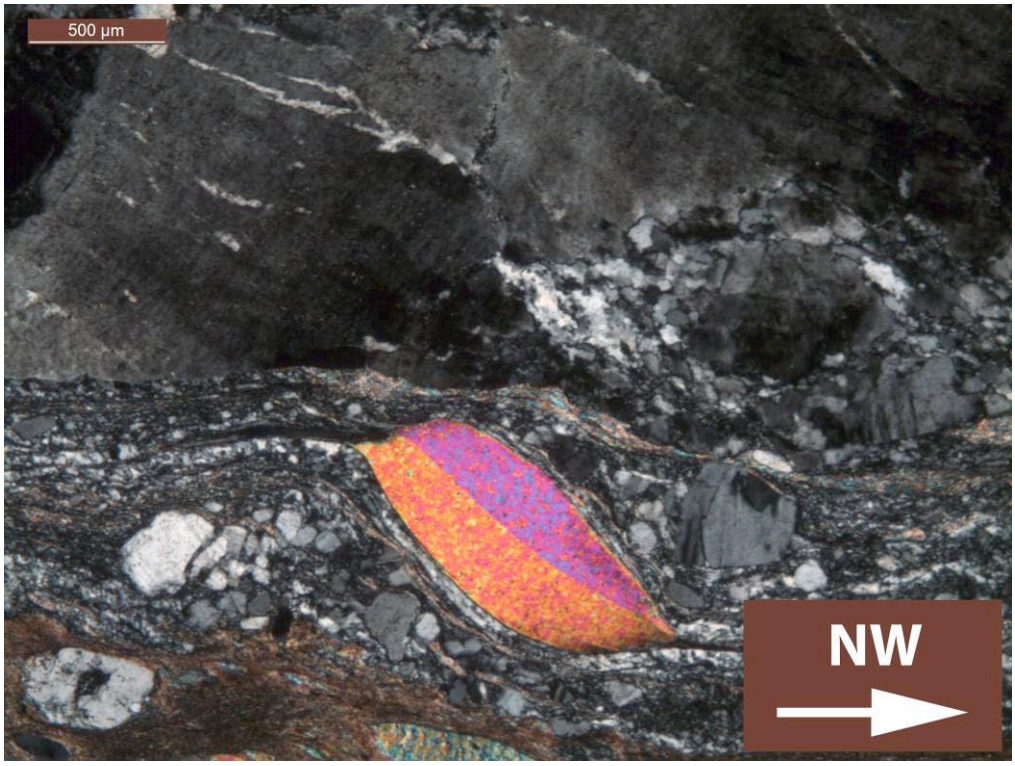

Figure 2.66: Mica fish indicating southerly shear sense; WH030302-1, CLP.

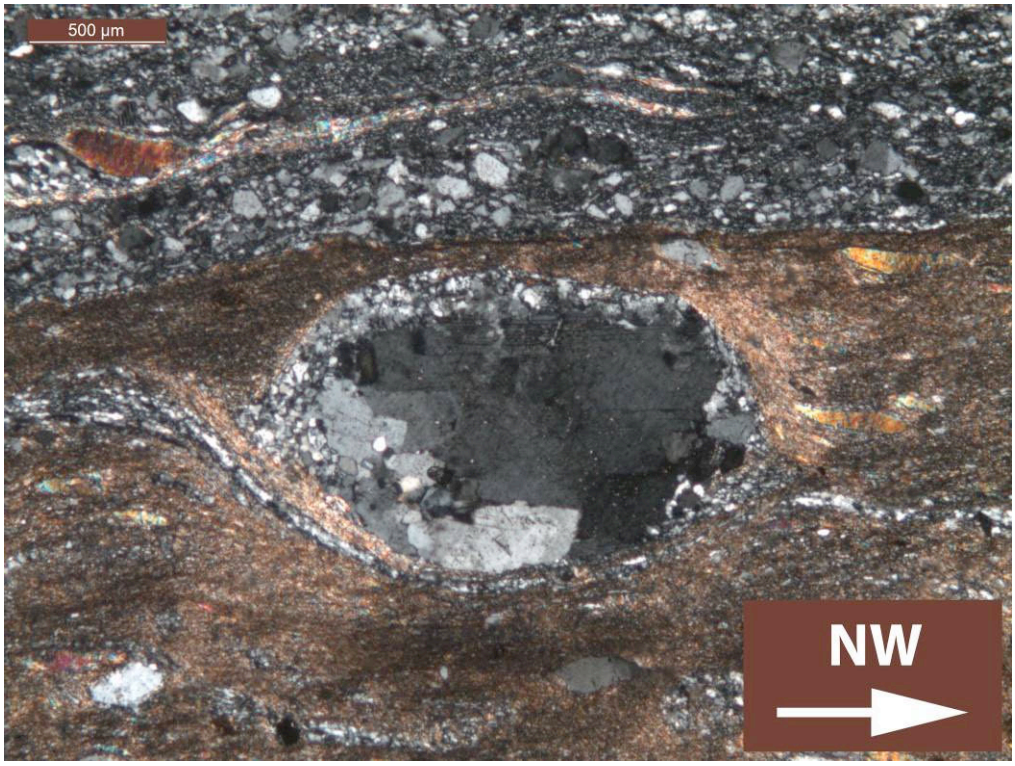

Figure 2.67: Feldspar d-porphyroclast indicating southerly shear sense; WH030302-3, CLP.

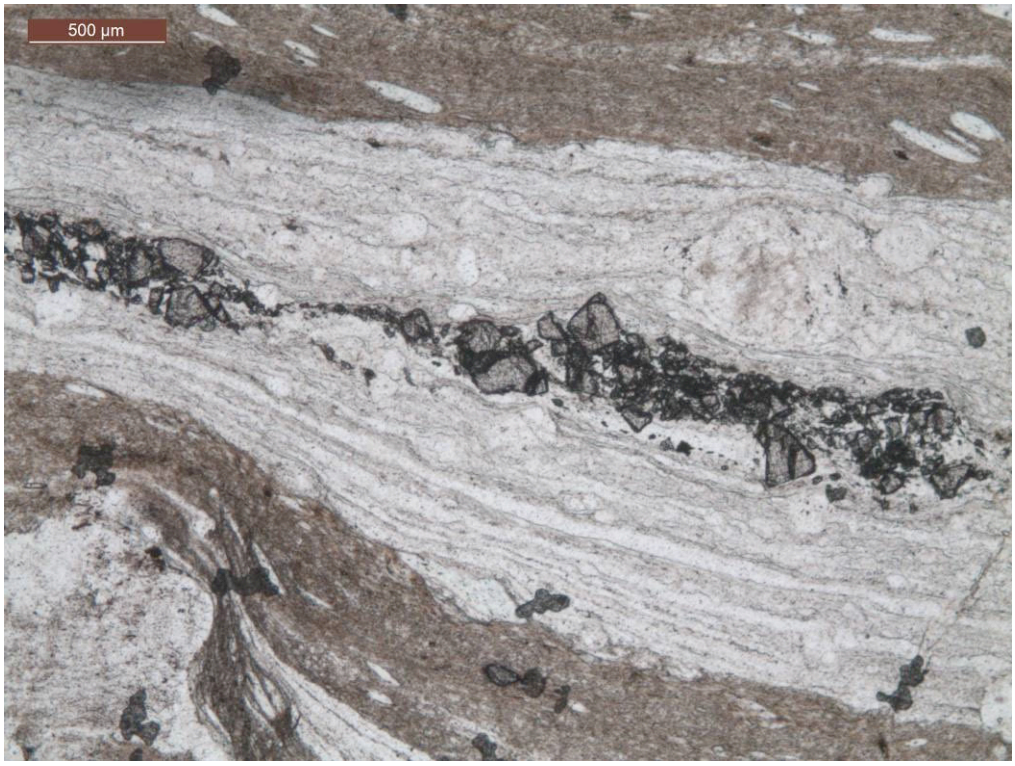

Figure 2.68: Comminuted and dispersed garnet in quartzo-feldspathic band; WH030303-2, PPL.

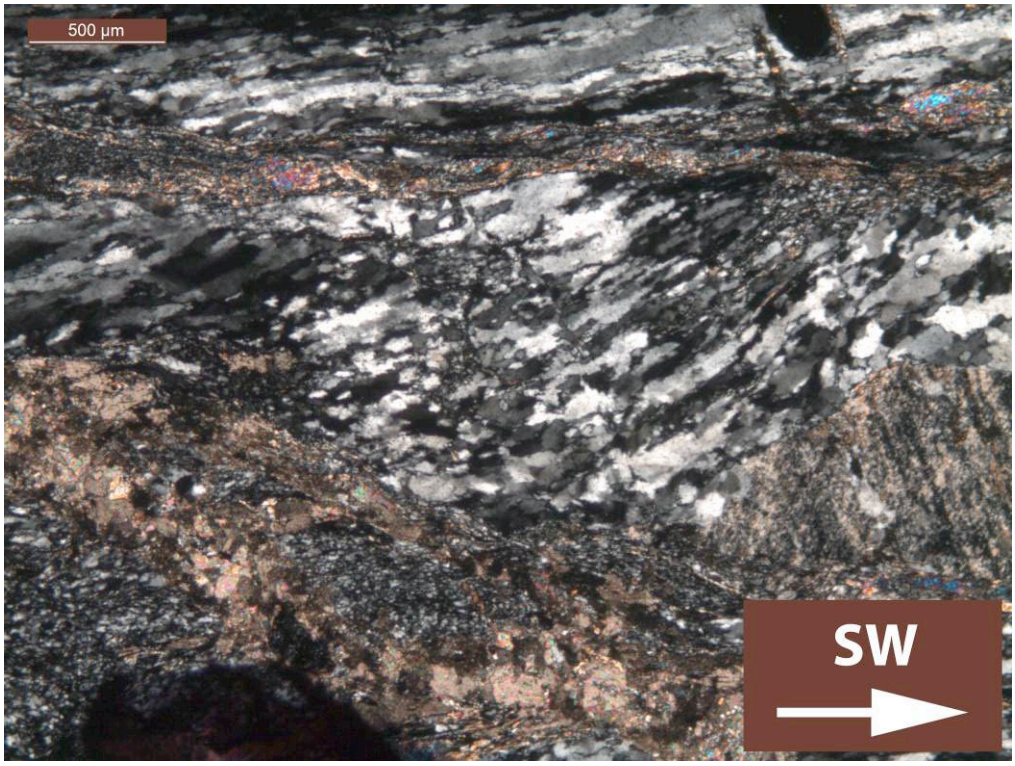

Figure 2.69: Dynamically recrystallized quartz and feldspar oblique foliation indicating top-to-SW sense of shear; WH060101-3 CLP.

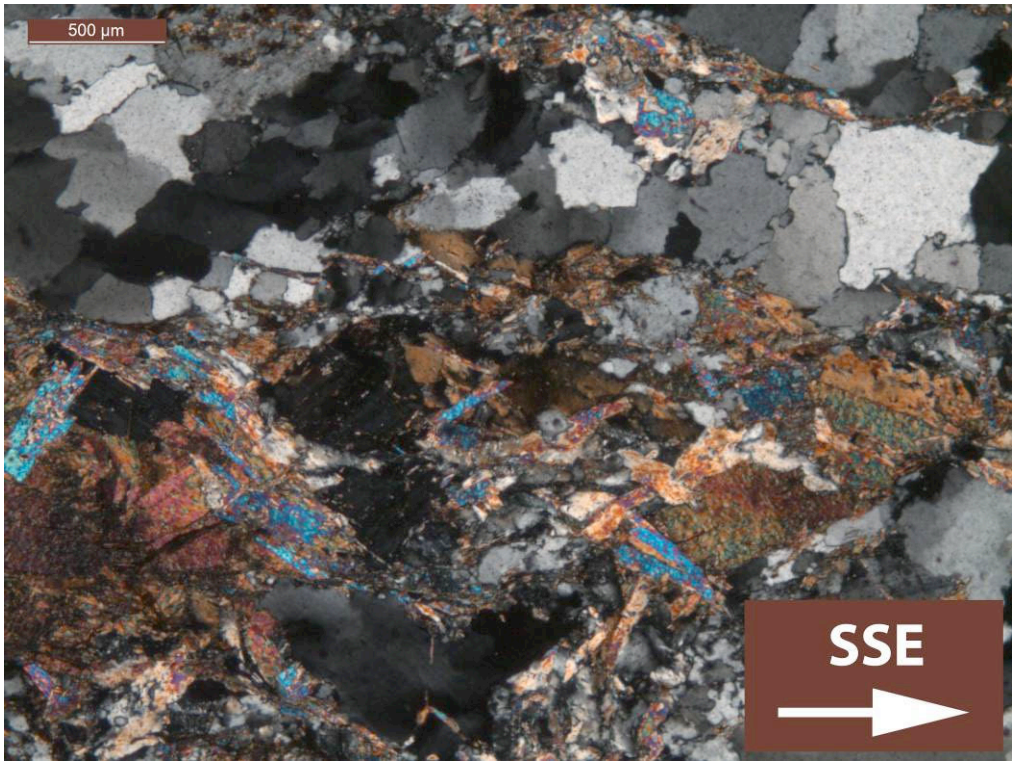

Figure 2.70: No ductile matrix, lobate grain boundaries indicate that quartz is still dynamically recrystallized; WH070101-1, CLP.

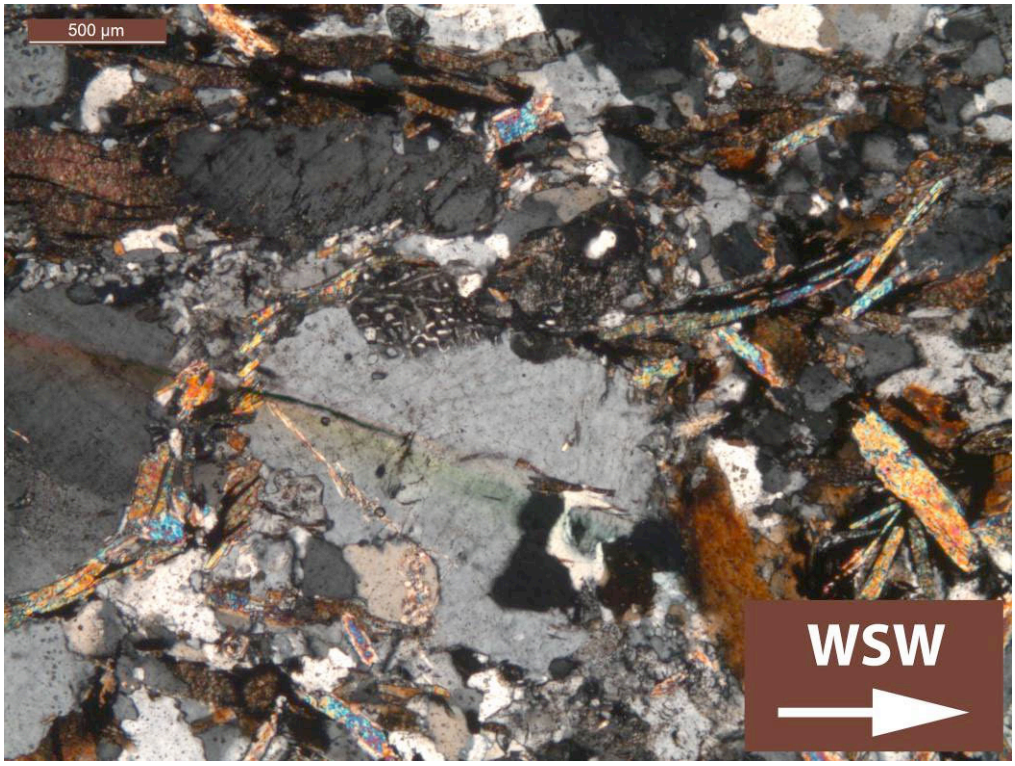

Figure 2.71: C/S-structures of mica indicating top-to-WSW sense of shear, no ductile matrix; WH090203-1, CLP.

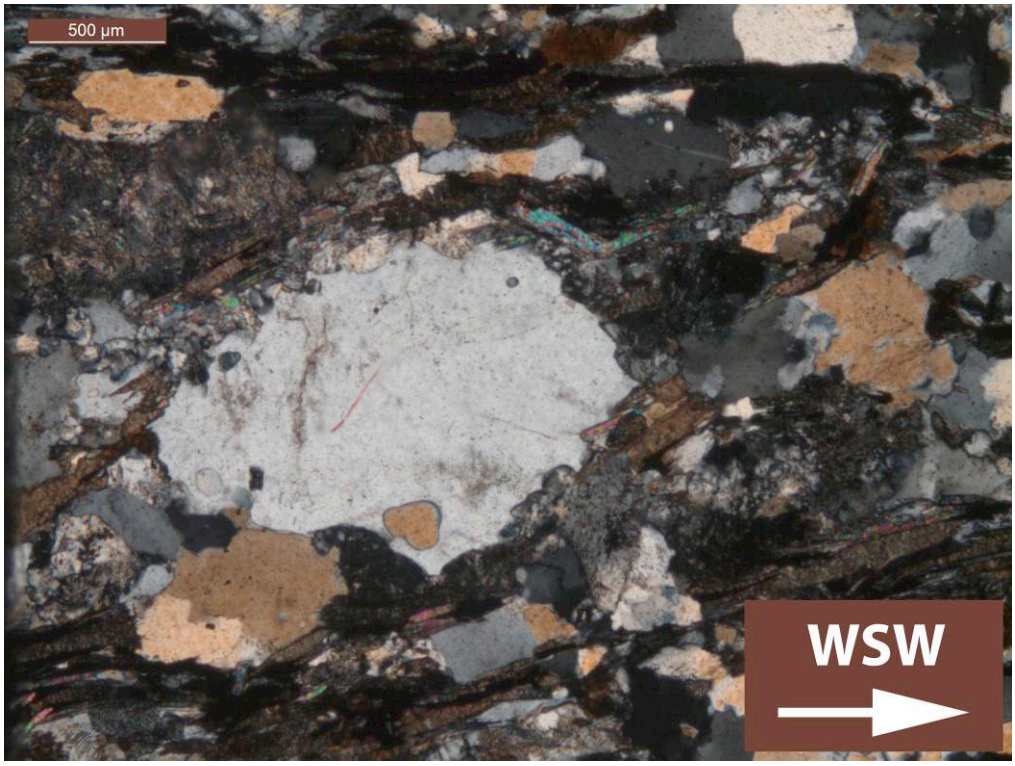

Figure 2.72: C/S-structures indicating top-to-WSW sense of shear, no ductile matrix; WH090203-2, CLP.

Figure 2.73: Large pegmatites intruded the gneiss.

Figure 2.74: Brittle faults affecting gneiss and pegmatites.

Figure 2.75: Boudinaged pegmatite indicating top-to-SSE sense of shear, quartz precipitation in strain shadow.

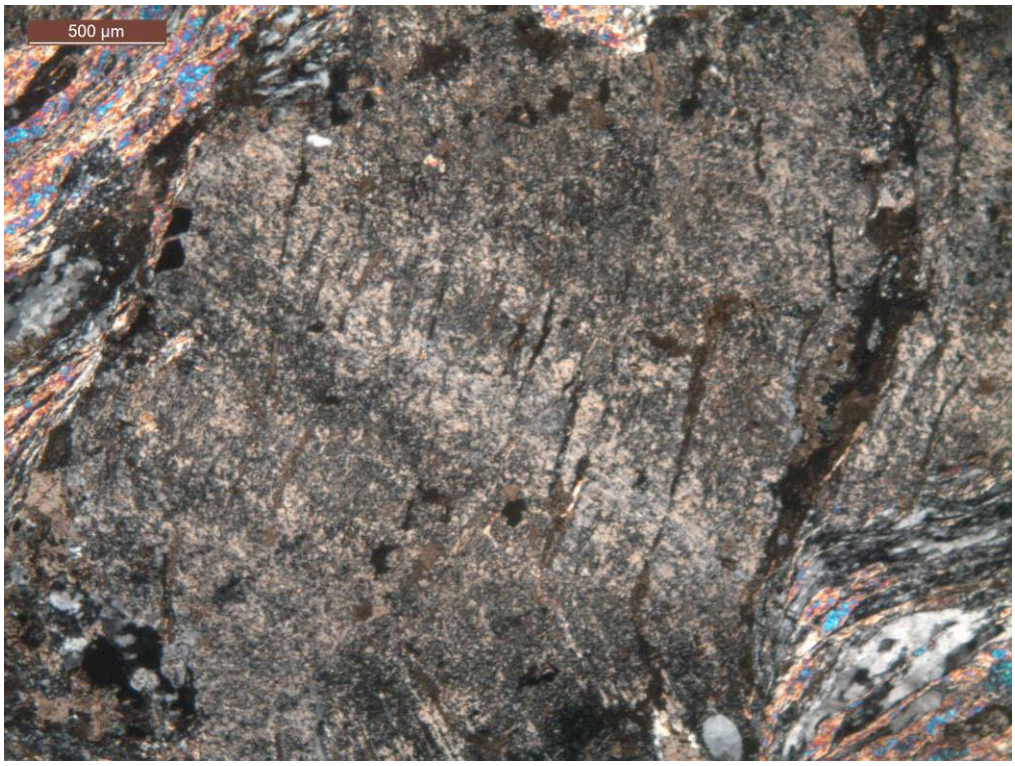

Figure 2.76: Pervasive sericitization of bent feldspar, ductile matrix; WH060101-4, CLP.

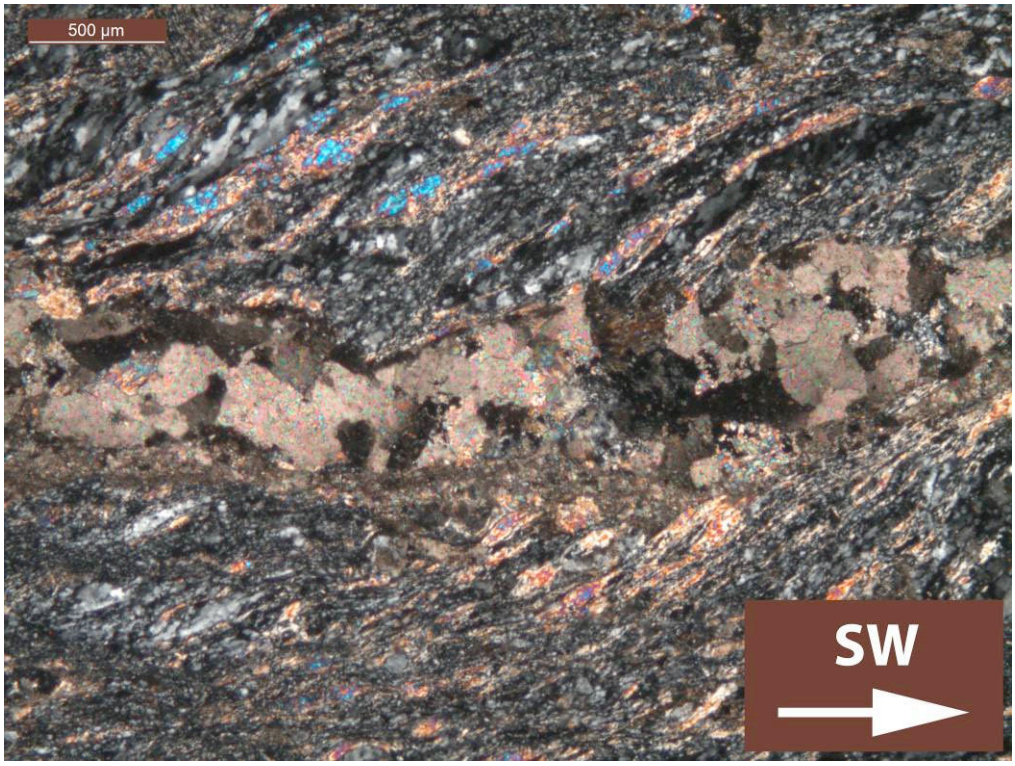

Figure 2.77: Magnesite vein, ductile matrix with C/S-structures of quartz, feldspar and muscovite indicating top-to-SW sense of shear; WH060101-1, CLP.

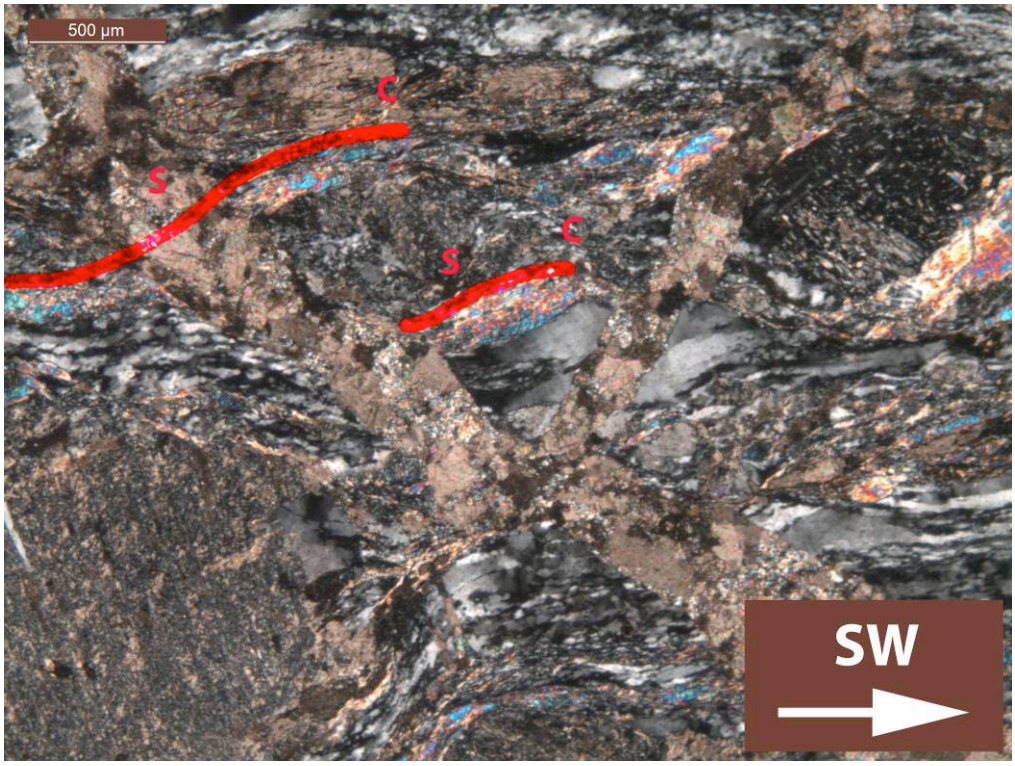

Figure 2.78: Magnesite veins intersecting C/S-structures of muscovite, quartz and feldspar, which indicate top-to-SW sense of shear; WH060101-2, CLP.

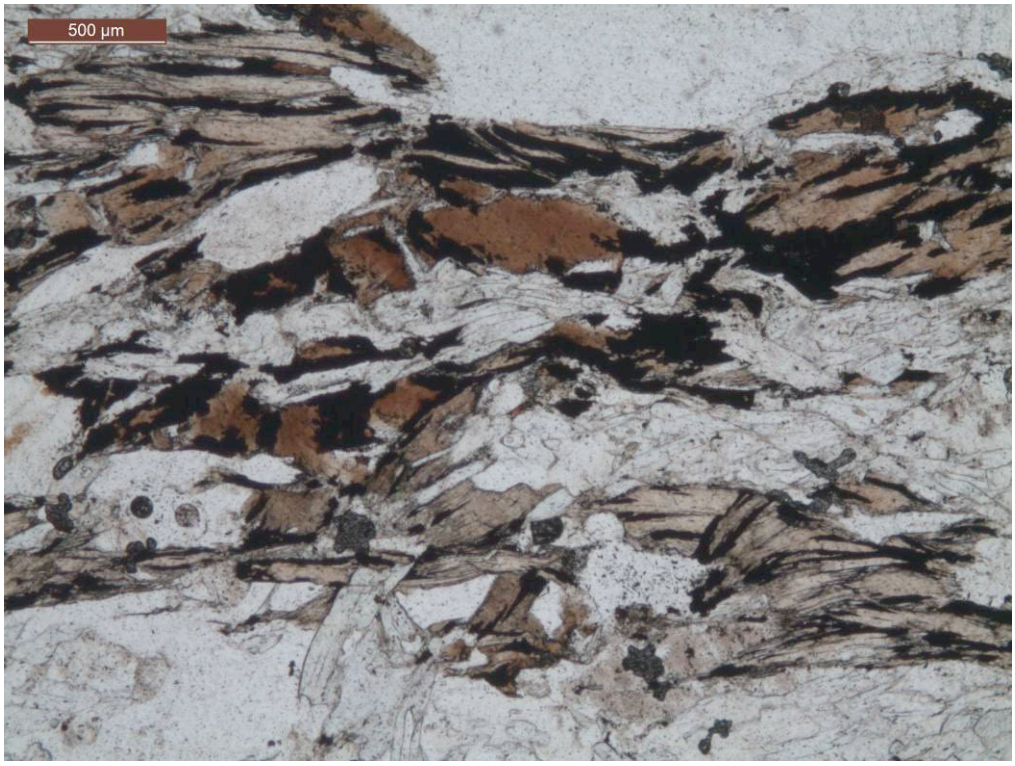

Figure 2.79: Intense replacement of biotite by oxides; WH020301-1, PPL.

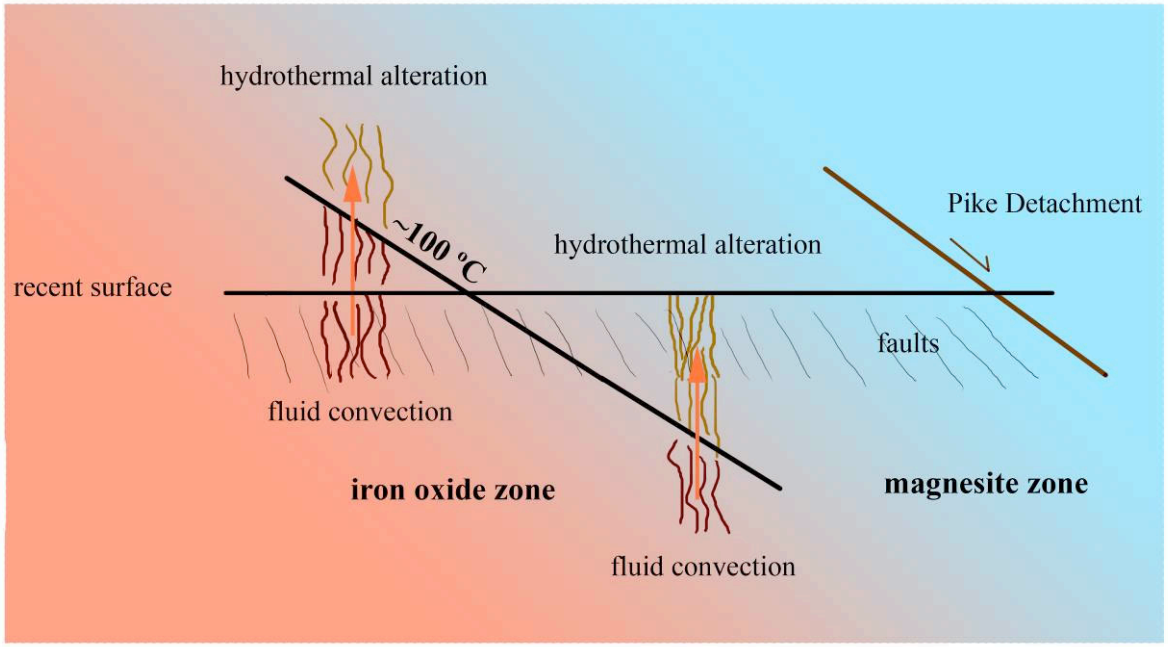

Figure 2.80: Possible hydrothermal context of iron oxides and magnesite: brittle fracturing and faulting induces convection of hydrothermal fluids, at temperatures above 100 ºC at structurally deeper levels CO_2-rich fluids cause the replacement of biotite by iron oxides and are thus enriched in Mg, closer to the detachment where temperatures are lower conditions for precipitation of magnesite ($MgCO_3$) are reached, the present surface truncates the structure; the angle of the detachment fault is oversteepenend.

2.2.4. Buckland Peaks

The Buckland Peaks consist of the Buckland Granite, which appears to be a syntectonic pluton (Spell et al. 2000). The granite represents a member of the Rahu Suite with a mean age of 109.6 ±1.7 Ma (Muir et al. 1994). Due to their proximity to the northern Ohika Detachment, the Buckland Peaks were investigated during fieldwork because evidence for tectonic deformation is likely to be found there. Although mylonitic zones, C/S-fabrics, stretching lineations and asymmetric feldspar porhyroclasts were reported from the Lower Buller Gorge in the vicinity of the Ohika Detachment (cf. Tulloch & Kimbrough 1989; Muir et al. 1994), none of these features were found on the Buckland Peaks.

The Buckland Granite consists mainly of coarse-grained feldspar, quartz and biotite with large muscovite flakes of a size of up to 2 cm. Garnet occurs as an accessory mineral in certain areas (Figure 2.81). There are at least two generations of aplite dikes intersecting each other (Figures 2.82, 2.83). They are long and straight and not affected by deformation. The subvertical set of dikes trends WNW-ESE and is therefore perpendicularly orientated to the extension direction of the core complex. These dikes are probably the lamprophyric dikes described by Adams & Nathan (1978).

A weak foliation of preferentially orientated minerals can be found in some places but it does not develop foliation planes (Figure 2.84). Because of the resulting lack of foliation-induced surfaces it is hard to measure the foliation and impossible to observe lineations, which might indicate a direction of transport. A relatively steep dip to the S/SSW can be inferred, however (Figure 2.85).

Several samples were taken at ten different locations (Figure 2.86) and cut in different orientations to rule out the possibility that a microscopic foliation was overlooked. The thin sections do not show the weak foliation because the granite is too coarsely grained to observe an alignment of minerals in a single view. There are no obvious deformational features or shear sense indicators whatsoever.

There are however several subtle indices for strain: many primary mica grains have a conspicuous subhorizontal orientation and show internal deformation as they are bent, kinked, broken and recrystallized (Figures 2.87, 2.88, 2.89, 2.90). Secondary muscovite and sericite replacing feldspar occur in association with myrmekite (Figures 2.91, 2.92). Quartz forms much larger grains than at previously described locations (Figure 2.93). However, there are isolated patches of dynamically recrystallized quartz and lobate grain boundaries (Figures 2.93, 2.94,

2.97, 2.98). Many plagioclase grains show microcline twinning (Figures 2.95, 2.96, 2.97), which also records strain (Fitz Gerald & McLaren 1982; Brown & Macaudière 1986).

The myrmekite and the associated muscovite and sericite indicate deformation under lower amphibolite facies conditions (Phillips et al. 1972; Simpson 1985; LaTour & Barnett 1987; Simpson & Wintsch 1989; Cesare et al. 2002; Menegon et al. 2006). As microcline is abundant the granite must have cooled slowly crossing the microcline – sanidine transition at 450-500 ºC (Steiger & Hart 1967; Carpenter & Salje 1994; Parsons 2010 and references therein) to allow microcline to form and subsequently to become mechanically twinned. Compared to the abundant microcline, myrmekite is less common. A possible reason could be a faster cooling rate at higher temperature as proposed by Spell et al. (2000).

Chlorite replacing muscovite and hematite staining of sericite occurs locally (Figures 2.98, 2.99) and records greenschist facies conditions. However, these alterations are rare. Deformation and retrogression at low metamorphic grades usually cause pervasive albitization of plagioclase (Moody et al. 1985, pers. comm. Shelley 2010). This cannot be observed in the granite of the Buckland Peaks. Thus no stress sufficiently high for deformation was applied to the granite when it cooled to lower temperatures.

Altogether this supports a lower amphibolite facies deformational regime. As sufficiently high temperatures have not been reached since the core complex development, deformation causing the subtle features is likely to be induced by the extension and the detachment faulting. Rocks at Cape Foulwind and south of Charleston with a similar distance to either of the detachments were deformed much more. Hence, the comparatively small amount of strain observed at Buckland Peaks poses questions on the relative timing of the pluton emplacement and its deformation. Feldspars and mica show more evidence for pervasive deformation than quartz. A possible explanation is that the deformation ceased shortly after the pluton was emplaced. Feldspars and mica already formed a stress-supporting crystal mush. Thus strain was accommodated in mechanical twinning of feldspars and deformation of mica flakes. By the time the pluton had cooled to low-grade conditions deformation had ceased. Thus the quartz is almost unstrained and albitization did not take place.

As there are no shear sense indicators it is not possible to infer whether the Ohika Detachment, the Pike Detachment or both detachments imposed the strain on the rocks of the Buckland Peaks.

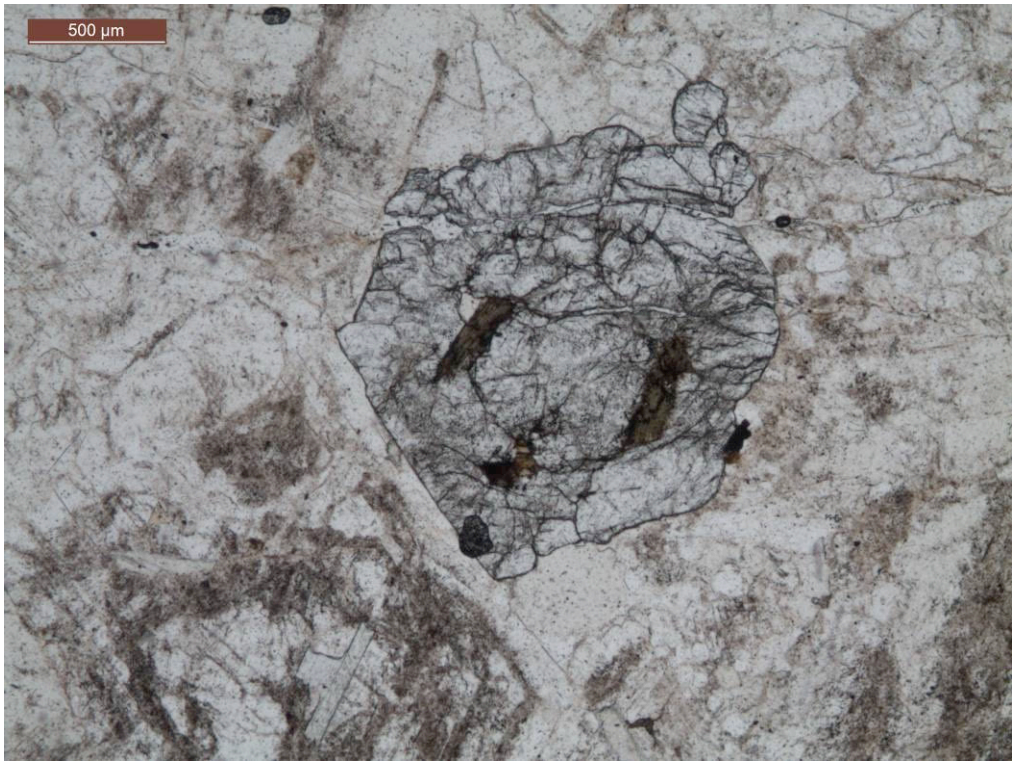

Figure 2.81: Euhedral garnet, BP020201-1, PPL.

Figure 2.82: Subhorizontal aplitic dikes on the Buckland Peaks.

Figure 2.83: Subvertical and subhorizontal dikes on the Buckland Peaks, subvertical set trending WNW, green backpack for scale.

Figure 2.84: Weak foliation indicated by red dashed line.

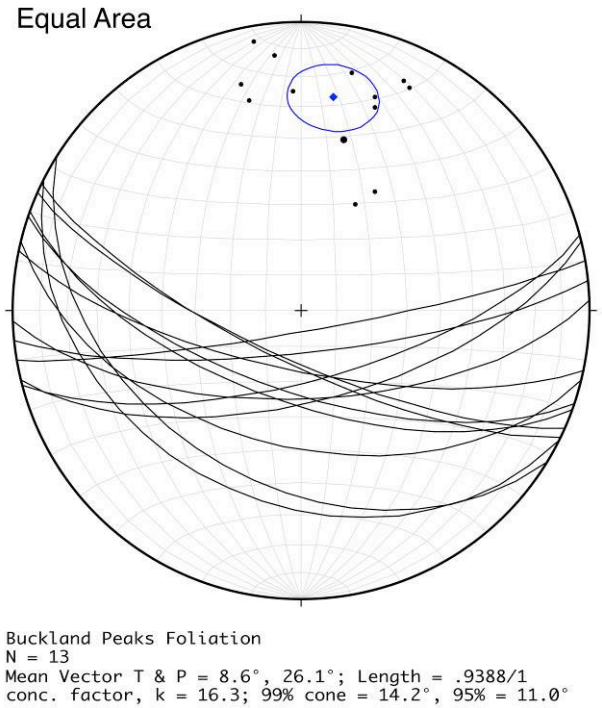

Figure 2.85: Stereographic projection of tentatively measured foliation on Buckland Peaks.

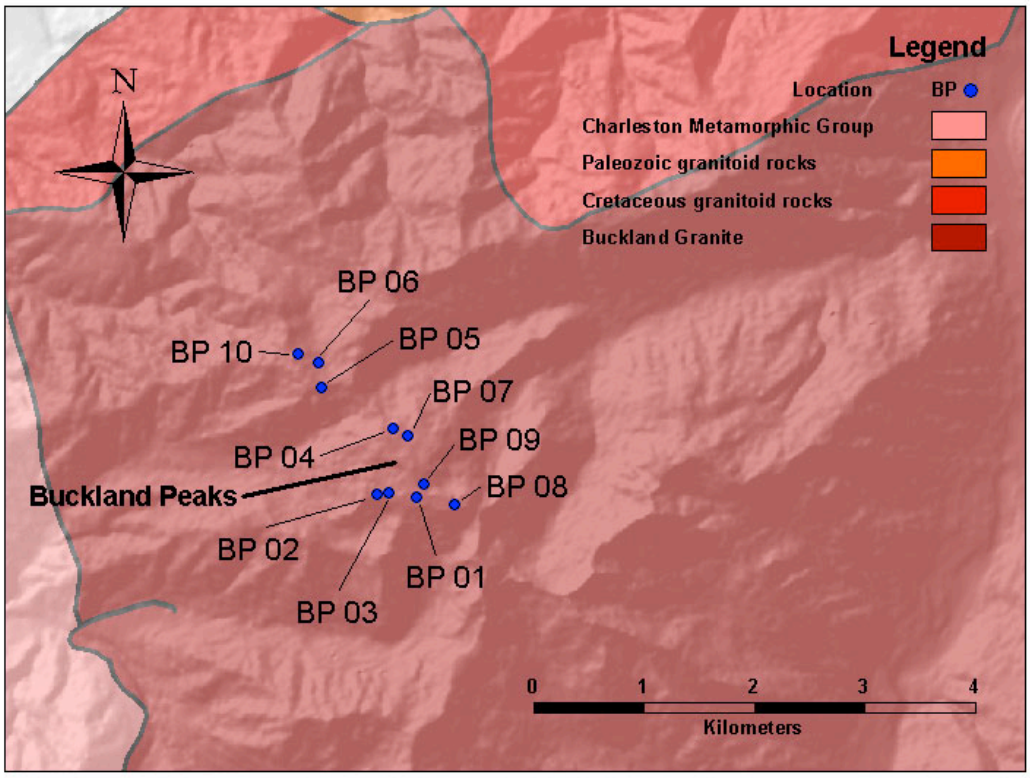

Figure 2.86: Sample area at Buckland Peaks; Geology after Rattenbury et al. (1998).

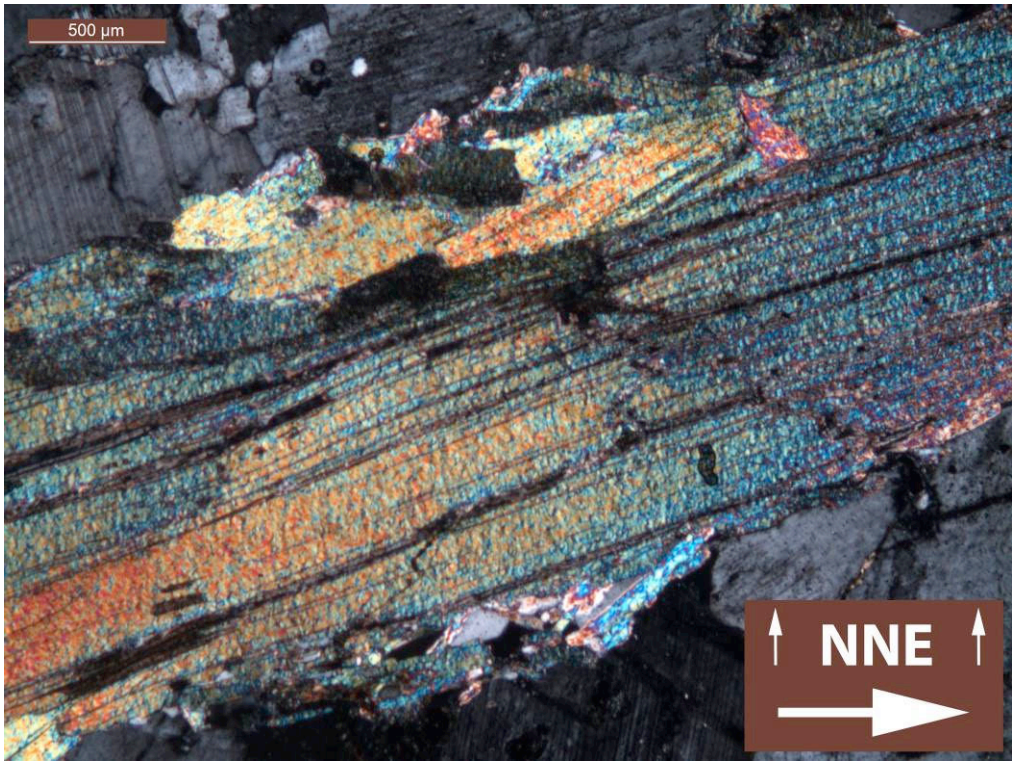

Figure 2.87: Broken muscovite; double arrow pointing upward, subhorizontally orientated; BP010103-1, CPL.

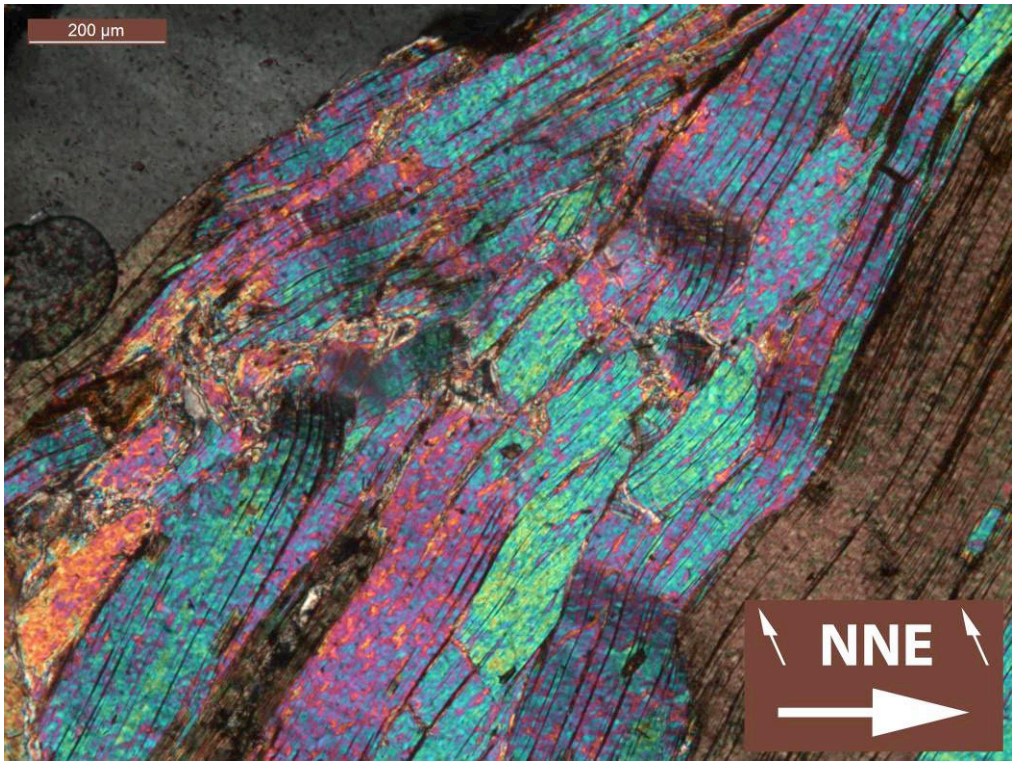

Figure 2.88: Bent, kinked and recrystallized muscovite and biotite; double arrow pointing upward; BP010206-1, CLP.

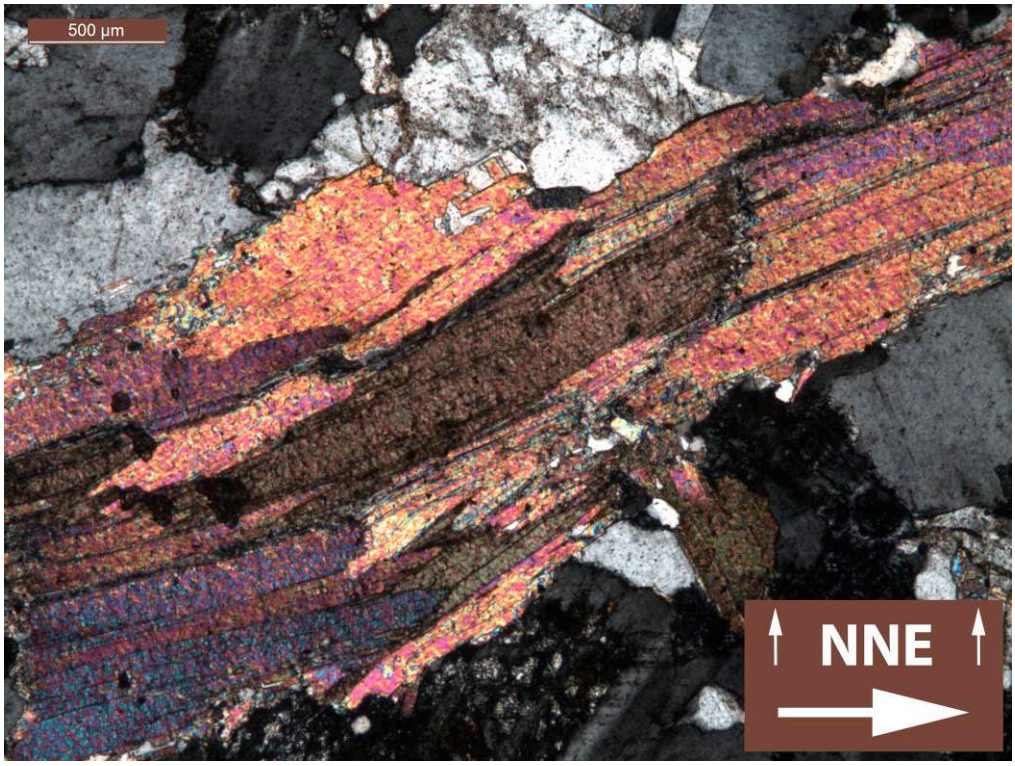

Figure 2.89: broken muscovite and biotite; double arrow pointing upward, subhorizontally orientated; BP020103-1, CLP.

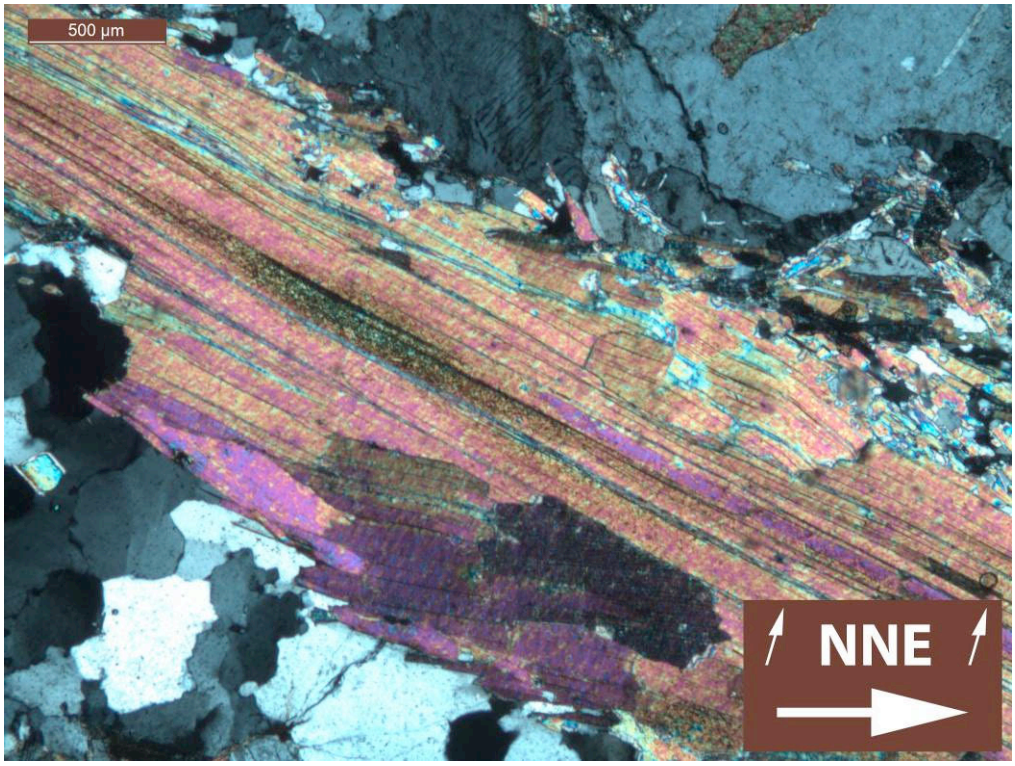

Figure 2.90: Bent, broken and recrystallized muscovite; double arrow pointing upward, orientated subhorizontally; BP020202-2, CLP.

Figure 2.91: Transition from sericite to muscovite replacing feldspar, cross-hatched microcline twinning; BP050102-1, CLP.

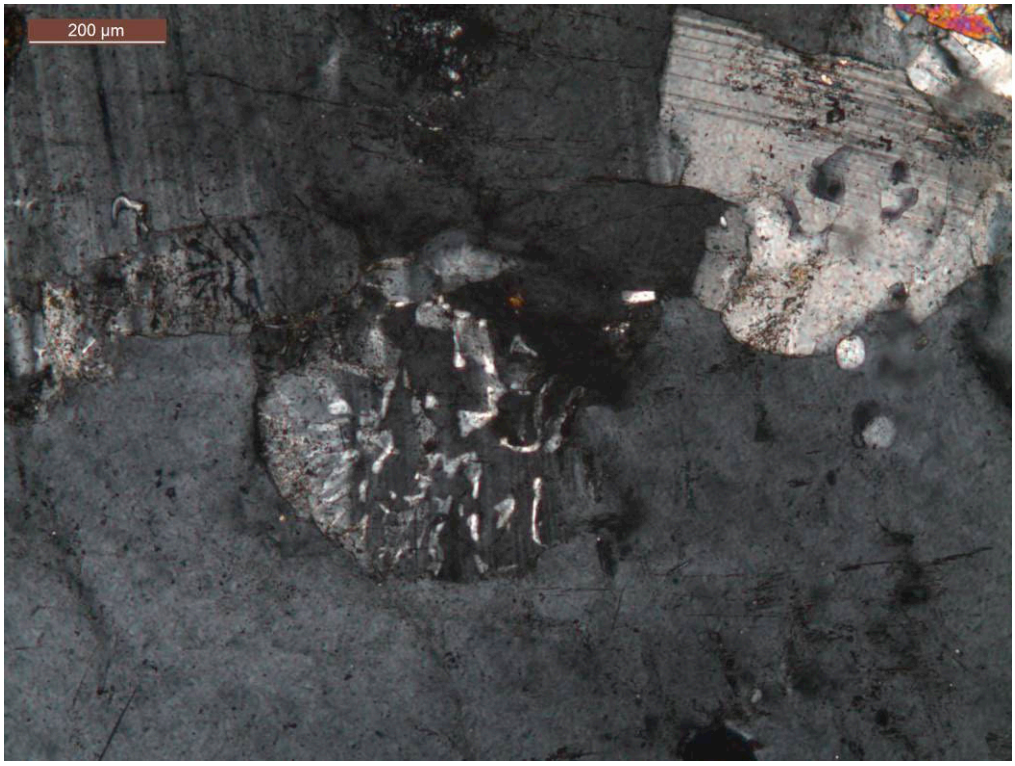

Figure 2.92: Myrmekite; BP010102-1, CLP.

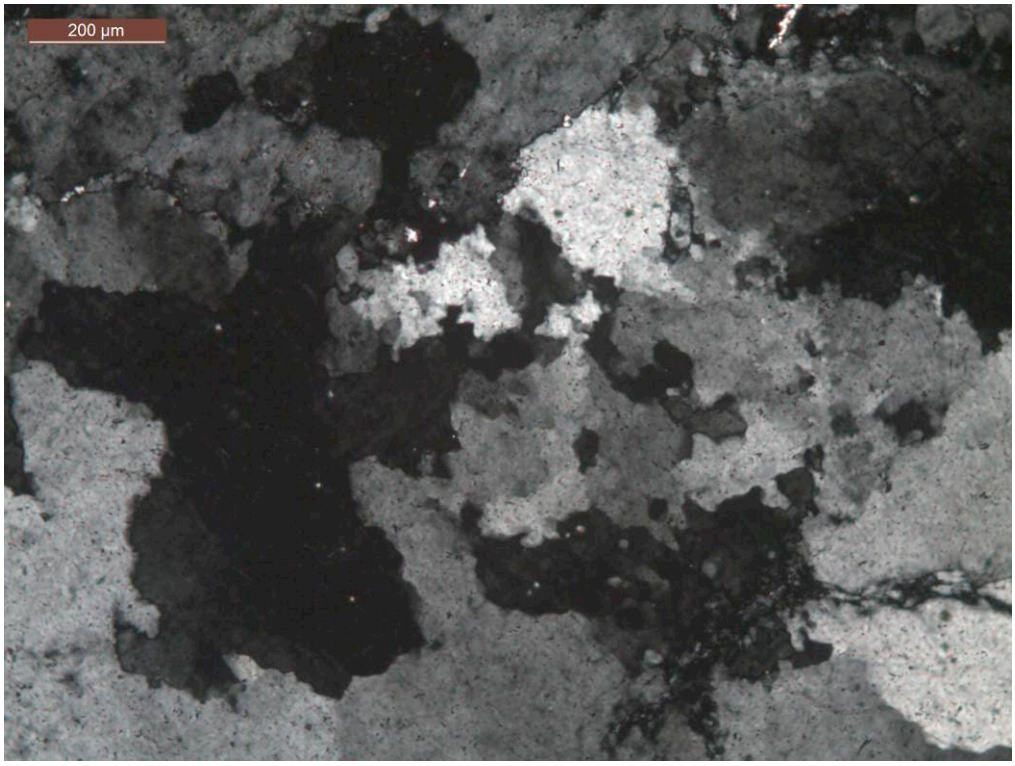

Figure 2.93: Larger quartz grains with lobate grain boundaries and a recrystallized patch in the middle; BP070101-1, CLP.

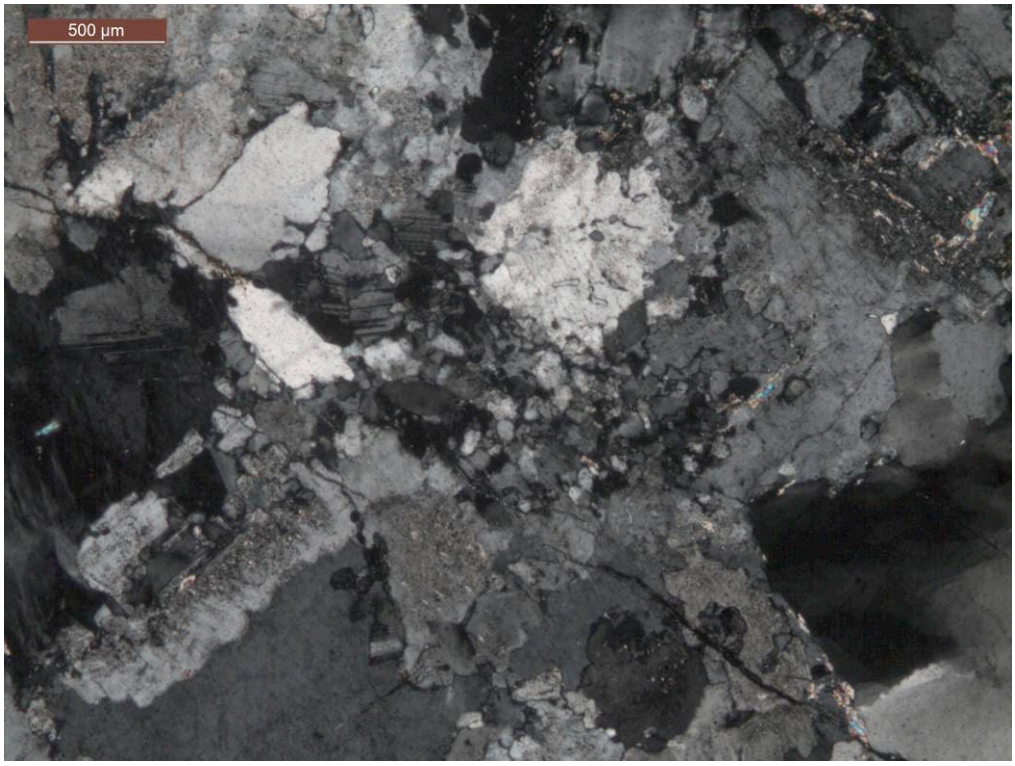

Figure 2.94: Patch of recrystallized quartz; BP010203-1, CLP.

Figure 2.95: Microcline (right side) and Myrmekite (left side); BP010201-1. CLP.

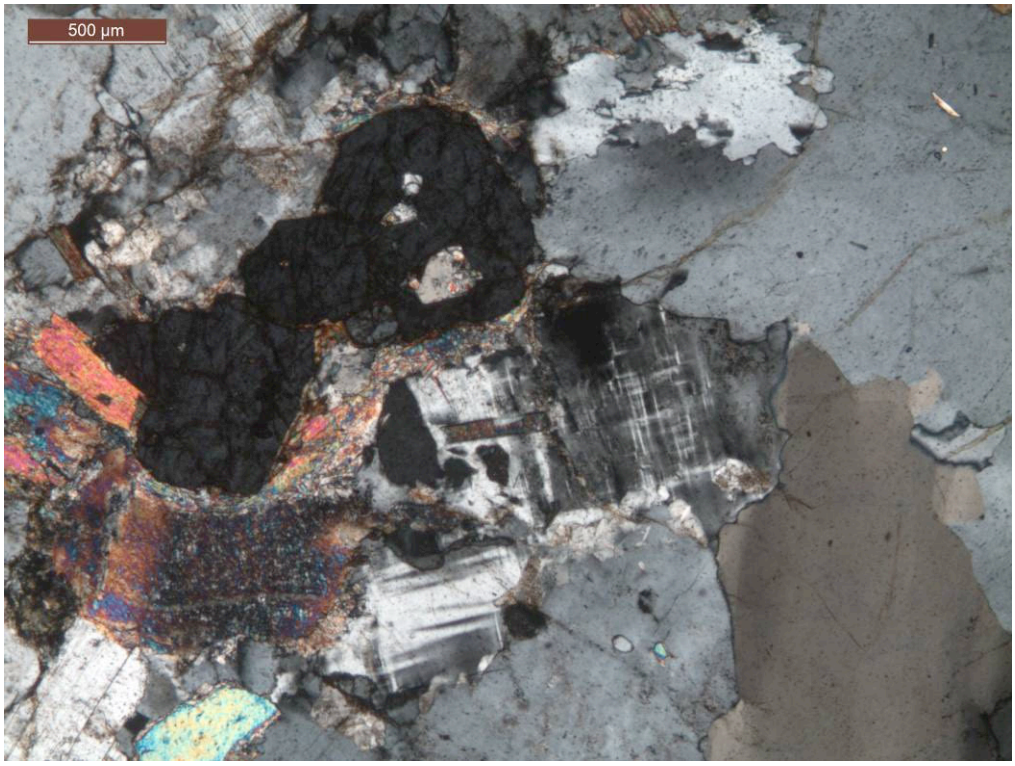

Figure 2.96: Microcline (middle); large quartz grain (right bottom), apatite (left top); BP060101-1, CLP.

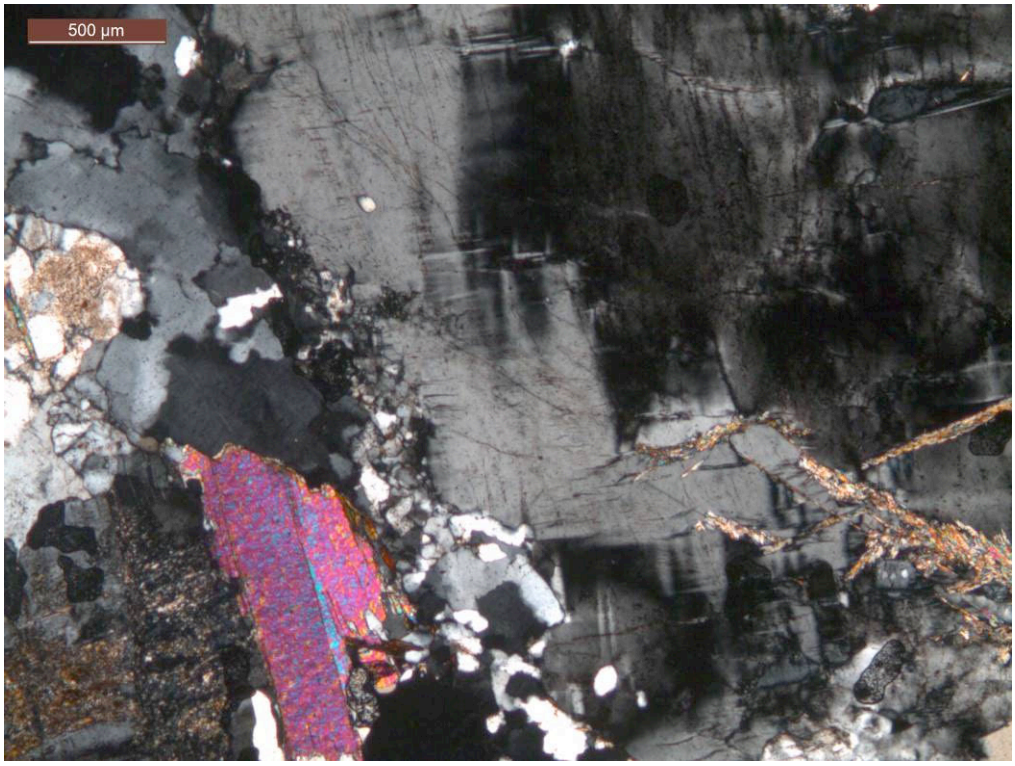

Figure 2.97: Microcline, patch of recrystallized quartz, sericite (left bottom) and recrystallized mucovite (right bottom); BP080101-2, CLP.

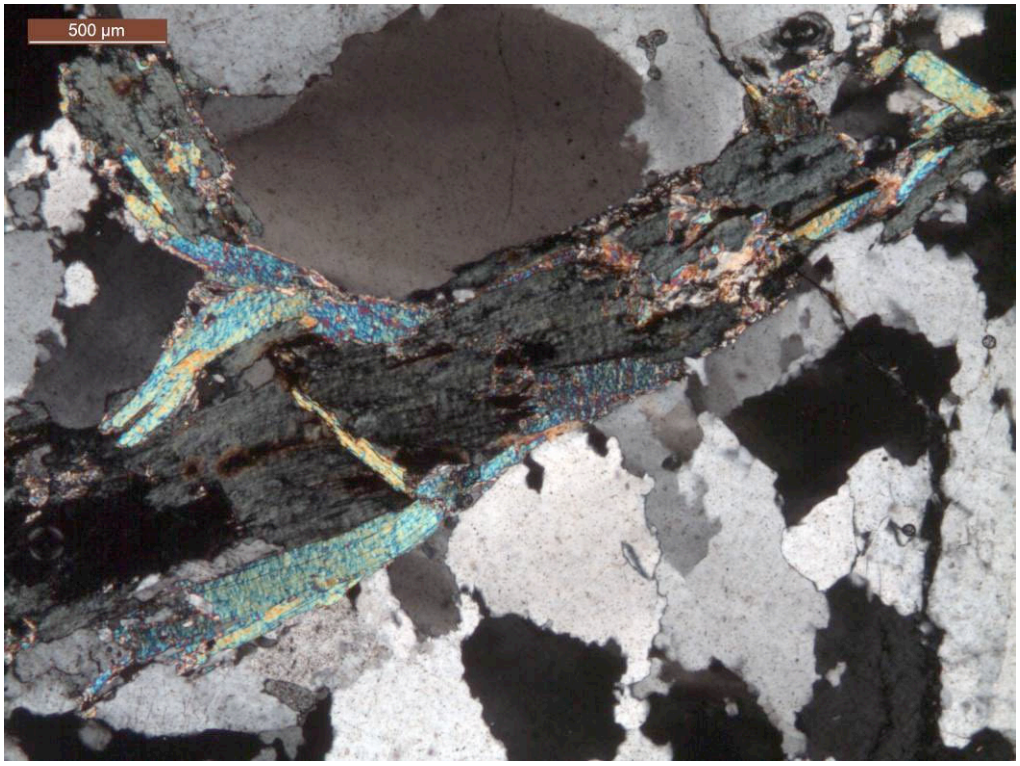

Figure 2.98: Chlorite replacing muscovite, large quartz grains with lobate grain boundaries; BP040201-1, CLP.

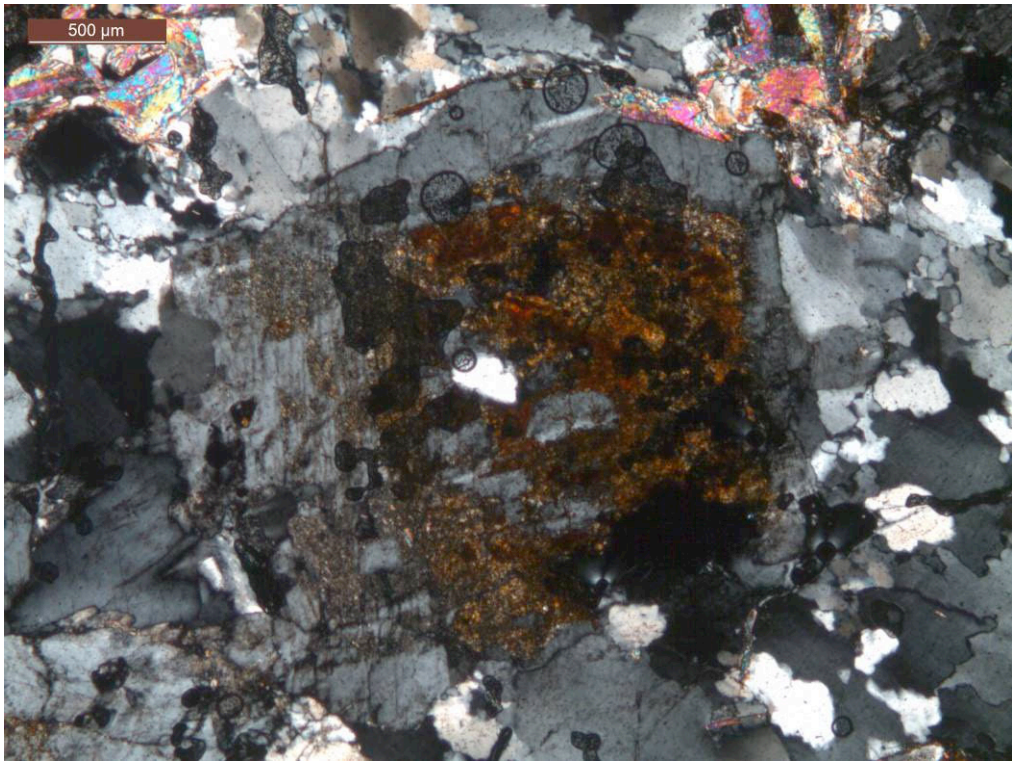

Figure 2.99: Sericite replacing feldspar stained by hematite; BP 080101-1, CLP.

2.2.5. Mount Kelvin

Mount Kelvin is one of the major peaks along the central ridge of the Paparoa Range (Figure 1.07). The Buckland Granite bulges into the gneisses of the CMG at Mount Kelvin. Together with the southward extension of the Buckland Granite at Mount Raoulia, this location represents the part of the Buckland Granite, which is the closest to the southern Pike detachment. Thus this spot is of particular interest to find out whether the southern detachment influenced the Buckland Granite or not and to narrow down the position of the hinge of the bivergent core complex. Twelve samples were taken at several different locations at Mount Kelvin and six further samples along the central ridge and at the Needle to the north (Figure 2.100).

The contact between the CMG and the Buckland Granite shows clearly the intrusive character of the latter. There is a gradual transition from large lensoid blocks of CMG floating as single chunks in the Buckland Granite (Figure 2.101) to massive CMG rocks, which are interveined by dikes of the Buckland Granite (Figure 2.102). The amount of xenoliths decreases in the Buckland Granite in a northward direction. A sharp margin of the pluton is difficult to determine

and the boundary on the map (Figure 2.100) has to be regarded as an approximation. Thus samples have been taken on both sides of the contact in adequate distance to the transition zone where each of the lithologies is respectively dominant.

The CMG rocks at Mount Kelvin consist mainly of quartz, feldspar and biotite (Figure 2.103). The biotite content is significantly higher than in the Buckland granite. This is expressed by a distinctively darker color (Figure 2.101). Grain size and the amount of deformation are heterogeneously distributed. Deformation ranges from patches of dynamically recrystallized quartz between large plagioclase grains with twinning lamellae over recrystallization in strain shadows to ductile deformation of quartz, feldspar and mica forming a foliation (Figures 2.104, 2.105, 2.106, 2.107). Some of the rocks have a granitoid fabric while others are fine-grained, foliated parallel to the granite's foliation and show internal folding (Figures 2.103, 2.108). However, the folding can be a primary feature of the gneiss as well and cannot be used to determine a shear sense for the core complex.

Samples of the CMG rocks were taken around the Buckland Granite bubble where accessible (Figure 2.100). In thin sections C/S-structures and porphyroclasts consistently show a top-to-SW sense of shear (Figures 2.109, 2.110, 2.111). Despite the relatively large lateral distance to the Pike Detachment, which translates to an even larger horizontal distance considering the dip angle of the detachment, these features are well developed and underline the pervasive nature of the deformation induced by the southern detachment. Ductile feldspar (Figures 2.106, 2.107, 2.110, 2.111), myrmekite (Figure 2.112), associated muscovite and sericite replacing feldspar (Figure 2.113) and the lack of albitization (Moody et al. 1985, pers. comm. Shelley 2010) indicate lower amphibolite facies conditions for the deformation of the CMG rocks.

The CMG rocks contain another type of xenoliths as well. Compared to the amount of CMG blocks in the Buckland Granite these other xenoliths are rather rare and small. They are brownish, very fine grained and look ductilely deformed or even smeared out (Figure 2.114). It is possible that these chunks represent Greenland Group xenoliths comparable to those at the coastline but much more altered. The intrusion of the granite or the earlier formation of the gneiss itself could have provided the heat necessary to weaken the blocks and deform them ductilely.

In some cases the Buckland Granite is only a few hundred meters away from the sampled CMG rocks. In contrast to these the Buckland Granite is barely deformed and shows only a weak foliation, which could be interpreted as a magmatic one (Figures 2.115, 2.122). But it is subparallel to the foliation in the CMG rocks (Figure 2.116) and thin sections show subtle signs for deformation like the rocks at the Buckland Peaks: bent and kinked muscovite flakes (Figure

2.117), patches of dynamically recrystallized quartz (Figures 2.118, 2.119) and deformation twinning in plagioclase (Figure 2.119). Therefore the granite must have been tectonically deformed. Sericite replacing feldspar (Figure 2.119), associated myrmekite and microcline twinning (Figure 2.120) suggest similar thermal conditions for the deformation. Yet the deformation appears to be somewhat more intense than at the Buckland Peaks. The foliation is better discernable (compare Figures 2.84, 2.115 and 2.122), myrmekite is more abundant and the deformation of quartz is stronger (Figure 2.121). Even so a shear sense cannot be obtained from thin sections.

However, some macroscopic structures indicate a top-to-SW sense of shear for the Buckland Granite. Previous workers have not observed this. Feldspar phenocrysts have sigmoid shapes with tails indicating southward shearing (Figures 2.122, 2.123) and a pegmatite parallel to the foliation shows well-developed C/S-structures with a top-to-SW sense of shear (Figure 2.124).

Both the Buckland Granite and the CMG show the same foliation and the same sense of shear to the SW. Thus the Pike Detachment is responsible for the deformation at Mount Kelvin and the hinge between the two detachments has to be further to the north.

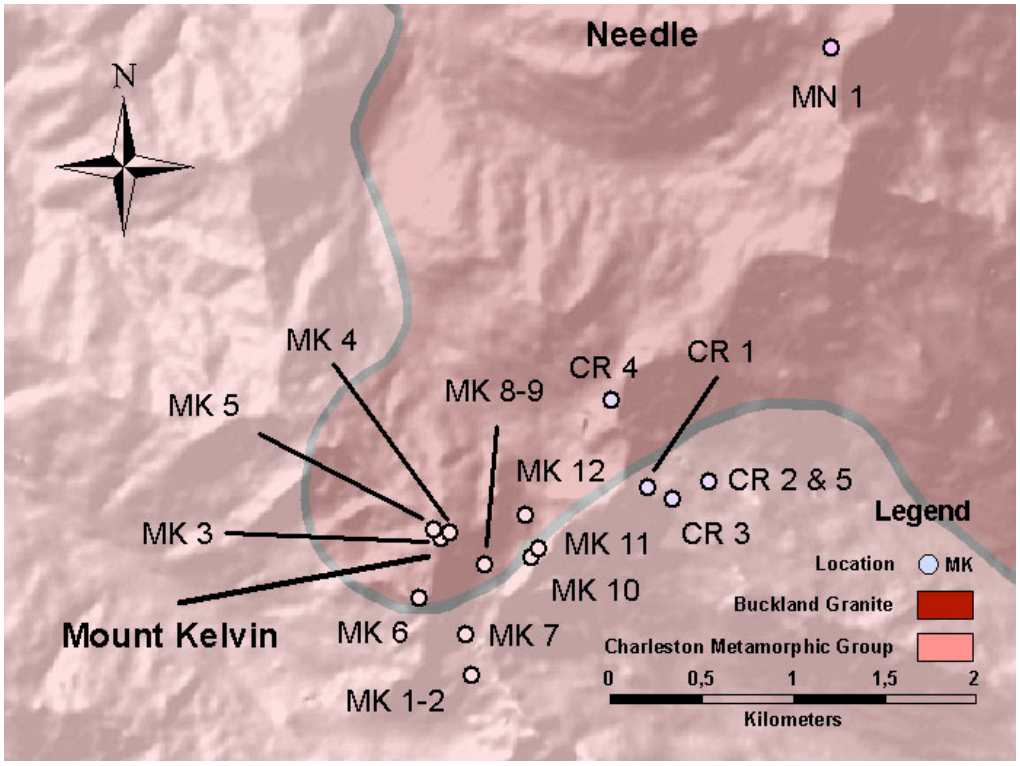

Figure 2.100: Sample area at Mount Kelvin; Geology after Rattenbury et al. (1998)

Figure 2.101: Xenoliths of CMG floating in Buckland Granite, CMG rocks display much darker color.

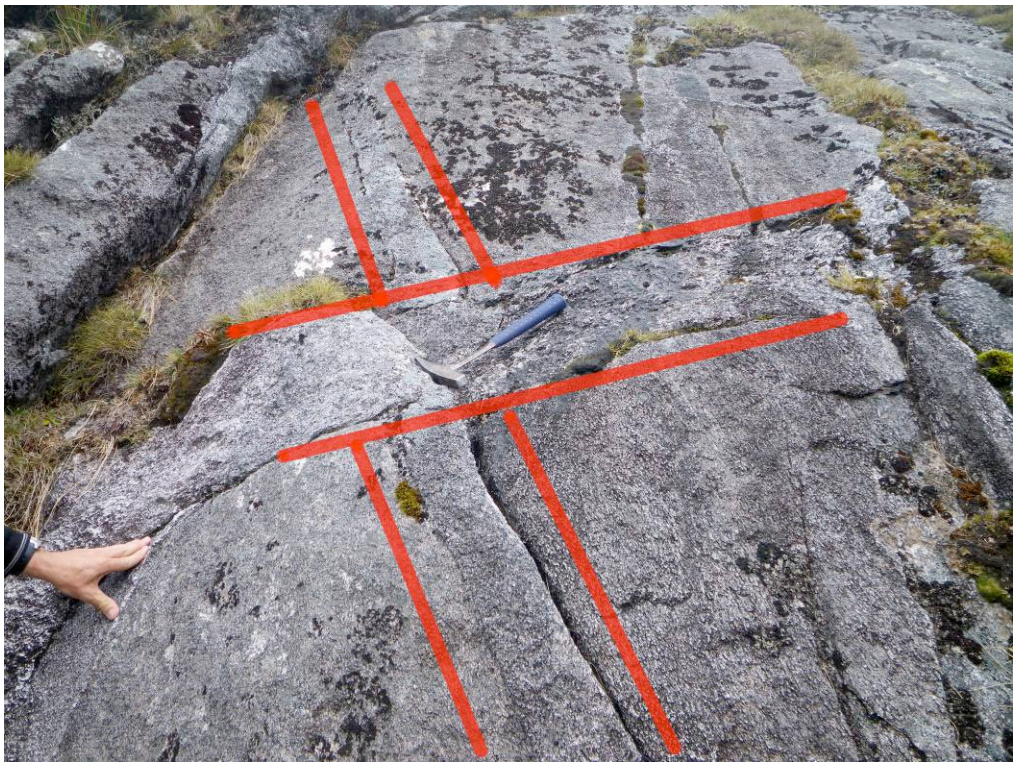

Figure 2.102: CMG gneiss interveined by intersecting Buckland Granite dikes.

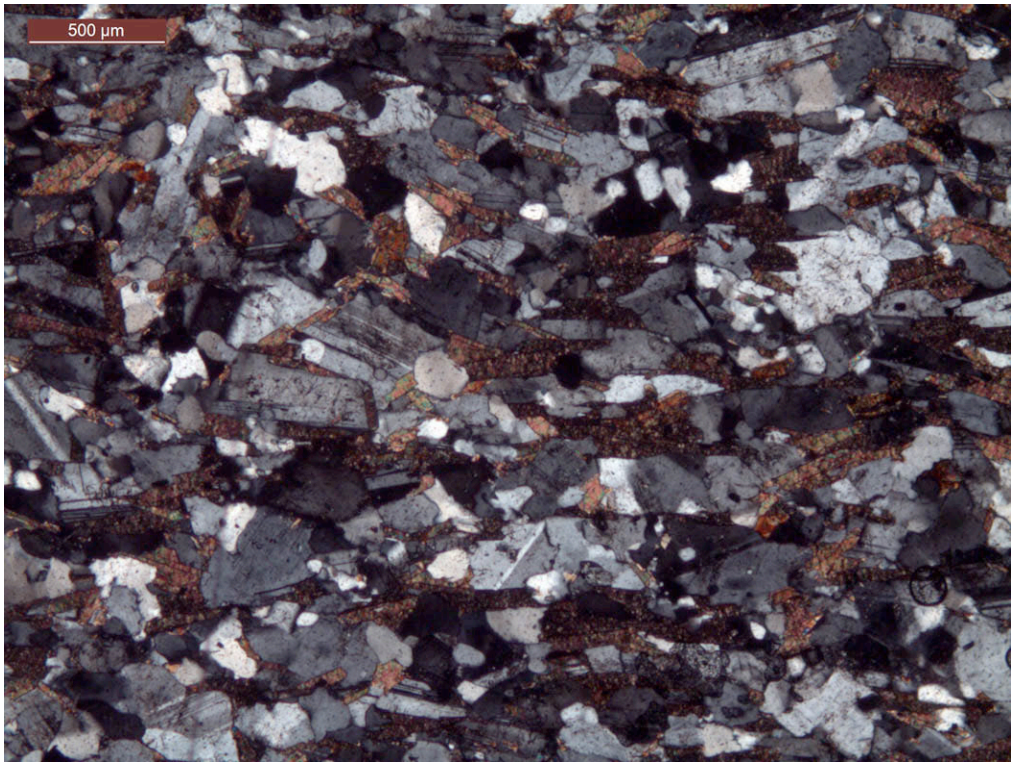

Figure 2.103: Fine-grained foliated CMG rock consisting mainly of quartz, feldspar and biotite; MK1001-1, CLP.

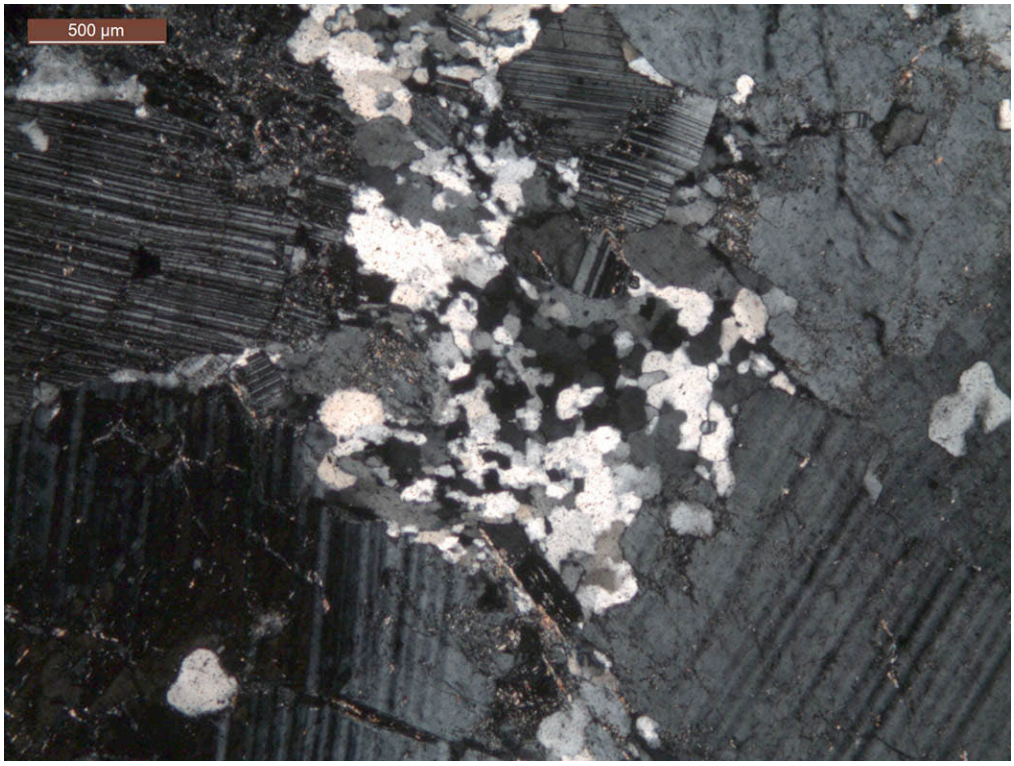

Figure 2.104: Patch of dynamically recrystallized quartz and deformational twining of feldspar; MK0201-1, CLP.

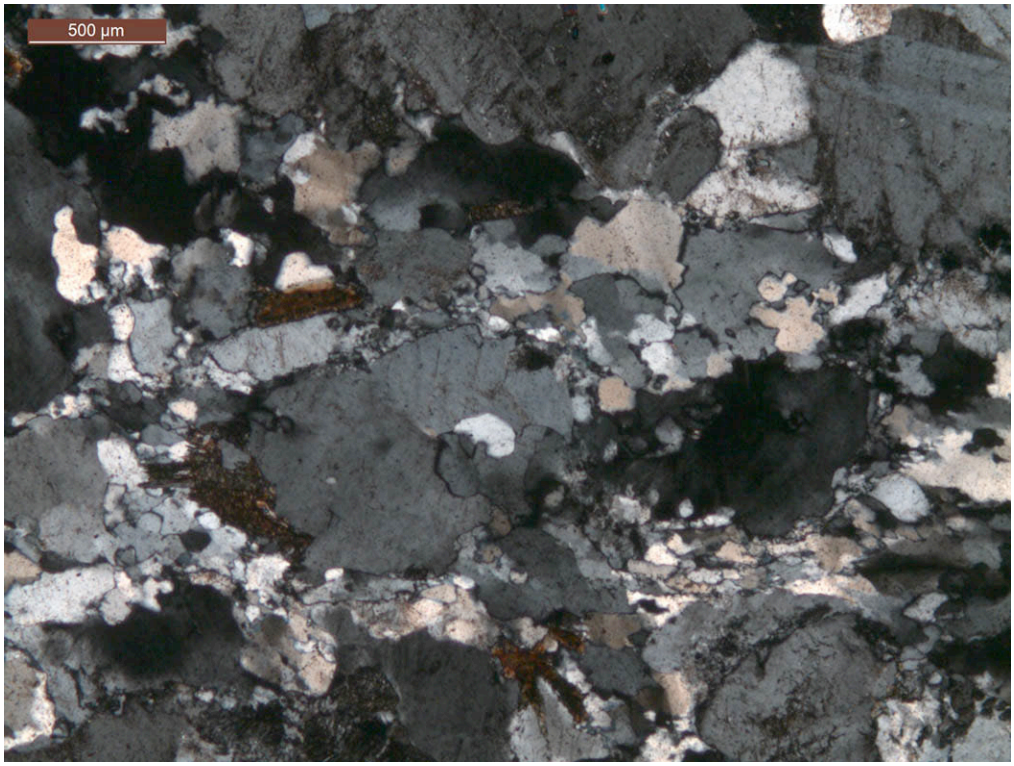

Figure 2.105: Dynamically recrystallizing quartz and feldspar begin to form layers, MK1101-2, CLP.

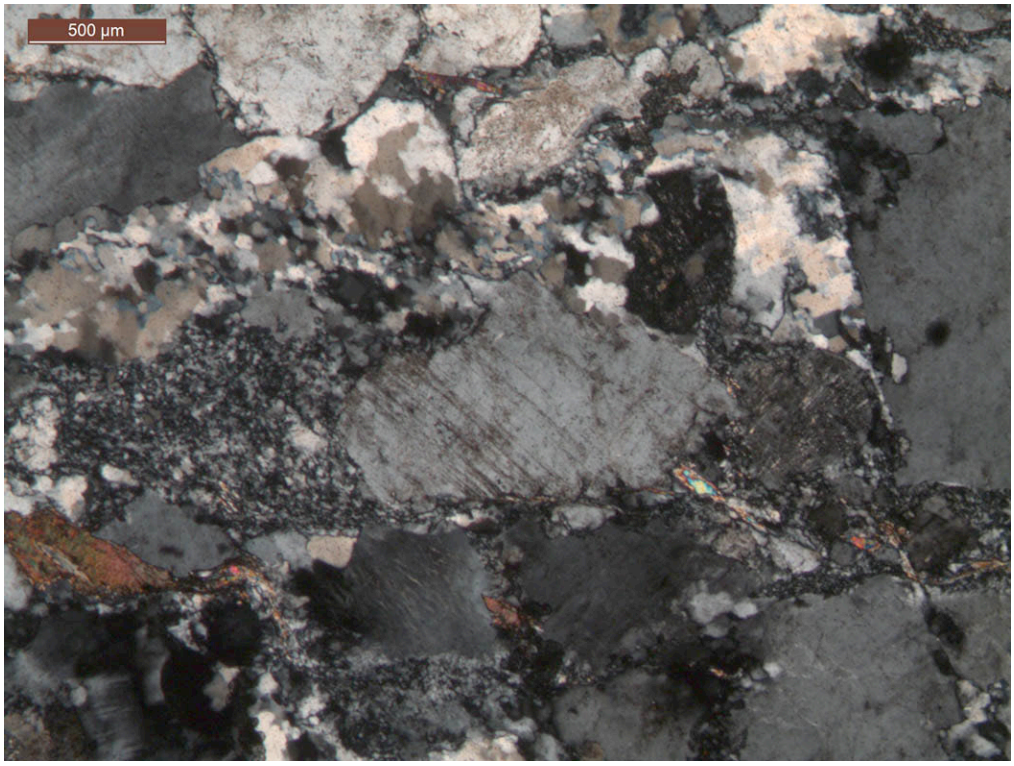

Figure 2.106: Quartz and feldspar ductilely deformed and recrystallized in a strain shadow; MK1102-1, CLP.

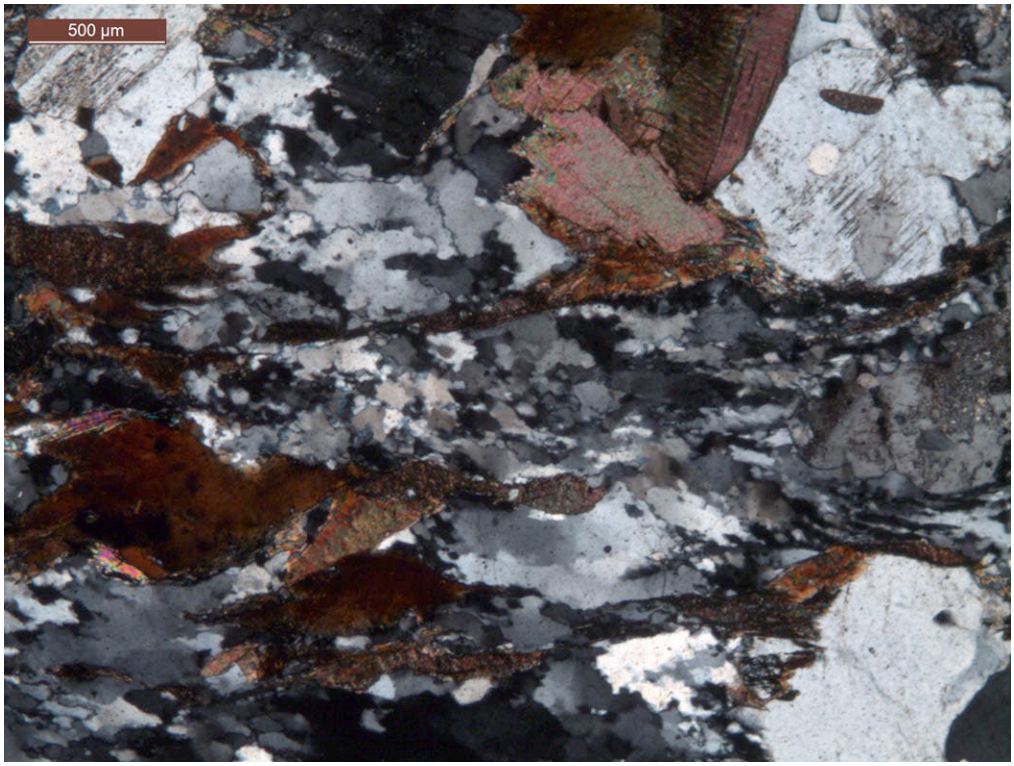

Figure 2.107: Dynamically recrystallized quartz, feldspar and mica forming a foliation; MK1101-3, CLP.

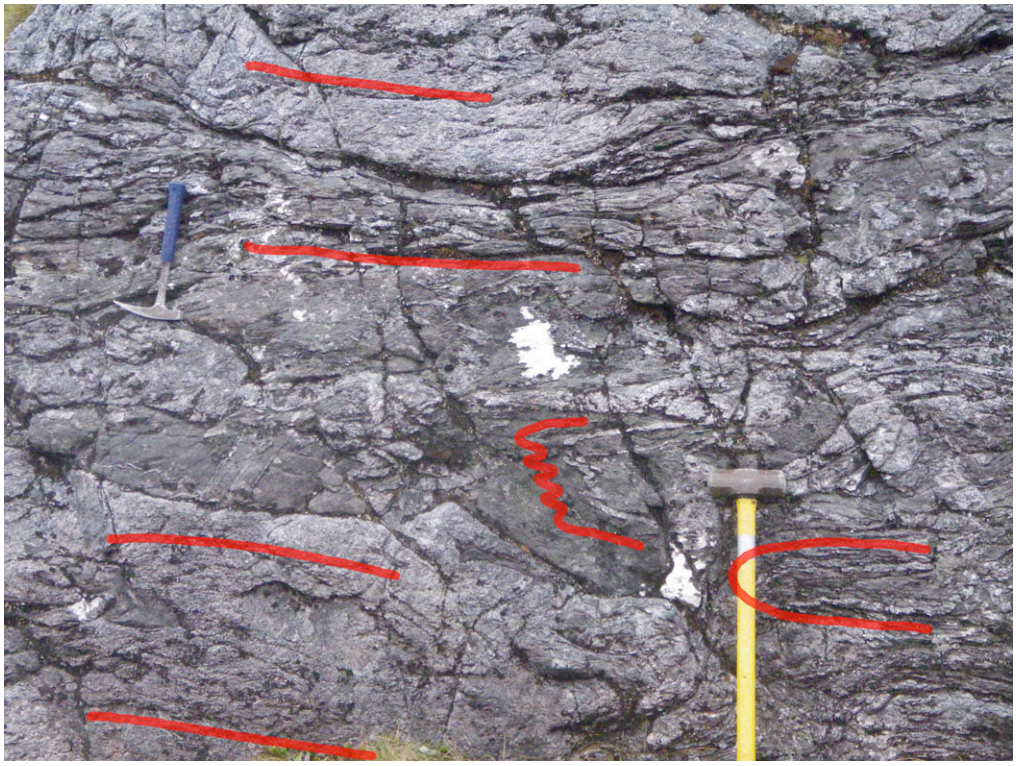

Figure 2.108: Foliated and folded CMG rocks, foliation parallel to Buckland Granite.

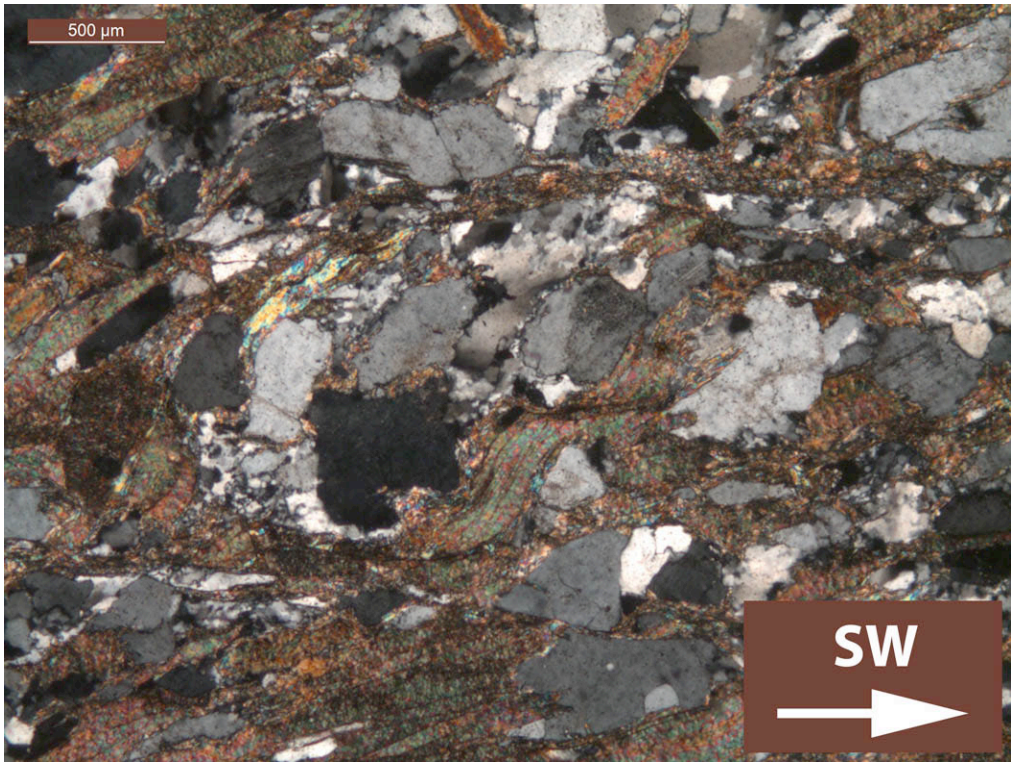

Figure 2.109: C/S-structures of biotite indicating top-to-SW sense of shear; MK0101-1, CLP.

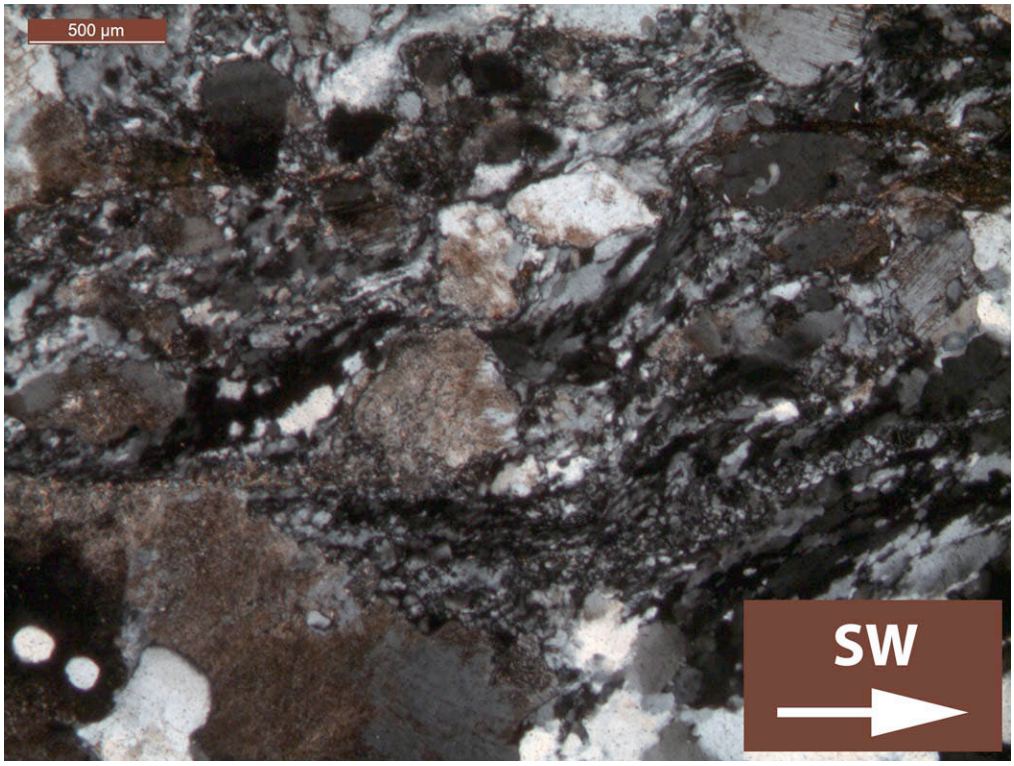

Figure 2.110: C/S-structures of dynamically recrystallized quartz and feldspar indicating top-to-SW sense of shear; CR0201-2, CLP.

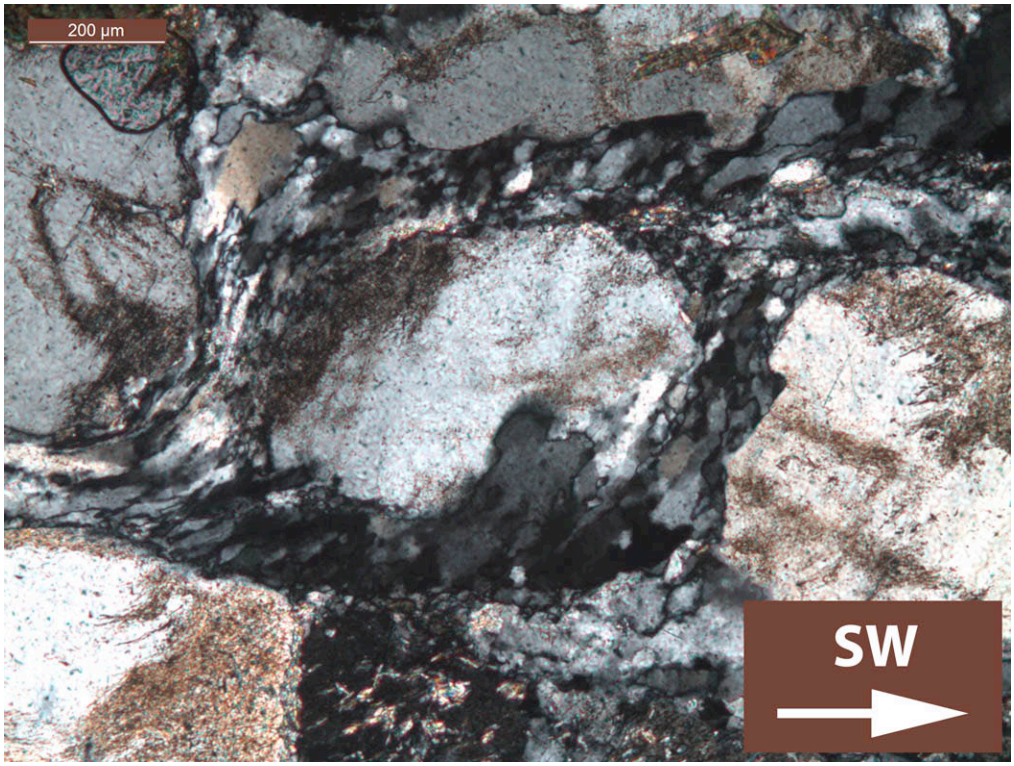

Figure 2.111: Feldspar porphyroclast and dynamically recrystallized quartz and feldspar indicating top-to-SW sense of shear; CR0201-1, CLP.

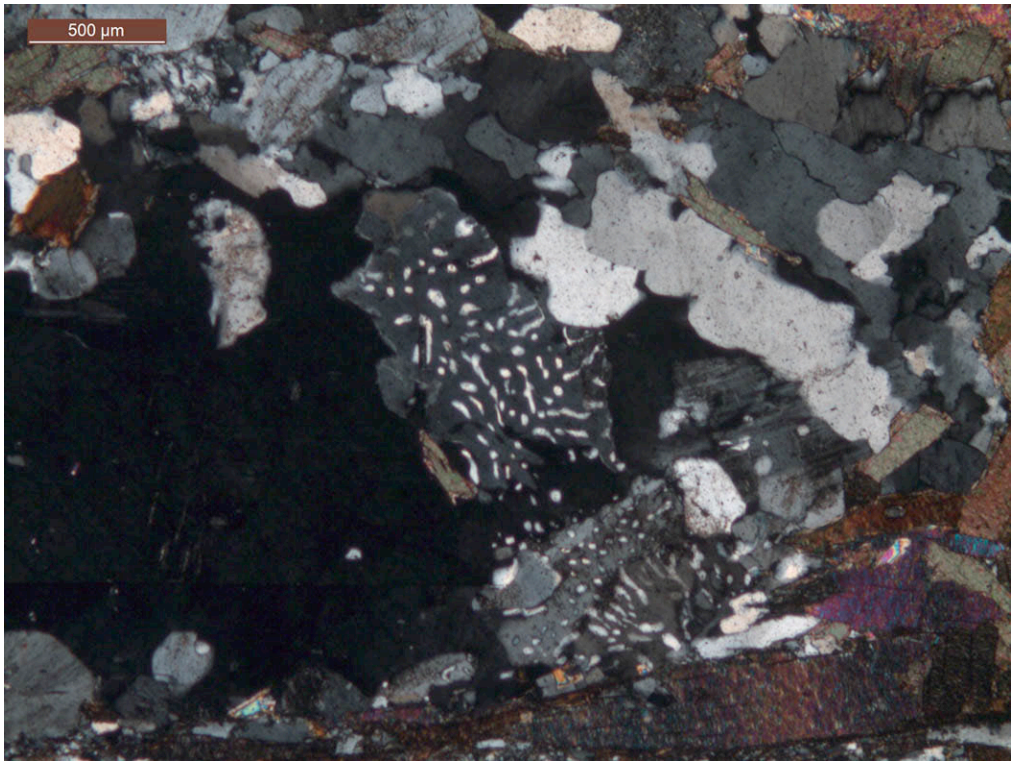

Figure 2.112: Myrmekite; MK1101-1, CLP.

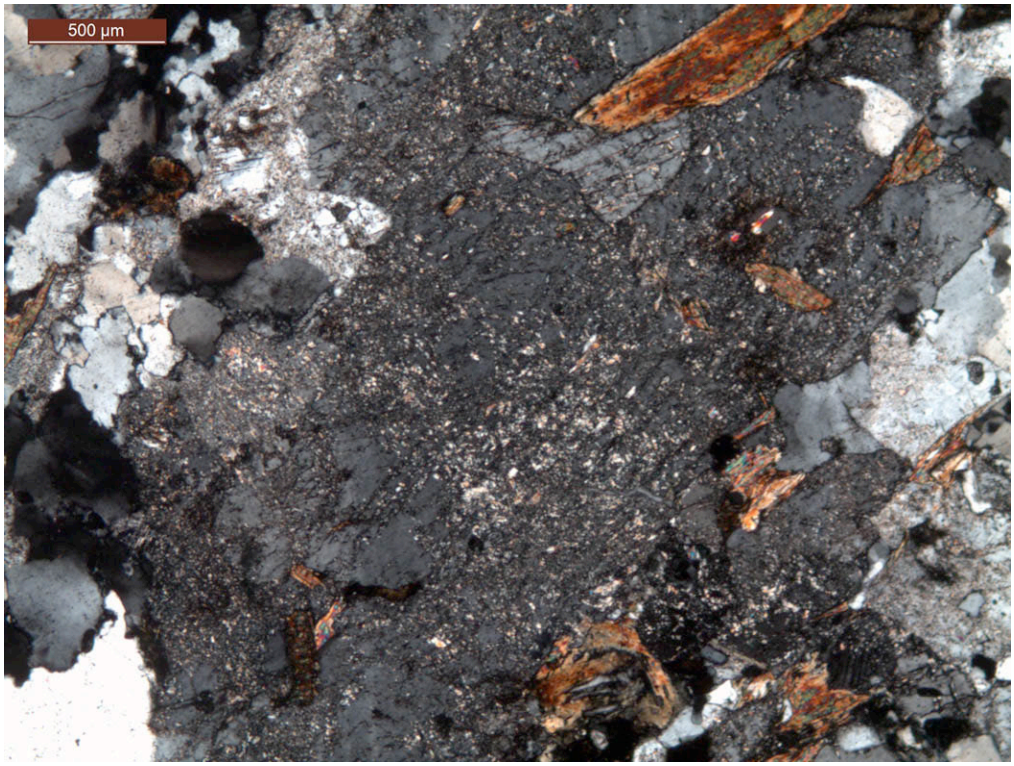

Figure 2.113: Transition from sericite to very fine-grained muscovite replacing feldspar; MK0701-1, CLP.

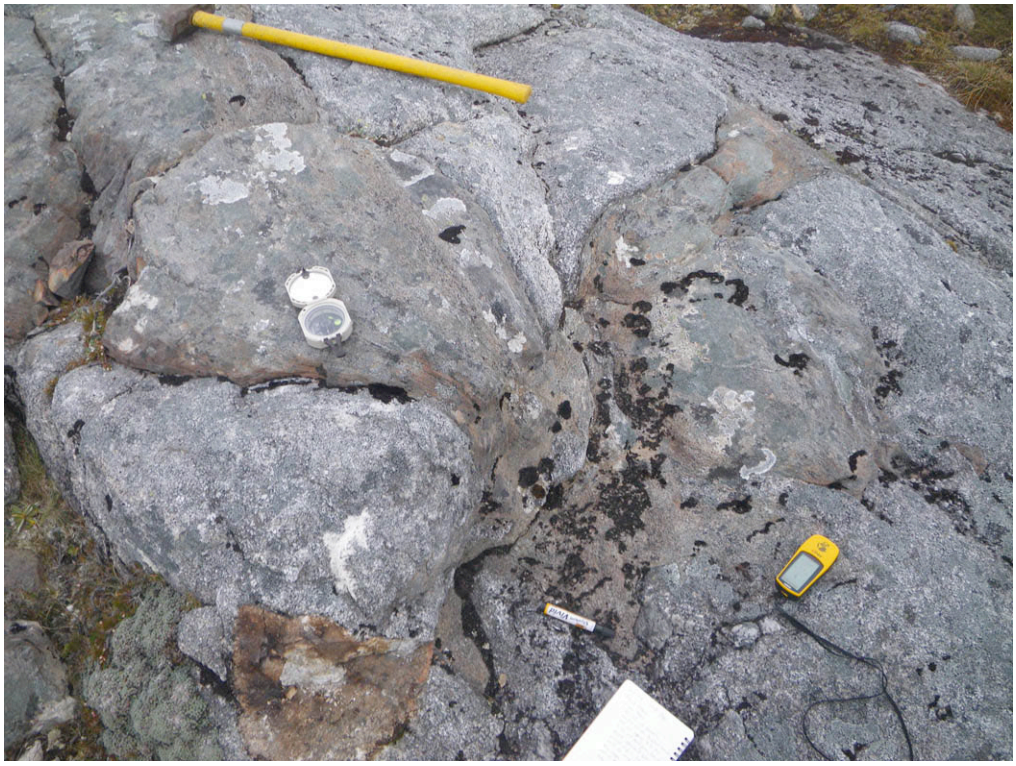

Figure 2.114: Ductilely deformed xenolith in CMG rocks, possibly intensely altered Greenland Group.

Figure 2.115: Weakly foliated Buckland Granite, foliation parallel to pencil.

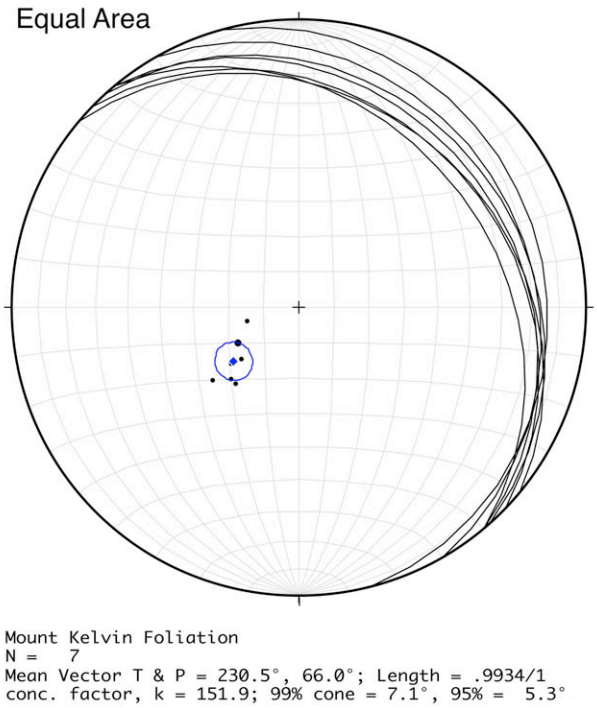

Figure 2.116: Stereographic projection of the foliation of CMG rocks and Buckland Granite at Mount Kelvin.

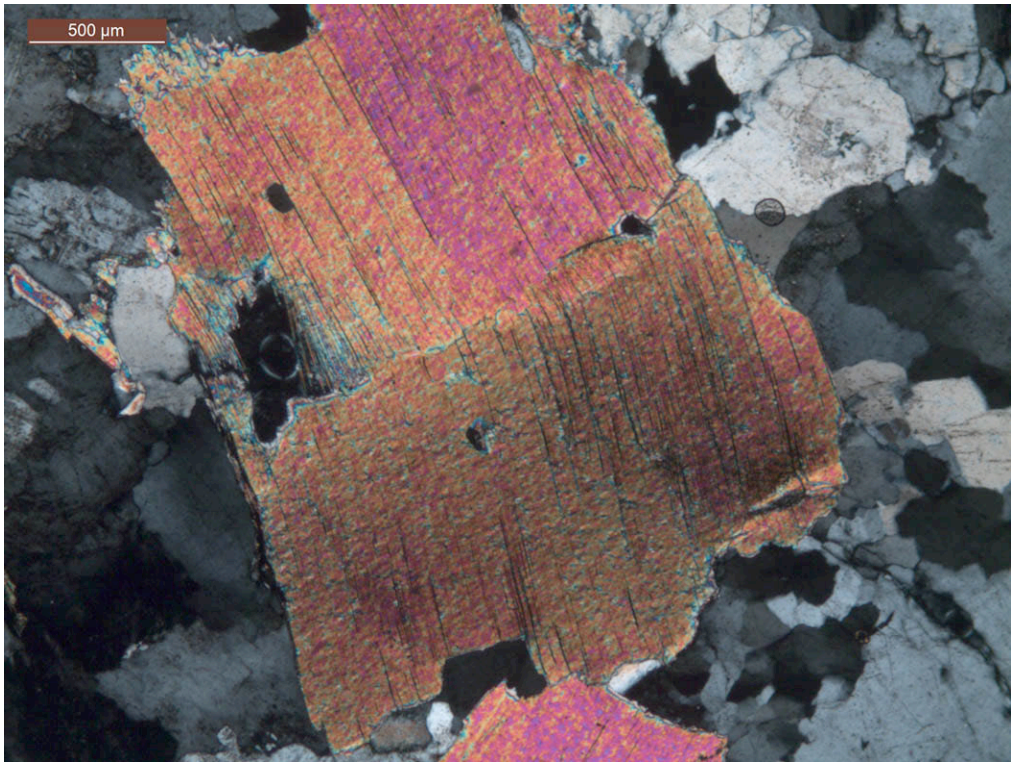

Figure 2.117: Bent and kinked muscovite; MK0401-1, CLP.

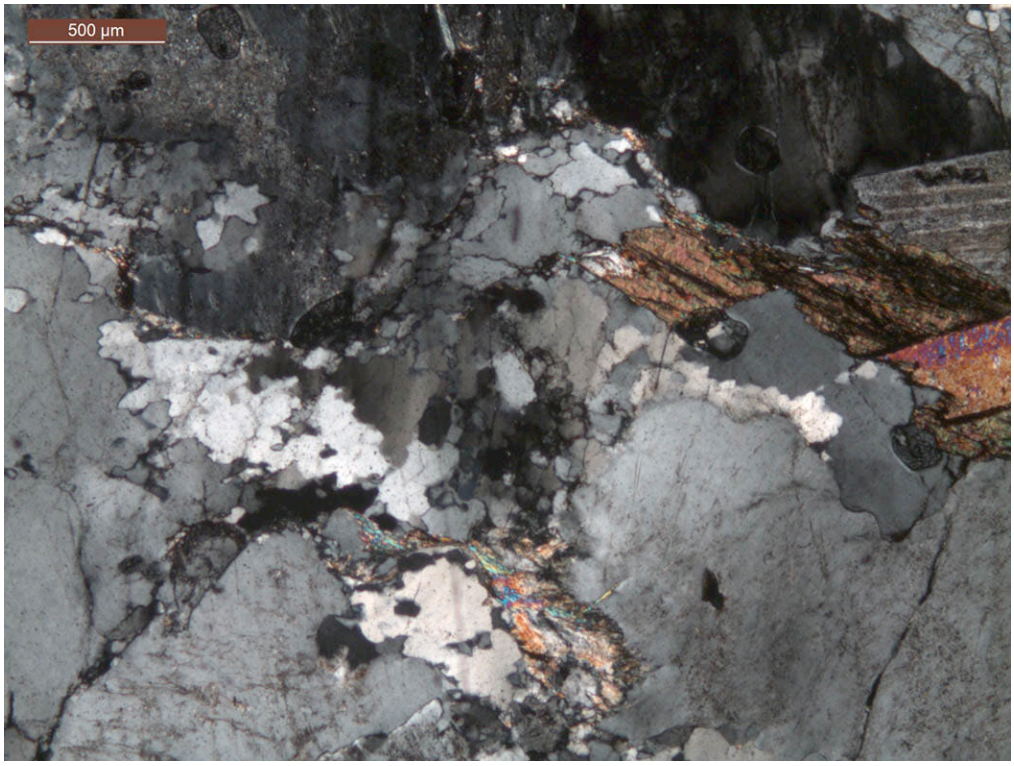

Figure 2.118: Patch of dynamically recrystallizing quartz; MK0501-1, CLP.

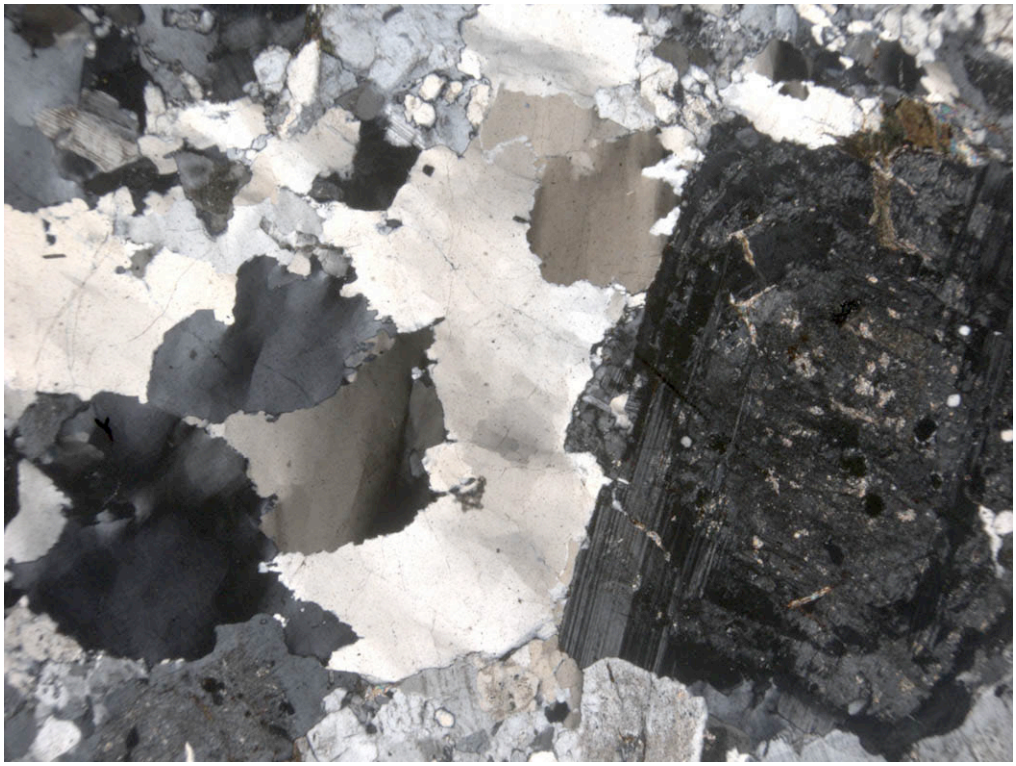

Figure 2.119: Sericite replacing feldspar, deformational twinning, undulatory quartz; MN0101-1, width of view 6.0 mm, CLP.

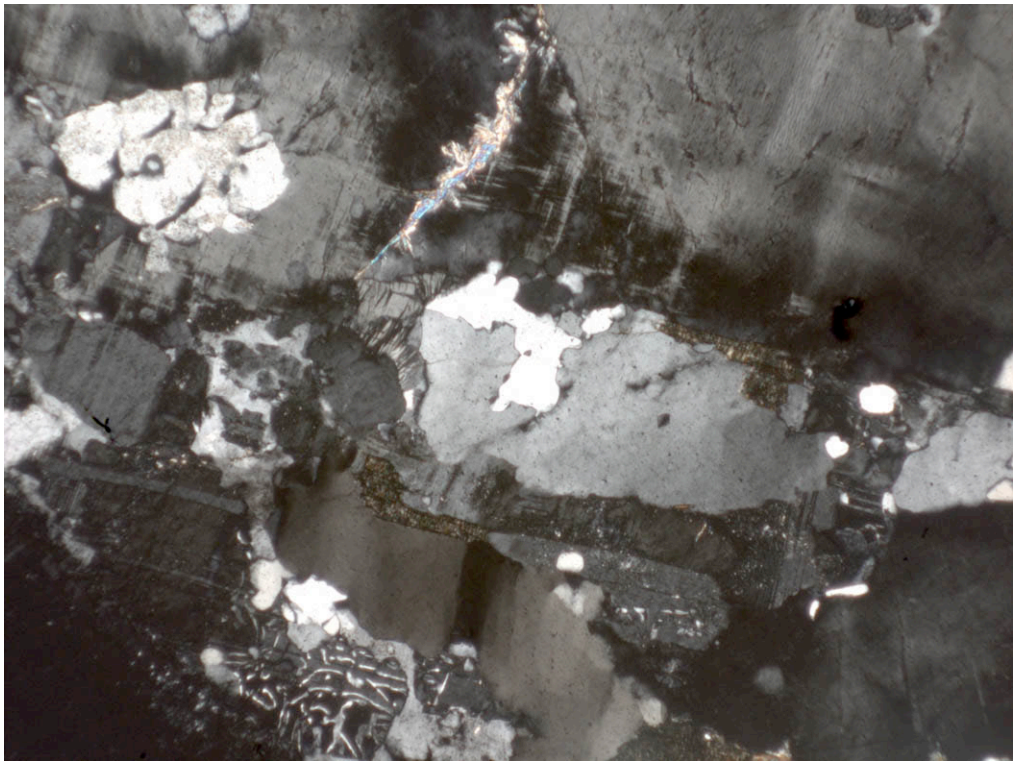

Figure 2.120: Myrmekite and microcline twinning; CR0401-1, width of view 2,52 mm, CLP.

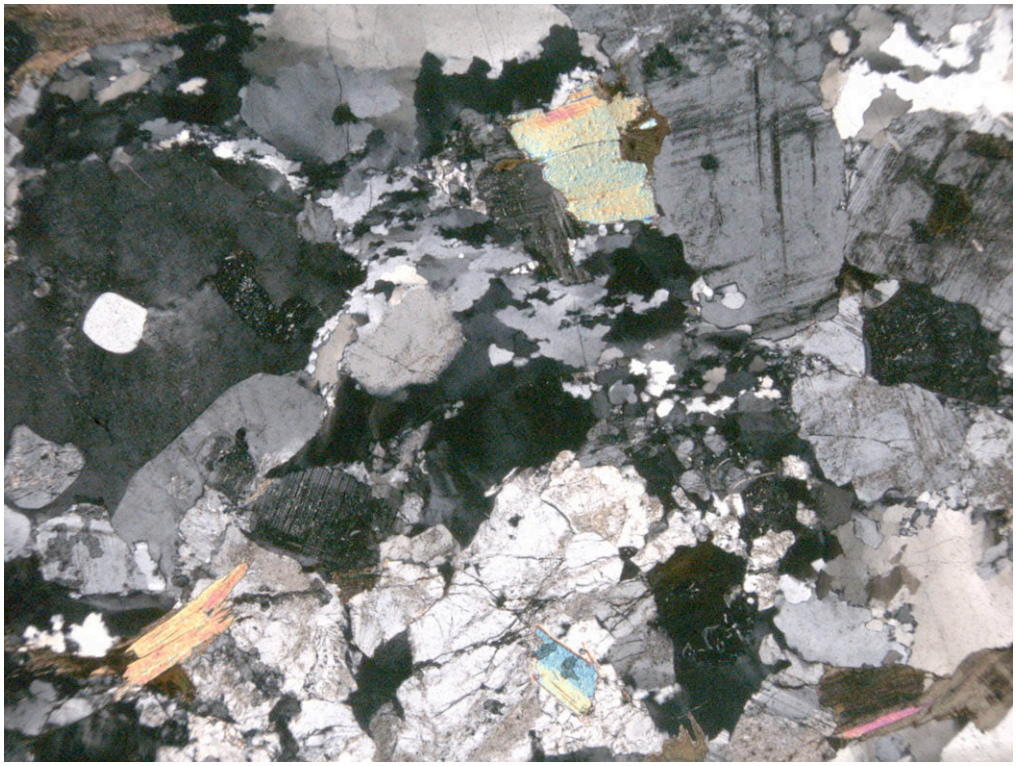

Figure 2.121: More intense dynamic recrystallization of quartz; CR0401-3, width of view 6.0 mm, CLP.

Figure 2.122: Sigmoid feldspar phenocryst indicating southward sense of shear, straight lines mark the foliation, sigmoid is exposed on surface nearly perpendicular to foliation.

Figure 2.123: Sigmoid feldspar phenocryst on a foliation plane indicating top-to-SW sense of shear.

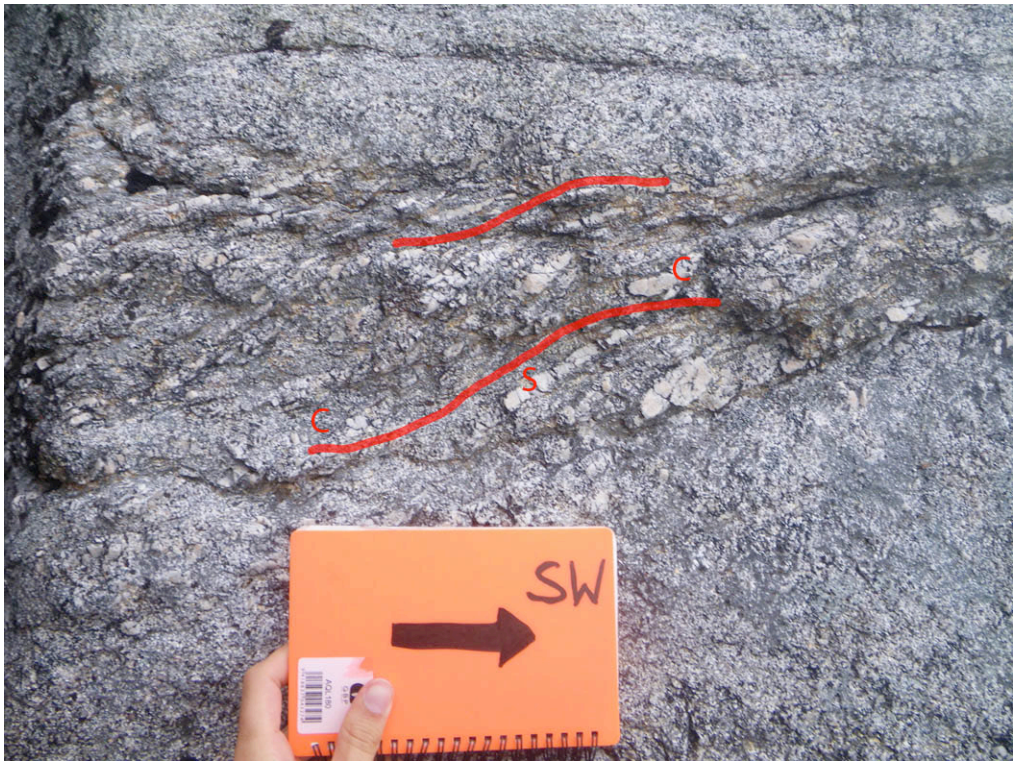

Figure 2.124: Sheared pegmatite with C/S-structures indicating top-to-SW sense of shear.

2.2.6. Mount Euclid, Mount Faraday and Mount Raoulia

In order to obtain some fission track samples from the hardly accessible Central Paparoa Range for future research, stopovers were made on the flight to Mount Kelvin at Mount Raoulia, Mount Faraday and Mount Euclid. A few orientated samples for petrographic analysis were taken on this occasion as well. Yet there was not enough time to investigate the areas thoroughly and the samples serve only as a counter-check for the results from Mount Kelvin and the Buckland Peaks.

Mount Raoulia consists of Buckland Granite and is located at the southern margin of the Paparoa Range (Figure 1.07). Together with Mount Kelvin this exposure of Buckland Granite is the closest to the Pike Detachment. A weak foliation dips with 301/28 gently to the NNW. Thin sections (Figures 2.125, 2.126, 2.127) do not show any structures different from those of the granite at Mount Kelvin and a sense of shear cannot be determined.

Mount Faraday is one of the major peaks of the central ridge of the Paparoa Range and consists of CMG rocks (Figure 1.07). The foliation of the gneiss dips with 043/23 gently to the NE (Figure 2.128). The rocks are rich in biotite and a southward sense of shear is discernible in thin section (Figure 2.129).

The stopover at Mount Euclid lasted longer. Therefore a small area was superficially surveyed and several samples were collected (Figure 2.130). Different rock types were identified at Mount Euclid, which is mapped as CMG area. The dominant one is foliated biotite-rich rock. The foliation is defined by the biotites and ductilely deformed quartz (Figure 2.131). It is folded on a submeter scale (Figure 2.132). As the foliation dips with 329/12 to the NNW and with 110/13 to the ESE at different places respectively a possible folding on a larger scale can be concluded as well (Figure 2.133). Lineations are not visible however. Beside the biotite rich rock there is another light-colored gneiss with a less pronounced foliation.

Xenoliths, which resemble those at the coastline and are possibly blocks of Greenland Group, can be found as well (Figure 2.134). Some of the xenoliths have a remarkable composition as they consist of almost pure biotite (Figures 2.135, 2.136). A correlation between dominant rock types and xenolith types could not be observed.

The rocks are obviously deformed and the strain was accommodated heterogeneously. Micas are broken, plagioclase shows twinning lamellae and quartz is ductilely deformed (Figures 2.137, 2.140) in less affected areas. In more deformed areas C/S-structures of mica and ductile quartz clearly indicate a top-to-SW sense of shear (Figure 2.138). Furthermore some of the feldspars show the conspicuous replacement by muscovite and sericite (Figure 2.139), which is associated

to myrmekite (Figure 2.140) and indicates deformation under lower amphibolite facies conditions (Phillips et al. 1972; Ashworth 1986; Simpson & Wintsch 1989; Cesare et al. 2002).

During the quick superficial survey the relations between the biotite-rich and the light-colored gneisses appeared to be complicated. Gradual transitions between the two types occurred as well. Many of the characteristics of the gneisses like the distinct difference in biotite content, multiple fold generations (Shelley 1970b), suspected Greenland Group xenoliths and metamorphic grade resemble those of the rocks at the coastline and it seems likely that they represent the orthogneiss and paragneiss members of the CMG. The deformational features are all consistent with those at Mount Kelvin and at the coastline and the shear sense is in agreement with a movement direction of the upper plate to the SW.

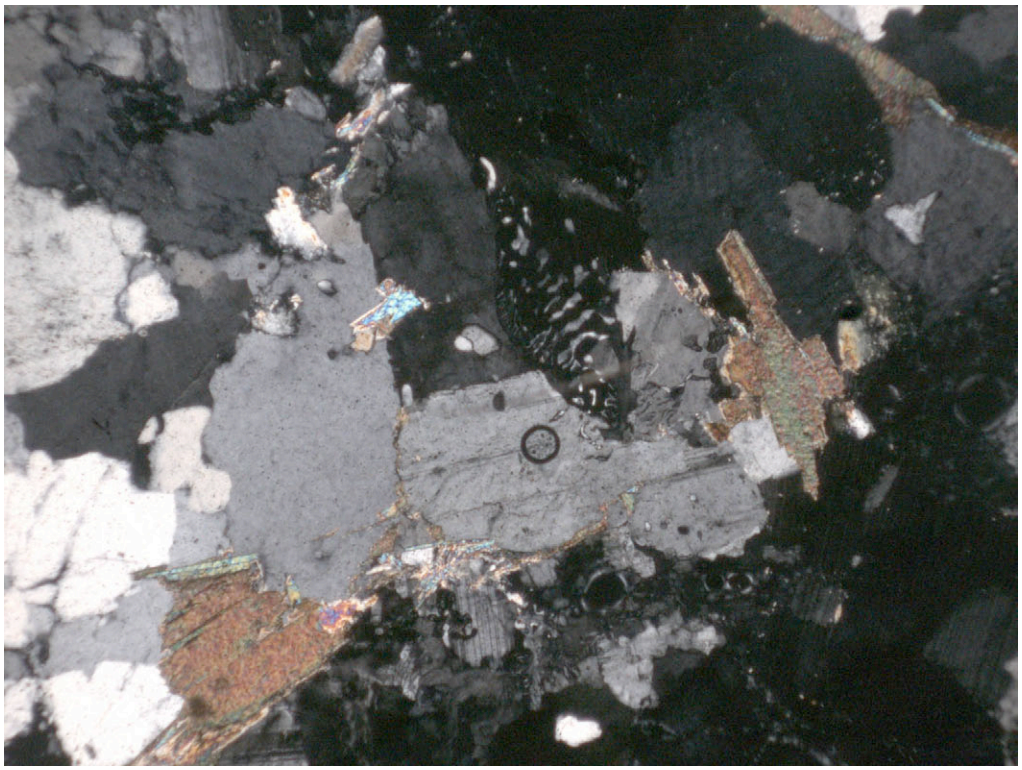

Figure 2.125: Myrmekite in Buckland Granite from Mount Raoulia; MR0101-1, width of view 2.9 mm, CLP.

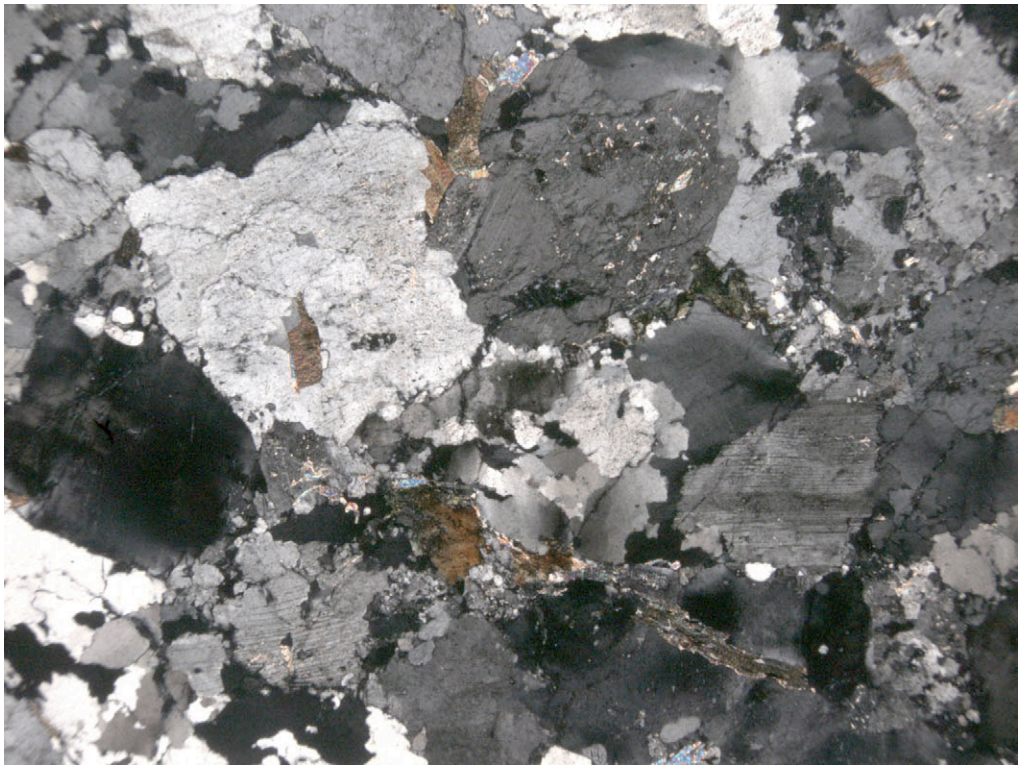

Figure 2.126: Sericite and muscovite replacing feldspar, ductilely deformed quartz, Buckland Granite from Mount Raoulia; MR0101-2, width of view 6.0 mm, CLP.

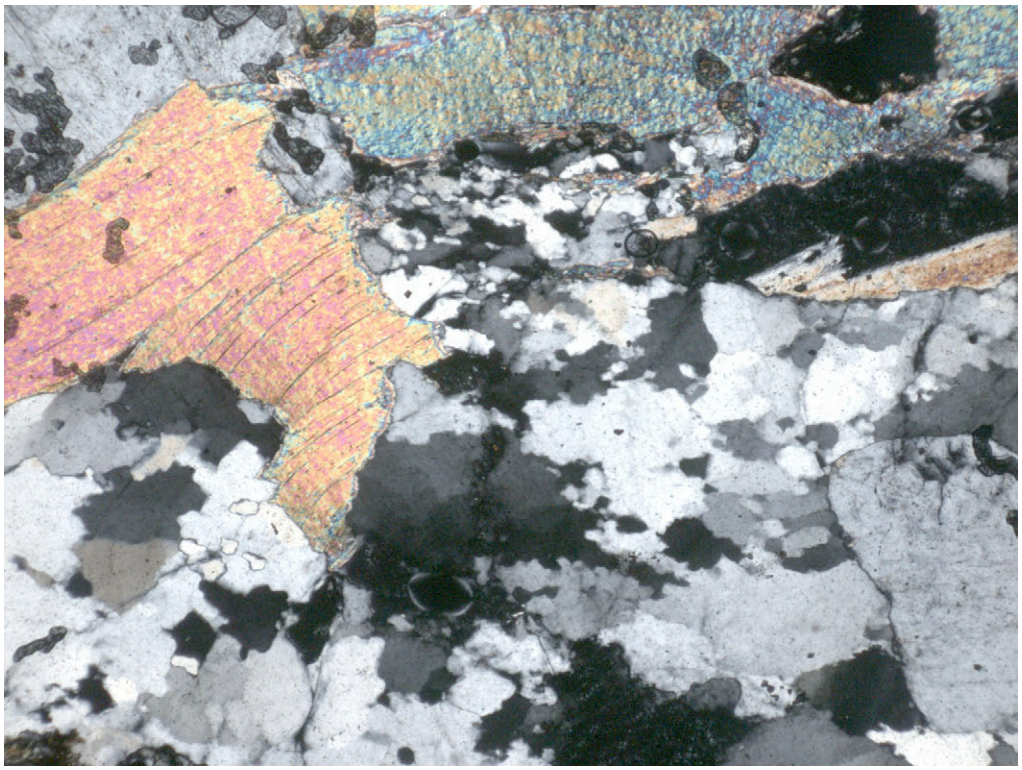

Figure 2.127: Deformed muscovite and ductilely deformed quartz in Buckland Granite from Mount Raoulia; MR0101-4, width of view 2.9 mm, CLP.

Figure 2.128: CMG gneisses at Mount Faraday, foliation dipping to the NE.

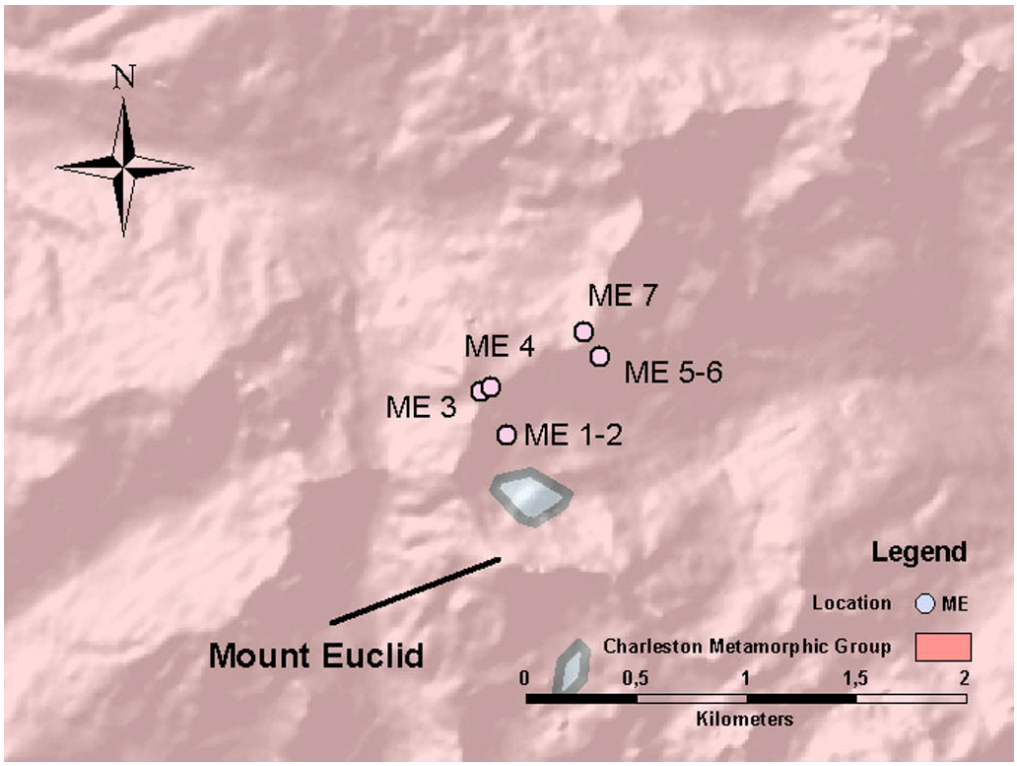

Figure 2.129: Sample area at Mount Euclid, Geology after Rattenbury et al. (1998)

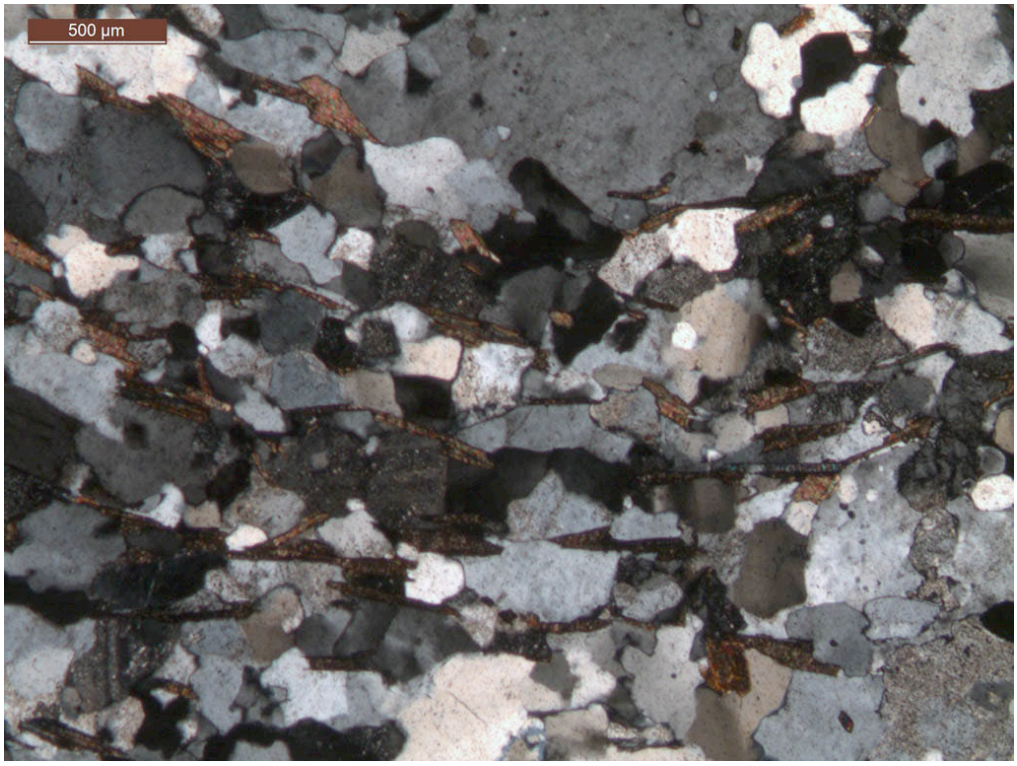

Figure 2.130: Aligned biotite und ductilely deformed quartz define foliation; ME0201-2, PPL.

Figure 2.131: Gneiss folded on submeter scale.

Figure 2.132: Foliated rocks on Mount Euclid, here dipping to the NW.

Figure 2.133: Xenolith in CMG rocks, possibly Greenland Group.

Figure 2.134: Xenolith consisting of coarse-grained biotites in light-colored gneiss.

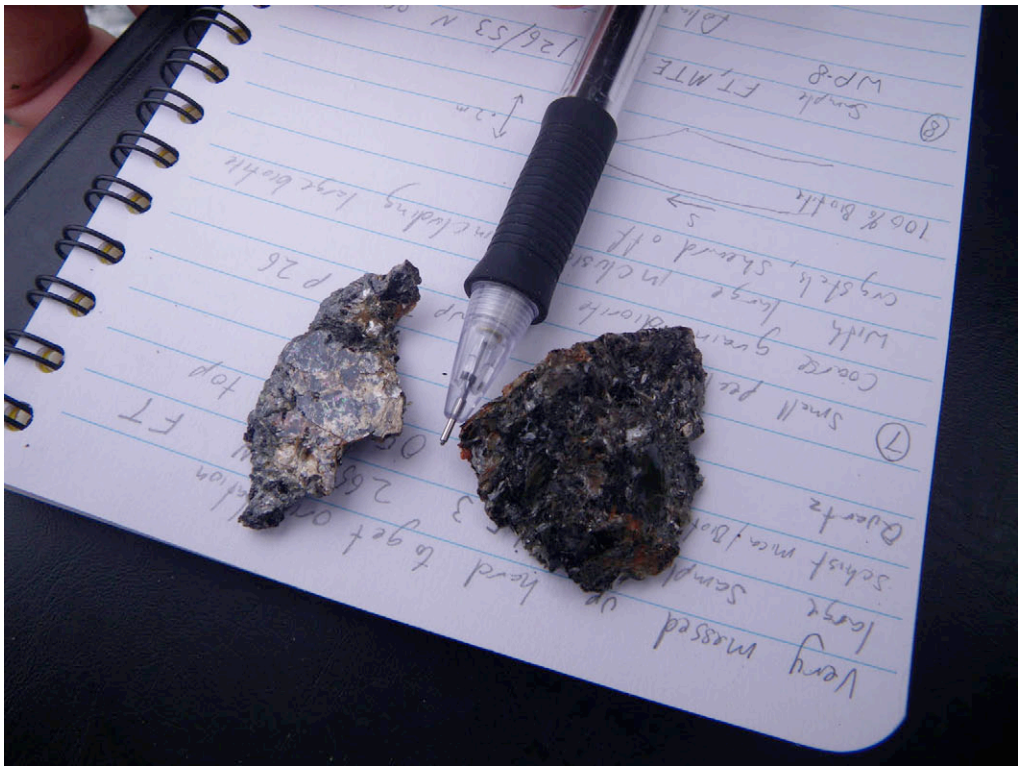

Figure 2.135: Some xenoliths consist of nearly pure biotite.

Figure 2.136: Broken biotite and deformational twinning lamellae in plagioclase; ME0101-2, CLP.

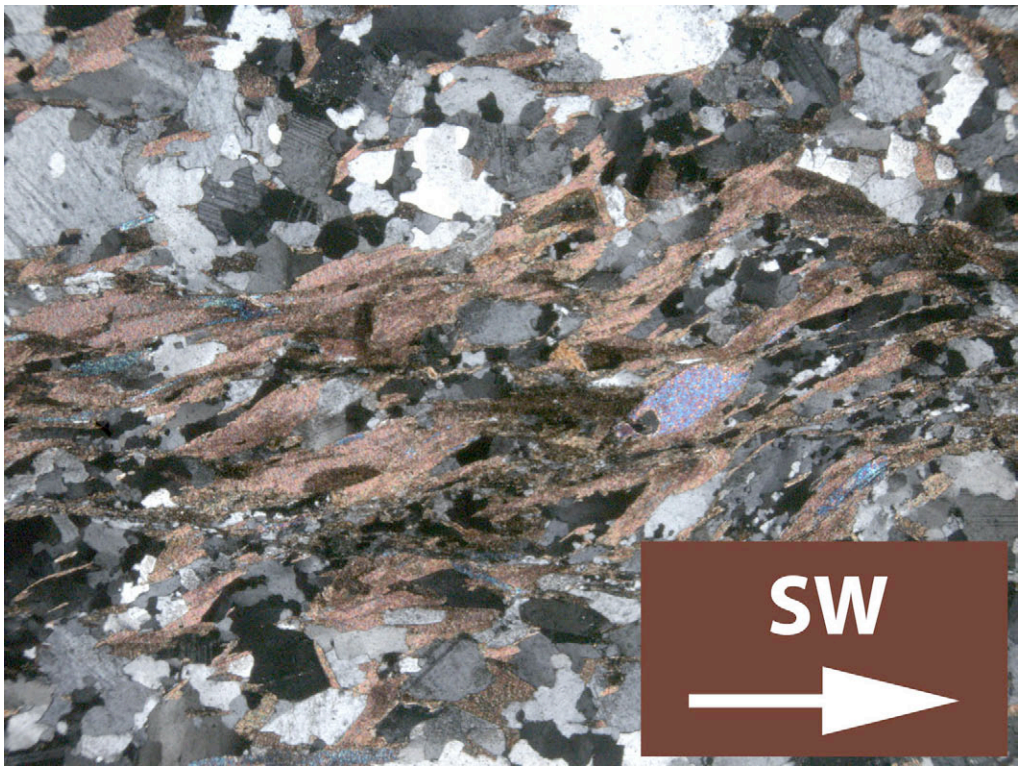

Figure 2.137: C/S-structures of ductilely deformed quartz and mica indicating a top-to-SW sense of shear; ME0301-1, width of view 6.0 mm, CLP.

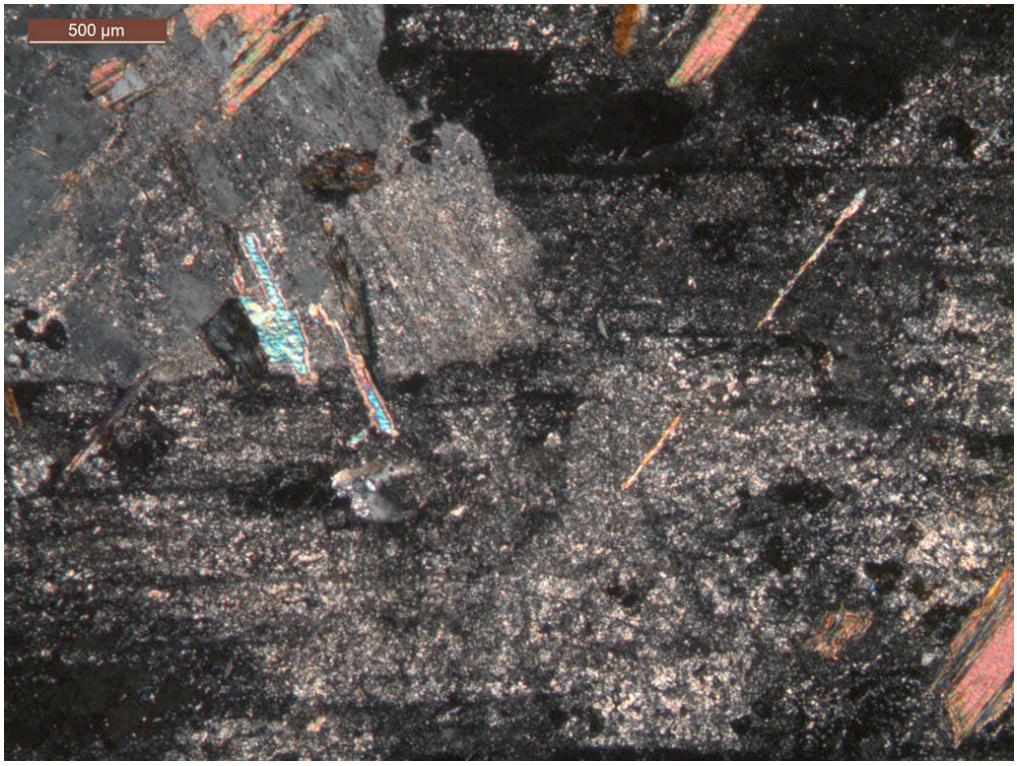

Figure 2.138: Transition of sericite to muscovite replacing feldspar; ME0101-1, CLP.

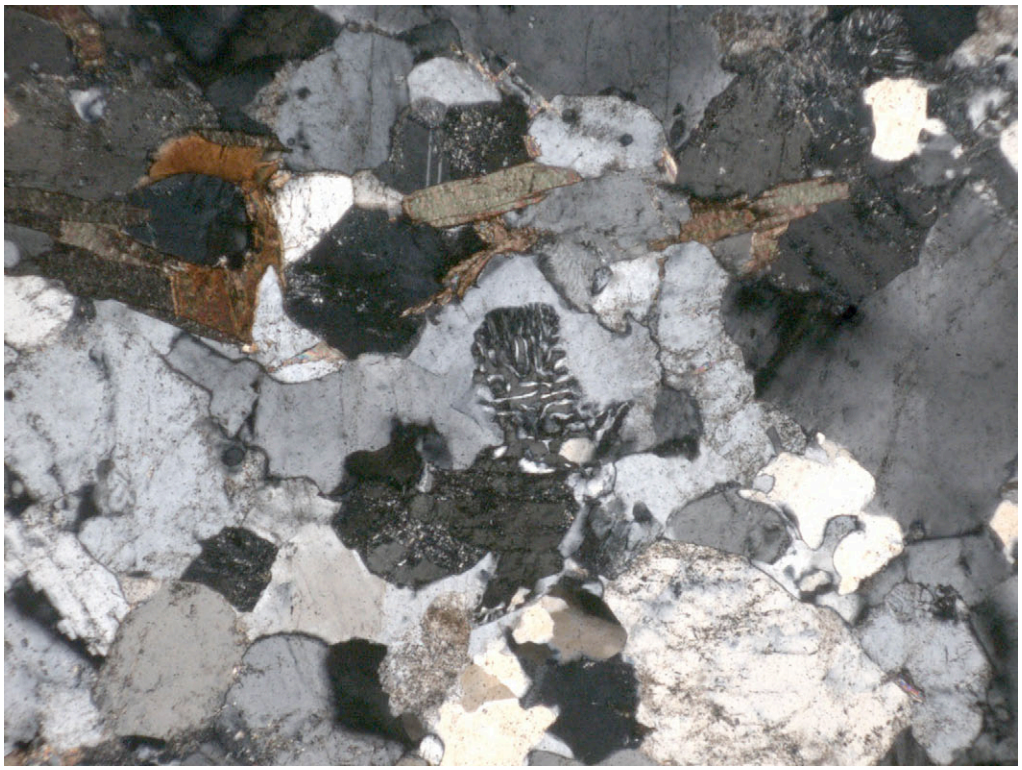

Figure 2.139: Myrmekite, quartz with lobate grain boundaries; ME0601-2, width of view 2.9 mm, CLP.

CHAPTER 3: FISSION TRACKS

3.1. Previous Work

Fission track analyses have already been carried out on the West Coast, and the Paparoa Range in particular (Seward 1989; Seward & White 1992). The results of the study of Seward (1989) show that the West Coast region between Westport and Greymouth is affected equally by a primary thermal signature ranging from 100 to 70 Ma, depending on the closing temperature of the mineral regarded. Seward tentatively related this to the separation of this region from Gondwana. While the FT were reset in many areas like the Paparoa Range due to Tertiary burial and subsequent uplift, the rocks on the coast between Westport and Greymouth stayed unaffected and therefore preserved the primary signature.

Seward & White (1992) focused on the Post-Cretaceous development of the Paparoa Range. They reconstructed the thermal history related to the burial and the associated formation of coal measures in the Paparoa Range. Their results reflect a differentiated burial- and uplift history of the Tertiary basin and show that the apatite FT were reset in the Paparoa Range and that two of their zircon samples possibly show partial annealing as well. Thus apatite FT from the Paparoa Range are unsuitable to reconstruct the Cretaceous thermal history of the core complex and zircon FT data have to be treated cautiously.

Neither study made kinematical implications for the core complex on the basis of the FT data. Spell et al. (2000) used the results of the FT analyses to refine the thermal history of the entire lower plate of the core complex and relied on K/Ar ages of muscovites to determine a slip rate of 4.4 km Ma^{-1} for the Pike Detachment. FT data have however been used in other areas to establish age-distance relationships and to investigate possible fault-related movements (e.g. Ring & Bernet 2010). The data presented below is the first attempt to use FT ages to put constraints on the kinematics of the Paparoa Metamorphic Core Complex.

The low coal rank of the Brunner Coal, which rests directly on the crystalline basement, and the unlithified overlying sediments on the coastline correspond to the unaltered primary FT ages (Seward 1989). Hence, FT ages from coastline samples are suitable to examine the kinematics of the core complex.

Uwe Ring collected 21 rock samples for fission track analysis in 2006, 2008 and 2009 mainly on the coastline between Cape Foulwind and the Fox River mouth and in the Lower Buller Gorge (cf. Figure 1.02). The unpublished data of this analysis is presented below.

3.2. Apatite Fission Tracks

The samples taken along the coastline display primary apatite fission track (AFT) ages of about 70 to 80 Ma (Table 3.1) with an average of ~75 Ma. The AFT ages of PCC08-6 and the ages of all samples taken in 2006 (beginning with "PCC06") are younger due to partially or entirely resetting as expected since these specimens are from the Lower Buller Gorge area where the rocks were buried to depths where the temperature reached the partial annealing zone for apatites in the Tertiary (Seward & White 1992). Partially reset samples fail the χ^2-test, i.e. a low $P\chi^2$ value < 5%, and suggest a bimodal distribution of the FT ages. It is not useful to retrieve the older, possibly Cretaceous ages, because the distribution is dominated by the younger ages. The obtained Tertiary ages match those of Seward & White (1992). As they do not reflect the Cretaceous cooling history anymore, they are disregarded for further determination of the kinematic development of the core complex. Sample PCC08-10 contained only 2 grains resulting in a very large error. Thus this sample is left out of consideration as well.

The data of the remaining twelve samples from the coastline (Figure 1.02) was used to examine possible slip rates. Although all AFT ages lie within their errors a trend of the ages becoming younger towards the Pike Detachment can be observed. Despite the obvious shear sense to the NE (see chapter 2.2.1.) this trend to the SW also persists at Cape Foulwind. A linear regression of the distance-age relationship along the entire coastline translates to an average slip rate of 6.7 +16.7/-4.2 (2 σ) km Ma^{-1} to the SW (Figure 3.1). The slip rate in the north is significantly lower than in the south and therefore is negligible. Due to lacking exposure of basement rocks between Cape Foulwind and Charleston the transition cannot be observed.

It is questionable if the apatite data are related to the primary core complex development, however. If the ultramylonites at Morrisey Creek are as old as 116.2 ± 5.9 Ma (Ring et al. 2006) and deformation continued until the AFT were retained at about 70 Ma, the core complex development would have lasted for about 40 Ma. With a minimal slip rate of 2.5 km Ma^{-1} top-to-SW on the Pike Detachment the core complex should have extended to a length of at least 100 km, but it is only about a third of the size. Furthermore, no core complexes that were active over such a long period of time have been described. It is more likely that some sort of resetting caused the relatively young late cretaceous ages.

PCC08-12 is collected from a Pororari Group breccia in a cave at the Fox River mouth, which is on the upper plate of the core complex, and therefore should have been left out of kinematic consideration, too. It is derived from the lower plate basement rocks across the detachment and was taken to show the age relation between the breccia and the lower plate rocks. As the thermal

overprint responsible for the late Cretaceous ages is unlikely to be related to the core complex development, the age of PCC08-12 was taken into account nevertheless.

The obtained ages are in agreement with the results of previous workers (Seward 1989). Yet, they also show a spatial pattern on the southwestern flank of the core complex, which has not been described so far. A trend of the central ages becoming younger towards the Pike Detachment and by association towards the former rift system is discernible.

Sample No.	Distance to Arbitrary Reference Point (km)	No. of Crystals	Age Dispersion ($P\chi^2$)	Central Age (Ma)	Error (± 2 σ)
PCC06-15	39.95	20	0.06% 89.0%	22.9	5.4
PCC06-16	39.80	20	50.2% <0.01%	33.6 (mixed age)	9.8
PCC08-1	31.15	20	0.04% 87%	**77.2**	**8.8**
PCC08-2	30.55	20	0.06% 88%	**80.4**	**9.4**
PCC08-3	30.00	20	0.01% 93.8%	**75.7**	**8.4**
PCC08-4	17.75	20	<0.01% >99%	**73.9**	**10.0**
PCC08-5	15.95	20	<0.01% >99%	**78.0**	**11.0**
PCC08-6	35.65	20	45.2% 0.02%	23.7 (mixed age)	6.6
PCC08-9	7.60	20	<0.01% 98.3%	**74.8**	**10.0**
PCC08-10	7.30	2	<0.01% 70.4%	71.9	34.2
PCC08-11	6.45	20	<0.01% >99%	**72.3**	**11.4**
PCC08-12	2.05	20	<0.01% >99%	**73.0**	**9.4**
PCC08-13	31.30	20	<0.01% 97.9%	**78.9**	**10.0**
PCC08-14	28.35	20	<0.01% >99%	**73.8**	**11.2**
PCC08-15	10.70	20	<0.01% >99%	**74.5**	**9.4**
PCC08-16	7.95	20	<0.01% >99%	**74.6**	**11.0**

Table 3.1: Apatite fission track data, red samples are excluded from further consideration due to resetting and the poor quality of the obtained ages, all accepted ages in bold print.

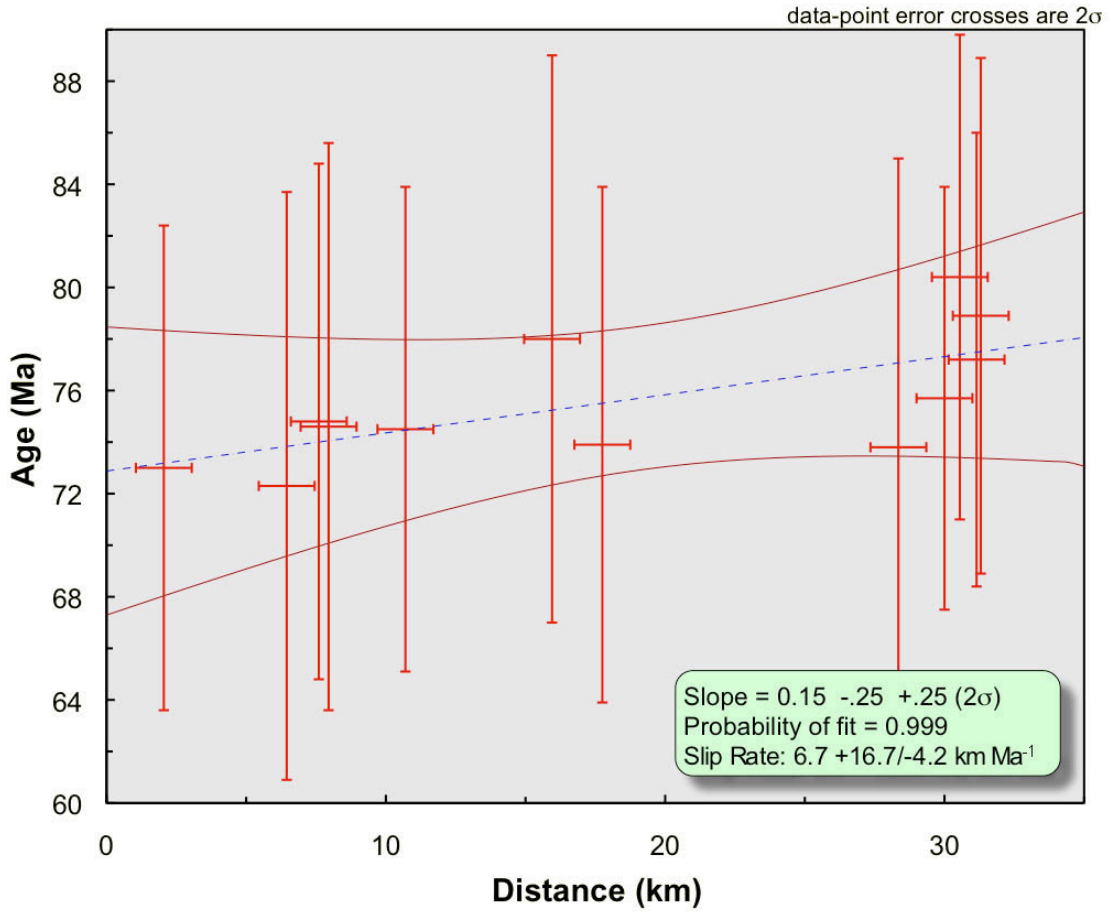

Figure 3.1: Age-distance relationship for AFT ages, linear regressions (dashed line) results in a slip rate of 6.7 +16.7/-4.2 km Ma^{-1} to the SW, red lines are error envelopes.

3.3. Zircon Fission Tracks

Further samples were collected along the coastline south of Charleston to fill some gaps in the profile across the core complex in 2009 (Figure 1.02). Samples PCC08-2, PCC08-10, PCC09-3 and PCC09-4 did not yield enough zircon grains, resulting in large errors. Thus they are disregarded for further consideration. Several of the remaining samples fail the χ^2-test (Table 3.2), suggesting a bimodal distribution of the FT ages. The relevant Cretaceous ages and their respective errors were extracted from the bimodal distributions to retain a larger data set. Except for PCC08-3 the fractions of the grains with a Middle- to Late Cretaceous age are high (i.e. > 0.85) and the errors are comparable to those of the other samples. Consequently PCC08-3 is discarded while the extracted ages of PCC08-1, PCC08-4, PCC08-9 are accepted. Samples PCC06-15 and PCC06-16 were taken inland near the Lower Buller Gorge and show very young ages of 72 to 75 Ma. Seward & White (1992) already suspected ZFT to be partially annealed in this area. These ages are tentatively disregarded to reduce the wide scatter range. Yet, samples

PCC09-2 and PCC09-5 remain with ages of 76 Ma and 77 Ma respectively as they were taken from the coastline and there is no reason to exclude them for the time being. The resulting ages scatter in a range from 90 to 76 Ma with several older outliers. It is not possible to derive a reliable slip rate from the ZFT ages as they are to close to each other within their errors and the probability of fit for the linear regression is close to zero (Figure 3.2). However, the data still contain valuable information. Most of the samples show an age younger than 90 Ma. This is too young to be related to the primary core complex stage considering that the deformation was already active at 116.2 ± 5.9 Ma (age of ultramylonites at Morrisey Creek dated by Ring et al. 2006). A later thermal event must be responsible for reheating and resetting the ZFT ages. Yet, PCC08-1, PCC08-5, PCC08-9 and PCC08-13 show ZFT ages between 94 and 106 Ma, which are likely to be related to the primary core complex stage. The sample locations are randomly distributed along the coast and no spatial pattern of this retention of older ages can be inferred. Many of the other samples with solid ages contain single grains with similarly old ages, too. Thus the temperature during the post core complex thermal event just reached the partial annealing zone for zircons resetting the majority of the ZFT ages and obscuring possible spatial patterns reflecting the slip, but keeping few unaltered.

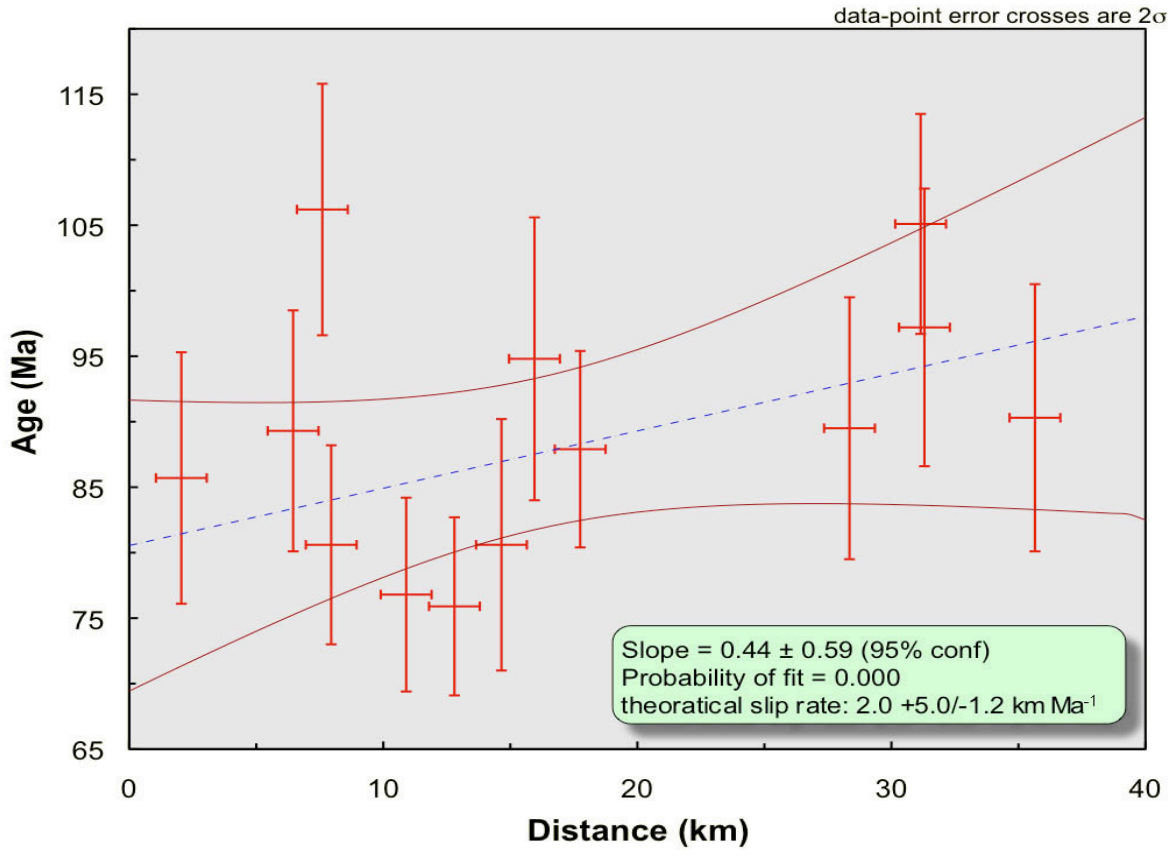

Figure 3.2: Age-distance relationship for ZFT ages, the linear regression (dashed line) is not convincing as the probability of fit is 0, a solid slip rate cannot be inferred due to the wide scatter and random distribution of ages, red lines are error envelopes.

Sample No.	Distance to Arbitrary Reference Point (km)	No. of Crystals	Age Dispersion (Pχ2)	Central Age (Ma)	Error (± 2 σ)	Extracted Relevant Age (Ma)	Error (± 2 σ)	Fraction
PCC06-15	39.95	20	27.5% <0.01%	84.1 (mixed age)	14.2	72.1	7.4	0.85
PCC06-16	39.8	20	<0.01% (97.1%)	75.3	8			
PCC08-1	31.15	20	29.0% <0.01%	125.5 (mixed age)	20.4	**105.1**	**8.4**	0.85
PCC08-2	30.55	6	<0.01% (82.2%)	87.3	16			
PCC08-3	30	20	21.2% (<0.01%)	122.7 (mixed age)	17.6	96.7	12	0.58
PCC08-4	17.75	20	16.3% (1.1%)	94.6 (mixed age)	12.2	**87.9**	**7.5**	0.96
PCC08-5	15.95	20	<0.01% (98.8%)	**94.8**	**10.8**			
PCC08-6	35.65	17	<0.01% (99.9%)	**90.3**	**10.2**			
PCC08-9	7.6	20	29.3% (<0.01%)	118.7 (mixed age)	20.4	**106.2**	**9.6**	0.91
PCC08-10	7.3	7	<0.01% (99.8%)	82.3	15.8			
PCC08-11	6.45	20	0.70% (55.7%)	**89.3**	**9.2**			
PCC08-12	2.05	20	<0.01% (99.6%)	**85.7**	**9.6**			
PCC08-13	31.3	20	0.88% (86.2%)	**97.2**	**10.6**			
PCC08-14	28.35	20	<0.01% (98.6%)	**89.5**	**10**			
PCC08-16	7.95	20	0.15% (77.6%)	**80.6**	**7.6**			
PCC09-2	12.8	20	0.08% (94.2%)	**75.9**	**6.8**			
PCC09-3	4.75	2	<0.01% (92.0%)	82	23.2			
PCC09-4	5.4	1	n/a	74.3	20.8			
PCC09-5	10.9	20	<0.01% (94.8%)	**76.8**	**7.4**			
PCC09-6	14.65	15	8.4% (23.6%)	**80.6**	**9.6**			

Table 3.2: Zircon fission track data, red samples are excluded from further consideration due to the poor quality of the obtained ages, relevant ages were extracted from samples with bimodal age distributions (printed in blue), all accepted ages in bold print.

3.4. Distribution of Zircon Fission Track Ages

Owing to the small amount of data and the fact that the ages are relatively close together with regard to their errors they do not show a clear bimodal distribution. Assuming that such a large scatter cannot relate to a single event, but that the range of ages is caused by the primary core complex cooling and a later thermal event, the population of obtained central ages can be

assigned to two reasonably independent ages (Figure 3.3): 101.9 ± 6.2 Ma (2 σ) representing the core complex stage and 83.3 ± 3.1 Ma (2 σ) representing the post core complex thermal event.

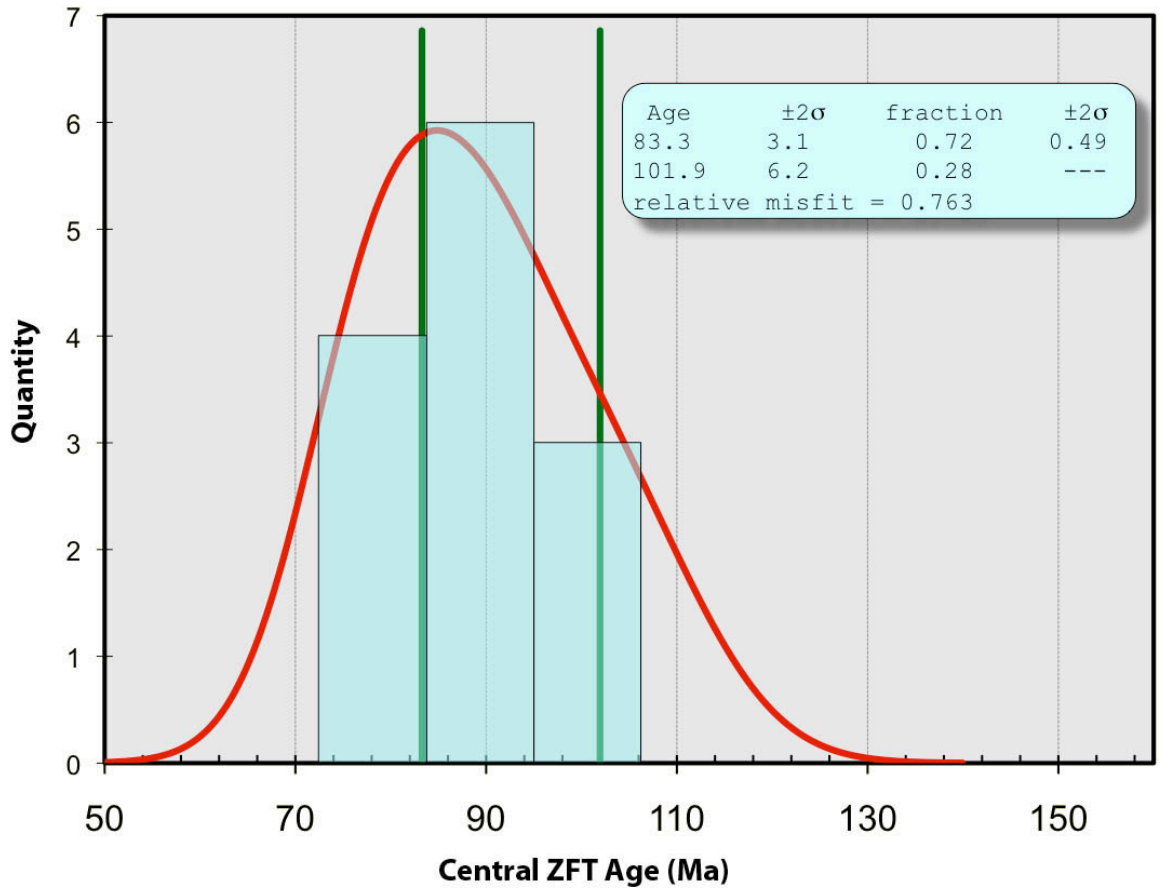

Figure 3.3: Although it is not clearly bimodal the distribution of the central fission track ages shows that they can be assigned to two reasonably independent ages: 83.3 ± 3.1 Ma and 101.9 ± 6.2 Ma, based on the 13 accepted central ages (see table 3.2).

Due to the low amount of accepted central ages the histogram does not illustrate the distribution very well as it only shows 3 intervals. Although it is not statistically meaningful, the tenfold dataset shows the bimodal peaks much better (Figure 3.4) and also reveals a younger third peak that may represent the partially reset ages caused by Tertiary annealing as suggested by Seward & White (1992). An attempt to unmix the ages of the single grains (see appendix for single grain ages) in order to obtain statistically sound results fails due to the wide scatter and the large errors of the single grain ages. Additionally, spatial patterns may obscure the peak ages.

However, as the three peak ages generated by the unmixing are reasonable with regard to the supposed tectonic history, the single grain ages were sorted by arbitrary intervals of 117 to 95 Ma for the core complex stage, 90 to 79 Ma for the subsequent thermal event and 77 to 60 Ma for the partially reset ages caused by Tertiary annealing, to check the age groups for potential spatial patterns in slip direction. The arbitrary intervals cover 76 % of all single grain ages, but

42 % of those not covered are older then 120 Ma and thus are not relevant for the 3 suggested events. Hence, 84 % of the single grain ages younger then 120 Ma are covered by the intervals. The older ages are mostly significantly older and therefore cause the mixed central ages of ~120 Ma despite their small fraction (see table 3.2).

The spatial distributions of the ages assigned to the Tertiary annealed group and the thermal event group show no meaningful pattern. Linear regressions of the age-distance relationships result in very shallow slopes translating to unreasonably high slip rates. The ages assigned to the core complex stage group represent 27 % of the single grains ages younger than 120 Ma and show a spatial pattern, which translates to a slip rate of 8.3 +12.2/- 6.3 km Ma^{-1} (2 σ) top-to-SW, i.e. a minimum slip rate of 2 km Ma^{-1} (Figure 3.5). As the errors of the single grain ages are very large the probability of fit is 1 and only very few, if any, grains account for each location. Consequently this slip rate is not statistically sound. Yet, the slip direction is consistent with the structural data and it is a reasonable slip rate with regard to the extent of the core complex of about 30 km parallel to extension, assuming that core complexes are only active for a couple of million years (e.g. Brichau et al. 2006; Thomson & Ring 2006; Brichau et al. 2007; Thomson et al. 2009).

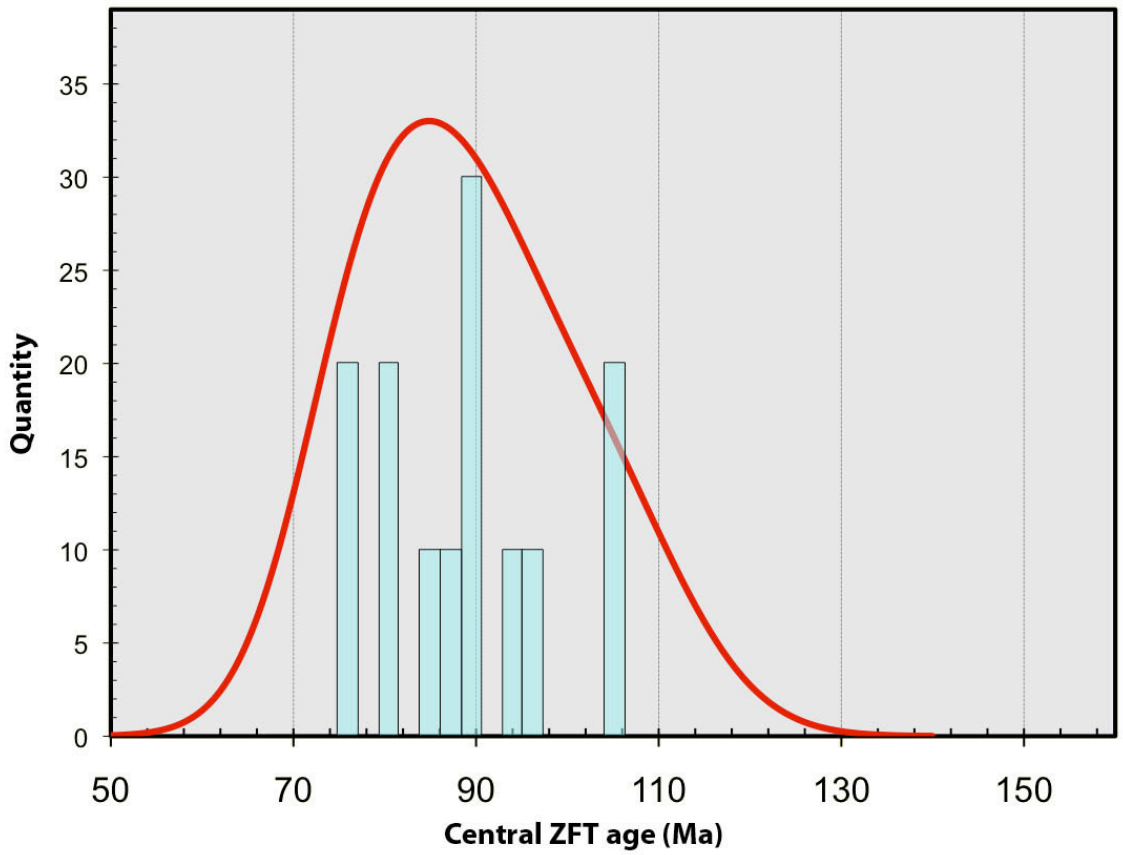

Figure 3.4: Although statistically not meaningful, the tenfold dataset reveals 3 peaks for the central ZFT ages, correlating well with the suggested thermal events.

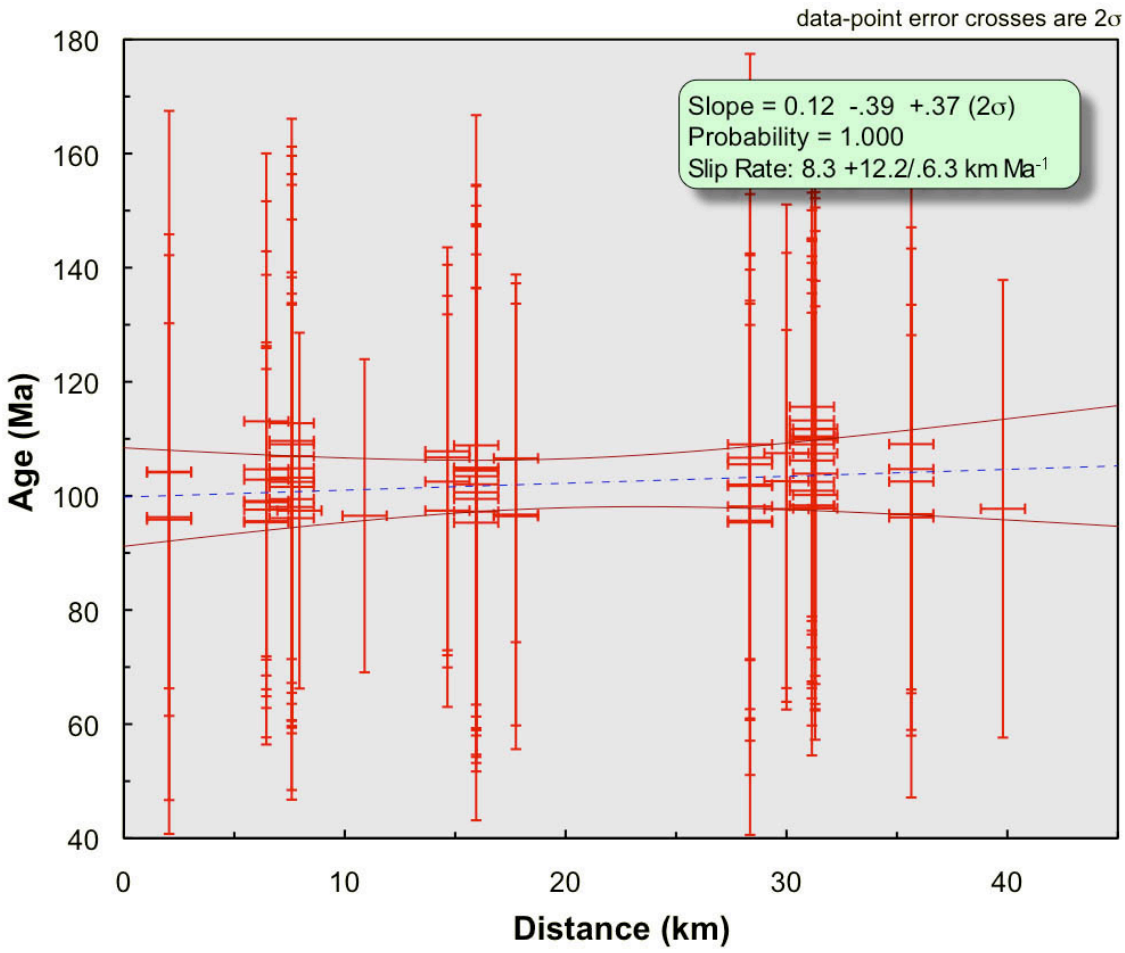

Figure 3.5: Age-distance relationship for sorted single grain ZFT ages belonging to the core complex stage, linear regressions (dashed line) results in a slip rate of 8.3 +12.2/-6.3 km Ma^{-1} to the SW, the probability of fit is 1 owing to the large error of the single grain ages, thus the statistical significance is questionable; red lines are error envelopes.

It is difficult to calculate cooling rates based on fission track data since this requires pairs of ZFT and AFT ages representing the same cooling event. Furthermore the data on hand do not allow determination of whether the younger peaks represent a continuous cooling event or separate ones, because of the large overlapping errors. Thus even a pair of solid ages from one location does not necessarily provide a meaningful cooling rate.

CHAPTER 4: DISCUSSION

4.1. Structural Geology

Many of the structural features described in chapter two are similar to those observed in metamorphic core complexes around the world (e.g. Coney 1980; Armstrong 1982; Brichau et al. 2007; Thomson et al. 2009) and are in agreement with the results of previous workers (cf. Shelley 1970a, 1972; Tulloch & Kimbrough 1989; Spell et al. 2000): the foliation of the basement rocks is folded, stretching lineations trend NE-SW to NNE-SSW, the metamorphic core is confined by two detachment systems and micro- and macroscopic structures in the lower plate suggest a top-to-NE and top-to-SW sense of shear away from the center of the core complex.

The microstructures are useful only to a limited extent in determining the metamorphic regime for the deformation; however, they do give a general idea. On the one hand crystal-plastic and brittle behavior of quartz and feldspar respectively, while on the other hand myrmekite with associated feldspar replacement by muscovite and sericite constrain the deformational conditions to the lower amphibolite facies. However, this is a lower constraint as these features only record the late stage of ductile deformation. Unroofing as a consequence of detachment faulting caused a steady decrease of metamorphic conditions. Thus deformation took place at higher conditions as well. Studies of White (1994) based on mineral assemblages provide higher temperatures and narrower boundaries for the metamorphic conditions of 600 ± 50°C, 4 ± 1 kbar, but refer to the metamorphism preceding the core complex stage. Therefore deformation must have started off at these conditions. This is in agreement with the findings in the field, as garnet remained brittle even in the ultramylonites indicating temperatures below 700 ºC (Ji & Martignole 1994; Storey & Prior 2005).

Although the observed structures in the field cannot help to put more precise constraints on the deformational regime, a clear asymmetry becomes apparent. The variable behavior of quartz and feldspar and the changing intensity of deformation along the coastline particularly indicate a differing control of the two detachment faults on the core complex development. While the granite to the north at Cape Foulwind shows relatively weak shearing top-to-NE and obviously brittle behavior of feldspar suggesting that the temperatures actually did not exceed lower amphibolite facies conditions, the CMG rocks south of Charleston record significantly higher temperatures and strain. Well-developed microstructures, the formation of ultramylonites and

ductile behavior of feldspar contrast with the findings to the North and indicate that upper amphibolite facies conditions were reached below the Pike Detachment. This is in agreement with a sillimanite isograde mapped in the Southern Paparoa Range (White 1994) suggesting that deeper levels of the crust were dragged out underneath the Pike Detachment.

Shear sense indicators showing a top-to-SW slip at Mount Kelvin add to this asymmetry. Although Mount Kelvin is located much closer to the Ohika Detachment than to the Pike Detachment, it is the southern fault that controlled the deformation of those rocks resulting in structures indicating a distinct top-to-SW sense of shear. This places the hinge of the bivergent detachment systems somewhere north of Mount Kelvin. Southwestern sense of shear at Charleston and northeastern sense of shear at Cape Foulwind support this idea. Therefore the hinge is much closer to the Ohika Detachment.

The asymmetry is a result of the dominant control of the Pike Detachment on the extension and the unroofing of the core complex while the northern detachment is rather a mere complexity. Previous workers proposed that the Ohika Detachment predates the Pike Detachment and that they were not contiguous or kinematically linked (Tulloch & Palmer 1990; Spell et al. 2000). Yet, this study suggests differently:

Due to its syntectonic age of 109.6 ± 1.7 Ma (Muir et al. 1994; Spell et al. 2000) the Buckland Granite plays an important role for the determination of the sequence of kinematic events. Compared to the adjacent rocks at Mount Kelvin the Buckland Granite shows barely pervasive deformation. However, few macroscopic structures show a distinct top-to-SW sense of shear. Therefore ductile deformation of the Pike Detachment cannot have lasted much longer than pluton emplacement. This is consistent with the age of 116.2 ± 5.9 Ma (Ring et al. 2006) for the ultramylonites at White Horse Creek. Thermal relaxation of the Buckland Granite may have caused the Pike Detachment to lock up, but not the Ohika Detachment as suggested by Spell et al. (2000). In fact the Ohika Detachment is a late structure that accommodated ongoing extension in the core complex.

The base of the Pororari Group in the Lower Buller Gorge contains the Stitts Tuff, which was dated as 101-102 Ma, and provides an upper constraint for the onset of extension on the Ohika Detachment at the surface (Muir et al. 1997). Compared to the age of the Buckland Granite, which was obviously influenced by ceasing ductile deformation on the southern normal fault, the Ohika Detachment must be significantly younger and cannot predate the Pike Detachment. Furthermore it should have easily imposed penetrating shearing on the Buckland Granite if it had been active before the Pike Detachment as the pluton must have been even easier to deform while it was still hot. Yet, this is not observed and the Buckland Granite shows deformation only

in the vicinity of the Ohika Detachment (Tulloch & Kimbrough 1989). Thus the Ohika Detachment is, as opposed to earlier suggestions (Tulloch & Palmer 1990; Spell et al. 2000), only a late complexity of the core complex and the Pike Detachment is the dominant feature accommodating most of the extension and controlling the unroofing.

It has to be pointed out that movement on the Pike Detachment may well have lasted longer in the upper crust without altering the Buckland Granite since the deformation becomes more localized the more brittle it gets. Furthermore the presently observed detachment may have splayed off according to the model of Lister & Davis (1989) after pluton emplacement. Thus the idea of Spell et al. (2000) that the movement on the Pike Detachment outlasted the Ohika Detachment is not necessarily invalidated – especially with regard to the southern Paparoa Range where a possible locking nature of the Buckland Granite would have had less or no influence.

This conciliates the new sequence of kinematic events with the idea of Spell et al. (2000) that the graben fill sediments of the Pororari Group currently adjacent to the Pike detachment were initially deposited in proximity to the unroofing Buckland Granite and displaced along the detachment afterwards as the breccia contains clasts derived from the pluton (Tulloch & Palmer 1990). The palynological Late Albian age of the Pororari Group (Raine 1984) confirms the results for the Ohika Detachment, but it cannot be used to infer that the Pike Detachment is younger than the Ohika Detachment as the base of the Pororari Group in the Southern Paparoa Range does not contain the Stitts Tuff. Therefore the palynological data of Raine (1984) show that some of the breccia is of Late Albian age, but as the base is truncated by faults and thus is not dated, initial sedimentation in the Southern Paparoa Range may well be older.

Another possible explanation for the Buckland Granite cobbles in the remote Southern Paparoa Range would be that the pluton was caught up in the deformation of the Pike Detachment and mylonitized similarly to the core complex model suggested by Lister & Davis (1989, see figure 1.01). This would have resulted in a larger lateral extent reaching further south, which could have been eroded subsequently. However, the Buckland Granite at Mount Kelvin does not show any mylonitization and the rare shear sense indicators in the granite contrast the strong deformation of the adjacent CMG rocks, which was obviously induced by the Pike Detachment. Furthermore Tulloch & Palmer (1990) did not report mylonitization of the granite cobbles in the southern Paparoa Range, but described the deformation as not intense. Hence, this possibility is unlikely.

4.2. Fission Tracks

Fission track analyses were undertaken to investigate possible spatial patterns of cooling histories of lower plate rocks. At least for ZFT the coastline was supposed to be promising to yield meaningful data related to the metamorphic core complex since Seward (1989) suggested that these rocks were not affected by Tertiary annealing. Yet, neither AFT nor ZFT central ages reflect the kinematic history of the core complex, as they are too young. For the apatites this is not surprising and confirms Seward's (1989) results. However, the results of the ZFT analysis somewhat disagree with earlier assumptions that the coastal strip from Cape Foulwind to Greymouth had been relatively stable and experienced continuously exhumation and cooling from Mid-Cretaceous to Early Eocene (Seward 1989). It has to be pointed out that Seward's (1989) samples were fewer (four samples at Cape Foulwind, only one sample south of Charleston) as the coastline was only a small part of the investigated area and that they contained only five to seven zircon grains each. Thus the more complex distribution of ZFT ages may not have been revealed in that study. Furthermore the core complex was only recognized in the same year (Tulloch & Kimbrough 1989) and this important aspect was probably not considered yet.

4.2.1. Apatite Fission Tracks

The AFT data show consistently late Cretaceous cooling with ages in the range of 80 to 72 Ma and a mean at ~75 Ma comparable to the results of Seward (1989), indicating tectonic uplift at that time. Additionally, the age-distance relationship reveals a slip rate of at least 2.5 km Ma^{-1} top-to-SW. A possible explanation would be a reactivation of the core complex movement plan, especially since the slip appears to have occurred mainly on the southwestern part of the Pike Detachment and not in the area that was supposedly locked up by the Buckland pluton. A second phase of extensional faulting at that time would also relate well to the continuing formation of basins and the deposition of the Paparoa Coal Measures further to the south (Laird 1994). Contemporaneous extrusion of alkaline basalts along the Cape Foulwind Fault Zone in this region (Laird 1994) would provide an additional heat source for local fission track annealing.

Increasing metamorphic mineral content upward through the stratigraphy of the Paparoa Basin supports the suggestion that the core complex was exhumed once again (Bassett et al. 2006). Yet, the sinistral offset of tens of kilometers, exceeding the core complex extent, along the Paparoa Tectonic Zone as suggested by Bassett et al. (2006) has to be rejected. The similarities

of the structures between the coastline rocks and the mountain range, in regard to their position along the extensional direction, clearly rule out a larger lateral offset along the fault zone. The lack of metamorphic grains in the lower parts of the basin is rather evidence for the core complex being entirely buried in considerable depth before renewed exhumation.

The obtained AFT central ages are too young to be directly related to the inception of seafloor spreading in the Tasman Sea at 84 Ma (Gaina et al. 1998). Nevertheless, the early rifting is the dominant tectonic event at that time. Considering half spreading rates of up to 20 km Ma^{-1} (Gaina et al. 1998) and the thermal disturbance of an evolving ocean ridge, the rifting has to be considered a likely trigger for some sort of tectonic and thermal activity causing the resetting of fission track ages even if the inception of seafloor spreading is not the immediate cause. The obtained AFT ages coincide well with the Late Maastrichtian to Paleocene extensional event suggested by Laird (1994). Formation of WNW-trending rift-parallel half grabens, like the Paparoa Basin, began earlier related to the inception of seafloor spreading at ~82 Ma and appears to have been continuous (Bassett et al. 2006 and references within). However the tectonic regime changed, possibly because of a shift of the spreading center in the north Tasman Sea to the west between 75 and 69 Ma (Weissel & Hayes 1977), resulting in a new extensional event with NNE-trending basins (Laird 1994). According to Laird (1994), Albian transform fault systems parallel to the modern coastline were reactivated as normal or transtensional faults. This transferred the opening of the New Caledonian Basin along the west coast of New Zealand via a rift corridor consisting of the West Coast Rift and the Taranaki Rift to link with the Tasman Sea spreading axis (Figure 4.1). The development of pull-apart basins between transtensional faults would be suitable to explain rejuvenation of normal faulting and southwestward slip in the Paparoa Range. Therefore the Late Maastrichtian extension suggested by Laird (1994) is likely to have caused anew exhumation of the core complex resulting in AFT ages recording this event. Conversely the AFT ages indicating a SW-directed slip in the Paparoa Range confirm that at least some basins developed as pull-apart basins at that time.

Yet, the renewed normal faulting is unlikely to be a reactivation of the detachment systems in the basement, since there is no evidence for further middle crust being dragged out to the surface at that time. Also the extent of the core complex would not allow for much additional crustal extension in that particular region. Thus deeper-seated extension must have been accommodated elsewhere and was possibly connected to this area by horizontal shear planes. Alternatively the normal faults were possibly steeply dipping and therefore did not require large amounts of crustal extension. In this case uplift, which has been suggested for the entire region by other workers (cf. Seward 1989; Laird 1994; Bassett et al. 2006), could have played a more important

role. The closure temperature of AFT is reached in ~4 km depth assuming a regular geothermal gradient of 30 ºC/km. The extrusion of alkaline basalts at that time (Laird 1994) may well have increased the geothermal gradient and therefore lowered the required depth from which the rocks would have had to be exhumed.

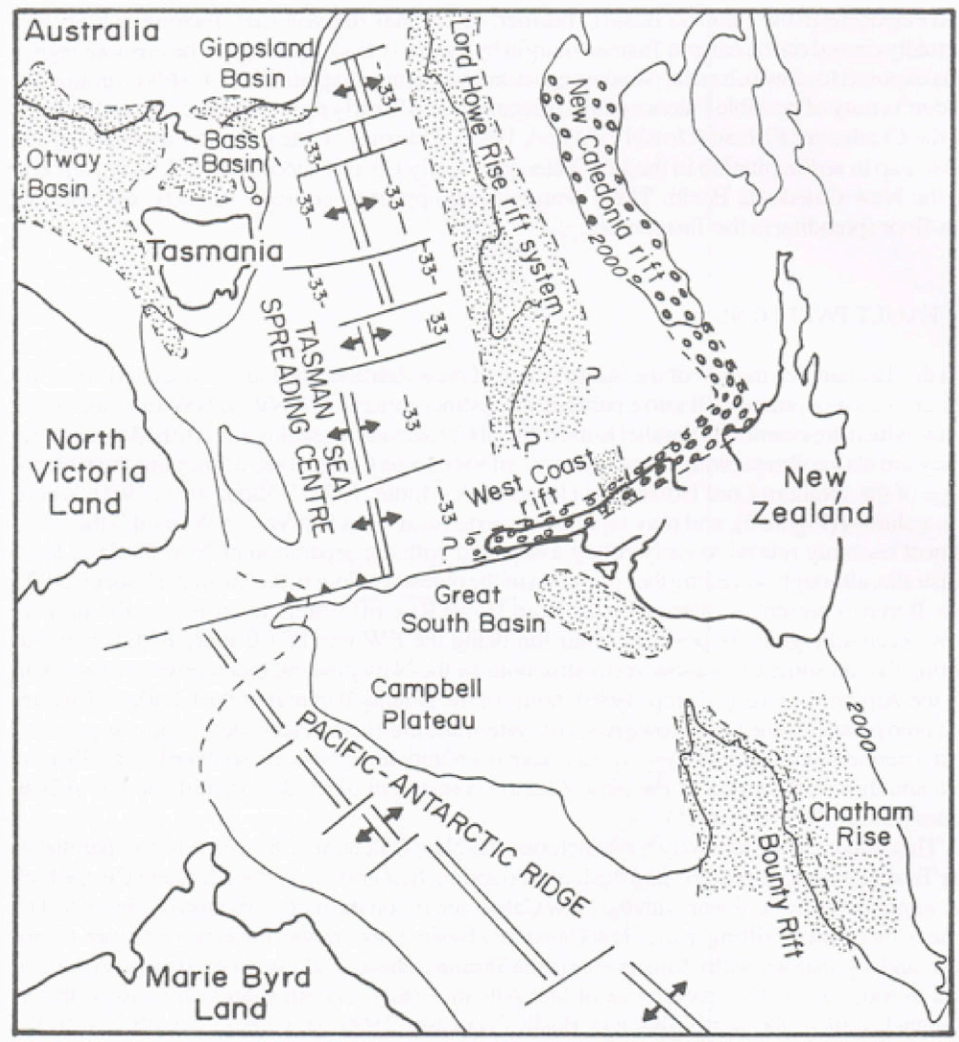

Figure 4.1: Sketch map of the southwest Pacific at ~72 Ma, showing the relationship of Cretaceous spreading centers and rift systems (Laird 1994). Stipple - Mid Cretaceous rift systems; circles – Late Maastrichtian rift systems.

By 50 Ma exhumation ceased and a regional peneplain developed across the West Coast of the South Island (Seward & White 1992). Subsequent Tertiary transgression deposited the Brunner Coal Measures, which rest directly on top of the basement rocks. AFT ages in the Central Paparoa Range reset by Tertiary burial and uplift have been reported by Seward & White (1992). They record the subsequent development of the Paparoa Range, which is related to the formation of the Brunner Coal Measure. Yet, that part of history is not covered by this thesis, since features reflecting this phase have not been investigated in this study.

4.2.2. Zircon Fission Track Ages

The ZFT data reveal new information about the thermal history of the basement rocks. The bimodal ages gained by tentative unmixing of 101.9 ± 6.2 Ma and 83.3 ± 3.1 Ma are not statistically sound due to the small amount of central ages. Yet, they coincide well with the late core complex stage on the one hand, during which the basement rocks cooled below ZFT closure temperature, and on the other hand with the inception of seafloor spreading, initial rifting and lamprophyric dikes in the Paparoa Range, indicating NNE-directed crustal extension. The latter three are a likely reason for major resetting of fission track ages affecting the entire Paparoa Range. Thus it is worthwhile to look at single grain ZFT ages (see appendix) and fractions that can be assigned to events proposed by others.

Previous workers suggested rapid cooling associated with the unroofing from ~110 to 90 Ma followed by continuous and slow cooling of the metamorphic core between 90 and 80 Ma (Seward 1989; Spell et al. 2000). K-Ar muscovite ages of 113 and 111 Ma from granite clasts in the Lower Buller Gorge (Tulloch & Palmer 1990) appear to support the idea that no major reheating occurred after the exhumation of the core complex and that the ages of the core rocks presently exposed are slightly younger due to ongoing exhumation in the Late Cretaceous.

Yet, the Ar-outgas temperature for muscovite can be as high as 500 ºC (Villa 1998). Therefore the K/Ar ratio in muscovites was not affected by later reheating, which only reached the required temperatures for the resetting of ZFT ages, i.e. ~250 ºC: Sample PCC08-12 from the breccia at Fox River mouth was deposited during the core complex stage and therefore must have had a fission track age similar to the K-Ar muscovite age of the granite cobbles in the Lower Buller Gorge. However, it shows a ZFT age of 85.7 Ma and an AFT age of 73.0 Ma. Thus the cooling history cannot be as simple as suggested by previous workers. Substantial burial and reheating must have caused resetting of fission track ages. The ZFT ages include older outliers that belong to the core complex stage indicating that presently exposed rocks already cooled below the ZFT closure temperature during core complex exhumation. However, the majority of the ZFT ages is overall too young, like the Fox River mouth sample, and scatters in too wide of a range to belong to the primary cooling, assuming that detachment faulting lasted only for a few million years and was already active at 116.2 ± 5.9 Ma (Ring et al. 2006). The present extent of only about 30 km in extension direction affirms the idea of a relatively short core complex stage for typical slip rates of a few kilometers per one million years. Assuming a slip rate of ~2 km Ma^{-1} and initial normal faulting at ~110 Ma, the core complex development would have ceased at ~95 Ma, while 2 km Ma^{-1} is not a particularly high slip rate for a detachment fault (cf. Brichau et al. 2006;

Thomson & Ring 2006; Brichau et al. 2007; Thomson et al. 2009). Also, 110 Ma is a very low estimate for the inception of extensional deformation, since the Buckland Granite at Mount Kelvin already records ceasing ductile deformation at 109.6 ± 1.7 Ma (Muir et al. 1994). As some of the ZFT ages fall in that time gap it can be inferred that presently exposed rocks were exhumed to shallower depths and cooled below closure temperature accordingly. The remaining majority of significantly younger ZFT ages must have been caused by later events.

It is unlikely that the ZFT ages, which are 20 to 30 million years younger, belong to the same cooling period. They are rather reset due to Tertiary partial annealing (Seward & White 1992), local heating by the alkaline basalts extruded along the Cape Foulwind Fault zone during the Late Maastrichtian extensional event (Laird 1994) or another event in the late Cretaceous. Since the Tertiary annealing did not affect the ZFT ages (Seward & White 1992), the alkaline basalts appear to be responsible for a minor accumulation of late Cretaceous ages at ~75 Ma. Thus the major peak between 90 and 80 Ma is probably caused by another independent event.

Assuming an average geothermal gradient of about 30 ºC/km and that the zircons already cooled below closure temperature during the primary unroofing, the rocks would have had to be exhumed from a depth of at least ~8 km for resetting ZFT ages after the core complex stage. This is not necessarily the required sediment overburden as the presently exposed rocks may well have been located several kilometers deep in the first place. However, precious metal mineralization has been reported from the Paparoa Metamorphic Core Complex and hydrothermal activity was associated with the detachment faults (Tulloch 1995). Iron oxide and magnesite mineralization observed on the coastline close to the Pike Detachment is probably linked to this hydrothermal activity. Therefore the low temperature range for magnesite formation suggests that the presently exposed rocks were actually exhumed to near surface depths. Hence, substantial sedimentation was required for sufficient burial depths after the core complex stage.

As the required exhumation coincides with the initial rifting in the Tasman Sea at ~84 Ma (Gaina et al. 1998) it is possibly related to it. Proximal inception of seafloor spreading may also have caused elevated geothermal gradients. For the East Coast in Australia the geothermal gradient during initial seafloor spreading is estimated to have reached up to 50 ºC/km (Moore et al. 1986). If this applies for New Zealand as well this lowers the required overburden for resetting ZFT ages of currently exposed rocks to ~5 km. After the core complex exhumation ceased, subsequent cooling may have caused a density increase and consequently the required subsidence so that the core complex was buried to significant depth.

Lamprophyric dikes in the Paparoa Range have been dated as 80 to 86 Ma (Adams & Nathan 1978; recalculated by Laird 1994) and are a likely source for additional heat at that time. Since these dikes occur in swarms, they did not only have a local influence, but they could have contributed to the major fission track resetting in the entire region. Thus it is reasonable to assume an elevated geothermal gradient and consequently a lower sediment overburden required for the resetting of fission track ages.

One could argue that the hydrothermal magnesite did not form during the core complex development, as it is quite possible that later thermal events caused hydrothermal activity as well. Yet, the hydrothermal magnesite and iron oxide alterations seem to be related to the core complex detachment system (cf. Figure 2.80). This suggests that the rocks were actually close to the surface after core complex exhumation, since the required temperatures for magnesite are low, and had to be buried afterwards for resetting. The lack of metamorphic grains in early deposits of the Paparoa Basin and the increase upwards through the stratigraphy (Bassett et al. 2006) confirm that the core complex was buried in significant depth before new exhumation. Thus it was probably both the increased geothermal gradient and substantial burial that caused the resetting of the ZFT at a depth of more than 5 km after the core complex stage.

The cooling below the temperature required for the retention of fission tracks was possibly caused by cessation of increased heating and by exhumation, since the event coincides well with an Early Campanian extensional event proposed by Laird (1994), which also initiated the formation of WNW-ESE-trending depositional environments like the Paparoa Basin. The ocean ridge-parallel alignment and the simultaneousness of events indicate that the inception of seafloor spreading caused the extension. Laird (1994) suggested that movement on faults first active in the Mid Cretaceous might have been rejuvenated in this event. This could have affected features of the Paparoa Metamorphic Core Complex as well. The subvertical set of dikes also trends WNW-ESE and indicates that the Paparoa Range was subject to NNE-directed extension, too. Yet, the associated ZFT grain ages do not show a slip rate even though this fraction is the biggest one. Furthermore the dikes are not deformed whatsoever. Hence, deformation – if present at all – was not pervasive but rather brittle and localized.

Due to the large errors the fission track data cannot show whether the transition of the two post core complex events was continuous or not. Yet, together with the results of the structural studies they show that Late Cretaceous cooling was not associated with the core complex development. The relatively young fission track ages do not record slowed exhumation and continuous cooling of the core complex, as suggested earlier (Spell et al. 2000), but show later burial and new tectonic activity on the New Zealand margin related to the opening of the Tasman

Sea (Laird 1994). On a large time scale this may well appear like slowed uplift and cooling if the structural evidence is left out of consideration. Since the fission track data is not useful to determine cooling rates for each single event, they only provide minimum temperatures for the different extensional phases. Therefore the results of Spell et al. (2000) are not invalidated, but more detail is added to the history of the development of the Paparoa Range.

CHAPTER 5: CONCLUSIONS

For over 20 years many scientists have worked on the Paparoa Metamorphic Core Complex and steadily increased the knowledge about it. This thesis confirms many previous results, adds some more details to what is already known and also opens up some new perspectives (Figure 5.1):

The Paparoa Metamorphic Core Complex developed in the Mid-Cretaceous due to continental extension conditioning the crust for the eventual breakup of the Gondwana Pacific Margin, which separated Australia and New Zealand (Tulloch & Kimbrough 1989; Laird & Bradshaw 2004). Most of the extension was accommodated on the SW-dipping Pike Detachment and was active at depth in the ductile crust as early as 116.2 ± 5.9 Ma (Ring et al. 2006) dragging out deeper crustal levels from underneath. Rocks along the present-day coast were deformed ductily and indicate that upper amphibolite facies conditions were reached in that process. Pervasive deformation on the Pike Detachment ended with the emplacement of the Buckland Granite at 109.6 ± 1.7 Ma (Muir et al. 1994), since the cooling pluton recorded ceasing ductile shearing to the SW.

The normal faulting eventually exhumed the lower plate of the core complex. This is shown by an increasingly brittle overprint of the deformed rocks and by cobbles derived from the Buckland Granite, which were deposited in grabens developing adjacent to the detachment faults (Tulloch & Palmer 1990). Hydrothermal magnesite suggests that presently exposed rocks were brought to near surface depths. Ongoing extension was accommodated on the NE-dipping Ohika Detachment and possibly on the southwestern end of the Pike Detachment transporting the debris from the Buckland Granite further to the south. The Stitts Tuff at the base of the Pororari Group deposits in the northern Paparoa Range shows that the Ohika Detachment was active on the surface since 101 Ma (Muir et al. 1997).

Fission track ages are obscured by later events and therefore cannot help to put solid constraints on the kinematics of the core complex. Yet, a fraction of ZFT ages of single grains provides a tentative slip rate of at least ~2 km Ma^{-1} top-to-SW. Although statistically not sound, this corresponds well with the geometry of the core complex: its size of 30 to 40 km in extensional direction with most of the extension accommodated on the southern detachment and a probable active phase of normal faulting in the range of ~115 to ~95 Ma require a southwestward displacement of the upper plate with a slip rate of that magnitude.

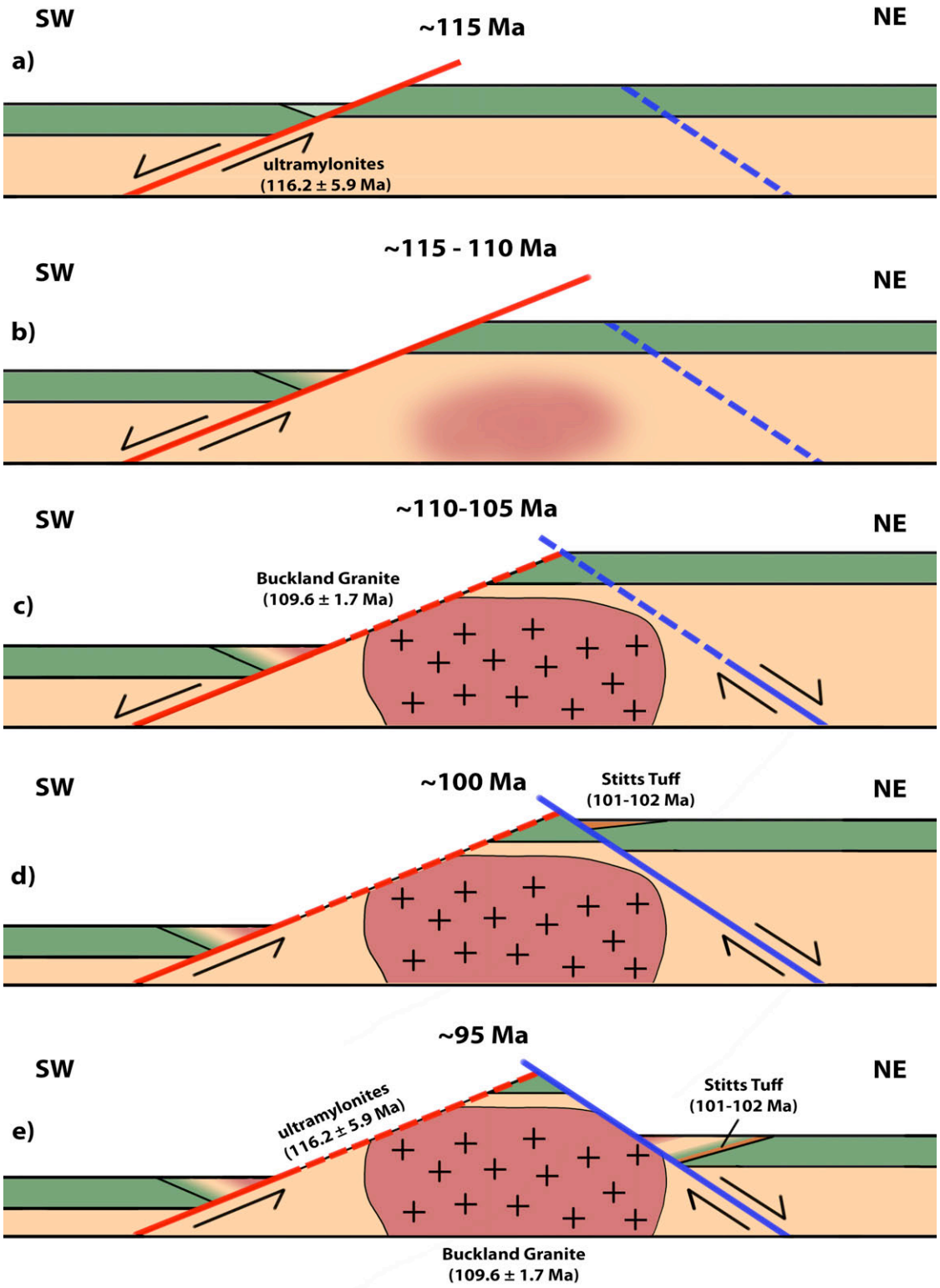

Figure 5.1: Schematic (not scaled) sequence of the core complex development: (a) normal faulting started on the Pike Detachment, ultramylonites record ductile deformation in the lower plate at 116.2 ± 5.9 Ma; (b) normal faulting on the Pike Detachment exhumed the core complex from about 115 to 110 Ma, exhumation and pressure relief probably generated magma; (c) pervasive deformation of the Pike Detachment ended with the emplacement of the Buckland Granite at 109.6 ± 5.9 Ma, the Ohika Detachment was developed as a separate fault to accommodate ongoing extension, displacement on the Pike Detachment probably continued further to the SW; (d) the Stitts Tuff marks the inception of the Ohika Detachment at the surface at 101-102 Ma, ongoing deformation on the southwestern Pike Detachment displaced the previously deposited debris of the exhumed core, the two detachments are different and independent faults; (e) core complex development is completed by ~95 Ma, the basement is unroofed and the covering upper plate has been eroded, the detachment faults show opposite sense of shear.

Instead of the core complex stage the majority of the fission track ages records the younger thermal history (Figure 5.2). After exhumation the core complex was buried to depths of at least ~5 km and reheated assuming a geothermal gradient comparable to the Australian East Coast of up to ~50 ºC/km (Moore et al. 1986). The increased heat flow and subsequent exhumation from ~90 to ~80 Ma was probably related to an Early Campanian extensional event (Laird 1994) induced by the inception of seafloor spreading in the Tasman Sea and caused the resetting of the majority of the ZFT ages. WNW-ESE trending lamprophyric dikes dated as 80 to 86 Ma (Adams & Nathan 1978; Laird 1994) indicate that the Paparoa Range was subject to this NNE-SSW-directed extension, but the detachment systems of the core complex were probably not rejuvenated, since the ZFT cooling ages do not show a trend which translates to a slip direction. Deposits in the adjacent Paparoa Basin lack metamorphic grain content (Bassett et al. 2006) and suggest that the core complex was not yet exhumed during that phase.

AFT ages record another phase of exhumation that occurred in the Late Maastrichtian by ~75 Ma and is also reported by other workers in the larger surrounding area (Seward 1989; Laird 1994; Bassett et al. 2006). The jump of the North Tasman Sea spreading center to the west (Weissel & Hayes 1977) changed the tectonic regime and possibly reactivated older structures as a transform fault system of the Tasman Sea ocean ridge parallel to the modern coast of New Zealand (Laird 1994). Pull-apart basins between transtensional faults are a likely reason for the rejuvenation of superficial normal faulting to the SW and exhumation of the Paparoa Metamorphic Core Complex, which is recorded by AFT ages and deposition of metamorphic grains in the younger strata of the adjacent Paparoa Basin (Bassett et al. 2006).

Figure 5.2 (next page): Schematic (not scaled) sequence of the post core complex development: (a) detachment faulting ceased by ~95 Ma. The core complex was entirely exhumed. A fraction of ZFT ages ranging up to ~115 Ma reflects the preceding unroofing; (b) subsequent deposition of Late Cretaceous sediments buried the currently exposed basement rocks to a depth of 5-8 km until ~85 Ma. Most fission track ages were reset, possibly reflecting the breakup unconformity; (c) the inception of seafloor spreading causes NNE directed extension and the development of WNW-ESE trending grabens like the Paparoa Basin. Lamprophyric dikes trending in the same direction indicate that the Paparoa Range was subject to the extension as well. Erosion and cooling led to the retention of the majority of ZFT ages from ~85 to 80 Ma; (d) a change of the tectonic regime caused transtensional faulting. Subsequent development of pull-apart basins and erosion brought the core complex up to shallow depths and caused the retention of AFT ages at that time.

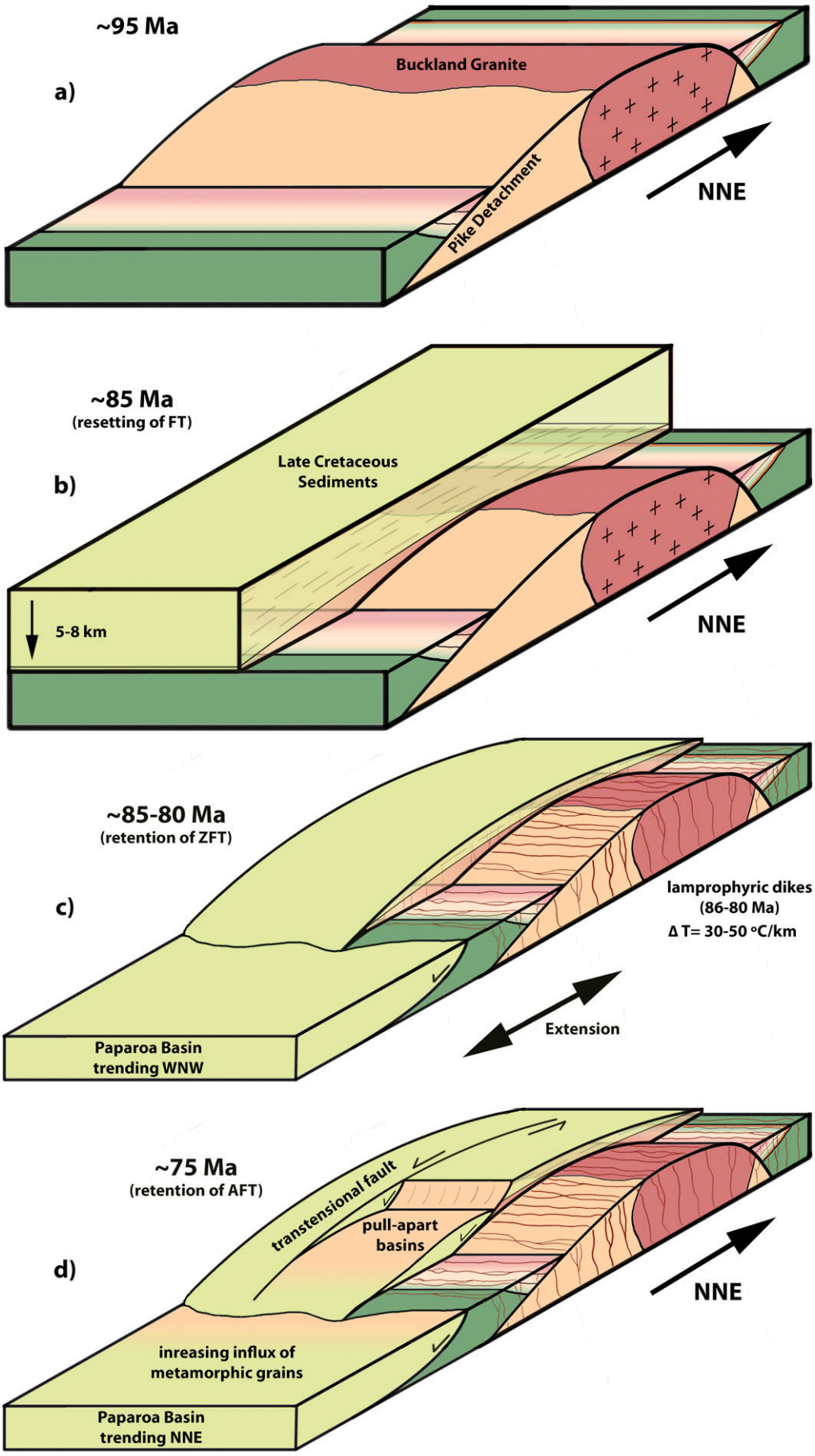
~95 Ma
a)
Buckland Granite
Pike Detachment
NNE
~85 Ma
(resetting of FT)
b)
Late Cretaceous
Sediments
5-8 km
NNE
~85-80 Ma
(retention of ZFT)
c)
lamprophyric dikes
(86-80 Ma)
Δ T= 30-50 °C/km
Extension
Paparoa Basin
trending WNW
~75 Ma
(retention of AFT)
transtensional fault
pull-apart
basins
d)
NNE
inreasing influx of
metamorphic grains
Paparoa Basin
trending NNE

FURTHER RESEARCH

During the fieldwork in the Paparoa Range further rock samples were taken for fission track dating. Since this study shows that multimodal distributions for ZFT ages have to be expected, a sufficient number of grains should be extracted from each sample to obtain statistically solid, and therefore better, results. This could help to confirm the sequence and also further constrain the timing of proposed events suggested in this thesis.

Depending on the intrusion depth of the Buckland Granite it cannot be ruled out that the pluton was sheared and dragged to the south in shallower depths when deformation was already more localized. A thorough investigation of granitic clasts in the lower parts of the Hawks Craig Breccia would help to determine whether the pluton was sheared and therefore had a much larger lateral extent or not, and would also help to narrow down the relative timing of emplacement with respect to the activity of the Pike Detachment. If the Buckland Granite was dragged to the south it should be strongly mylonitized. According structures in the Buckland Granite clasts of lowest parts of the breccia should reflect such deformation.

The stratigraphic ages of the sections of the Paparoa Basin, which record the increasing metamorphic grain content could be very helpful to constrain the timing of the renewed exhumation of the core complex.

APPENDIX: ZIRCON FISSION TRACK ANALYSIS DATA SHEETS

Sample Number	**PCC06 15**		Mineral	**Zircon**
Position (#)	64		Glass (U ppn	49.4
Area of Graticule Square	6.400E-07		Irradiation	UA-Z1
No. of Crystals	20		Analyst	SNT
Zeta Factor ± Error	121.1	3.5		
Rho d (% Relative Error)	5.071E+05	1.76		
N d	3246			

N s	N i	N g	Rho s	Rho i	Rho s / Rho i	U ppm	Age (Ma)	Age error	50% Age	"+95%"	"-95%"
101	48	30	5.260E+06	2.500E+06	2.1042	243.5	**64.29**	**11.48**	**65.16**	**27.28**	**19.93**
77	31	20	6.016E+06	2.422E+06	2.4839	235.9	**75.82**	**16.33**	**77.30**	**41.36**	**27.82**
68	26	15	7.083E+06	2.708E+06	2.6154	263.8	**79.81**	**18.60**	**81.62**	**48.55**	**31.39**
47	22	15	4.896E+06	2.292E+06	2.1364	223.2	**65.27**	**17.00**	**67.20**	**46.10**	**28.56**
105	44	20	8.203E+06	3.438E+06	2.3864	334.9	**72.86**	**13.31**	**73.88**	**31.95**	**23.01**
66	25	16	6.445E+06	2.441E+06	2.6400	237.8	**80.56**	**19.11**	**82.45**	**50.26**	**32.19**
80	33	16	7.813E+06	3.223E+06	2.4242	313.9	**74.01**	**15.51**	**75.38**	**38.91**	**26.52**
80	30	9	1.389E+07	5.208E+06	2.6667	507.4	**81.36**	**17.63**	**82.95**	**44.85**	**29.96**
176	31	20	1.375E+07	2.422E+06	5.6774	235.9	**172.01**	**34.01**	**174.50**	**84.54**	**57.07**
86	36	15	8.958E+06	3.750E+06	2.3889	365.3	**72.94**	**14.69**	**74.18**	**36.33**	**25.20**
158	60	20	1.234E+07	4.688E+06	2.6333	456.6	**80.35**	**12.48**	**81.14**	**28.67**	**21.71**
105	52	30	5.469E+06	2.708E+06	2.0192	263.8	**61.70**	**10.67**	**62.49**	**25.10**	**18.58**
64	27	18	5.556E+06	2.344E+06	2.3704	228.3	**72.37**	**16.79**	**74.03**	**43.62**	**28.44**
82	34	24	5.339E+06	2.214E+06	2.4118	215.6	**73.63**	**15.22**	**74.96**	**38.00**	**26.05**
49	25	8	9.570E+06	4.883E+06	1.9600	475.7	**59.90**	**14.86**	**61.53**	**39.36**	**25.17**
67	23	14	7.478E+06	2.567E+06	2.9130	250.1	**88.83**	**21.68**	**91.01**	**57.80**	**36.28**
82	32	28	4.576E+06	1.786E+06	2.5625	174.0	**78.21**	**16.51**	**79.66**	**41.57**	**28.16**
44	19	16	4.297E+06	1.855E+06	2.3158	180.8	**70.72**	**19.56**	**73.05**	**54.63**	**32.52**
241	40	30	1.255E+07	2.083E+06	6.0250	203.0	**182.39**	**31.75**	**184.40**	**75.72**	**53.77**
340	56	20	2.656E+07	4.375E+06	6.0714	426.2	**183.78**	**27.22**	**185.22**	**61.95**	**46.54**
**********	**********	**********	**********	**********	**********	**********	**********	**********	**********	**********	**********
2118	694	384	8.618E+06	2.824E+06	3.0519	275.1	**93.03**	**5.14**	**93.11**	**8.33**	**7.71**

Pooled Ratio	3.0519	±	0.1687	
Mean Ratio	2.9403	±	0.2927	
Pooled Age	93.03	±	5.14	1 S.E.
Mean Crystal Age	89.66	±	8.98	1 S.E.
Binomial Age	93.11	+	8.33	"+95%"
		-	7.71	"-95%"
Central Age	**84.14**	**±**	**7.05**	

Age Dispersion	**27.52**	%		
Chi-squared	**78.525**	with	19	degrees of freedom
P (Chi-Sq)	**0.00**	%		

Sample Number	**PCC06 16**		Mineral	**Zircon**
Position (#)	65		Glass (U ppm	49.4
Area of Graticule Square	6.400E-07		Irradiation	UA-Z1
No. of Crystals	20		Analyst	SNT
Zeta Factor ± Error	121.1	3.5		
Rho d (% Relative Error)	5.053E+05	1.76		
N d	3234			

N s	N i	N g	Rho s	Rho i	Rho s / Rho i	U ppm	Age (Ma)	Age error	50% Age	"+95%"	"-95%"
144	67	50	4.500E+06	2.094E+06	2.1493	204.7	**65.43**	**9.93**	**66.05**	**22.57**	**17.36**
104	42	14	1.161E+07	4.688E+06	2.4762	458.3	**75.32**	**14.00**	**76.40**	**33.81**	**24.15**
102	40	18	8.854E+06	3.472E+06	2.5500	339.5	**77.55**	**14.70**	**78.71**	**35.73**	**25.30**
80	39	20	6.250E+06	3.047E+06	2.0513	297.9	**62.46**	**12.38**	**63.51**	**30.34**	**21.36**
86	36	16	8.398E+06	3.516E+06	2.3889	343.7	**72.68**	**14.64**	**73.92**	**36.20**	**25.11**
70	36	15	7.292E+06	3.750E+06	1.9444	366.6	**59.22**	**12.31**	**60.34**	**30.59**	**21.20**
81	36	20	6.328E+06	2.813E+06	2.2500	275.0	**68.48**	**13.91**	**69.68**	**34.45**	**23.89**
127	54	30	6.615E+06	2.813E+06	2.3519	275.0	**71.56**	**11.87**	**72.38**	**27.71**	**20.64**
132	46	24	8.594E+06	2.995E+06	2.8696	292.8	**87.20**	**15.22**	**88.28**	**36.15**	**26.25**
103	39	30	5.365E+06	2.031E+06	2.6410	198.6	**80.30**	**15.34**	**81.51**	**37.40**	**26.35**
100	40	20	7.813E+06	3.125E+06	2.5000	305.5	**76.04**	**14.46**	**77.18**	**35.15**	**24.88**
143	53	24	9.310E+06	3.461E+06	2.6981	337.3	**82.03**	**13.48**	**82.92**	**31.44**	**23.36**
77	35	14	8.594E+06	3.906E+06	2.2000	381.9	**66.96**	**13.84**	**68.18**	**34.44**	**23.75**
86	33	18	7.465E+06	2.865E+06	2.6061	280.1	**79.25**	**16.45**	**80.66**	**41.18**	**28.07**
99	37	20	7.734E+06	2.891E+06	2.6757	282.6	**81.35**	**15.91**	**82.63**	**39.10**	**27.28**
108	49	21	8.036E+06	3.646E+06	2.2041	356.4	**67.09**	**11.78**	**67.96**	**27.88**	**20.44**
71	29	15	7.396E+06	3.021E+06	2.4483	295.3	**74.48**	**16.61**	**76.04**	**42.56**	**28.21**
178	60	30	9.271E+06	3.125E+06	2.9667	305.5	**90.13**	**13.80**	**90.97**	**31.60**	**23.93**
103	32	18	8.941E+06	2.778E+06	3.2188	271.6	**97.74**	**20.05**	**99.39**	**50.24**	**34.05**
65	29	16	6.348E+06	2.832E+06	2.2414	276.9	**68.21**	**15.41**	**69.71**	**39.57**	**26.22**
**********	**********	**********	**********	**********	**********	**********	**********	**********	**********	**********	**********
2059	832	433	7.430E+06	3.002E+06	2.4748	293.5	**75.28**	**4.01**	**75.33**	**6.31**	**5.88**

Pooled Ratio	2.4748	±	0.1317	
Mean Ratio	2.4716	±	0.0714	
Pooled Age	75.28	±	4.01	1 S.E.
Mean Crystal Age	75.18	±	2.18	1 S.E.
Binomial Age	75.33	+	6.31	"+95%"
		-	5.88	"-95%"
Central Age	**75.28**	**±**	**4.01**	

Age Dispersion	**0.00**	%		
Chi-squared	**9.158**	with	19	degrees of freedom
P (Chi-Sq)	**97.08**	%		

Sample Number	**PCC08 1**		Mineral	**Zircon**
Position (#)	67		Glass (U ppm	49.4
Area of Graticule Square	6.400E-07		Irradiation	UA-Z1
No. of Crystals	20		Analyst	SNT
Zeta Factor ± Error	121.1	3.5		
Rho d (% Relative Error)	5.017E+05	1.76		
N d	3211			

N s	N i	N g	Rho s	Rho i	Rho s / Rho i	U ppm	Age (Ma)	Age error	50% Age	"+95%"	"-95%"
154	46	15	1.604E+07	4.792E+06	3.3478	471.8	**100.91**	**17.30**	**102.07**	**40.96**	**29.74**
248	68	16	2.422E+07	6.641E+06	3.6471	653.9	**109.85**	**15.49**	**110.68**	**34.78**	**26.82**
188	50	20	1.469E+07	3.906E+06	3.7600	384.6	**113.22**	**18.42**	**114.37**	**43.01**	**31.68**
150	46	14	1.674E+07	5.134E+06	3.2609	505.5	**98.31**	**16.90**	**99.45**	**40.04**	**29.08**
89	24	10	1.391E+07	3.750E+06	3.7083	369.2	**111.68**	**25.96**	**114.07**	**68.28**	**43.36**
368	47	25	2.300E+07	2.938E+06	7.8298	289.2	**233.57**	**37.03**	**235.62**	**85.74**	**62.73**
184	37	20	1.438E+07	2.891E+06	4.9730	284.6	**149.33**	**27.38**	**151.20**	**66.38**	**46.40**
198	54	15	2.063E+07	5.625E+06	3.6667	553.9	**110.43**	**17.36**	**111.48**	**40.15**	**29.93**
141	40	15	1.469E+07	4.167E+06	3.5250	410.3	**106.20**	**19.36**	**107.59**	**46.74**	**33.12**
153	45	40	5.977E+06	1.758E+06	3.4000	173.1	**102.47**	**17.72**	**103.67**	**42.08**	**30.44**
181	45	24	1.178E+07	2.930E+06	4.0222	288.5	**121.04**	**20.58**	**122.38**	**48.69**	**35.24**
414	52	18	3.594E+07	4.514E+06	7.9615	444.5	**237.43**	**35.85**	**239.31**	**81.81**	**60.85**
244	81	36	1.059E+07	3.516E+06	3.0123	346.2	**90.87**	**12.05**	**91.49**	**26.59**	**20.98**
192	50	21	1.429E+07	3.720E+06	3.8400	366.3	**115.61**	**18.77**	**116.78**	**43.81**	**32.27**
88	27	8	1.719E+07	5.273E+06	3.2593	519.3	**98.26**	**21.87**	**100.22**	**56.42**	**36.84**
276	50	21	2.054E+07	3.720E+06	5.5200	366.3	**165.54**	**26.05**	**167.04**	**60.34**	**44.50**
369	32	15	3.844E+07	3.333E+06	11.5313	328.2	**341.11**	**63.91**	**345.21**	**154.63**	**105.88**
181	50	18	1.571E+07	4.340E+06	3.6200	427.4	**109.04**	**17.81**	**110.17**	**41.62**	**30.65**
341	121	36	1.480E+07	5.252E+06	2.8182	517.1	**85.05**	**9.45**	**85.45**	**19.92**	**16.44**
264	47	18	2.292E+07	4.080E+06	5.6170	401.7	**168.41**	**27.27**	**170.02**	**63.66**	**46.48**
**********	**********	**********	**********	**********	**********	**********	**********	**********	**********	**********	**********
4423	1012	405	1.706E+07	3.904E+06	4.3706	384.4	**131.42**	**6.39**	**131.48**	**9.26**	**8.68**

Pooled Ratio	4.3706	±	0.2124	
Mean Ratio	4.6160	±	0.4877	
Pooled Age	131.42	±	6.39	1 S.E.
Mean Crystal Age	138.72	±	14.80	1 S.E.
Binomial Age	131.48	+	9.26	"+95%"
		-	8.68	"-95%"
Central Age	**125.50**	**±**	**10.24**	

Age Dispersion	**29.03**	%		
Chi-squared	**110.801**	with	19	degrees of freedom
P (Chi-Sq)	**0.00**	%		

Sample Number	**PCC08 2**		Mineral	**Zircon**
Position (#)	68		Glass (U ppm	49.4
Area of Graticule Square	6.400E-07		Irradiation	UA-Z1
No. of Crystals	6		Analyst	SNT
Zeta Factor ± Error	121.1	3.5		
Rho d (% Relative Error)	4.999E+05	1.77		
N d	3199			

N s	N i	N g	Rho s	Rho i	Rho s / Rho i	U ppm	Age (Ma)	Age error	50% Age	"+95%"	"-95%"
44	18	18	3.819E+06	1.563E+06	2.4444	154.4	**73.57**	**20.73**	**76.07**	**58.56**	**34.32**
73	20	8	1.426E+07	3.906E+06	3.6500	386.0	**109.55**	**27.90**	**112.39**	**76.17**	**46.11**
111	37	15	1.156E+07	3.854E+06	3.0000	380.9	**90.17**	**17.39**	**91.53**	**42.62**	**29.74**
100	42	20	7.813E+06	3.281E+06	2.3810	324.3	**71.67**	**13.40**	**72.72**	**32.38**	**23.12**
133	47	25	8.313E+06	2.938E+06	2.8298	290.3	**85.09**	**14.72**	**86.12**	**34.88**	**25.41**
73	20	8	1.426E+07	3.906E+06	3.6500	386.0	**109.55**	**27.90**	**112.39**	**76.17**	**46.11**
**********	**********	**********	**********	**********	**********	**********	**********	**********	**********	**********	**********
534	184	94	8.876E+06	3.059E+06	2.9022	302.2	**87.25**	**8.02**	**87.52**	**16.09**	**13.78**

Pooled Ratio	2.9022	±	0.2669	
Mean Ratio	2.9925	±	0.2284	
Pooled Age	87.25	±	8.02	1 S.E.
Mean Crystal Age	89.95	±	6.91	1 S.E.
Binomial Age	87.52	+	16.09	"+95%"
		-	13.78	"-95%"
Central Age	**87.25**	**±**	**8.02**	

Age Dispersion	**0.00**	%		
Chi-squared	**3.250**	with	5	degrees of freedom
P (Chi-Sq)	**66.14**	**%**		

Sample Number	**PCC08 3**		Mineral	**Zircon**
Position (#)	69		Glass (U ppm	49.4
Area of Graticule Square	6.400E-07		Irradiation	UA-Z1
No. of Crystals	20		Analyst	SNT
Zeta Factor ± Error	121.1	3.5		
Rho d (% Relative Error)	4.981E+05	1.77		
N d	3188			

N s	N i	N g	Rho s	Rho i	Rho s / Rho i	U ppm	Age (Ma)	Age error	50% Age	"+95%"	"-95%"
126	30	16	1.230E+07	2.930E+06	4.2000	290.6	**125.44**	**25.84**	**127.50**	**65.06**	**43.54**
104	21	16	1.016E+07	2.051E+06	4.9524	203.4	**147.66**	**35.68**	**150.96**	**95.69**	**58.81**
173	36	21	1.287E+07	2.679E+06	4.8056	265.7	**143.33**	**26.70**	**145.20**	**65.08**	**45.24**
115	32	18	9.983E+06	2.778E+06	3.5938	275.5	**107.49**	**21.79**	**109.23**	**54.46**	**36.93**
222	40	30	1.156E+07	2.083E+06	5.5500	206.6	**165.25**	**28.93**	**167.11**	**69.16**	**49.08**
106	21	21	7.887E+06	1.563E+06	5.0476	155.0	**150.47**	**36.30**	**153.81**	**97.31**	**59.82**
223	36	21	1.659E+07	2.679E+06	6.1944	265.7	**184.17**	**33.66**	**186.41**	**81.55**	**56.77**
60	20	12	7.813E+06	2.604E+06	3.0000	258.3	**89.85**	**23.40**	**92.37**	**64.20**	**38.82**
200	42	18	1.736E+07	3.646E+06	4.7619	361.6	**142.04**	**24.59**	**143.64**	**58.55**	**41.90**
173	53	21	1.287E+07	3.943E+06	3.2642	391.1	**97.70**	**15.69**	**98.69**	**36.47**	**27.10**
142	34	15	1.479E+07	3.542E+06	4.1765	351.3	**124.75**	**24.19**	**126.55**	**59.68**	**40.99**
100	33	18	8.681E+06	2.865E+06	3.0303	284.1	**90.75**	**18.48**	**92.28**	**46.12**	**31.45**
123	39	24	8.008E+06	2.539E+06	3.1538	251.8	**94.42**	**17.65**	**95.74**	**42.86**	**30.21**
106	37	30	5.521E+06	1.927E+06	2.8649	191.1	**85.83**	**16.65**	**87.15**	**40.84**	**28.49**
223	34	20	1.742E+07	2.656E+06	6.5588	263.4	**194.84**	**36.47**	**197.32**	**89.02**	**61.31**
193	35	28	1.077E+07	1.953E+06	5.5143	193.7	**164.20**	**30.68**	**166.32**	**74.85**	**51.79**
96	33	21	7.143E+06	2.455E+06	2.9091	243.5	**87.15**	**17.83**	**88.64**	**44.55**	**30.38**
120	35	16	1.172E+07	3.418E+06	3.4286	339.0	**102.58**	**20.01**	**104.13**	**49.35**	**34.07**
237	82	50	7.406E+06	2.563E+06	2.8902	254.1	**86.59**	**11.47**	**87.18**	**25.30**	**19.99**
230	40	21	1.711E+07	2.976E+06	5.7500	295.2	**171.13**	**29.88**	**173.04**	**71.38**	**50.67**
**********	**********	**********	**********	**********	**********	**********	**********	**********	**********	**********	**********
3072	733	437	1.098E+07	2.621E+06	4.1910	259.9	**125.18**	**6.67**	**125.26**	**10.49**	**9.72**

Pooled Ratio	4.1910	±	0.2233	
Mean Ratio	4.2823	±	0.2726	
Pooled Age	125.18	±	6.67	1 S.E.
Mean Crystal Age	127.88	±	8.22	1 S.E.
Binomial Age	125.26	+	10.49	"+95%"
		-	9.72	"-95%"
Central Age	**122.66**	**±**	**8.81**	

Age Dispersion	**21.21**	%		
Chi-squared	**48.212**	with	19	degrees of freedom
P (Chi-Sq)	**0.02**	%		

Sample Number	**PCC08 4**		Mineral	**Zircon**
Position (#)	70		Glass (U ppm	49.4
Area of Graticule Square	6.400E-07		Irradiation	UA-Z1
No. of Crystals	20		Analyst	SNT
Zeta Factor ± Error	121.1	3.5		
Rho d (% Relative Error)	4.963E+05	1.77		
N d	3176			

N s	N i	N g	Rho s	Rho i	Rho s / Rho i	U ppm	Age (Ma)	Age error	50% Age	"+95%"	"-95%"
100	42	18	8.681E+06	3.646E+06	2.3810	362.9	**71.16**	**13.30**	**72.20**	**32.15**	**22.96**
88	32	12	1.146E+07	4.167E+06	2.7500	414.7	**82.11**	**17.18**	**83.60**	**43.19**	**29.25**
78	25	12	1.016E+07	3.255E+06	3.1200	324.0	**93.08**	**21.62**	**95.13**	**56.65**	**36.31**
130	46	20	1.016E+07	3.594E+06	2.8261	357.7	**84.37**	**14.75**	**85.42**	**35.06**	**25.45**
110	43	15	1.146E+07	4.479E+06	2.5581	445.8	**76.42**	**13.99**	**77.48**	**33.63**	**24.12**
89	30	12	1.159E+07	3.906E+06	2.9667	388.8	**88.54**	**18.93**	**90.19**	**48.04**	**32.10**
119	42	15	1.240E+07	4.375E+06	2.8333	435.5	**84.59**	**15.45**	**85.73**	**37.20**	**26.57**
93	30	9	1.615E+07	5.208E+06	3.1000	518.4	**92.49**	**19.67**	**94.19**	**49.87**	**33.33**
211	59	20	1.648E+07	4.609E+06	3.5763	458.8	**106.58**	**16.11**	**107.52**	**36.84**	**27.84**
54	18	9	9.375E+06	3.125E+06	3.0000	311.1	**89.53**	**24.55**	**92.32**	**68.98**	**40.48**
97	30	12	1.263E+07	3.906E+06	3.2333	388.8	**96.44**	**20.41**	**98.18**	**51.70**	**34.56**
120	37	15	1.250E+07	3.854E+06	3.2432	383.6	**96.73**	**18.48**	**98.14**	**45.24**	**31.57**
286	91	30	1.490E+07	4.740E+06	3.1429	471.8	**93.76**	**11.72**	**94.32**	**25.49**	**20.39**
109	42	16	1.064E+07	4.102E+06	2.5952	408.3	**77.52**	**14.32**	**78.61**	**34.55**	**24.67**
184	45	15	1.917E+07	4.688E+06	4.0889	466.6	**121.72**	**20.66**	**123.06**	**48.88**	**35.38**
247	35	16	2.412E+07	3.418E+06	7.0571	340.2	**208.66**	**38.34**	**211.19**	**92.98**	**64.44**
63	24	10	9.844E+06	3.750E+06	2.6250	373.3	**78.41**	**18.99**	**80.34**	**50.36**	**31.93**
141	46	24	9.180E+06	2.995E+06	3.0652	298.1	**91.46**	**15.84**	**92.56**	**37.57**	**27.28**
164	63	24	1.068E+07	4.102E+06	2.6032	408.3	**77.76**	**11.82**	**78.48**	**26.99**	**20.58**
134	30	18	1.163E+07	2.604E+06	4.4667	259.2	**132.85**	**27.21**	**134.98**	**68.43**	**45.80**
**********	**********	**********	**********	**********	**********	**********	**********	**********	**********	**********	**********
2617	810	322	1.270E+07	3.931E+06	3.2309	391.2	**96.37**	**5.07**	**96.43**	**7.90**	**7.35**

Pooled Ratio	3.2309	±	0.1699	
Mean Ratio	3.2616	±	0.2299	
Pooled Age	96.37	±	5.07	1 S.E.
Mean Crystal Age	97.28	±	6.91	1 S.E.
Binomial Age	96.43	+	7.90	"+95%"
		-	7.35	"-95%"
Central Age	**94.58**	**±**	**6.12**	

Age Dispersion	**16.30**	%		
Chi-squared	**35.790**	with	19	degrees of freedom
P (Chi-Sq)	**1.12**	%		

Sample Number	**PCC08 5**		Mineral	**Zircon**
Position (#)	71		Glass (U ppm	49.4
Area of Graticule Square	6.400E-07		Irradiation	UA-Z1
No. of Crystals	20		Analyst	SNT
Zeta Factor ± Error	121.1	3.5		
Rho d (% Relative Error)	4.945E+05	1.78		
N d	3165			

N s	N i	N g	Rho s	Rho i	Rho s / Rho i	U ppm	Age (Ma)	Age error	50% Age	"+95%"	"-95%"
110	30	20	8.594E+06	2.344E+06	3.6667	234.1	**108.86**	**22.72**	**110.73**	**57.40**	**38.39**
152	36	21	1.131E+07	2.679E+06	4.2222	267.6	**125.20**	**23.59**	**126.90**	**57.67**	**40.06**
93	29	16	9.082E+06	2.832E+06	3.2069	282.9	**95.31**	**20.53**	**97.10**	**52.31**	**34.71**
87	32	12	1.133E+07	4.167E+06	2.7188	416.2	**80.90**	**16.95**	**82.36**	**42.62**	**28.87**
109	31	12	1.419E+07	4.036E+06	3.5161	403.2	**104.43**	**21.55**	**106.19**	**54.18**	**36.48**
65	21	20	5.078E+06	1.641E+06	3.0952	163.9	**92.02**	**23.31**	**94.44**	**63.24**	**38.76**
89	34	12	1.159E+07	4.427E+06	2.6176	442.3	**77.90**	**15.93**	**79.26**	**39.69**	**27.22**
81	23	8	1.582E+07	4.492E+06	3.5217	448.8	**104.59**	**24.97**	**106.98**	**66.29**	**41.64**
217	70	20	1.695E+07	5.469E+06	3.1000	546.3	**92.16**	**13.05**	**92.88**	**29.29**	**22.67**
119	44	30	6.198E+06	2.292E+06	2.7045	228.9	**80.48**	**14.46**	**81.54**	**34.61**	**24.93**
109	36	24	7.096E+06	2.344E+06	3.0278	234.1	**90.03**	**17.57**	**91.41**	**43.26**	**30.02**
77	23	12	1.003E+07	2.995E+06	3.3478	299.2	**99.47**	**23.88**	**101.78**	**63.47**	**39.85**
108	33	25	6.750E+06	2.063E+06	3.2727	206.0	**97.25**	**19.62**	**98.84**	**48.90**	**33.36**
53	15	9	9.201E+06	2.604E+06	3.5333	260.2	**104.94**	**30.90**	**108.63**	**90.36**	**50.15**
83	33	30	4.323E+06	1.719E+06	2.5152	171.7	**74.87**	**15.62**	**76.23**	**39.14**	**26.67**
105	31	14	1.172E+07	3.460E+06	3.3871	345.6	**100.63**	**20.85**	**102.35**	**52.46**	**35.32**
101	29	16	9.863E+06	2.832E+06	3.4828	282.9	**103.45**	**22.07**	**105.32**	**56.15**	**37.26**
79	23	15	8.229E+06	2.396E+06	3.4348	239.3	**102.03**	**24.42**	**104.38**	**64.88**	**40.75**
84	29	12	1.094E+07	3.776E+06	2.8966	377.2	**86.15**	**18.78**	**87.83**	**47.97**	**31.82**
110	35	21	8.185E+06	2.604E+06	3.1429	260.2	**93.42**	**18.41**	**94.88**	**45.47**	**31.39**
**********	**********	**********	**********	**********	**********	**********	**********	**********	**********	**********	**********
2031	637	349	9.093E+06	2.852E+06	3.1884	284.9	**94.77**	**5.37**	**94.85**	**8.83**	**8.14**

Pooled Ratio	3.1884	±	0.1807	
Mean Ratio	3.2205	±	0.0917	
Pooled Age	94.77	±	5.37	1 S.E.
Mean Crystal Age	95.72	±	2.75	1 S.E.
Binomial Age	94.85	+	8.83	"+95%"
		-	8.14	"-95%"
Central Age	**94.77**	**±**	**5.37**	

Age Dispersion	**0.00**	%		
Chi-squared	**7.821**	with	19	degrees of freedom
P (Chi-Sq)	**98.84**	%		

Sample Number	**PCC08 6**		Mineral	**Zircon**
Position (#)	72		Glass (U ppm	49.4
Area of Graticule Square	6.400E-07		Irradiation	UA-Z1
No. of Crystals	17		Analyst	SNT
Zeta Factor ± Error	121.1	3.5		
Rho d (% Relative Error)	4.927E+05	1.78		
N d	3153			

N s	N i	N g	Rho s	Rho i	Rho s / Rho i	U ppm	Age (Ma)	Age error	50% Age	"+95%"	"-95%"
118	38	18	1.024E+07	3.299E+06	3.1053	330.7	**91.98**	**17.44**	**93.31**	**42.54**	**29.84**
170	52	20	1.328E+07	4.063E+06	3.2692	407.3	**96.80**	**15.69**	**97.80**	**36.55**	**27.08**
176	62	40	6.875E+06	2.422E+06	2.8387	242.8	**84.14**	**12.75**	**84.91**	**29.11**	**22.15**
138	39	18	1.198E+07	3.385E+06	3.5385	339.4	**104.71**	**19.32**	**106.11**	**46.82**	**33.01**
157	54	28	8.761E+06	3.013E+06	2.9074	302.1	**86.16**	**13.90**	**87.05**	**32.30**	**24.07**
117	36	16	1.143E+07	3.516E+06	3.2500	352.5	**96.24**	**18.63**	**97.68**	**45.79**	**31.79**
59	16	10	9.219E+06	2.500E+06	3.6875	250.7	**109.08**	**30.97**	**112.62**	**89.01**	**50.45**
147	48	18	1.276E+07	4.167E+06	3.0625	417.8	**90.72**	**15.39**	**91.76**	**36.30**	**26.55**
97	28	12	1.263E+07	3.646E+06	3.4643	365.5	**102.53**	**22.27**	**104.46**	**57.01**	**37.53**
74	26	8	1.445E+07	5.078E+06	2.8462	509.2	**84.35**	**19.44**	**86.21**	**50.67**	**32.77**
111	38	18	9.635E+06	3.299E+06	2.9211	330.7	**86.56**	**16.53**	**87.84**	**40.38**	**28.32**
109	36	8	2.129E+07	7.031E+06	3.0278	705.0	**89.70**	**17.51**	**91.08**	**43.10**	**29.91**
115	44	12	1.497E+07	5.729E+06	2.6136	574.4	**77.50**	**13.99**	**78.54**	**33.51**	**24.13**
102	35	14	1.138E+07	3.906E+06	2.9143	391.7	**86.36**	**17.17**	**87.75**	**42.49**	**29.32**
80	29	12	1.042E+07	3.776E+06	2.7586	378.6	**81.78**	**17.94**	**83.40**	**45.87**	**30.42**
128	41	30	6.667E+06	2.135E+06	3.1220	214.1	**92.47**	**16.89**	**93.70**	**40.73**	**28.97**
113	38	20	8.828E+06	2.969E+06	2.9737	297.7	**88.11**	**16.79**	**89.40**	**41.00**	**28.75**
**********	**********	**********	**********	**********	**********	**********	**********	**********	**********	**********	**********
2011	660	302	1.040E+07	3.415E+06	3.0470	342.4	**90.27**	**5.08**	**90.34**	**8.31**	**7.67**

Pooled Ratio	3.0470	±	0.1714	
Mean Ratio	3.0765	±	0.0698	
Pooled Age	90.27	±	5.08	1 S.E.
Mean Crystal Age	91.13	±	2.08	1 S.E.
Binomial Age	90.34	+	8.31	"+95%"
		-	7.67	"-95%"
Central Age	**90.27**	**±**	**5.08**	

Age Dispersion	**0.00**	%		
Chi-squared	**3.330**	with	16	degrees of freedom
P (Chi-Sq)	**99.97**	**%**		

Sample Number	**PCC08 9**		Mineral	**Zircon**
Position (#)	73		Glass (U ppm	49.4
Area of Graticule Square	6.400E-07		Irradiation	UA-Z1
No. of Crystals	20		Analyst	SNT
Zeta Factor ± Error	121.1	3.5		
Rho d (% Relative Error)	4.909E+05	1.78		
N d	3141			

N s	N i	N g	Rho s	Rho i	Rho s / Rho i	U ppm	Age (Ma)	Age error	50% Age	"+95%"	"-95%"
71	28	10	1.109E+07	4.375E+06	2.5357	440.3	**74.93**	**16.91**	**76.54**	**43.60**	**28.67**
123	37	15	1.281E+07	3.854E+06	3.3243	387.9	**98.06**	**18.69**	**99.48**	**45.71**	**31.90**
233	51	15	2.427E+07	5.313E+06	4.5686	534.6	**134.39**	**21.27**	**135.64**	**49.35**	**36.48**
332	24	28	1.853E+07	1.339E+06	13.8333	134.8	**398.60**	**85.33**	**404.81**	**215.32**	**138.80**
72	26	14	8.036E+06	2.902E+06	2.7692	292.0	**81.79**	**18.92**	**83.61**	**49.34**	**31.90**
88	23	12	1.146E+07	2.995E+06	3.8261	301.4	**112.74**	**26.68**	**115.23**	**70.70**	**44.42**
103	34	12	1.341E+07	4.427E+06	3.0294	445.5	**89.42**	**17.95**	**90.88**	**44.58**	**30.59**
93	25	9	1.615E+07	4.340E+06	3.7200	436.8	**109.64**	**24.98**	**111.89**	**65.19**	**41.80**
273	26	30	1.422E+07	1.354E+06	10.5000	136.3	**304.78**	**63.41**	**309.37**	**159.56**	**104.25**
305	54	30	1.589E+07	2.813E+06	5.6481	283.0	**165.74**	**25.11**	**167.11**	**57.53**	**42.95**
422	88	30	2.198E+07	4.583E+06	4.7955	461.2	**140.99**	**17.20**	**141.74**	**37.21**	**29.67**
62	18	8	1.211E+07	3.516E+06	3.4444	353.8	**101.58**	**27.41**	**104.58**	**76.76**	**45.07**
127	35	21	9.449E+06	2.604E+06	3.6286	262.1	**106.96**	**20.74**	**108.54**	**51.09**	**35.28**
138	33	15	1.438E+07	3.438E+06	4.1818	345.9	**123.12**	**24.22**	**124.95**	**60.05**	**40.99**
64	18	10	1.000E+07	2.813E+06	3.5556	283.0	**104.83**	**28.19**	**107.89**	**78.87**	**46.32**
154	44	24	1.003E+07	2.865E+06	3.5000	288.3	**103.20**	**17.99**	**104.43**	**42.83**	**30.87**
111	30	12	1.445E+07	3.906E+06	3.7000	393.1	**109.05**	**22.74**	**110.92**	**57.44**	**38.41**
118	35	12	1.536E+07	4.557E+06	3.3714	458.6	**99.44**	**19.44**	**100.95**	**47.95**	**33.10**
114	35	9	1.979E+07	6.076E+06	3.2571	611.5	**96.10**	**18.85**	**97.57**	**46.55**	**32.13**
205	59	30	1.068E+07	3.073E+06	3.4746	309.2	**102.46**	**15.53**	**103.37**	**35.54**	**26.86**
**********	**********	**********	**********	**********	**********	**********	**********	**********	**********	**********	**********
3208	723	346	1.449E+07	3.265E+06	4.4371	328.6	**130.56**	**6.97**	**130.64**	**10.96**	**10.15**

Pooled Ratio	4.4371	±	0.2368	
Mean Ratio	4.5332	±	0.6163	
Pooled Age	130.56	±	6.97	1 S.E.
Mean Crystal Age	133.36	±	18.29	1 S.E.
Binomial Age	130.64	+	10.96	"+95%"
		-	10.15	"-95%"
Central Age	**118.70**	**±**	**10.17**	

Age Dispersion	**29.28**	%		
Chi-squared	**84.930**	with	19	degrees of freedom
P (Chi-Sq)	**0.00**	%		

Sample Number	**PCC08 10**		Mineral	**Zircon**
Position (#)	74		Glass (U ppm	49.4
Area of Graticule Square	6.400E-07		Irradiation	UA-Z1
No. of Crystals	7		Analyst	SNT
Zeta Factor ± Error	121.1	3.5		
Rho d (% Relative Error)	4.890E+05	1.79		
N d	3130			

N s	N i	N g	Rho s	Rho i	Rho s / Rho i	U ppm	Age (Ma)	Age error	50% Age	"+95%"	"-95%"
123	47	30	6.406E+06	2.448E+06	2.6170	247.3	**77.03**	**13.47**	**77.99**	**31.95**	**23.27**
41	14	12	5.339E+06	1.823E+06	2.9286	184.2	**86.13**	**26.82**	**89.64**	**80.33**	**43.50**
52	19	28	2.902E+06	1.060E+06	2.7368	107.1	**80.53**	**21.76**	**83.00**	**60.53**	**36.06**
70	26	15	7.292E+06	2.708E+06	2.6923	273.6	**79.23**	**18.39**	**81.01**	**48.00**	**31.03**
22	7	12	2.865E+06	9.115E+05	3.1429	92.1	**92.39**	**40.22**	**99.85**	**153.03**	**61.57**
77	27	25	4.813E+06	1.688E+06	2.8519	170.5	**83.89**	**18.98**	**85.66**	**49.12**	**32.04**
82	27	30	4.271E+06	1.406E+06	3.0370	142.1	**89.30**	**20.05**	**91.14**	**51.81**	**33.81**
**********	**********	**********	**********	**********	**********	**********	**********	**********	**********	**********	**********
467	167	152	4.801E+06	1.717E+06	2.7964	173.4	**82.27**	**7.93**	**82.55**	**16.10**	**13.68**

Pooled Ratio	2.7964	±	0.2694	
Mean Ratio	2.8581	±	0.0721	
Pooled Age	82.27	±	7.93	1 S.E.
Mean Crystal Age	84.07	±	2.13	1 S.E.
Binomial Age	82.55	+	16.10	"+95%"
		-	13.68	"-95%"
Central Age	**82.27**	**±**	**7.93**	

Age Dispersion	**0.00**	%		
Chi-squared	**0.424**	with	6	degrees of freedom
P (Chi-Sq)	**99.86**	**%**		

Sample Number	**PCC08 11**		Mineral	**Zircon**
Position (#)	75		Glass (U ppm	49.4
Area of Graticule Square	6.400E-07		Irradiation	UA-Z1
No. of Crystals	20		Analyst	SNT
Zeta Factor ± Error	121.1	3.5		
Rho d (% Relative Error)	4.872E+05	1.79		
N d	3118			

N s	N i	N g	Rho s	Rho i	Rho s / Rho i	U ppm	Age (Ma)	Age error	50% Age	"+95%"	"-95%"
59	26	20	4.609E+06	2.031E+06	2.2692	206.0	**66.60**	**15.84**	**68.21**	**41.50**	**26.81**
108	46	20	8.438E+06	3.594E+06	2.3478	364.4	**68.89**	**12.35**	**69.82**	**29.47**	**21.38**
149	60	24	9.701E+06	3.906E+06	2.4833	396.1	**72.85**	**11.41**	**73.58**	**26.23**	**19.86**
95	31	15	9.896E+06	3.229E+06	3.0645	327.4	**89.78**	**18.82**	**91.37**	**47.46**	**31.94**
250	74	28	1.395E+07	4.129E+06	3.3784	418.7	**98.90**	**13.51**	**99.61**	**30.07**	**23.45**
142	35	12	1.849E+07	4.557E+06	4.0571	462.1	**118.59**	**22.74**	**120.27**	**55.89**	**38.60**
237	70	30	1.234E+07	3.646E+06	3.3857	369.7	**99.11**	**13.90**	**99.86**	**31.14**	**24.10**
104	35	10	1.625E+07	5.469E+06	2.9714	554.5	**87.07**	**17.27**	**88.46**	**42.72**	**29.48**
116	30	12	1.510E+07	3.906E+06	3.8667	396.1	**113.07**	**23.48**	**114.98**	**59.24**	**39.62**
190	74	20	1.484E+07	5.781E+06	2.5676	586.2	**75.30**	**10.63**	**75.90**	**23.79**	**18.55**
228	70	14	2.545E+07	7.813E+06	3.2571	792.2	**95.38**	**13.43**	**96.11**	**30.12**	**23.31**
88	32	21	6.548E+06	2.381E+06	2.7500	241.4	**80.62**	**16.87**	**82.07**	**42.41**	**28.72**
83	37	15	8.646E+06	3.854E+06	2.2432	390.8	**65.84**	**13.21**	**66.96**	**32.57**	**22.71**
173	53	21	1.287E+07	3.943E+06	3.2642	399.8	**95.58**	**15.35**	**96.55**	**35.68**	**26.52**
123	35	15	1.281E+07	3.646E+06	3.5143	369.7	**102.85**	**20.01**	**104.38**	**49.33**	**34.06**
132	41	21	9.821E+06	3.051E+06	3.2195	309.3	**94.28**	**17.16**	**95.53**	**41.36**	**29.42**
93	26	9	1.615E+07	4.514E+06	3.5769	457.7	**104.66**	**23.49**	**106.76**	**60.91**	**39.42**
120	39	20	9.375E+06	3.047E+06	3.0769	308.9	**90.14**	**16.89**	**91.41**	**41.06**	**28.94**
82	33	14	9.152E+06	3.683E+06	2.4848	373.4	**72.89**	**15.23**	**74.22**	**38.18**	**26.02**
100	30	12	1.302E+07	3.906E+06	3.3333	396.1	**97.59**	**20.58**	**99.33**	**52.11**	**34.83**
**********	**********	**********	**********	**********	**********	**********	**********	**********	**********	**********	**********
2672	877	353	1.183E+07	3.882E+06	3.0468	393.6	**89.26**	**4.61**	**89.31**	**7.07**	**6.60**

Pooled Ratio	3.0468	±	0.1574	
Mean Ratio	3.0556	±	0.1183	
Pooled Age	89.26	±	4.61	1 S.E.
Mean Crystal Age	89.52	±	3.49	1 S.E.
Binomial Age	89.31	+	7.07	"+95%"
		-	6.60	"-95%"
Central Age	**89.26**	**±**	**4.62**	

Age Dispersion	**0.70**	%		
Chi-squared	**17.489**	with	19	degrees of freedom
P (Chi-Sq)	**55.67**	%		

Sample Number	**PCC08 12**		Mineral	**Zircon**
Position (#)	76		Glass (U ppm	49.4
Area of Graticule Square	6.400E-07		Irradiation	UA-Z1
No. of Crystals	20		Analyst	SNT
Zeta Factor ± Error	121.1	3.5		
Rho d (% Relative Error)	4.854E+05	1.79		
N d	3107			

N s	N i	N g	Rho s	Rho i	Rho s / Rho i	U ppm	Age (Ma)	Age error	50% Age	"+95%"	"-95%"
76	26	16	7.422E+06	2.539E+06	2.9231	258.4	**85.34**	**19.61**	**87.20**	**51.07**	**33.03**
88	31	12	1.146E+07	4.036E+06	2.8387	410.8	**82.90**	**17.54**	**84.42**	**44.31**	**29.81**
106	37	24	6.901E+06	2.409E+06	2.8649	245.2	**83.66**	**16.23**	**84.94**	**39.82**	**27.78**
90	37	25	5.625E+06	2.313E+06	2.4324	235.3	**71.10**	**14.09**	**72.27**	**34.70**	**24.20**
148	49	32	7.227E+06	2.393E+06	3.0204	243.5	**88.17**	**14.84**	**89.16**	**34.91**	**25.61**
133	41	21	9.896E+06	3.051E+06	3.2439	310.5	**94.64**	**17.21**	**95.89**	**41.47**	**29.50**
79	30	15	8.229E+06	3.125E+06	2.6333	318.0	**76.94**	**16.71**	**78.45**	**42.51**	**28.39**
94	32	16	9.180E+06	3.125E+06	2.9375	318.0	**85.76**	**17.79**	**87.27**	**44.68**	**30.27**
111	36	18	9.635E+06	3.125E+06	3.0833	318.0	**89.99**	**17.53**	**91.37**	**43.14**	**29.94**
66	20	12	8.594E+06	2.604E+06	3.3000	265.0	**96.27**	**24.79**	**98.86**	**67.88**	**41.06**
50	14	12	6.510E+06	1.823E+06	3.5714	185.5	**104.12**	**31.68**	**108.04**	**94.36**	**51.16**
94	40	21	6.994E+06	2.976E+06	2.3500	302.9	**68.70**	**13.18**	**69.76**	**32.09**	**22.70**
110	35	15	1.146E+07	3.646E+06	3.1429	371.0	**91.72**	**18.07**	**93.15**	**44.65**	**30.82**
143	40	15	1.490E+07	4.167E+06	3.5750	424.0	**104.23**	**18.98**	**105.58**	**45.81**	**32.45**
118	40	20	9.219E+06	3.125E+06	2.9500	318.0	**86.13**	**16.03**	**87.33**	**38.84**	**27.50**
66	26	15	6.875E+06	2.708E+06	2.5385	275.6	**74.18**	**17.36**	**75.89**	**45.37**	**29.32**
59	24	12	7.682E+06	3.125E+06	2.4583	318.0	**71.85**	**17.57**	**73.67**	**46.65**	**29.56**
122	43	40	4.766E+06	1.680E+06	2.8372	170.9	**82.85**	**14.96**	**83.95**	**35.90**	**25.75**
138	42	30	7.188E+06	2.188E+06	3.2857	222.6	**95.85**	**17.20**	**97.08**	**41.30**	**29.51**
105	37	20	8.203E+06	2.891E+06	2.8378	294.2	**82.87**	**16.09**	**84.15**	**39.50**	**27.55**
**********	**********	**********	**********	**********	**********	**********	**********	**********	**********	**********	**********
1996	680	391	7.976E+06	2.717E+06	2.9353	276.6	**85.70**	**4.79**	**85.77**	**7.80**	**7.21**

Pooled Ratio	2.9353	±	0.1642	
Mean Ratio	2.9412	±	0.0785	
Pooled Age	85.70	±	4.79	1 S.E.
Mean Crystal Age	85.87	±	2.31	1 S.E.
Binomial Age	85.77	+	7.80	"+95%"
		-	7.21	"-95%"
Central Age	**85.70**	**±**	**4.79**	

Age Dispersion	**0.00**	%		
Chi-squared	**6.417**	with	19	degrees of freedom
P (Chi-Sq)	**99.67**	%		

Sample Number	**PCC08 13**		Mineral	**Zircon**
Position (#)	77		Glass (U ppm	49.4
Area of Graticule Square	6.400E-07		Irradiation	UA-Z1
No. of Crystals	20		Analyst	SNT
Zeta Factor ± Error	121.1	3.5		
Rho d (% Relative Error)	4.836E+05	1.80		
N d	3095			

N s	N i	N g	Rho s	Rho i	Rho s / Rho i	U ppm	Age (Ma)	Age error	50% Age	"+95%"	"-95%"
85	28	18	7.378E+06	2.431E+06	3.0357	248.3	**88.28**	**19.47**	**90.03**	**49.99**	**32.90**
84	26	12	1.094E+07	3.385E+06	3.2308	345.8	**93.92**	**21.32**	**95.87**	**55.41**	**35.84**
64	23	15	6.667E+06	2.396E+06	2.7826	244.7	**80.97**	**19.88**	**83.00**	**53.08**	**33.30**
110	36	18	9.549E+06	3.125E+06	3.0556	319.2	**88.86**	**17.33**	**90.22**	**42.65**	**29.60**
134	43	28	7.478E+06	2.400E+06	3.1163	245.1	**90.61**	**16.18**	**91.76**	**38.75**	**27.80**
93	26	21	6.920E+06	1.935E+06	3.5769	197.6	**103.90**	**23.32**	**105.98**	**60.47**	**39.14**
73	29	16	7.129E+06	2.832E+06	2.5172	289.3	**73.29**	**16.28**	**74.81**	**41.71**	**27.65**
129	34	12	1.680E+07	4.427E+06	3.7941	452.2	**110.15**	**21.56**	**111.80**	**53.32**	**36.61**
148	40	20	1.156E+07	3.125E+06	3.7000	319.2	**107.44**	**19.49**	**108.82**	**47.02**	**33.31**
74	24	30	3.854E+06	1.250E+06	3.0833	127.7	**89.66**	**21.28**	**91.72**	**56.22**	**35.66**
83	38	20	6.484E+06	2.969E+06	2.1842	303.3	**63.64**	**12.65**	**64.72**	**31.10**	**21.79**
110	29	16	1.074E+07	2.832E+06	3.7931	289.3	**110.12**	**23.29**	**112.06**	**59.15**	**39.26**
138	41	20	1.078E+07	3.203E+06	3.3659	327.2	**97.81**	**17.71**	**99.08**	**42.66**	**30.35**
126	40	20	9.844E+06	3.125E+06	3.1500	319.2	**91.58**	**16.91**	**92.83**	**40.93**	**28.98**
131	38	15	1.365E+07	3.958E+06	3.4474	404.3	**100.16**	**18.77**	**101.55**	**45.69**	**32.05**
154	40	21	1.146E+07	2.976E+06	3.8500	304.0	**111.76**	**20.20**	**113.17**	**48.68**	**34.49**
176	38	28	9.821E+06	2.121E+06	4.6316	216.6	**134.21**	**24.44**	**135.90**	**59.13**	**41.52**
97	30	12	1.263E+07	3.906E+06	3.2333	399.0	**93.99**	**19.89**	**95.68**	**50.40**	**33.68**
231	57	20	1.805E+07	4.453E+06	4.0526	454.9	**117.59**	**17.85**	**118.61**	**40.90**	**30.75**
224	77	40	8.750E+06	3.008E+06	2.9091	307.2	**84.63**	**11.54**	**85.24**	**25.65**	**20.10**
**********	**********	**********	**********	**********	**********	**********	**********	**********	**********	**********	**********
2464	737	402	9.577E+06	2.865E+06	3.3433	292.6	**97.16**	**5.25**	**97.23**	**8.34**	**7.73**

Pooled Ratio	3.3433	±	0.1807	
Mean Ratio	3.3255	±	0.1246	
Pooled Age	97.16	±	5.25	1 S.E.
Mean Crystal Age	96.65	±	3.65	1 S.E.
Binomial Age	97.23	+	8.34	"+95%"
		-	7.73	"-95%"
Central Age	**97.16**	**±**	**5.26**	

Age Dispersion	**0.88**	%		
Chi-squared	**15.937**	with	19	degrees of freedom
P (Chi-Sq)	**66.15**	%		

Sample Number	**PCC08 14**		Mineral	**Zircon**
Position (#)	78		Glass (U ppm	49.4
Area of Graticule Square	6.400E-07		Irradiation	UA-Z1
No. of Crystals	20		Analyst	SNT
Zeta Factor ± Error	121.1	3.5		
Rho d (% Relative Error)	4.818E+05	1.80		
N d	3084			

N s	N i	N g	Rho s	Rho i	Rho s / Rho i	U ppm	Age (Ma)	Age error	50% Age	"+95%"	"-95%"
99	37	30	5.156E+06	1.927E+06	2.6757	197.6	**77.59**	**15.18**	**78.81**	**37.31**	**26.02**
177	48	40	6.914E+06	1.875E+06	3.6875	192.2	**106.69**	**17.74**	**107.83**	**41.68**	**30.49**
49	13	20	3.828E+06	1.016E+06	3.7692	104.1	**109.03**	**34.22**	**113.37**	**103.87**	**54.89**
52	19	18	4.514E+06	1.649E+06	2.7368	169.1	**79.35**	**21.44**	**81.78**	**59.66**	**35.53**
75	26	20	5.859E+06	2.031E+06	2.8846	208.3	**83.61**	**19.24**	**85.43**	**50.13**	**32.42**
103	37	21	7.664E+06	2.753E+06	2.7838	282.3	**80.70**	**15.71**	**81.96**	**38.58**	**26.91**
39	12	24	2.539E+06	7.813E+05	3.2500	80.1	**94.12**	**31.24**	**98.42**	**97.48**	**49.97**
73	30	30	3.802E+06	1.563E+06	2.4333	160.2	**70.60**	**15.50**	**72.04**	**39.51**	**26.38**
152	56	40	5.938E+06	2.188E+06	2.7143	224.3	**78.70**	**12.59**	**79.51**	**29.16**	**21.85**
74	21	18	6.424E+06	1.823E+06	3.5238	186.9	**101.99**	**25.45**	**104.54**	**68.87**	**42.23**
102	32	28	5.692E+06	1.786E+06	3.1875	183.1	**92.32**	**18.97**	**93.89**	**47.55**	**32.22**
35	12	15	3.646E+06	1.260E+06	2.9167	128.2	**84.63**	**28.42**	**88.56**	**89.00**	**45.58**
116	33	30	6.042E+06	1.719E+06	3.5152	176.2	**101.74**	**20.37**	**103.35**	**50.70**	**34.58**
207	73	50	6.469E+06	2.281E+06	2.8356	233.9	**82.20**	**11.53**	**82.84**	**25.80**	**20.08**
186	51	40	7.266E+06	1.992E+06	3.6471	204.3	**105.53**	**17.06**	**106.59**	**39.77**	**29.38**
107	38	24	6.966E+06	2.474E+06	2.8158	253.7	**81.63**	**15.66**	**82.85**	**38.29**	**26.85**
139	41	32	6.787E+06	2.002E+06	3.3902	205.3	**98.15**	**17.76**	**99.42**	**42.77**	**30.43**
135	41	40	5.273E+06	1.602E+06	3.2927	164.2	**95.35**	**17.31**	**96.59**	**41.70**	**29.67**
109	33	40	4.258E+06	1.289E+06	3.3030	132.2	**95.65**	**19.28**	**97.20**	**48.05**	**32.77**
108	39	30	5.625E+06	2.031E+06	2.7692	208.3	**80.28**	**15.25**	**81.47**	**37.14**	**26.16**
**********	**********	**********	**********	**********	**********	**********	**********	**********	**********	**********	**********
2137	692	590	5.659E+06	1.833E+06	3.0882	187.9	**89.47**	**4.96**	**89.54**	**8.02**	**7.41**

Pooled Ratio	3.0882	±	0.1712	
Mean Ratio	3.1066	±	0.0886	
Pooled Age	89.47	±	4.96	1 S.E.
Mean Crystal Age	90.00	±	2.58	1 S.E.
Binomial Age	89.54	+	8.02	"+95%"
		-	7.41	"-95%"
Central Age	**89.47**	**±**	**4.96**	

Age Dispersion	**0.00**	%		
Chi-squared	**8.035**	with	19	degrees of freedom
P (Chi-Sq)	**98.63**	%		

Sample Number	**PCC08 16**		Mineral	**Zircon**
Position (#)	79		Glass (U ppm	49.4
Area of Graticule Square	6.400E-07		Irradiation	UA-Z1
No. of Crystals	20		Analyst	SNT
Zeta Factor ± Error	121.1	3.5		
Rho d (% Relative Error)	4.800E+05	1.80		
N d	3072			

N s	N i	N g	Rho s	Rho i	Rho s / Rho i	U ppm	Age (Ma)	Age error	50% Age	"+95%"	"-95%"
113	41	12	1.471E+07	5.339E+06	2.7561	549.4	**79.61**	**14.77**	**80.73**	**35.70**	**25.39**
225	70	20	1.758E+07	5.469E+06	3.2143	562.8	**92.75**	**13.08**	**93.46**	**29.34**	**22.71**
252	88	30	1.313E+07	4.583E+06	2.8636	471.7	**82.70**	**10.62**	**83.23**	**23.23**	**18.51**
179	53	16	1.748E+07	5.176E+06	3.3774	532.7	**97.42**	**15.59**	**98.39**	**36.21**	**26.91**
213	65	20	1.664E+07	5.078E+06	3.2769	522.6	**94.54**	**13.78**	**95.32**	**31.18**	**23.89**
270	92	30	1.406E+07	4.792E+06	2.9348	493.1	**84.74**	**10.63**	**85.25**	**23.11**	**18.51**
272	86	36	1.181E+07	3.733E+06	3.1628	384.2	**91.27**	**11.71**	**91.85**	**25.63**	**20.37**
95	30	10	1.484E+07	4.688E+06	3.1667	482.4	**91.39**	**19.39**	**93.05**	**49.15**	**32.84**
210	90	30	1.094E+07	4.688E+06	2.3333	482.4	**67.46**	**8.80**	**67.92**	**19.29**	**15.41**
196	79	40	7.656E+06	3.086E+06	2.4810	317.6	**71.71**	**9.86**	**72.25**	**21.92**	**17.23**
197	64	25	1.231E+07	4.000E+06	3.0781	411.7	**88.85**	**13.14**	**89.61**	**29.83**	**22.80**
188	82	20	1.469E+07	6.406E+06	2.2927	659.3	**66.29**	**9.06**	**66.80**	**20.08**	**15.85**
125	41	15	1.302E+07	4.271E+06	3.0488	439.5	**88.01**	**16.12**	**89.19**	**38.90**	**27.67**
189	70	15	1.969E+07	7.292E+06	2.7000	750.4	**78.00**	**11.23**	**78.64**	**25.28**	**19.56**
232	93	30	1.208E+07	4.844E+06	2.4946	498.5	**72.10**	**9.18**	**72.56**	**20.01**	**16.05**
139	46	12	1.810E+07	5.990E+06	3.0217	616.4	**87.23**	**15.13**	**88.28**	**35.92**	**26.07**
118	48	12	1.536E+07	6.250E+06	2.4583	643.2	**71.06**	**12.40**	**71.95**	**29.39**	**21.48**
142	52	12	1.849E+07	6.771E+06	2.7308	696.8	**78.88**	**13.07**	**79.76**	**30.55**	**22.63**
82	36	8	1.602E+07	7.031E+06	2.2778	723.6	**65.86**	**13.36**	**67.01**	**33.08**	**22.94**
234	89	20	1.828E+07	6.953E+06	2.6292	715.6	**75.97**	**9.81**	**76.47**	**21.46**	**17.12**
**********	**********	**********	**********	**********	**********	**********	**********	**********	**********	**********	**********
3671	1315	413	1.389E+07	4.975E+06	2.7916	512.0	**80.63**	**3.78**	**80.66**	**5.24**	**4.95**

Pooled Ratio	2.7916	±	0.1308	
Mean Ratio	2.8149	±	0.0780	
Pooled Age	80.63	±	3.78	1 S.E.
Mean Crystal Age	81.30	±	2.27	1 S.E.
Binomial Age	80.66	+	5.24	"+95%"
		-	4.95	"-95%"
Central Age	**80.63**	**±**	**3.78**	

Age Dispersion	**0.15**	%		
Chi-squared	**14.128**	with	19	degrees of freedom
P (Chi-Sq)	**77.62**	%		

Sample Number	**PCC09 02**		Mineral	**Zircon**
Position (#)	80		Glass (U ppm	49.4
Area of Graticule Square	6.400E-07		Irradiation	UA-Z1
No. of Crystals	20		Analyst	SNT
Zeta Factor ± Error	121.1	3.5		
Rho d (% Relative Error)	4.782E+05	1.81		
N d	3060			

N s	N i	N g	Rho s	Rho i	Rho s / Rho i	U ppm	Age (Ma)	Age error	50% Age	"+95%"	"-95%"
122	40	18	1.059E+07	3.472E+06	3.0500	358.7	**87.71**	**16.26**	**88.92**	**39.38**	**27.88**
113	44	15	1.177E+07	4.583E+06	2.5682	473.5	**73.94**	**13.38**	**74.93**	**32.06**	**23.08**
99	40	20	7.734E+06	3.125E+06	2.4750	322.8	**71.27**	**13.57**	**72.34**	**33.01**	**23.36**
147	64	24	9.570E+06	4.167E+06	2.2969	430.4	**66.17**	**10.16**	**66.81**	**23.21**	**17.73**
143	58	24	9.310E+06	3.776E+06	2.4655	390.1	**71.00**	**11.31**	**71.74**	**26.13**	**19.68**
191	70	30	9.948E+06	3.646E+06	2.7286	376.6	**78.53**	**11.29**	**79.17**	**25.42**	**19.67**
130	46	14	1.451E+07	5.134E+06	2.8261	530.4	**81.31**	**14.22**	**82.32**	**33.80**	**24.53**
462	182	49	1.473E+07	5.804E+06	2.5385	599.5	**73.09**	**6.86**	**73.32**	**13.83**	**11.83**
144	54	20	1.125E+07	4.219E+06	2.6667	435.8	**76.75**	**12.52**	**77.58**	**29.15**	**21.72**
128	50	18	1.111E+07	4.340E+06	2.5600	448.4	**73.70**	**12.55**	**74.58**	**29.53**	**21.73**
190	64	32	9.277E+06	3.125E+06	2.9688	322.8	**85.39**	**12.68**	**86.13**	**28.81**	**22.02**
223	97	30	1.161E+07	5.052E+06	2.2990	521.9	**66.23**	**8.37**	**66.65**	**18.17**	**14.64**
224	77	30	1.167E+07	4.010E+06	2.9091	414.3	**83.69**	**11.42**	**84.30**	**25.36**	**19.88**
234	100	30	1.219E+07	5.208E+06	2.3400	538.0	**67.40**	**8.37**	**67.82**	**18.12**	**14.65**
980	345	100	1.531E+07	5.391E+06	2.8406	556.9	**81.73**	**5.83**	**81.86**	**10.73**	**9.59**
152	59	21	1.131E+07	4.390E+06	2.5763	453.5	**74.17**	**11.65**	**74.91**	**26.83**	**20.26**
144	60	20	1.125E+07	4.688E+06	2.4000	484.2	**69.12**	**10.88**	**69.82**	**25.03**	**18.94**
308	102	36	1.337E+07	4.427E+06	3.0196	457.3	**86.85**	**10.35**	**87.32**	**22.23**	**18.01**
182	80	24	1.185E+07	5.208E+06	2.2750	538.0	**65.54**	**9.07**	**66.05**	**20.16**	**15.87**
234	94	30	1.219E+07	4.896E+06	2.4894	505.8	**71.68**	**9.09**	**72.14**	**19.78**	**15.88**
**********	**********	**********	**********	**********	**********	**********	**********	**********	**********	**********	**********
4550	1726	585	1.215E+07	4.610E+06	2.6362	476.2	**75.88**	**3.36**	**75.91**	**4.32**	**4.11**

Pooled Ratio	2.6362	±	0.1167	
Mean Ratio	2.6146	±	0.0558	
Pooled Age	75.88	±	3.36	1 S.E.
Mean Crystal Age	75.27	±	1.62	1 S.E.
Binomial Age	75.91	+	4.32	"+95%"
		-	4.11	"-95%"
Central Age	**75.88**	**±**	**3.36**	

Age Dispersion	**0.08**	%		
Chi-squared	**10.418**	with	19	degrees of freedom
P (Chi-Sq)	**94.19**	**%**		

Sample Number	**PCC09 03**		Mineral	**Zircon**
Position (#)	81		Glass (U ppm	49.4
Area of Graticule Square	6.400E-07		Irradiation	UA-Z1
No. of Crystals	2		Analyst	SNT
Zeta Factor ± Error	121.1	3.5		
Rho d (% Relative Error)	4.764E+05	1.81		
N d	3049			

N s	N i	N g	Rho s	Rho i	Rho s / Rho i	U ppm	Age (Ma)	Age error	50% Age	"+95%"	"-95%"
136	48	18	1.181E+07	4.167E+06	2.8333	432.1	**81.22**	**13.91**	**82.18**	**32.87**	**24.03**
70	24	8	1.367E+07	4.688E+06	2.9167	486.1	**83.59**	**19.98**	**85.56**	**52.85**	**33.51**
**********	**********	**********	**********	**********	**********	**********	**********	**********	**********	**********	**********
206	72	26	1.238E+07	4.327E+06	2.8611	448.7	**82.01**	**11.57**	**82.65**	**25.92**	**20.14**

Pooled Ratio	2.8611	±	0.4037	
Mean Ratio	2.8750	±	0.0417	
Pooled Age	82.01	±	11.57	1 S.E.
Mean Crystal Age	82.40	±	1.20	1 S.E.
Binomial Age	82.65	+	25.92	"+95%"
		-	20.14	" 95%"
Central Age	**82.01**	**±**	**11.57**	

Age Dispersion	**0.00**	%		
Chi-squared	**0.010**	with	1	degrees of freedom
P (Chi-Sq)	**92.04**	**%**		

Sample Number	**PCC09 04**		Mineral	**Zircon**
Position (#)	81		Glass (U ppm	49.4
Area of Graticule Square	6.400E-07		Irradiation	UA-Z1
No. of Crystals	1		Analyst	SNT
Zeta Factor ± Error	121.1	3.5	Count Date	2.3.2011
Rho d (% Relative Error)	4.746E+05	1.81	Locality	
N d	3037		Rock Type	

N s	N i	N g	Rho s	Rho i	Rho s / Rho i	U ppm	Age (Ma)	Age error	50% Age	"+95%"	"-95%"
191	74	25	1.194E+07	4.625E+06	2.5811	481.4	**73.75**	**10.41**	**74.34**	**23.29**	**18.15**
**********	**********	**********	**********	**********	**********	**********	**********	**********	**********	**********	**********
191	74	25	1.194E+07	4.625E+06	2.5811	481.4	**73.75**	**10.41**	**74.34**	**23.29**	**18.15**

Pooled Ratio	2.5811	±	0.3642		
Mean Ratio	2.5811	±	#DIV/0!		
Pooled Age	73.75	±	10.41	1 S.E.	
Mean Crystal Age	73.75	±	#DIV/0!	1 S.E.	
Binomial Age	74.34	+	23.29	"+95%"	
		-	18.15	"-95%"	
Central Age	**#DIV/0!**	**±**	**#DIV/0!**		

Age Dispersion	**#DIV/0!**	%		
Chi-squared	**0.000**	with	0	degrees of freedom
P (Chi-Sq)	**#NUM!**	%		

Sample Number	**PCC09 05**		Mineral	**Zircon**
Position (#)	83		Glass (U ppm	49.4
Area of Graticule Square	6.400E-07		Irradiation	UA-Z1
No. of Crystals	20		Analyst	SNT
Zeta Factor ± Error	121.1	3.5		
Rho d (% Relative Error)	4.728E+05	1.82		
N d	3026			

N s	N i	N g	Rho s	Rho i	Rho s / Rho i	U ppm	Age (Ma)	Age error	50% Age	"+95%"	"-95%"
53	19	12	6.901E+06	2.474E+06	2.7895	258.5	**79.37**	**21.39**	**81.78**	**59.50**	**35.44**
203	78	30	1.057E+07	4.063E+06	2.6026	424.5	**74.08**	**10.19**	**74.64**	**22.65**	**17.77**
76	32	12	9.896E+06	4.167E+06	2.3750	435.3	**67.64**	**14.44**	**68.94**	**36.42**	**24.66**
133	56	20	1.039E+07	4.375E+06	2.3750	457.1	**67.64**	**11.02**	**68.38**	**25.59**	**19.16**
118	56	14	1.317E+07	6.250E+06	2.1071	653.0	**60.04**	**9.96**	**60.74**	**23.18**	**17.36**
90	38	12	1.172E+07	4.948E+06	2.3684	517.0	**67.45**	**13.25**	**68.54**	**32.51**	**22.78**
125	47	16	1.221E+07	4.590E+06	2.6596	479.6	**75.69**	**13.21**	**76.63**	**31.33**	**22.82**
231	68	30	1.203E+07	3.542E+06	3.3971	370.0	**96.52**	**13.72**	**97.27**	**30.85**	**23.78**
304	113	40	1.188E+07	4.414E+06	2.6903	461.2	**76.56**	**8.83**	**76.95**	**18.78**	**15.39**
186	63	20	1.453E+07	4.922E+06	2.9524	514.3	**83.97**	**12.57**	**84.72**	**28.62**	**21.83**
202	68	21	1.503E+07	5.060E+06	2.9706	528.6	**84.49**	**12.19**	**85.18**	**27.49**	**21.19**
122	41	20	9.531E+06	3.203E+06	2.9756	334.7	**84.63**	**16.55**	**85.78**	**37.54**	**26.70**
133	44	15	1.385E+07	4.583E+06	3.0227	478.9	**85.96**	**15.23**	**87.04**	**36.39**	**26.21**
133	46	20	1.039E+07	3.594E+06	2.8913	375.5	**82.25**	**14.35**	**83.25**	**34.08**	**24.74**
153	57	20	1.195E+07	4.453E+06	2.6842	465.3	**76.39**	**12.14**	**77.17**	**28.05**	**21.07**
198	71	30	1.031E+07	3.698E+06	2.7887	386.4	**79.35**	**11.31**	**79.98**	**25.39**	**19.68**
242	91	30	1.260E+07	4.740E+06	2.6593	495.2	**75.69**	**9.66**	**76.17**	**21.07**	**16.85**
170	61	20	1.328E+07	4.766E+06	2.7869	497.9	**79.29**	**12.14**	**80.04**	**27.79**	**21.09**
94	40	14	1.049E+07	4.464E+06	2.3500	466.4	**66.93**	**12.84**	**67.96**	**31.27**	**22.12**
155	67	20	1.211E+07	5.234E+06	2.3134	546.9	**65.89**	**9.89**	**66.50**	**22.46**	**17.27**
**********	**********	**********	**********	**********	**********	**********	**********	**********	**********	**********	**********
3121	1156	416	1.172E+07	4.342E+06	2.6998	453.7	**76.83**	**3.73**	**76.87**	**5.36**	**5.05**

Pooled Ratio	2.6998	±	0.1309	
Mean Ratio	2.6880	±	0.0692	
Pooled Age	76.83	±	3.73	1 S.E.
Mean Crystal Age	76.50	±	1.98	1 S.E.
Binomial Age	76.87	+	5.36	"+95%"
		-	5.05	"-95%"
Central Age	**76.83**	**±**	**3.73**	

Age Dispersion	**0.00**	%		
Chi-squared	**10.198**	with	19	degrees of freedom
P (Chi-Sq)	**94.79**	%		

Sample Number	**PCC09 06**		Mineral	**Zircon**
Position (#)	84		Glass (U ppm	49.4
Area of Graticule Square	6.400E-07		Irradiation	UA-Z1
No. of Crystals	15		Analyst	SNT
Zeta Factor ± Error	121.1	3.5		
Rho d (% Relative Error)	4.710E+05	1.82		
N d	3014			

N s	N i	N g	Rho s	Rho i	Rho s / Rho i	U ppm	Age (Ma)	Age error	50% Age	"+95%"	"-95%"
85	34	12	1.107E+07	4.427E+06	2.5000	464.3	**70.91**	**14.59**	**72.16**	**36.40**	**24.95**
161	67	24	1.048E+07	4.362E+06	2.4030	457.5	**68.17**	**10.18**	**68.79**	**23.10**	**17.76**
96	39	15	1.000E+07	4.063E+06	2.4615	426.1	**69.82**	**13.47**	**70.91**	**32.90**	**23.17**
113	46	12	1.471E+07	5.990E+06	2.4565	628.2	**69.68**	**12.42**	**70.60**	**29.60**	**21.47**
101	43	12	1.315E+07	5.599E+06	2.3488	587.2	**66.64**	**12.35**	**67.60**	**29.74**	**21.32**
128	42	10	2.000E+07	6.563E+06	3.0476	688.3	**86.33**	**15.63**	**87.47**	**37.59**	**26.85**
183	48	20	1.430E+07	3.750E+06	3.8125	393.3	**107.82**	**17.87**	**108.96**	**41.97**	**30.70**
200	53	20	1.563E+07	4.141E+06	3.7736	434.3	**106.73**	**16.89**	**107.75**	**39.14**	**29.09**
150	60	20	1.172E+07	4.688E+06	2.5000	491.6	**70.91**	**11.10**	**71.61**	**25.51**	**19.31**
129	56	18	1.120E+07	4.861E+06	2.3036	509.8	**65.36**	**10.70**	**66.09**	**24.85**	**18.61**
77	30	8	1.504E+07	5.859E+06	2.5667	614.6	**72.79**	**15.86**	**74.23**	**40.39**	**26.97**
226	82	20	1.766E+07	6.406E+06	2.7561	671.9	**78.13**	**10.42**	**78.67**	**23.00**	**18.16**
77	27	6	2.005E+07	7.031E+06	2.8519	737.5	**80.82**	**18.29**	**82.53**	**47.34**	**30.88**
148	43	12	1.927E+07	5.599E+06	3.4419	587.2	**97.42**	**17.20**	**98.61**	**41.12**	**29.51**
192	53	16	1.875E+07	5.176E+06	3.6226	542.9	**102.50**	**16.28**	**103.49**	**37.77**	**28.07**
**********	**********	**********	**********	**********	**********	**********	**********	**********	**********	**********	**********
2066	723	225	1.435E+07	5.021E+06	2.8575	526.6	**80.98**	**4.46**	**81.05**	**7.17**	**6.64**

Pooled Ratio	2.8575	±	0.1574		
Mean Ratio	2.8564	±	0.1407		
Pooled Age	80.98	±	4.46	1 S.E.	
Mean Crystal Age	80.95	±	4.01	1 S.E.	
Binomial Age	81.05	+	7.17	"+95%"	
		-	6.64	"-95%"	
Central Age	**80.62**	**±**	**4.79**		

Age Dispersion	**8.40**	%		
Chi-squared	**17.383**	with	14	degrees of freedom
P (Chi-Sq)	**23.63**	%		

REFERENCES

Adams CJD 1975. Discovery of Precambrian rocks in New Zealand: Age relations of the Greenland Group and Constant Gneiss, West Coast, South Island. Earth and Planetary Science Letters 28: 98-104.

Adams CJD, Nathan S 1978. Cretaceous chronology of the Lower Buller Valley, South Island New Zealand. New Zealand Journal of Geology and Geophysics 21: 455-462.

Allmendinger R 2002. Stereonet. Version 6.3.3

Altenberger U, Hamm N, Kruhl J 1987. Movements and metamorphism north of the Insubric Line between Val Loana and Val d'Ossola (Italy). Jahrbuch der Geologischen Bundesanstalt (Austria) 130: 365-374.

Armstrong RL 1972. Low-Angle (Denudation) Faults, Hinterland of the Sevier Orogenic Belt, Eastern Nevada and Western Utah. Geological Society of America Bulletin 83: 1729-1754.

Armstrong RL 1982. Cordilleran Metamorphic Core Complexes -- From Arizona to Southern Canada. Annual Review of Earth and Planetary Sciences 10: 129-154.

Armstrong RL, Hansen E 1966. Cordilleran infrastructure in the eastern Great Basin. American Journal of Science 264: 112-127.

Ashworth JR 1986. Myrmekite replacing albite in prograde metamorphism. American Mineralogist 71: 895-899.

Bassett K, Ettmuller F, Bernet M 2006. Provenance analysis of the Paparoa and Brunner Coal Measures using integrated SEM-cathodoluminescence and optical microscopy. New Zealand Journal of Geology and Geophysics 49: 241 - 254.

Bernet M 2009. A field-based estimate of the zircon fission-track closure temperature. Chemical Geology 259: 181-189.

Berthé D, Choukroune P, Jegouzo P 1979. Orthogneiss, mylonite and non coaxial deformation of granites: the example of the South Armorican Shear Zone. Journal of Structural Geology 1: 31-42.

Bertotti G, Podladchikov Y, Daehler A 2000. Dynamic link between the level of ductile crustal flow and style of normal faulting of brittle crust. Tectonophysics 320: 195-218.

Bradshaw JD 1989. Cretaceous geotectonic patterns in the New Zealand Region. Tectonics 8: 803-820.

Bradshaw JD 1993. A review of the Median Tectonic Zone: Terrane boundaries and terrane amalgamation near the Median Tectonic Line. New Zealand Journal of Geology and Geophysics 36: 117 - 125.

Brandon MT, Roden-Tice MK, Garver JI 1998. Late Cenozoic exhumation of the Cascadia accretionary wedge in the Olympic Mountains, northwest Washington State. Geological Society of America Bulletin 110: 985-1009.

Brichau S, Ring U, Ketcham RA, Carter A, Stockli D, Brunel M 2006. Constraining the long-term evolution of the slip rate for a major extensional fault system in the central Aegean, Greece, using thermochronology. Earth and Planetary Science Letters 241: 293-306.

Brichau S, Ring U, Carter A, MoniÈ P, Bolhar R, Stockli D, Brunel M 2007. Extensional faulting on Tinos Island, Aegean Sea, Greece: How many detachments? Tectonics 26: TC4009.

Brown WL, Macaudière J 1986. Mechanical twinning of plagiclase in a deformed meta-anorthosite - the production of M-twinning. Contributions to Mineralogy and Petrology 92: 44-56.

Bruhn RL, Parry WT, Yonkee WA, Thompson T 1994. Fracturing and hydrothermal alteration in normal fault zones. Pure and Applied Geophysics 142: 609-644.

Bucher K, Frey M 2002. Petrogenesis of Metamorphic Rocks. 7th ed. Berlin Heidleberg New York, Springer-Verlag. 341 p.

Buck WR 1991. Modes of Continental Lithospheric Extension. J. Geophys. Res. 96: 20161-20178.

Carpenter MA, Salje EH 1994. Thermodynamics of nonconvergent cation ordering in minerals. American Mineralogist 79: 1084-1098.

Cesare B, Marchesi C, Connolly JAD 2002. Growth of myrmekite coronas by contact metamorphism of granitic mylonites in the aureole of Cima di Vila, Eastern Alps, Italy. Journal of Metamorphic Geology 20: 203-213.

Coney PJ 1974. Structural Analysis of the Snake Range "Décollement", East-Central Nevada. Geological Society of America Bulletin 85: 973-978.

Coney PJ 1980. Cordilleran metamorphic core complexes: An overview. In: Crittenden MD, Coney PJ, Davis GH ed. Cordilleran Metamorphic Core Complexes, Geological Society of America, Memoirs: 7-31.

Cooper RA 1975. Age of the Greenland and Waiuta Groups, South Island, New Zealand. New Zealand Journal of Geology and Geophysics 17: 955-962.

Cooper RA 1989. Early Paleozoic Terranes of New Zealand. Journal of the Royal Society of New Zealand 19: 73-112.

Crittenden MD 1980. Metamorphic core complexes of the North American Cordillera: Summary. In: Crittenden MD, Coney PJ, Davis GH ed. Cordilleran Metamorphic Core Complexes, Geological Society of America, Memoirs: 485-490.

Davis GA, Lister GS 1988. Detachment faulting in continental extension: perspectives from southwestern U.S. Cordillera. Geological Society of America Special Paper 218: 133-159.

Davis GA, Lister GS, Reynolds SJ 1983. Interpretation of Cordilleran core complexes as evolving crustal shear zones in an extending orogen. Geological Society of America Abstracts 12: 311.

Davis GA, Lister GS, Reynolds SJ 1986. Structural evolution of the Whipple and South mountains shear zones, southwestern United States. Geology 14: 7-10.

Davis GH 1980. Structural characteristics of metamorphic core complexes, southern Arizona. In: Crittenden MD, Coney PJ, Davis GH ed. Cordilleran Metamorphic Core Complexes, Geological Society of America, Memoirs: 35-77.

Davis GH 1987. A shear-zone model for the structural evolution of metamorphic core complexes in southeastern Arizona. Geological Society, London, Special Publications 28: 247-266.

Davis GH, Coney PJ 1979. Geologic development of the Cordilleran metamorphic core complexes. Geology 7: 120-124.

Ece ÖI, Osamu M, Çoban F 2005. Genesis of hydrothermal stockwork-type magnesite deposits associated with ophiolite complexes in the Kutahya-Eskisehir region, Turkey. Neues Jahrbuch für Mineralogie - Abhandlungen 181: 191-205.

Eisbacher GH 1970. Deformation Mechanics of Mylonitic Rocks and Fractured Granites in Cobequid Mountains, Nova Scotia, Canada. Geological Society of America Bulletin 81: 2009-2020.

Eskola PE 1949. The Problem of mantled gneiss domes. Quarterly Journal of the Geological Society 104: 461-476.

Espejo IS, Lopez-Gamundi OR 1994. Source versus depositional controls on sandstone composition in a foreland basin; the El Imperial Formation (Mid Carboniferous-Lower Permian), San Rafael Basin, western Argentina. Journal of Sedimentary Research 64: 8-16.

Fallick AE, Ilich M, Russell MJ 1991. A stable isotope study of the magnesite deposits associated with the alpine-type ultramafic rocks of Yugoslavia. Economic Geology 86: 847-861.

Fitz Gerald JD, McLaren AC 1982. The Microstructures of Microcline from Some Granitic Rocks and Pegmatites. Contributions to Mineralogy and Petrology 80: 219-229.

Gaina C, Müller DR, Royer J-Y, Stock J, Hardebeck J, Symonds P 1998. The tectonic history of the Tasman Sea: A puzzle with 13 pieces. Journal of Geophysical Research - Solid Earth 103: 12413-12433.

Galbraith RF, Laslett GM 1993. Statistical models for mixed fission track ages. Nuclear Tracks and Radiation Measurements 21: 459-470.

Gibson GM, McDougall I, Ireland TR 1988. Age constraints on metamorphism and the development of a metamorphic core complex in Fiordland, southern New Zealand. Geology 16: 405-408.

Gleadow AJW, Duddy IR, Green PF, Lovering JF 1986a. Confined fission track lengths in apatite: a diagnostic tool for thermal history analysis. Contributions to Mineralogy and Petrology 94: 405-415.

Gleadow AJW, Duddy IR, Green PF, Hegarty KA 1986b. Fission track lengths in the apatite annealing zone and the interpretation of mixed ages. Earth and Planetary Science Letters 78: 245-254.

Green PF, Duddy IR, Laslett GM, Hegarty KA, Gleadow AJW, Lovering JF 1989. Thermal annealing of fission tracks in apatite 4. Quantitative modelling techniques and extension to geological timescales. Chemical Geology: Isotope Geoscience section 79: 155-182.

Hayman NW, Knott JR, Cowan DS, Nemser E, Sarna-Wojcicki AM 2003. Quaternary low-angle slip on detachment faults in Death Valley, California. Geology 31: 343-346.

Herd M 2007. Continental Extensional Tectonics - The Paparoa Metamorphic Core Complex of Westland, New Zealand. Unpublished thesis, University of Canterbury, Christchurch. 189 p.

Hippertt JoFM 1993. V-pull-apart microstructures: a new shear-sense indicator. Journal of Structural Geology 15: 1393-1403.

Hume BJ 1977. The Relationship Between the Charleston Metamorphic Group and the Greenland Group in the Central Paparoa Range, South Island New Zealand. Journal of the Royal Society of New Zealand 7: 379-392.

Hurford AJ, Green PF 1983. The zeta age calibration of fission-track dating. Isotope Geoscience 1: 285-317.

Ireland TR, Gibson GM 1998. SHRIMP monazite and zircon geochronology of high-grade metamorphism in New Zealand. Journal of Metamorphic Geology 16: 149-167.

Jackson JA 1987. Active normal faulting and crustal extension. Geological Society, London, Special Publications 28: 3-17.

Jackson JA, White NJ 1989. Normal faulting in the upper continental crust: observations from regions of active extension. Journal of Structural Geology 11: 15-36.

Jacobs J, Breitkreuz C 2003. Zircon and apatite fission-track thermochronology of Late Carboniferous volcanic rocks of the NE German Basin. International Journal of Earth Sciences 92: 165-172.

Ji S, Martignole J 1994. Ductility of garnet as an indicator of extremely high temperature deformation. Journal of Structural Geology 16: 985-996.

Kerrich R, Rehrig W 1987. Fluid motion associated with Tertiary mylonitization and detachment faulting: 18O/16O evidence from the Picacho metamorphic core complex, Arizona. Geology 15: 58-62.

Ketcham RA, Donelick RA, Carlson WD 1999. Variability of apatite fission-track annealing kinetics; III, Extrapolation to geological time scales. American Mineralogist 84: 1235-1255.

Kimbrough DL, Tulloch AJ 1989. Early Cretaceous age of orthogneiss from the Charleston Metamorphic Group, New Zealand. Earth and Planetary Science Letters 95: 130-140.

Klepeis KA, King D, De Paoli M, Clarke GL, Gehrels G 2007. Interaction of strong lower and weak middle crust during lithospheric extension in western New Zealand. Tectonics 26: TC4017.

Laird MG 1967. Field Relations of the Constant Gneiss and Greenland Group of the Central Paparoa Range, West Coast, South Island. New Zealand Journal of Geology and Geophysics 10: 247-256.

Laird MG 1994. Geologic aspects of the opening of the Tasman Sea, In: Evolution of the Tasman Sea Basin : proceedings of the Tasman Sea Conference, Christchurch, New Zealand, 27-30 November 1992 / edited by Gerrit J. Van Der Lingen, Kerry M. Swanson & Roderick J. Muir. Rotterdam ; Brookfield :, A.A. Balkema.

Laird MG, Bradshaw JD 2004. The Break-up of a Long-term Relationship: the Cretaceous Separation of New Zealand from Gondwana. Gondwana Research 7: 273-286.

Landis CA, Coombs DS 1967. Metamorphic belts and orogenesis in southern New Zealand. Tectonophysics 4: 501-518.

LaTour TE, Barnett RL 1987. Mineralogical changes accompanying mylonitization in the Bitterroot dome of the Idaho batholith: Implications for timing of deformation. Geological Society of America Bulletin 98: 356-363.

Lewthwaite KJ 1995. The Charleston metamorphic group> Paleoyoic and Cretaceous deformation and metamporphism, and development of the Paparoa metamorphic core complex. Unpublished thesis, University of Canterbury, Christchurch. 199 p.

Lister GS, Snoke AW 1984. S-C Mylonites. Journal of Structural Geology 6: 617-638.

Lister GS, Davis GA 1989. The origin of metamorphic core complexes and detachment faults formed during Tertiary continental extension in the northern Colorado River region, U.S.A. Journal of Structural Geology 11: 65-94.

Lister GS, Banga G, Feenstra A 1984a. Metamorphic core complexes of Cordilleran type in the Cyclades, Aegean Sea, Greece. Geology 12: 221-225.

Lister GS, Davis GA, McClelland WC, Marcott DT 1984b. Complexities in the evolution of low-angle crustal shear zones during continental extension. Geological Society of America Abstracts 16: 577.

Ludwig KR 2008. Isoplot: A Geochronological Toolkit for Microsoft Excel. Version 3.72, Berkeley Geochronology Center, Special Publication No. 4.

Marchev P, Kaiser-Rohrmeier M, Heinrich C, Ovtcharova M, von Quadt A, Raicheva R 2005. 2: Hydrothermal ore deposits related to post-orogenic extensional magmatism and core complex formation: The Rhodope Massif of Bulgaria and Greece. Ore Geology Reviews 27: 53-89.

McNamara MJ 1966. Chlorite-Biotite Equilibrium Reactions in Carbonate-Free Systems. Journal of Petrology 7: 404-413.

Menegon L, Pennacchioni G, StÜNitz H 2006. Nucleation and growth of myrmekite during ductile shear deformation in metagranites. Journal of Metamorphic Geology 24: 553-568.

Misch P 1960. Regional structural reconnaissance in Central-northeast Nevada and some adjacent areas: Observations and interpretations. Intermountain Association of Petroleum Geologists Guidebook for the 11th Annual Field Conference: 17-42.

Moody JB, Jenkins JE, Meyer D 1985. An experimental investigation of the albitization of plagioclase. Can Mineral 23: 583-596.

Moore ME, Gleadow AJW, Lovering JF 1986. Thermal evolution of rifted continental margins: new evidence from fission tracks in basement apatites from southeastern Australia. Earth and Planetary Science Letters 78: 255-270.

Muir RJ, Ireland TR, Weaver SD, Bradshaw JD 1994. Ion microprobe U---Pb zircon geochronology of granitic magmatism in the Western Province of the South Island, New Zealand. Chemical Geology 113: 171-189.

Muir RJ, Ireland TR, Weaver SD, Bradshaw JD, Waight TE, Jongens R, Eby GN 1997. SHRIMP U-Pb geochronology of Cretaceous magmatism in northwest Nelson-Westland, South Island, New Zealand. New Zealand Journal of Geology and Geophysics 40: 453-463.

Münker C, Cooper RA 1995. The Island Arc Setting of a New Zealand Cambrian Volcano-Sedimentary Sequence: Implications for the Evolution of the SW Pacific Gondwana Fragments. The Journal of Geology 103: 687-700.

Naeser CW, Faul H 1969. Fission Track Annealing in Apatite and Sphene. J. Geophys. Res. 74: 705-710.

Nathan S 1975. Geological Map of New Zealand, Foulwind and Charleston, sheets S23 and S30, scale 1:63,360. Wellington, N.Z. Dep. of Sci. and Ind. Res.

Nathan S 1978. Geological Map of New Zealand, Buller-Lyell, sheets S31 and S32, scale 1:63,360. Wellington, N.Z. Dep. of Sci. and Ind. Res.

Parsons I 2010. Feldspars defined and described: a pair of posters published by the Mineralogical Society. Sources and supporting information. Mineral Mag 74: 529-551.

Passchier CW, Simpson C 1986. Porphyroclast systems as kinematic indicators. Journal of Structural Geology 8: 831-843.

Passchier CW, Trouw RAJ 1996. Microtectonics. 2nd ed. Berlin Heidelberg, Springer-Verlag. 286 p.

Passchier CW, Trouw RAJ 2005. Microtectonics. 2nd ed. Berlin Heidelberg New York, Springer-Verlag. 366 p.

Phillips ER, Ransom DM, Vernon RH 1972. Myrmekite and muscovite developed by retrograde metamorphism at Broken Hill, New South Wales. Mineralogical Magazine 38: 570-578.

Platt JP, Vissers RLM 1980. Extensional structures in anisotropic rocks. Journal of Structural Geology 2: 397-410.

Price RA, Mountjoy EW 1970. Geologic structure of the Canadian Rocky Mountains between Bow and Athabasca Rivers - A progress report. Geological Association of Canada, Special Paper 6: 7-25.

Proffett JM 1977. Cenozoic geology of the Yerrington district, Nevada, and implications for the nature and origin of Basin and Range faultin. Geological Society of America Bulletin 88: 247-266.

Rahn MK, Brandon MT, Batt GE, Garver JI 2004. A zero-damage model for fission-track annealing in zircon. American Mineralogist 89: 473-484.

Raine JI 1984. Outline of a palynological zonation of Cretaceous to Paleogene terrestrial sediments in West Coast region, South Island, New Zealand. New Zealand Geological Survey Report 109.

Rattenbury MS, Cooper RA, Johnston MR (compilers) 1998. Geology of the Nelson area. Institute of Geological & Nuclear Science 1:250 000 geological map 9. 1 sheet + 67 p. Lower Hutt, New Zealand: Institute of Geological & Nuclear Sciences Limited.

Reiners PW, Brandon MT 2006. USING THERMOCHRONOLOGY TO UNDERSTAND OROGENIC EROSION. Annual Review of Earth and Planetary Sciences 34: 419-466.

Reynolds SJ, Rehrig WA 1980. Mid-Tertiary plutonism and mylonitization, South Mountains, central Arizona. In: Crittenden MD, Coney PJ, Davis GH ed. Cordilleran Metamorphic Core Complexes, Geological Society of America, Memoirs: 159-175.

Ring U, Herd M, Bohlar R, Glodny J, Palin M 2006. Dating mylonitisation in the Paparoa Core Complex, Westland. Abstract for the Geological Society of New Zealand Conference, Palmerston North, 4-7 December.

Ring UWE, Bernet M 2010. Fission-track analysis unravels the denudation history of the Bonar Range in the footwall of the Alpine Fault, South Island, New Zealand. Geological Magazine FirstView: 1-13.

Rosenbaum G, Regenauer-Lieb K, Weinberg R 2005. Continental extension: From core complexes to rigid block faulting. Geology 33: 609-612.

Seward D 1989. Cenozoic basin histories determined by fission-track dating of basement granites, South Island, New Zealand. Chemical Geology: Isotope Geoscience section 79: 31-48.

Seward D, White PJ 1992. Evolution and eversion of a tertiary sedimentary basin, Paparoa Range, West Coast, South Island, New Zealand: Evidence from fission-track dating. New Zealand Journal of Geology and Geophysics 35: 265 - 271.

Shelley D 1970a. The origin of myrmekitic intergrowths and a comparison with rod eutectics in metals. Mineralogical Magazine 37: 674-681.

Shelley D 1970b. The structure and petrography of the Constant Gneiss near Charleston, South-west Nelson. New Zealand Journal of Geology and Geophysics 13: 370-391.

Shelley D 1972. Structure of the Constant Gneiss near Cape Foulwind, South-west Nelson, and its bearing on the regional tectonics of the West Coast. New Zealand Journal of Geology and Geophysics 15: 33-48.

Simpson C 1985. Deformation of granitic rocks across the brittle-ductile transition. Journal of Structural Geology 7: 503-511.

Simpson C, Schmid SM 1983. An evaluation of criteria to deduce the sense of movement in sheared rocks. Geological Society of America Bulletin 94: 1281-1288.

Simpson C, Wintsch RP 1989. Evidence for deformation-induced K-feldspar replacement by myrmekite. Journal of Metamorphic Geology 7: 261-275.

Spell TL, McDougall I, Tulloch AJ 2000. Thermochronologic constraints on the breakup of the Pacific Gondwana margin: The Paparoa metamorphic core complex, South Island, New Zealand. Tectonics 19: 433-451.

Steiger RH, Hart SR 1967. The Microcline-Orthoclase Transition within a Contact Aureole. American Mineralogist 52: 87-116.

Storey CD, Prior DJ 2005. Plastic Deformation and Recrystallization of Garnet: A Mechanism to Facilitate Diffusion Creep. Journal of Petrology 46: 2593-2613.

Stringham BF 1952. Fields of formation of some common hydrothermal-alteration minerals. Economic Geology 47: 661-664.

Tagami T, Galbraith RF, Yamada R, Laslett GM 1998. Revised annealing kinetics of fission tracks in zircon and geological implications. In: Van den haute P, De Corte F ed. Advances in Fission-Track Geochronology. New York, Springer: 99-112.

Tareen J, Krishnamurthy K 1981. Hydrothermal stability of hematite and magnetite. Bulletin of Materials Science 3: 9-13.

ten Grotenhuis SM, Trouw RAJ, Passchier CW 2003. Evolution of mica fish in mylonitic rocks. Tectonophysics 372: 1-21.

Thomson SN, Ring U 2006. Thermochronologic evaluation of postcollision extension in the Anatolide orogen, western Turkey. Tectonics 25: TC3005.

Thomson SN, Ring U, Brichau S, Glodny J, Will TM 2009. Timing and nature of formation of the Ios metamorphic core complex, southern Cyclades, Greece. Geological Society, London, Special Publications 321: 139-167.

Tullis J 1983. Deformation of Feldspars. In: Ribbe PH ed. Feldspar Mineralogy, Mineralogical Society of America, Reviews in Mineralogy & Geochemistry: 297-323.

Tulloch AJ 1988. Batholiths, plutons and suites: Nomenclature for the granitoid rocks of Westland-Nelson. New Zealand Journal of Geology and Geophysics 31: 505-509.

Tulloch AJ 1995. Precious metal mineralisation associated with the Cretaceous Paparoa metamorphic core complex, New Zealand. Proceedings of the 1995 PACRIM Congress. Pp. 575-580.

Tulloch AJ, Kimbrough DL 1989. The Paparoa Metamorphic Core Complex, New Zealand: Cretaceous extension associated with fragmeotation of the Pacific margin of Gondwana. Tectonics 8: 1217-1234.

Tulloch AJ, Palmer K 1990. Tectonic implications of the granite cobbles from the mid-Cretaceous Pororari Group, southwest Nelson, New Zealand. New Zealand Journal of Geology and Geophysics 33: 205-217.

Tulloch AJ, Ramezani J, Mortimer N, Mortensen J, Van den Bogaard P, Maas R 2009. Cretaceous felsic volcanism in New Zealand and Lord Howe Rise (Zealandia) as a precursor to final Gondwana break-up. In: Ring U, Wernicke B ed. Extending a continent: architecture, rheology and heat budget, Geological Society Special Papers: 89-118.

Vidal J-L, Kubin L, Debat P, Soula J-C 1980. Deformation and dynamic recrystallization of K feldspar augen in orthogneiss from Montagne Noire, Occitania, Southern France. Lithos 13: 247-255.

Villa 1998. Isotopic closure. Terra Nova 10: 42-47.

Voll G 1976. Recrystallization of quartz, biotite and feldspars from Erstfeld to the Leventina nappe, Swiss Alps, and its geological significance. Schweiz Mineral Petrogr Mitt 56: 641-647.

Weissel JK, Hayes DE 1977. Evolution of the Tasman Sea reappraised. Earth and Planetary Science Letters 36: 77-84.

Wernicke B, Burchfiel BC 1982. Modes of extensional tectonics. Journal of Structural Geology 4: 105-115.

White PJ 1994. Thermobarometry of the Charleston Metamorphic Group and implications for the evolution of the Paparoa Metamorphic Core Complex, New Zealand. New Zealand Journal of Geology and Geophysics 37: 201 - 209.

Wickham SM 1987. Crustal Anatexis and Granite Petrogenesis During Low-pressure Regional Metamorphism: The Trois Seigneurs Massif, Pyrenees, France. Journal of Petrology 28: 127-169.

Wijns C, Weinberg R, Gessner K, Moresi L 2005. Mode of crustal extension determined by rheological layering. Earth and Planetary Science Letters 236: 120-134.